



**UNIVERSIDAD DE CHILE
FACULTAD DE CIENCIAS FISICAS Y MATEMATICAS
DEPARTAMENTO DE INGENIERÍA ELÉCTRICA**

**BRAIN MAGNETIC RESONANCE IMAGE SEGMENTATION FOR THE
CONSTRUCTION OF AN ANATOMICAL MODEL DEDICATED TO
MECHANICAL SIMULATION**

**TESIS PARA OPTAR AL GRADO DE DOCTOR EN
INGENIERÍA ELÉCTRICA**

FRANCISCO JOSÉ GALDAMES GRÜNBERG

**PROFESOR GUIA:
DR. CLAUDIO PEREZ FLORES**

**MIEMBROS DE LA COMISION:
DR. MARCELO GUARINI HERRMANN
DR. CLAUDIO HELD BARRANDEGUY
DR. PABLO IRARRÁZABAL MENA**

Este trabajo ha sido parcialmente financiado por los proyectos FONDEF D04I1237 y D08I1060, FONDECYT 1120613, ECOS-CONICYT C06E04, el programa ALFA-IPECA, y el proyecto PLOMO.

**SANTIAGO DE CHILE
OCTUBRE 2012**

Segmentación de Imágenes Cerebrales de Resonancia Magnética Nuclear para la Construcción de un Modelo Anatómico Destinado al Modelamiento Mecánico

Resumen: Durante una neurocirugía se debe contar con información anatómica precisa, la cual es comúnmente obtenida por medio de un registro entre la posición del paciente y datos pre-operatorios. Uno de los principales problemas para realizar este registro es la deformación del cerebro durante la cirugía, fenómeno conocido como *Brain Shift*. Para solucionar este problema se han creado modelos mecánicos del cerebro, con los cuales es posible aproximar la deformación real. Estos modelos mecánicos requieren un modelo anatómico del paciente, el cual se obtiene, en la mayor parte de los casos, por medio de una segmentación manual o semi-manual. El objetivo de esta tesis es mejorar la obtención del modelo anatómico, proponiendo un método automático para obtener un modelo anatómico del cerebro, adaptado a la anatomía particular del paciente y adecuado para un posterior modelamiento mecánico.

El método propuesto realiza una pre-segmentación del cerebro, seguida de una segmentación basada en modelos deformables para identificar las estructuras anatómicas más relevantes para el modelamiento mecánico. Se incluyen las estructuras comúnmente utilizadas en la literatura: superficie cortical, superficie interna del cráneo y ventrículos. Además, se incluyen las membranas internas del cerebro: falx cerebri y tentorium cerebelli. Estas membranas se han incorporado en los modelos de muy pocas publicaciones, aun cuando su importancia es reconocida en la literatura.

La segmentación por modelos deformables que se ha implementado está principalmente basada en mallas simplex, las cuales son duales topológicos de las mallas de triángulos. Para aprovechar las cualidades complementarias de estas dos representaciones, se ha desarrollado un nuevo método de transformación entre ellas. Nuestro método usa una interpolación geométrica basada en la distancia a los planos tangentes a los vértices de las mallas. El método de transformación fue evaluado usando mallas estándar y obtuvo excelentes resultados al compararlo con el método actualmente más usado, el cual emplea el centro de gravedad de las caras de las mallas. En nuestro método de segmentación las estructuras son segmentadas de manera secuencial y respetando las relaciones anatómicas entre ellas. La segmentación obtenida fue evaluada empleando las bases de datos en línea más usadas (BrainWeb, IBSR, SVE). La segmentación de cada estructura fue evaluada de manera independiente y se realizaron algunas comparaciones con métodos de segmentación populares y establecidos, obteniendo resultados superiores. Las segmentaciones de la superficie cortical, la superficie interna del cráneo y los ventrículos fueron evaluadas usando los índices de Jaccard (J) y Dice (κ). Los resultados para la superficie cortical fueron: $J = 0.904$ y $\kappa = 0.950$ en BrainWeb; $J = 0.902$ y $\kappa = 0.948$ en IBSR; $J = 0.946$ y $\kappa = 0.972$ en SVE. Los resultados para la superficie interna del cráneo fueron $J = 0.945$ y $\kappa = 0.972$ en BrainWeb. Los resultados para los ventrículos fueron: $J = 0.623$ y $\kappa = 0.766$ en IBSR. Las segmentaciones de las membranas internas del cerebro fueron evaluadas midiendo la distancia entre nuestra segmentación y la posición estimada de las membranas en la base de datos IBSR. La distancia media para el tentorium cerebelli fue 1.673 mm, y para el falx cerebri fue 0.745 mm.

Palabras clave: Brain Shift, Segmentación de Imágenes de Resonancia Magnética (IRM) Cerebrales, Modelamiento Biomecánico, Malla Simplex, Modelos Deformables.

Brain Magnetic Resonance Image Segmentation for the Construction of an Anatomical Model Dedicated to Mechanical Simulation

Abstract: The availability of accurate anatomical information is of paramount importance during a neurosurgery. This information is usually obtained by a registration between the patient's position and pre-operative data. One of the main problems to perform the registration is that the brain suffers deformations during the neurosurgery in a process called *Brain Shift*. Mechanical models of the brain have been developed to approximate its real deformation as a solution to improve the registration. These mechanical models require an associated patient specific anatomical model which is commonly obtained by manual or semi-manual segmentation. The aim of this thesis is to propose and implement an automated method to obtain a patient specific anatomical model of the brain suitable for a subsequent mechanical modeling.

The proposed method performs a pre-segmentation of the brain followed by a segmentation based on deformable models to identify the most relevant structures for mechanical modeling. The most commonly used structures in the literature are included: cortical surface, inner surface of the skull, and ventricles. Moreover, the internal membranes of the brain are also included: falx cerebri and tentorium cerebelli. Even though the importance of these structures is stated in the literature, only a few publications include them in their models.

The implemented segmentation by deformable models is mainly based on simplex meshes, which are topological duals of triangle meshes. To take advantage of the complementary qualities of these two representations, a new transformation method between them has been developed. Our method uses a geometric interpolation based on the distance to the tangent planes of the vertices of the meshes. The transformation method was evaluated using standard meshes, and it was compared with the most used method, which uses the center of mass of the faces of the meshes, obtaining excellent results. In our segmentation method, the structures are segmented sequentially and maintaining the anatomical relationships between them. The segmentation obtained with our method was evaluated using the most used online databases (BrainWeb, IBSR, SVE). The segmentation of each structure was evaluated independently, and comparisons were performed with established segmentation methods obtaining better results. The segmentations of the cortical surface, the inner surface of the skull, and the ventricles were evaluated using the Jaccard (J) and Dice (κ) indices. The results for the cortical surface were: $J = 0.904$ and $\kappa = 0.950$ on BrainWeb; $J = 0.902$ and $\kappa = 0.948$ on IBSR; $J = 0.946$ and $\kappa = 0.972$ on SVE. The results for the inner surface of the skull were: $J = 0.945$ and $\kappa = 0.972$ on BrainWeb. The results for the ventricles were: $J = 0.623$ and $\kappa = 0.766$ on IBSR. The segmentations of the internal membranes of the brain were evaluated by measuring the distance between our segmentation and the estimated position of the membranes in the IBSR database. The mean distance for the tentorium cerebelli was 1.673 mm, and for the falx cerebri was 0.745 mm.

Keywords: Brain Shift, Magnetic Resonance Imaging (MRI) Brain Segmentation, Biomechanical Modeling, Simplex Mesh, Deformable Model.

To my parents.

Acknowledgment

I would like to thank my advisor in Chile, Claudio Perez. I have worked with him for most of my post-graduate studies and I have always counted with his support, experience and guide. I also thanks my advisors in France, Fabrice Jaillet and Johan Payan, for all the support they gave me. I am especially grateful to Fabrice for his sincere friendship, all the help he gave me in France, the trips, and his hospitality in Concepción during the time he worked there.

I would also thank the members of the commission for their reviews and suggestions: Marcelo Guarini, Claudio Held and Pablo Irrarrázabal.

Thanks to the members of the Centro de Modelamiento Matemático of the Universidad de Chile with whom I worked in the beginning of this project: Raul Gouet, Fabrice Chassat and Takeshi Asahi. I also thank the members of the Instituto de Neurocirugía Asenjo with whom I worked during my stay at the radiology department.

Thanks to the members of the LIRIS laboratory for their welcome during my stay in France: Behzad Shariat, Saida Bouakaz, Jacques Saadé, Hichem Barki, Youssef Roummieh and Yehia Taher. Special thanks to Jean-Michel Moreau and Florence Zara for the corrections of my dissertation.

I thank Jacques Demongeot for his strong support during the general crisis of the projects.

Special thanks to my closest friend in this double PhD between Chile and France, Leo Causa. We have been through so much together. I also thank those who started with me as members of the ALFA project in Chile : Marek Bucki, Claudio Lobos and Alfredo Lopez.

Thanks to my friends at the imaging laboratory of the Universidad de Chile: Luis, Cristian, Cament, JP, Jacob, Jorge, Carlos, Alonso, Shulz, Carloncho, Pablo. They have made from this laboratory not only a good place to work, but also to stay and share. Also, I am grateful to all those friends who have always been with me, supporting and trusting me: Pipo, Vargas, Daniela, Cristian, Palma, Juanita, Javiera, Cecile, Paris, Christian Peña, Lucci, Paz, Diana, Doriane, Valentina, Clau, Pita... I know they will be with me for much longer.

I wish to thank all the friends I made in Lyon. They are many, but I can mention a few: Cynthia, Ramiro, William, Boris, Bexen, Gaby, Pacho, Amelie. Special thanks to Johan and Pamela for letting me stay in their homes.

Finally, all the thanks in the world to my family. Thanks to my parents for their unconditional support and love, and to my brother for his friendship and help.

This thesis has been financially supported by the FONDEF projects D04I1237 and D08I1060, FONDECYT project 1120613, ECOS-CONICYT project C06E04, ALFA-IPECA program, and PLOMO project.

Contents

Abbreviations And Acronyms	1
1 Introduction	4
1.1 General Motivation	4
1.2 Definition of the Problem	7
1.2.1 Computer Assisted Surgery	7
1.2.2 Computer Assisted Neurosurgery	9
1.2.3 Brain Mechanical Models	12
1.2.4 Obtaining the Anatomical Model	16
1.2.4.1 Cortical Surface Segmentation	16
1.2.4.2 Skull Segmentation	18
1.2.4.3 Ventricle Segmentation	20
1.2.4.4 Membrane Segmentation	22
1.3 Objectives	23
1.3.1 General Objectives	23
1.3.2 Specific Objectives	23
1.4 Proposed Solution	24
1.5 Structure of the Document	25
2 Methodology	26
2.1 Simplex Meshes	30
2.1.1 General Definition	30
2.1.1.1 Simplex Meshes and Triangulations	31
2.1.1.2 Local Geometry of 2-Simplex Meshes	33
2.1.1.3 Local Geometry of Contours in 2-Simplex Meshes	36
2.1.2 Mesh Deformation	38
2.1.3 Internal Forces	39
2.1.3.1 Internal Forces on a Contour	41
2.1.4 External Forces	41
2.1.4.1 External Forces on a Contour	43
2.2 Transformation Between Triangulations and Simplex Meshes	44
2.2.1 Interpolation Based on Tangent Planes	46
2.2.1.1 Weights Computation	48
2.2.2 From Triangulation to Simplex Mesh	50

2.2.3	From Simplex Mesh to Triangulation	51
2.2.4	Transformation Results	52
2.3	MRI Segmentation	58
2.3.1	Pre-segmentation	60
2.3.1.1	Background Elimination	62
2.3.1.2	Brain Identification	63
2.3.1.3	Modeling by Gaussians	68
2.3.2	Initial Generic Meshes	74
2.3.3	Geometric Adjustment of the Meshes	75
2.3.4	Cortical Surface Segmentation	77
2.3.4.1	First Mesh Deformation	77
2.3.4.2	Second Mesh Deformation	78
2.3.4.3	Third Mesh Deformation	81
2.3.4.4	Mesh Self-intersection Control	82
2.3.4.5	Cortical Surface Segmentation as a Skull Strip- ping Method	85
2.3.5	Skull Mesh Deformation	86
2.3.6	Ventricle Mesh Deformation	90
2.3.7	Open Meshes	91
2.3.7.1	Tentorium Mesh Deformation	93
2.3.7.2	Falx Mesh Deformation	95
2.3.8	Final Mesh	98
3	Experiments and Results	100
3.1	Databases and Performance Measurements	100
3.1.1	Evaluation of Closed Meshes Segmentation	102
3.1.2	Evaluation of Open Meshes Segmentation	106
3.2	Segmentation Results	108
3.2.1	Cortical Surface Segmentation	108
3.2.2	Skull Segmentation	114
3.2.3	Ventricles Segmentation	116
3.2.4	Tentorium Cerebelli and Falx Cerebri Segmentation	118
4	Discussion and Conclusions	120
4.1	Discussion	121
4.2	Conclusion and Prospects	125
4.3	Publications	126

Bibliography	128
A Anatomical Terms of Location	160
A.1 Directional Terms	160
A.2 Anatomical Orientation Planes	162
B Brain Anatomy	163
B.1 General Brain Anatomy	163
B.2 Cerebral Hemispheres	165
B.2.1 Cerebral Cortex	166
B.2.2 White Matter	167
B.3 Cerebellum	168
B.4 Meninges	170
B.4.1 Dura Mater	170
B.4.2 Arachnoid Mater	171
B.4.3 Pia Mater	171
B.5 Cerebrospinal Fluid	172
B.5.1 Ventricles	173
C Magnetic Resonance Imaging	175
C.1 Magnetic Resonance	175
C.2 Image acquisition	177

Abbreviations and Acronyms

κ : Dice Coefficient [Dice 1945].

J : Jaccard similarity index [Jaccard 1912].

AM: Active Models.

ANN: Artificial Neural Networks.

ANOVA: Analysis of Variance.

ASM: Active Shape Model.

BeaST: Brain Extraction based on nonlocal Segmentation Technique [Eskildsen 2012].

BEM: Boundary Element Method.

BEMA: Brain Extraction Meta Algorithm [Rex 2004].

BET: Brain Extraction Tool [Smith 2002, Jenkinson 2005].

BSE: Brain Surface Extractor [Sandor 1997, Shattuck 2001].

CAS: Computed Assisted Surgery.

CNS: Central Nervous System.

CSF: Cerebrospinal Fluid.

CT: Computed Tomography.

DT-MRI: Diffusion Tensor Magnetic Resonance Imaging.

DTI: Diffusion Tensor Imaging.

EEG: Electroencephalography.

FE: Finite Element.

FEM: Finite Element Method.

FID: Free Induction Decay.

fMRI: Functional Magnetic Resonance Imaging.

FMRIB: Functional MRI of the Brain [FMRIB].

FN: False Negative.

FNR: False Negative Rate.

FP: False Positive.

FPR: False Positive Rate.

FS: FreeSurfer [Fischl 2002, Fischl 2004].

FSL: FMRIB Software Library [FMRIB].

GCUT: Graph Cuts Skull Stripping [Sadanathan 2010].

GM: Gray Matter.

GNU: GNU's Not Unix.

HNN: Hopfield Neural Network.

HWA: Hybrid Watershed Algorithm [Ségonne 2004].

IBSR: Internet Brain Segmentation Repository [Center for Morphometric Analysis 1995].

IGS: Image Guided Surgery.

ITK: Insight Segmentation and Registration Toolkit [ITK].

KAM: Knowledge-guided Active Model [Shan 2007].

LDDMM: Large Deformation Diffeomorphic Metric Mapping [Beg 2005].

LEGION: Locally Excitatory Globally Inhibitory Network [Belardinelli 2003].

LONI: Laboratory of Neuro Imaging, at University of California, Los Angeles.

MAPS: Multi-Atlas Propagation and Segmentation [Leung 2011].

McStrip: Minneapolis Consensus Strip [Rehm 2004].

MEG: Magnetoencephalography.

MI: Mutual Information.

MR: Magnetic Resonance.

mRG: modified Region Growing [Yoon 2001].

MRI: Magnetic Resonance Imaging.

PD: Proton Density.

PDM: Point Distribution Model.

PET: Positron Emission Tomography.

RMS: Root Mean Square.

ROBEX: Robust Learning-Based Brain Extraction [Iglesias 2011].

SD: Standard Deviation.

SMDS: Simplex Mesh Diffusion Snake [Tejos 2009].

SPECT: Single Photon Emission Computed Tomography.

SPECTRE: Simple Paradigm for Extra-Cerebral Tissue Removal [Carass 2011].

SPM: Statistical Parametric Mapping [Ashburner 2000].

SSB: Scalp-Skull-Brain.

SVE: Segmentation Validation Engine [Shattuck 2009].

SVM: Support Vector Machine.

TN: True Negative.

TP: True Positive.

US: UltraSound.

WM: White Matter.

XFEM: Extended Finite Element Method.

CHAPTER 1

Introduction

Contents

1.1	General Motivation	4
1.2	Definition of the Problem	7
1.2.1	Computer Assisted Surgery	7
1.2.2	Computer Assisted Neurosurgery	9
1.2.3	Brain Mechanical Models	12
1.2.4	Obtaining the Anatomical Model	16
1.3	Objectives	23
1.3.1	General Objectives	23
1.3.2	Specific Objectives	23
1.4	Proposed Solution	24
1.5	Structure of the Document	25

1.1 General Motivation

The basis of modern medical imaging began when the professor of physics Wilhelm Conrad Röntgen accidentally discovered the X-rays on the 8th of November of 1895 (Fig. 1.1). The discovery of Röntgen was described by Henri Poincaré at the French Academy of Sciences in January of 1896, where the physicist Henri Becquerel was present. The new discovery encouraged Becquerel to do further research, and the same year he began new experiments, discovering the natural radiation in uranium salts. This type of emission was then called Becquerel rays. In 1897, Marie Skłodowska Curie began, under the supervision of Henri Becquerel, the studies for her doctoral thesis on radioactivity which was presented in 1903. With the help of her husband, Pierre Curie, she purified thorium and discovered

its radioactivity. Moreover, she purified and discovered two new radioactive elements: polonium and radium. In 1897, Joseph John Thomson discovered that the cathode ray used to generate X-rays is formed by negative particles that he called “corpuscles”, but nowadays are known as electrons. Ernest Rutherford, the pupil of Thomson, studied the Becquerel rays and made a publication in 1899 where he stated that they are composed of two different types of radiation: α rays and β rays. Finally, in 1900, Paul Villard discovered a new kind of radiation. This radiation was more penetrating than the Becquerel α and β rays, and it was called γ rays by Rutherford in 1903. These different types of radiation, identified in only a few years after the discovery of X-rays, are the physical bases upon which many of the main types of medical imaging have been developed [Hendee 2002].

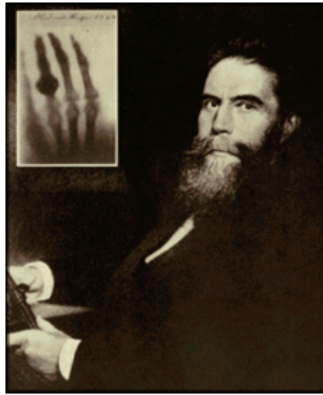


Figure 1.1: Wilhelm Conrad Röntgen (1895) with the first x-ray image. The image shows the hand of his wife's hand with the wedding ring. (Source: [AccessExcell 2012].)

After these pioneering discoveries, medical imaging has evolved considerably, slowly first and quite fast in the last 50 years. Nowadays, medical imaging is used in research, diagnosis, treatment, surgical planning, image guided surgeries, etc. The concept of *Image Guided Surgery* (IGS) or *Computed Assisted Surgery* (CAS) is explained more in details in section 1.2.1. However, to introduce the context of this thesis, we can say that, in the operating room, the CAS takes into account all the computational techniques deployed to assist the surgeon. Images of the operation area, mechanical arms to manipulate tools, or spatial localizers to know the positions of the tools, count among popular techniques. As its name suggests, the main part of a CAS systems are the images, which are used, for example, to provide the surgeon with information or to guide other components, e.g., a robot.

The general problem that motivates the work developed in this thesis is: “*how to obtain anatomical information in the operating room?*”. Specifically, we will consider a particular case of operating room scenario, *Neurosurgery*. In this kind of surgery, the anatomical information is usually provided by Magnetic Resonance (MR) images (Appx. C), since they allow to clearly visualize brain soft tissues. MR images are acquired before surgery for diagnosis and planning. Preoperative images are also usually used during the surgery, because it is complex and expensive to acquire MRI images in the operating room. These images provide valuable anatomical information, enabling the surgeon to carry out the planned surgery. A registration between these images and the patient position in the operating room has to be carried out, in order to define the spatial position of the anatomy shown in the images. The problem is that the brain suffers deformations during the surgery, in a process called *brain shift*. These alterations imply that the computed spatial position (registration) of the image loses validity a short time after the beginning of the surgery. To correct the registration, information acquired in the operating room during the surgery may be used, for example, the position of the exposed surface of the brain or UltraSound (US) images localized in 3D. Thus, the registration is corrected using the measured position of the brain surface, or the position of some anatomical structures that can be identified in the US. The new registration will compensate the problem to a certain extent. Nevertheless, sufficient information is lacking, leading to a flawed registration.

Mechanical models of the brain have been developed as a solution to improve this registration. Using these models, it is possible to compute an estimated brain deformation under certain boundary conditions. Moreover, the boundary conditions can be updated using the same kind of information mentioned above to correct the registration. In the literature, there are a variety of methods for implementing these models, with different equation laws for continuum mechanic [Miga 2000, Xu 2001, Miller 2002, Clatz 2003, Taylor 2004, Wittek 2004, Lunn 2006], and different reported mechanical properties of the tissues [Metz 1970, Miga 1999b, Gefen 2004, Miller 2005a, Schiavone 2009]. However, a patient specific anatomical model is always required. The aim of this thesis is to propose and implement a method to obtain a model of the brain fitted to the patient’s anatomy and suitable for mechanical modeling. The model will include external and internal brain structures, relevant for mechanical simulations.

1.2 Definition of the Problem

The context of the problem addressed in the thesis as well as the scope of the solution are explained in this section. An introduction to the general concept of *Computer Assisted Surgery* (CAS) will be given first.

1.2.1 Computer Assisted Surgery

Computer Assisted Surgery (CAS) is the utilization of computational techniques to assist the surgeon in all stages of the surgical process: diagnosis, planning and execution. This concept includes, for example, methods of image acquisition, visualization and simulation. CAS takes place conceptually between the patient and the surgeon, without attempting to replace him, which is still impossible with the available techniques.

CAS is also called Image-Guided Surgery, and as its name implies, the main stage is the acquisition of images to provide the surgeon with additional information [Peters 2006]. In some cases, this information may consist of a model of the patient, that contains anatomical information of the area where the surgery takes place, but it may also incorporate functional information, such as blood flow, pressure, temperature, etc.

Medical Image Modalities. Images used in CAS can be acquired by a variety of methods, in 2D or 3D format. Among the most popular medical imaging systems to acquire 3D images, we can find: 3D UltraSound (US), Magnetic Resonance Imaging (MRI), Computed Tomography (CT), Single Photon Emission Computed Tomography (SPECT) or Positron Emission Tomography (PET) [Bankman 2000, Hendee 2002]. All these systems provide different kind of information, that can be divided into *functional* and *anatomical*. CT and US are images that provide anatomical information. MRI is another imaging technique that can provide anatomical information. This image system is based on the electromagnetic behavior of the tissue. MRI is the most commonly used imaging modality in neurosurgery, because of its great flexibility and its ability to provide different types of information about the tissue. The most popular types of images produced by MRI are: T₁-weighted, T₂-weighted and spin density weighted MRI (Appx. C). Moreover, this technique can be used to obtain functional MRI (fMRI) [Belliveau 1991, Ogawa 1993] or diffusion tensor imaging (DTI), which allows to follow the path of fibers in the brain tissue [Basser 1994, Heiervang 2006]. Among the medical imaging modalities that

provide 3D functional information we can mention SPECT and PET. These two modalities use radioactive tracers to acquire images.

Image Processing. No matter the method or technique, images must be processed to obtain as much information as possible. The image *registration* is among the most common processing [den Elsen 1993, Maintz 1998], whereby information provided by different imaging systems can be complemented. Image registration is the process of transforming different images into the same coordinate system such that the anatomical structures match. In this way, the information provided by each image, at a particular position relative to the coordinate system, corresponds to information obtained from the same position in the real space (the same place in the patient's body). Images to be registered may be of the same modality (monomodal registration) or of different modalities (multimodal registration). Moreover, inter-patient registration can be performed, for example, to create an anatomical atlas. *Segmentation* is another typical processing performed on medical images [Pham 2000, Withey 2007, McInerney 1996]. Segmentation is the identification of a particular tissue or structure, recognizing its position and shape. Geometric information of the anatomical structures can be obtained using this processing, for example: relative location, size, volume, detection and recognition of abnormal shapes, etc.

The above mentioned processes can be used to create a 3D model of the patient. The information provided by different modalities may be incorporated to the model, including anatomical and functional information. In the treatment of a patient, the model can be first used for diagnosis and surgical planning. At this stage, techniques for visualizing and manipulating images are used to plan the surgery in a virtual environment [Gering 2001, Scharf 2009].

The same patient model used for surgical planning can then be used to assist the surgeon during surgery. In the operating room, the information can be displayed using 3D visualization techniques, such as *Virtual Reality* [Suzuki 2005] and *Augmented Reality* [Shuhaiber 2004, Liao 2008] (Fig. 1.2). Nevertheless, if the model is not positioned in the same reference system used for the patient within the operating room (real space), much of the geometrical information is lost. If there is no spatial relationship between the image (or model) and the patient, the surgeon does not hold quantitative information and should base his movements only on qualitative information. To avoid this, a new *registration* should be performed between the model and the patient position in the operating room, i.e., set the image and the patient in the same reference system to

match the anatomical structures [Audette 2003b]. Among the methods used for this registration, the most common is the stereotactic frame [Maciunas 1994] used in neurosurgery. Others methods are optical localizers using reflective markers or infrared diodes fixed to a rigid body, such as the Optotrak® and Polaris® systems (Northern Digital Inc., Ontario, Canada) [Shahidi 2002, West 2004, Sun 2005]. Passive articulated frames [Sandeman 1994] and electromagnetic localizers [Raab 1979, Shahidi 2002, Atuegwu 2008] are also popular solutions. In addition, to update preoperative images registered with the patient position during surgery, intraoperative images can also be used, e.g., US images with spatial localization [Pennec 2001] or MRI [Nimsky 2001]. However, intraoperative imaging is often expensive and difficult to acquire, which prevent its routine use.

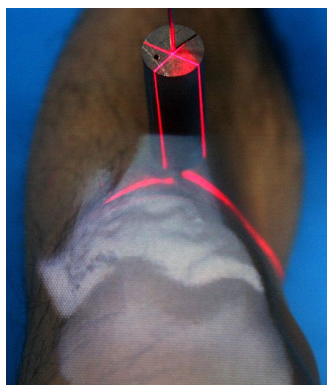


Figure 1.2: Image of an Augmented Reality system for knee surgery, created using laser guidance techniques and 3D autostereoscopic images [Liao 2008]. The image shows a segmented CT superimposed on the patient's knee.

CAS systems can be divided into *passive* and *active* [Cinquin 2011]. Passive systems, or surgical navigation systems, provide the surgeon with information in the planning and execution stages (real time). On the other hand, active systems have the ability to perform some automatic actions during operation, for example, using a robot [Lee 2010, daVinciSurgi] (Fig. 1.3).

1.2.2 Computer Assisted Neurosurgery

To give an overview and a better understanding of the subject, the technical anatomical terms of location and the brain anatomy are presented in Appendices A and B, respectively.

Neurosurgery is one of the surgical specialties in which accuracy is of great importance, and therefore CAS has known great evolution in this

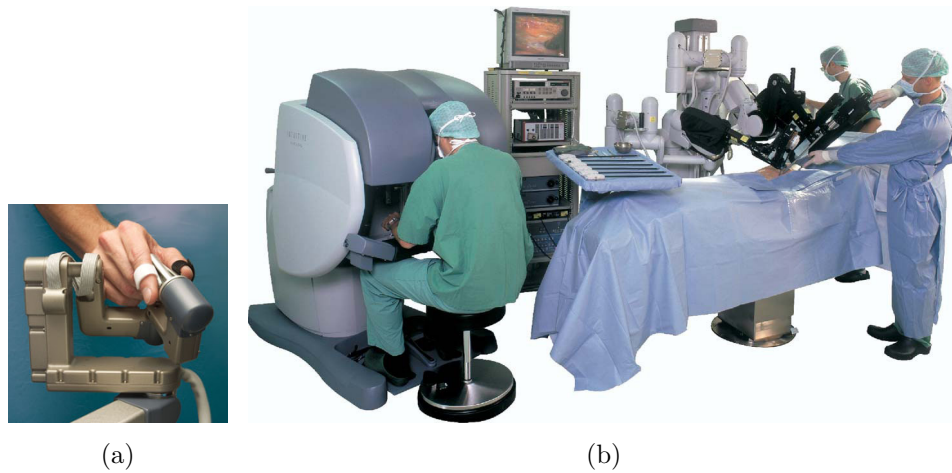


Figure 1.3: *Da Vinci* robotic surgery system created by *Intuitive Surgical*®. This robotic system for computer-assisted surgery is designed to perform minimally invasive surgeries. The surgeon can operate the system through manual controls (a) that move robotic arms holding the instruments (b). [daVinciSurgi]

area [Barnett 2005]. Even minimal damage on certain brain anatomical structures may lead to serious problems for the patient, even death. Despite this, before new imaging and 3D positioning techniques were commonly used, neurosurgery was based on qualitative approaches. These approaches relied on the surgeon's manual skill guided by indirect information from projective radiography (ventriculography, pneumoencephalography, etc.) and clinical evidence. For these reasons, surgeries lasted longer, and consequently were costlier; sometimes it was very difficult to localize the interest area, and serious consequences were caused to the patient due to intense tissue manipulation.

High-quality 3D images are necessary in neurosurgery because of the fragility of the involved structures [Clatz 2005]. Suitable intraoperative images can be obtained by using systems such as intraoperative CT [Lunsford 1982] or MRI [Sutherland 1999]; however both are expensive and involve additional problems: CT systems release ionizing radiation and do not provide good quality images of soft tissues, whereas MRI systems are incompatible with conventional surgical instruments due to the high magnetic fields they generate.

Another option to have images related to the patient position in the operating room is to register a pre-operative image with the patient position [Audette 2003b] (sec. 1.2.1). The brain has been a historical candidate for this type of registration, because, although being a soft tissue, it keeps an almost

rigid position relative to the skull. Indeed, neurosurgery was one of the first areas in which reference systems were used to provide the surgeon with quantitative information relating preoperative images with the patient position in the operating room. Those first reference systems were based on stereotactic frames (Fig. 1.4). They consist of a rigid structure that is fixed to the patient's skull, usually with screws. The structure has a coordinate system with moving parts to locate any point in space. To relate a point in the real space of the operating room to a point in the image, the frame must be visible in the image. Therefore, preoperative images must be acquired with the frame fixed to the skull. However, the stereotactic frames are uncomfortable for the patient and restrict the surgeon's movements during the surgery. Many systems have been developed to solve these problems, including those mentioned previously in section 1.2.1. However, although a good initial registration may be obtained by a rigid transformation, this registration loses validity as the brain undergoes deformation during surgery. This phenomenon is called *brain shift*.

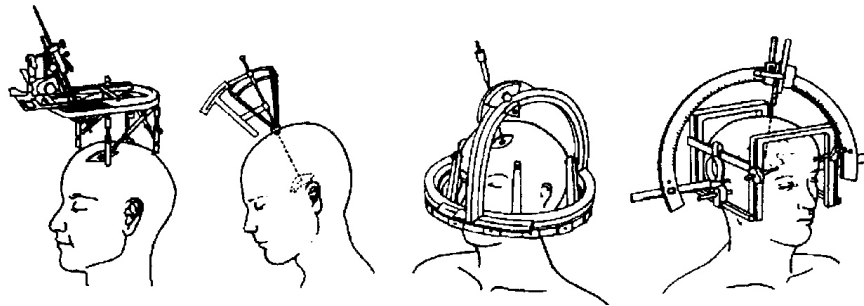


Figure 1.4: Different types of stereotactic frames. [Maciunas 1994]

The Brain Shift Phenomenon. Brain deformation during surgery, or *brain shift*, is mainly caused by gravity [Miga 1999b, Nabavi 2001] and loss of cerebrospinal fluid (CSF). Other factors that may affect the deformation are: administered drugs, blood pressure, patient characteristics, extracted tissue, tissue retraction, and so on. The deformation occurs during the whole surgery, and can take a variable course even in opposite directions through the surgery [Nabavi 2001]. This deformation can influence the success, for example, of surgeries for tumor extraction, such as in [Benveniste 2005] where the probability of success in a surgery with brain shift is evaluated.

Brain shift has been measured in some works, and its characteristics and causes have been largely studied. Some of the methods used to measure

the deformation are: US [Buchholz 1997, Letteboer 2005], displacement of the exposed cortical surface [Roberts 1998, Sinha 2005], or MRI [Dickhaus 1997, Nimsky 2000, Nabavi 2001, Penney 2002, Hartkens 2003, Hastreiter 2004]. Mean deformations of even 24.0 mm have been reported [Nabavi 2001, Nimsky 2000], and the degree of deformation changes from the cortex to the deeper areas of the brain. In [Hastreiter 2004], deformations up to 30.9 mm on the position of tumors in the brain are reported. It is stated that the largest deformation takes place in the same side of the brain in which the surgery is performed, and that the deformation is larger when there is tissue extraction. It is also concluded that the deformation of the cortex and the deeper structures are not strongly related, showing the complexity of the phenomenon.

1.2.3 Brain Mechanical Models

A solution to avoid the problems derived from brain shift, allowing to update the registration between the preoperative image and the patient position, is to use an intraoperative image that is easy to acquire. This image is usually of low resolution, but the preoperative image can be register with it, allowing to update its spatial transformation. Intraoperative US imaging [Pennec 2001] is a good candidate. Nevertheless, intraoperative data (provided by images or other means) may not be available or be sufficient to perform a suitable refresh of the registration. To compensate this, *mechanical models* of the brain have been developed. Using an adequate mechanical model the brain deformation can be predicted by subjecting the model to the restrictions resulting from intraoperative measurements. Such model should incorporate the biomechanical properties of the tissues in order to predict their behavior correctly [Franceschini 2006].

Bio-mechanical Parameters. It is important to know the mechanical properties of the brain in order to model its deformation. Many studies to measure the biomechanical properties of the brain have been developed. One of the differences among these studies is the way in which the measurements are performed. In [Gefen 2004], changes in the properties of porcine brain tissue are studied, comparing in-vivo, in-situ and in-vitro measurements. Alterations in mechanical properties described in this study support those described in [Miller 2000], where the properties of porcine brain tissue are measured in-vivo by indentation; however they do not agree with [Metz 1970], where a cylinder is inflated inside live, dead, and fixed brain tissues. The differences between these studies could be due

to the area in the brain where samples were taken. Most of the experiments were performed in the brain cortex or in outer tissues of the brain, but the deeper tissue could have different properties. Some differences have also been found by performing tension [Miller 2005a] and compression tests [Miller 2002]. Other works on the subject can be found in [Franceschini 2006], where the measurements are performed in-vitro using human tissue modeled according to the Consolidation Theory [Biot 1941], or as in [Davis 2006] in which a fractional Zener derivative model [Zener 1948, Schiessel 1995] is used. An approach based on the strain energy density function is employed in [Kohandel 2006]. Rotational shear experiments are performed in [Hrapko 2006], assuming a differential viscoelastic model. Even in-vivo measurements have been performed in humans [Schiavone 2009], by using an aspiration device in the cerebral cortex during surgery and modeling the tissue by a Mooney-Rivlin constitutive law [Mooney 1940, Rivlin 1948]. In summary, the mechanical properties of the brain have been measured in many ways and different theoretical models have been used; however no consensus on a definitive model has been reached yet.

Mechanical Models. Besides the variety of ways in which the mechanical properties of the brain tissue have been measured, there is a range of models that have been used to simulate the deformation. The anatomical structures or tissues considered by these models are not always the same. However, the most important tissue for this mechanical modeling is the brain parenchyma which includes the white matter (WM) and gray matter (GM) (see Appendix B). Most of the models are based on the finite element method (FEM) in which the continuum mechanics equations can be directly used, yielding realistic results. However, the amount of computation can be very large and some boundary conditions are difficult to handle. The mass-spring models, which are widely used in computer graphics, have also been employed. The mass-spring models are very simple and fast, however they are heuristics ad-hoc models, and therefore realistic behavior is difficult to achieve. Moreover, the parameters of mass-spring models are mesh-dependent. On the other hand, some boundary conditions are easier to handle in mass-spring models than in FEM. Besides these two main types of models there are others which have been employed to a lesser extent. Bellow, a brief review of these models and the tissues taken into account is presented.

One of the first attempts to model the brain shift using mass-spring models is presented in [Buchholz 1997], where localized intraoperative US images are registered with preoperative MRI and CT images. The tissue is classified into 3 classes

according to its level of deformation: low (skull), moderate (brain parenchyma) and high (CSF) deformation (see Appendix B). A later work that uses a 3D mass-spring model is [Skrinjar 1999], in which a Kelvin solid model [Pamidi 1978] is used. However, they changed their model in later works to a finite element (FE) one [Skrinjar 2001, Skrinjar 2002]. The FE models of the brain had already been previously used. The first FE models for brain deformations were developed for modeling high-speed traumas [Voo 1996], such as those produced in car crashes. However, these high speed conditions are very different from those found in an operating room, where the forces are smaller and applied for a longer time.

Because the FE method can be used to solve any partial differential equation, many continuum mechanics models can be implemented using it, such as linear or nonlinear models. There are monophasic models, such as simple elastic models [Warfield 2002], or biphasic models consisting of a porous elastic solid saturated by a fluid [Miga 2000]. Each of these models has its advantages and drawbacks, and their respective scopes can be debated.

A work in which a linear model is driven by the reconstruction of the exposed brain surface acquired using a pair of cameras is presented in [Skrinjar 2002]. In [Clatz 2003], a linear elastic model is described, in which the level of CSF is used to guide the deformation. Another linear elastic model is introduced in [Warfield 2000, Ferrant 2001, Nabavi 2001, Ferrant 2002, Warfield 2002], which is driven using the exposed surface of the brain. In [Hagemann 1999], a linear elastic model is implemented in 2D. Later, this model was improved in [Hagemann 2002], by including incompressible fluid (cerebrospinal fluid) in addition to rigid (bone) and elastic tissues (soft tissue). Linear elastic models assume small deformations. Although this could be true for certain types of surgeries, such as the implantation of electrodes for epilepsy treatment, it is not valid in general. In some surgeries the tissue deformation is substantial [Nimsky 2000, Nabavi 2001] and therefore the validity domain for linear elastic models is not met. However, the model update during the surgery, through the acquisition of points or surfaces, can reduce the importance of these problems, making the boundary conditions and model constraints more important.

A nonlinear model, based on FE and permitting large deformation and small forces, is presented in [Xu 2001]. A linear hyper-viscoelastic model was introduced in [Miller 1999, Miller 2000], which uses FE and polynomial equations with time-varying coefficients. The model was improved in [Miller 2002] by using a nonlinear hyper-viscoelastic model. All the above models assume that the brain tissue is homogeneous, not considering the cerebrospinal fluid. A nonlinear

model for large deformations that attempts to model the interactions with surgical tools and which uses the same equations of the above model is introduced in [Wittek 2004]. The model uses a generic mesh that is adapted to the patient and does not take into account the CSF nor the ventricles. Later, a similar model, valid for small deformations, is used in [Wittek 2007]. But this time, it is focused on tissue deformations. The mesh of the above model is built manually, and the ventricles are considered by changing the parameters to a very soft and compressible elastic solid.

Brain tissue has also been modeled applying a biphasic model based on a porous solid and an interstitial fluid (the model is called “Consolidation Theory”) [Nagashima 1990a, Nagashima 1990b, Tada 1994]. The attempts of a research group to build a biomechanical model of the brain using the aforementioned theory can be found in [Miga 1998, Miga 1999b, Miga 2000]. Their models are based on FE, assume that the brain is uniform, and do not consider the ventricles. On the other hand, the work of [Miller 1997] states that the biphasic model is not suitable for modeling brain tissue. In [Taylor 2004] and [Miller 2005b], a biphasic model for slow deformations is presented, such as the ones occurring in a pathology, e.g., hydrocephalus [Taylor 2004]. According to these publications, the monophasic viscoelastic model is suitable for modeling fast deformations (e.g., a surgery), and the biphasic model for slow deformations (e.g., a pathology). There are also attempts to model two separate phases, with an emphasis on the fluid/structure interaction between them. For example, a method for modeling the CSF/parenchyma interaction within the brain is presented in [Araya 2007].

Modeling tissue cutting is not easy when using FE, as it implies discontinuities that cannot be handled within the elements. For this reason, most of the models do not take into account neither tissue resection nor retraction. An attempt to model these situations is presented in [Miga 2001]. Tissue retraction is handled by generating nodes along the retraction position before separating the tissue; and tissue resection is achieved by manually selecting all elements that need to be removed, and then applying boundary conditions to the new surface. In [Serby 2001], a technique for modeling cuttings is also introduced. Here, the existing nodes are displaced, instead of inserting new ones. A way to model resection and retraction by using Extended Finite Element Method (XFEM) can be found in [Vigneron 2004, Vigneron 2009].

Apart from the models based on mass-spring modeling and FE, there are other variants that have been studied. A variant of the FE method is proposed in [Davatzikos 2001], which models tissue deformation by using a statistical model

combined with a linear elastic biomechanical FE model. A Boundary Element Method (BEM) is used in [Ecabert 2003] for 2D modeling of brain shift. Another approach using an atlas built with precomputed deformations of a FE biphasic model is introduced in [Dumpuri 2007]. This atlas includes the possible deformations due to factors such as gravity, cerebrospinal fluid and drugs, combining them properly by using the exposed surface of the brain captured by a laser scanner.

1.2.4 Obtaining the Anatomical Model

Most of the works about the mechanical modeling of the brain, presented in section 1.2.3, obtain the associated anatomical model by manual segmentation or using a mix of semi-manual methods. To define the brain parenchyma, which is the most important structure for this modeling, the cortical surface must be segmented. Also the CSF is incorporated in most of the models, usually taking into account the ventricles, which are filled with this fluid. The rigid tissues must be incorporated as well, as boundary conditions or as a segmentation of the skull. Finally, the falx cerebri and the tentorium cerebelli have been taken into account only in few publications, although their importance has been stated in the literature. A review of the segmentation methods for these structures appears next.

1.2.4.1 Cortical Surface Segmentation

As we have just seen, the cortical surface segmentation is an important step in the construction of a mechanical model of the brain (section 1.2.3), because this surface defines the brain parenchyma. The segmentation of this structure also eliminates the non-brain tissue present in the image, a procedure called *Skull Stripping* or brain extraction process. This process is also a required preliminary step for many other methods, before being able to employ MR images in medical or research applications. Among these processing methods, it is important to include: image registration [Klein 2010], inhomogeneity correction [Wels 2011], tissue classification [de Boer 2010, Jia 2011], analysis of cortical structure [Thompson 2001], cortical surface reconstruction [Tosun 2006], cortical thickness estimation [MacDonald 2000], voxel-based morphometry [Acosta-Cabronero 2008] and/or identification of brain parts [Zhao 2010]. Therefore, it is imperative to have accurate Skull Stripping methods available to avoid time consuming manual corrections, that are not sys-

tematic and therefore can't be applied routinely. The reliability of this processes is essential because any error at this first step will be difficult to correct in subsequent processing steps.

Many Skull Stripping methods have been proposed [Kapur 1996, Atkins 1998, Lemieux 1999, Dale 1999, Ashburner 2000, Yoon 2001, Lemieux 2003, Shattuck 2001]. Among the most commonly used methods are the Brain Extraction Tool (BET) [Smith 2002, Jenkinson 2005], Brain Surface Extractor (BSE) [Sandor 1997, Shattuck 2001] and the Hybrid Watershed Algorithm (HWA) [Ségonne 2004]. In BET, a mask is initially created using two thresholds estimated from the image histogram. Then, a spherical deformable model is initialized at the center of gravity of the mask. Finally, this deformable model is pushed to the brain surface by local adaptive forces. The BSE performs brain segmentation using a sequence of anisotropic diffusion filters, Marr-Hildreth edge detection [Marr 1980], and morphological processing. The HWA is a hybrid method that combines the Watershed edge detection algorithm with a deformable surface model, which includes shape restrictions based on a brain atlas. Another of the most commonly used methods is the 3dIntracranial [Cox 1996, Ward 1999]. This method first models the gray levels of different tissues using Gaussian functions, and extracts upper and lower boundaries to identify brain voxels. Then, a connected component analysis is carried out slice-by-slice to identify the brain, followed by a 3D envelope process over all the slices. Finally, a neighborhood analysis is performed on each voxel to include or exclude misclassified voxels.

Another example of Skull Stripping methods is the Watershed Modified Algorithm proposed in [Hahn 2000]. The method presented in [Grau 2004] is also based on a watershed transformation that uses prior information. Elastic deformations based on atlas [Sandor 1997], Level Set methods [Baillard 2001, Zhuang 2006], and Region Growing algorithms [Park 2009] have also been employed. In [Huang 2006], a hybrid method combining expectation maximization and geodesic active contours is used. A method based on an implicit deformable model which is described by radial basis functions is introduced in [Liu 2009]. An algorithm called Bridge Burner is presented in [Mikheev 2008]. The algorithm is based on thresholding, removal of narrow connections between structures, and a morphological operator of constrained growing. A more recent example, also using removal of narrow connections but employing a graph theoretic image segmentation technique, is [Sadanathan 2010]. A method that uses watershed segmentation, a clustering based on fitting Gaussian functions to the

tissue gray level, and a modification of BET is employed in [Merisaari 2009] to segment MRI images of premature infant brains. Techniques for combining different Skull Stripping algorithms to improve the segmentation have also been proposed, such as the Brain Extraction Meta Algorithm (BEMA) [Rex 2004]. Recently, the Multi-Atlas Propagation and Segmentation (MAPS) method was presented in [Leung 2011]. This method generates the brain segmentation by combining many segmentations performed by atlas registration. Another recent method which uses thresholding, run length scheme, and morphological operators can be seen in [Somasundaram 2011]. The Robust Learning-Based Brain Extraction (ROBEX) system is presented in [Iglesias 2011], which is based on a Point Distribution Model (PDM) adjusted by using a voxel classification with the Random Forest Algorithm. A fast Level Set method which uses a speedup operator is introduced in [Hwang 2011]. The Simple Paradigm for Extra-Cerebral Tissue Removal (SPECTRE), that is based on a watershed principle and combines elastic registration, tissue segmentation, and morphological operators, is described in [Carass 2011].

BET, BSE, ANALIZE 4.0 [Richard 2000] and modified Region Growing (mRG) [Yoon 2001] methods are compared in [Lee 2003]. Boesen et al. compare their Minneapolis Consensus Strip (McStrip) [Rehm 2004] method with Statistical Parametric Mapping v2 (SPM) [Ashburner 2000], BET, and BSE in [Boesen 2004]. A comparison among methods HWA, BET, BSE, and 3dIntracranial was carried out in [Fennema-Notestine 2006]. More recently, a comparison study between HWA, BET and BSE has been performed in [Shattuck 2009]. The aforementioned studies of comparison show that, among these methods, HWA has the highest sensitivity in general but the lowest specificity [Fennema-Notestine 2006, Shattuck 2009]. HWA is prone to include unwanted subarachnoid space and non-brain tissue, particularly dura, in the segmentation. By contrast, HWA seems to be more robust to the change of parameters than other methods [Shattuck 2009].

1.2.4.2 Skull Segmentation

When a brain mechanical model is created, some boundary conditions must be applied to the brain surface to incorporate the interaction between the brain and skull. These boundary conditions are commonly defined manually or using a segmentation of the inner surface of the skull. Usually the skull is segmented in CT images [Soltanian-Zadeh 1997, Rifai 2000, Dogdas 2005], because its better contrast. However, the most used modality in neurosurgery is the MRI, since

it provides better images of soft tissues. Moreover, the CT exposes the patient to ionizing radiation. Therefore, to have a segmentation method that uses T_1 -weighted MRI is desirable.

To build a mechanical model of the brain only the internal surface of the skull is needed. This surface can also be obtained using a method that segments the entire skull. A review of these methods is presented next.

Among the earliest works on the segmentation of the skull, we can mention [Conforto 1996], in which the main tissues such as scalp, brain and skull are recognized using Kohonen self organizing feature maps. The voxels are classified as belonging to a tissue in the above work, however the structure of the skull is not segmented. A semiautomatic method that uses thresholding and region growing to segment bone in MRI volumes is presented in [Heinonen 1997]. In [Held 1997], a method which uses Markov random fields to segment the image into GM, WM, CSF, scalp-bone, and background, is introduced. This method does not guarantee the continuity of the tissues, and is not an appropriate method for skull segmentation. The method introduced in [Haque. 1998] uses thresholding and manual segmentation in 2D slices to detect the boundaries of the skull and scalp in order to create a scalp-skull-brain (SSB) head model for forward modeling in Magnetoencephalography (MEG). A 3D method to segment the bone by using Level Set deformable models is introduced in [Rifai 2000]. The method uses a pre-segmentation by morphological operators and region growing.

Some methods use more than one type of images to perform the segmentation. In [Akahn 2001], a hybrid algorithm that uses spin density and T_1 weighted MRI to segment skull, scalp, CSF, eyes, WM and GM is introduced. The method is based on deformable contours, region growing, morphological operators, and thresholding. Another method that uses spin density and T_1 weighted MRI to segment the skull, but using adaptive fuzzy c-means clustering and extended region growing, is presented in [Wolters 2002, Wolters 2003]. In order to use spin density and T_1 weighted MRI in the segmentation, both images must be registered. The spin density images are used because the inner skull boundary can be determined more accurately in these images, since the CSF produces a stronger signal than skull. The aforementioned BET2 algorithm [Jenkinson 2005, Pechaud 2006] can also segment the inner skull surface by using complementary information from registered T_1 and T_2 weighted MRI. BET2 can also perform this segmentation using only a T_1 weighted MRI, however the result is less accurate in this case.

In [Belardinelli 2003], the skull and other structures are segmented in 2D

T_1 weighted MRI images by using a variation of the Locally Excitatory Globally Inhibitory Network (LEGION) neural algorithm. Morphological operators are used in [Dogdas 2005] to segment the skull and scalp to construct models usable in electroencephalography (EEG) and MEG. A method which utilizes a Knowledge-guided Active Model (KAM) is presented in [Shan 2007]. The KAM in this work is based on age-specific skull mesh models segmented from CT images using a conditional region growing algorithm. The mesh models are transformed to the training MRI images using a registration algorithm based on an affine transformation and normalized mutual information. A skull segmentation algorithm for T_1 weighted MRI of newborns is introduced in [Ghadimi 2008]. The method is based on a level set deformable model guided by a probability map constructed by using atlases on the image. A deformable model is adapted to a pre-segmentation of the skull in [Lüthi 2008]. The upper part of the skull is segmented in [Wang 2009] by using Active Shape Models (ASM) built from CT images. The ASM of the above method is guided by landmarks detected by using the image gradient in the CT and MRI images. A recent method that uses a hybrid algorithm in which a Bayesian classifying framework is combined with a Hopfield Neural Network (HNN) is presented in [Daliri 2010]. The method introduced in [Bertelsen 2010] uses a set of atlases, with skull labels, which are registered to the MRI image, and then the labels are combined to produce the most probable segmentation. Another recent method introduced in [Yang 2010] uses the Radon transform of the image to segment the skull using a bilateral filter.

1.2.4.3 Ventricle Segmentation

The CSF has particular mechanical properties, and much of it is in the ventricles (Appx. B.5). Therefore, these structures are very important to perform a mechanical modeling of the brain. A review of the methods used to segment the ventricles is presented next.

Many methods use labeled atlas to segment the subcortical structures, such as the ventricles. In these approaches, the atlas may be a single labeled image or a set of images. To perform the segmentation the atlas is registered to the MR target image and then the labels are combined to obtain the segmentation. Among the earliest works to use this approach are [Gee 1993, Collins 1995, Iosifescu 1997].

Other methods that have been used for ventricle segmentation are the following. Genetic algorithms have been used, for example, in [Sonka 1996], where the cerebral structures are segmented including the third and lateral ventricles. One

of the first works in which Active Models (AM) were used is [Wang 1998]. In this work, the method is tested in brain ventricles and heart. In [Worth 1998], the lateral ventricles and the caudate nucleus are segmented in T_1 weighted coronal MR images by using thresholding and histogram analysis. An atlas-based registration as a precursor for a region growing method guided by a fuzzy model of regions of interest is proposed in [Xue 2001]. Another method that uses region growing and morphological operators is introduced in [Schnack 2001]. In [Kaus 2001], a technique called adaptive template-moderate classification is used to segment the skin surface, ventricles, brain, and tumor in patients with brain neoplasms. The template-moderate classification technique is based on statistical gray level classification and registration with an atlas. A method that also uses registration with an atlas to segment the lateral ventricles is presented in [Holden 2001], in which the registration is guided by Mutual Information (MI). A deformable model method based on level sets and initialized by the registration with an atlas is introduced in [Baillard 2001]. In [Fischl 2002], 37 subcortical structures, including the ventricles, are segmented by using gray level probabilistic information, structure specific models by Markov Random Fields, and registration with an atlas. The ventricular system is segmented in [Xia 2004]. The method divides the ventricular system into sub-regions within which a region growing technique, modulated by local statistics to prevent leakage with external areas, is used. In [Pitiot 2004], deformable models constrained by statistical shape models and expert prior knowledge, and initialized by a registration, are used to segment subcortical structures. Some subcortical structures are segmented by using competitive level sets driven by fuzzy control in [Ciofalo 2005].

More recent atlas-based segmentation methods are the following. Different schemes for constructing a mean-shape anatomical atlas for atlas-based segmentation of MR brain images are evaluated in [Wang 2005]. To build the atlases and segment the images, a non-rigid intensity-based registration by a viscous fluid deformation model was used. An atlas-based segmentation which uses registrations with fuzzy templates of the structures is used in [Zhou 2005] to segment five subcortical structures. In [Heckemann 2006], the results of atlas-based segmentations are combined by using decision fusion. An atlas-based segmentation method that combines piecewise linear registrations for coarse alignment with the demons algorithm [Thirion 1998] for voxel-level refinement is introduced in [Wu 2006]. Another atlas-based segmentation method which uses a probabilistic atlas is presented in [Gouttard 2007]. An atlas-based segmentation method which introduces an intensity renormalization procedure that automatically ad-

justs the prior atlas intensity model to the input data is introduced in [Han 2007]. In [Akselrod-Ballin 2007], graphs at multiple scales, in which prior knowledge information is incorporated through a Bayesian formulation, are used with a probabilistic atlas to segment structures in brain MRI.

The ITK-SNAP software for semi-manual segmentation based on level sets is presented in [Yushkevich 2006], showing results in ventricle segmentation. The probabilistic-based FreeSurfer (FS) method [Fischl 2002, Fischl 2004] is combined with the Large Deformation Diffeomorphic Metric Mapping (LDDMM) method [Beg 2005] in [Khan 2008] to perform MRI segmentation. Global and local statistical shape models of the brain structures, combined with discriminative models that incorporate features such as intensity, gradient, curvature, and location, are used in [Tu 2008]. A comparison among four automated segmentation methods of subcortical structures is presented in [Babalola 2009]. The above comparison includes two atlas-based methods and two methods that use statistical models of shape and appearance. Artificial neural networks (ANN) and support vector machine (SVM) are used to improve the performance of an atlas-based segmentation in the work presented in [Powell 2008]. A method based on atlases, which uses a non-local patch-based label fusion is introduced in [Coupé 2011]. A comprehensive testing protocol for MRI neuroanatomical segmentation techniques is presented in [Kempton 2011] and applied to a segmentation method for lateral ventricles.

1.2.4.4 Membrane Segmentation

Other structures that have been incorporated more recently into the brain shift modeling are the internal membranes of the brain: *falx cerebri* and *tentorium cerebelli*. The falx cerebri is a membrane located between the cerebral hemispheres; and the tentorium cerebelli is also a membrane, located between the brain and cerebellum. A more detailed anatomy description of these membranes is presented in Appendix B.4.1. Although some studies acknowledge that these structures should be included into the models [Maurer 1998, Warfield 2002], works in the literature generally do not take them into account. In [Miga 1999a], the falx cerebri is manually segmented in a sagittal view of the patient's volume, and it is then incorporated into a biphasic model. The same method is also used in [Dumpuri 2007] and [Dumpuri 2010] to segment the falx cerebri. In [Witteck 2005], the falx cerebri is manually marked in the model. A more recent study that also incorporates the tentorium cerebelli is introduced in [Garg 2010] and improved in [Chen 2011]. In this study, a manual segmentation is used to

obtain the brain surface, and a semi-manual segmentation is performed for the tentorium cerebelli. To segment the tentorium, a set of points is manually marked in the membrane to define a plane. Then the plane is manually deformed into the tentorium surface using a technique based on 3D thin plate splines. The lack of reliable automated segmentation methods for these membranes does not allow a fast construction of anatomical models customized for each patient.

1.3 Objectives

The general and specific objectives of this thesis are stated in the next sections.

1.3.1 General Objectives

The general objective of this thesis is to develop an automated method to segment T_1 -weighted MRI brain images. The method will be focused on the construction of an anatomical model of the brain suitable for use in mechanical modeling. The new segmentation method will be based mainly on deformable model techniques. Also, the anatomical model will incorporate all the structures of interest for mechanical modeling such as the tentorium cerebelli and the falx cerebri.

1.3.2 Specific Objectives

The specific objectives of this thesis are:

- To develop a new segmentation method for the brain structures relevant to mechanical modeling: cortical surface, ventricles, surface of the skull, falx cerebri and tentorium cerebelli. The method will be based mainly on deformable model techniques adapted to this type of segmentation, incorporating other tools such as histogram analysis or morphological operators.
- To incorporate the anatomical structures (cortex, ventricles, surface of the skull, falx cerebri and tentorium cerebelli) in a general model. To include these structures, 3D methods of mesh manipulation will be developed and adapted by using fusion, decimation and mesh transformation algorithms.
- To validate the segmentation method by comparing its performance with other methods using standard databases.

1.4 Proposed Solution

The solution proposed and implemented in this thesis is introduced here.

Instead of using a generic mesh and adapt it to the patient’s anatomy, our method segments each structure separately. This approach provides greater flexibility to the method. It could even be possible to substitute the segmentation of a particular structure without affecting the rest of the process. Furthermore, the method is not based on machine learning techniques [Perez 2005], hence a training database is not required.

Deformable models have been widely used in image segmentation and *Simplex meshes* [Delingette 1994, Delingette 1997, Delingette 1999, Montagnat 1998] are a good option to implement them. These meshes have great properties for deformable model techniques, such as simplicity and stable computation of curvature-based internal forces. They have been successfully and widely applied, for example, to the segmentation of 4D US cardiac images [Gérard 2002] and cardiac SPECT images [Montagnat 2005]. A semi-automatic segmentation of cardiac and lung MRI that uses simplex meshes is introduced in [Böttger 2007]. A method called Simplex Mesh Diffusion Snake (SMDS) is used to segment MRI in [Tejos 2009]. The method uses simplex meshes to extend the Diffusion Snakes [Cremers 2002] segmentation method to 3D. More recently, multi-resolution simplex meshes with medial representation are used to segment musculoskeletal MRI in [Gilles 2010]. There are also efforts on renal segmentation [Galdames 2005] and registration [Galdames 2007, Galdames 2011].

Another important property of this kind of meshes is that the external borders of a surface represented by a simplex mesh, can be controlled independently of the surface (sec. 2.1.3.1). Thus, the contours that represent the external borders can be used as boundary conditions for the mesh deformation. This property is very important in our model. The anatomical model proposed in this work takes into account the internal membranes of the brain –Tentorium Cerebelli and Falx Cerebri– (Appx. B.4.1), and represents them by open surfaces. The borders of these membranes have anatomical relationships with the neighboring structures. Therefore, to freely deform the meshes that represent the membranes while maintaining their anatomical relationships, it is necessary to apply restrictions on the membrane borders. This is done by using contours at the borders of the open meshes (sec. 2.3.7).

On the other hand, simplex meshes have another favorable characteristic. They are topological duals of triangle meshes, i.e. there is a direct relation be-

tween both representations. Thus, the virtues of simplex meshes as deformable models can be very easily complemented with the good properties of triangle meshes for other tasks. Some of these tasks are computing of intersections, rendering, and construction of volumetric meshes. In our work, starting by using simplex meshes for segmentation, we need next to compute intersections to integrate all the structures in a final mesh (Fig. 2.36), which should be used, in turn, to construct volumetric meshes for mechanical modeling. Therefore, conversion between the two representations will allow us to use the complementary characteristics of both meshes. This duality has been noticed, for example, in [Audette 2003a] where simplex meshes are used for segmentation and then transformed into a triangulation to build a model of FE. In [de Putter 2006], simplex meshes are used to segment vascular walls, and next the dual triangle meshes are utilized as well to generate the FE model. Furthermore, we developed a new, efficient and direct method for converting simplex and triangle meshes, which is presented in section 2.2. For the above reasons, the dual pair Simplex/Triangle meshes is the perfect platform to develop our segmentation method, focused on the construction of an anatomical model for mechanical simulation of the brain.

1.5 Structure of the Document

The thesis is organized as follows.

The developed method is described in Chapter 2. It begins (2.1) with an introduction to simplex meshes, which are the main tool used in the method. Then a new transformation method between simplex meshes and triangulations is explained in section 2.2. This transformation method is used in our segmentation because simplex meshes are more appropriate for some tasks and triangulations for others. In this way, we can take advantage of the properties of each type of mesh. The proposed segmentation method, including the incorporation of the anatomical structures, is presented in section 2.3.

The experiments performed to evaluate our method, and the obtained results, are presented in Chapter 3. The online databases, indices to measure the performance of the segmentation, and methods used for comparison are introduced in section 3.1. Then the segmentation results of each anatomical structure are shown in section 3.2, and some comparisons with previously published results are presented.

The discussions and conclusions of the work developed in this thesis are presented in Chapter 4.

CHAPTER 2

Methodology

Contents

2.1	Simplex Meshes	30
2.1.1	General Definition	30
2.1.2	Mesh Deformation	38
2.1.3	Internal Forces	39
2.1.4	External Forces	41
2.2	Transformation Between Triangulations and Simplex Meshes	44
2.2.1	Interpolation Based on Tangent Planes	46
2.2.2	From Triangulation to Simplex Mesh	50
2.2.3	From Simplex Mesh to Triangulation	51
2.2.4	Transformation Results	52
2.3	MRI Segmentation	58
2.3.1	Pre-segmentation	60
2.3.2	Initial Generic Meshes	74
2.3.3	Geometric Adjustment of the Meshes	75
2.3.4	Cortical Surface Segmentation	77
2.3.5	Skull Mesh Deformation	86
2.3.6	Ventricle Mesh Deformation	90
2.3.7	Open Meshes	91
2.3.8	Final Mesh	98

Deformable models have proven to be a robust method to segment MRI images [Smith 2002, Ségonne 2004, Liu 2009]. In addition, simplex meshes are a

simple and efficient way to implement these models and have yielded excellent results in many applications [Delingette 1999, Matula 2002, Böttger 2007, Tejos 2009, Gilles 2010, Galdames 2011]. The main advantage of this type of meshes over other techniques is that they provide a convenient way to control the internal forces of the mesh in order to handle curvature and regularity. Moreover, the contours of simplex meshes can be handled independently acting as boundary conditions for surface mesh deformation (sec. 2.1.3.1). This property is very useful to control the deformation of open surfaces, such as those used in the present work to segment the internal membranes of the brain. On the other hand, triangle meshes, which are the topological duals of simplex meshes, can perfectly deal with actions such as computing of intersections, rendering, or construction of volumetric meshes. Intersections between meshes and other tasks for which the triangle meshes are more efficient are used in our method. So, we have developed an efficient and direct method of transformation between both types of meshes (sec. 2.2). The transformation method is based on a geometric interpolation that minimizes the distance between the interpolated point and the tangent planes of the vertices of the meshes. The Simplex/Triangle mesh pairing gives us an excellent approach to address the segmentation of images by deformable models.

The segmentation method proposed in this work is fundamentally based on simplex meshes. A generic mesh for each structural part is geometrically adjusted in order to coarsely match the anatomical structures in the MRI image. Then, each anatomical structure (Appx. B) is segmented individually. The external forces, which control the mesh deformation to reach the borders of anatomical structures, are computed using the image information and the position of the previously segmented structures (relative neighborhood). The main image information used here is the image gradient, and the relationship between local gray level and gray level estimates of specific tissues in the image. Different tissues have distinctive gray levels in MRI (as seen on Fig. C.6), therefore the frontier between them is usually denoted by a high gradient. Thus, the image gradient can be used to accurately find the borders of the anatomical structures. Moreover, an estimation of the characteristic tissue gray level in the image gives us information about the tissue that is present at a certain point; and in which direction the border of the structure must be searched. For reasons that will be detailed further, but mainly for their mechanical importance, the considered anatomical structures will be: cortical surface, internal skull surface, ventricles, falx cerebri and tentorium cerebelli. As presented in section 1.2.3 and 1.2.4, most of the

mechanical models of the brain only take into account the brain parenchyma and skull surface (or boundary restrictions similar to this surface), and some of them consider the ventricles. Only a few previous papers consider the internal membranes: falx cerebri and tentorium cerebelli [Miga 1999a, Wittek 2005, Dumpuri 2007, Dumpuri 2010, Garg 2010, Chen 2011]. However, there are studies which state that these structures must be imperatively integrated to obtain suitable mechanical models [Maurer 1998, Warfield 2002]. Besides, when considered, these membranes are segmented in a manually or semi-manually way. In this work, our main goal is to obtain a method that adequately handles the construction of a patient specific anatomical model which considers all the relevant structures. The method is presented as follows.

Overview of the Proposed Method. Simplex meshes are introduced in section 2.1. A general definition of these meshes (sec. 2.1.1) and how they are deformed (sec. 2.1.2) is explained. Simplex meshes are closely related to triangulations (meshes of triangles), and both mesh types are used for different tasks in this work. Therefore, a new method to convert simplex meshes into triangulations, and vice-versa, is presented in section 2.2.

The segmentation method of MRI brain images is explained in section 2.3. To segment the MRI brain images, a pre-segmentation is carried out first to remove all non-brain tissue in the image (sec. 2.3.1). The elimination of these tissues allows to find an optimal initialization for our deformable model, which is critical for this type of methods. The deformable model is based on a generic anatomical model of the brain which incorporates all the relevant structures for mechanical modeling (sec. 1.2.4). Each structure is first represented in the model by an independent mesh (sec. 2.3.2). These meshes are deformed to segment the anatomical structures in a particular T_1 -weighted MRI. Each mesh is deformed independently, but in a logical sequence to take advantage of the position of the previously segmented structures as input information for the next one. When all the meshes have been deformed, they are joined together into a final model representing the whole brain anatomy. This scheme of segmentation provides great flexibility to our method. The segmentation of any structure can be modified without affecting the rest of the chain. Another method could even be used to segment a specific structure, and then the new result could be integrated into the segmentation chain. Also, the derived problem of handling a complex non-manifold mesh is avoided by using independent simplex meshes. A brief introduction to the deformation process is presented below:

- First, each mesh of the generic model is geometrically adjusted using the pre-segmented image (sec. 2.3.3). The geometric adjustment is mainly driven by the cortex and ventricles meshes, as the borders of these structures become evident in the pre-segmentation.
- Since the meshes get close enough to the searched structures with the previous adjustment, a more local deformation is performed:
 - The cortex mesh is the first to be deformed (sec. 2.3.4), because the cortex surface is the structure that presents the most obvious edges in the pre-segmented image. After deforming it using the pre-segmented image, another deformation is performed using the original image in order to obtain an accurate segmentation.
 - The skull mesh is the second to be deformed (sec. 2.3.5) by using the original image. The cortex mesh is also used to drive the skull mesh deformation, as those two meshes should not intersect.
 - After the skull mesh deformation, the ventricle mesh is deformed (sec. 2.3.6) according to the image and the gray level information acquired with the previous segmentations.
 - After deforming the closed meshes, the open meshes that represent the internal membranes of the brain are deformed. The tentorium cerebelli mesh is deformed first (sec. 2.3.7.1) by using the image information and the skull mesh. The tentorium cerebelli is attached to the skull, therefore the border of the first must slide over the surface of the last.
 - After the tentorium mesh deformation, the falx cerebri mesh is deformed (sec. 2.3.7.2). The border of the falx cerebri is attached to the skull and the tentorium cerebelli, and the deformation is performed accordingly.
- Finally, all deformed meshes are joined together (sec. 2.3.8) obtaining the final patient-specific anatomical model of the brain.

As pointed out in this section, simplex meshes are of great importance in our method, therefore they will be introduced in the following section, before explaining the particular application developed.

2.1 Simplex Meshes

Simplex meshes [Delingette 1994, Delingette 1997, Delingette 1999, Montagnat 1998] have good properties to be used in deformable models techniques, e.g., easy handling and a convenient way to model internal forces (shape preservation) as well as external forces (driven by the image), as we will see later. Thus, they have been successfully applied, for example, to the segmentation of cardiac 4D US [Gérard 2002] and SPECT [Montagnat 2005] images. A work on semi-automatic segmentation of cardiac and lung MRI that uses simplex meshes is also presented in [Böttger 2007]. In [Tejos 2009], a simplex mesh diffusion snake is used to segment MRI. A segmentation of musculoskeletal MRI based on multi-resolution simplex meshes with medial representation is introduced in [Gilles 2010]. Also, previous works for renal segmentation [Galdames 2005] and registration [Galdames 2007, Galdames 2011] have used these meshes.

First we will introduce a general description of the simplex meshes, as well as some tools to manipulate them.

2.1.1 General Definition

In general, a k -simplex mesh has connectivity $(k+1)$, i.e., each vertex is connected with $k+1$ neighbors. In this way, simplex meshes have constant connectivity. Formally, a k -simplex mesh \mathcal{M} in \mathbb{R}^d is defined as $(V(\mathcal{M}), N(\mathcal{M}))$ where:

$$V(\mathcal{M}) = \{P_i\}, \{i = 1, \dots, n\}, P_i \in \mathbb{R}^d, \quad (2.1)$$

$$\begin{aligned} N(\mathcal{M}) : \{1, \dots, n\} &\rightarrow \{1, \dots, n\}^{k+1}, \\ i &\rightarrow (N_1(i), N_2(i), \dots, N_{k+1}(i)) \end{aligned} \quad (2.2)$$

$$\begin{aligned} \forall i \in \{1, \dots, n\}, \forall j \in \{1, \dots, k+1\}, \forall l \in \{1, \dots, k+1\}, l \neq j. \\ N_j(i) \neq i; \quad N_l(i) \neq N_j(i). \end{aligned} \quad (2.3)$$

Thus, $V(\mathcal{M})$ is the set of n vertices P_i of \mathcal{M} , i.e., it represents the geometry of \mathcal{M} ; and $N(\mathcal{M})$ is the connectivity function that links each vertex P_i with its neighbors. This connectivity function represents the topology of \mathcal{M} . Moreover, we can notice that equation (2.3) prevents the existence of cycles.

The name of “simplex mesh” comes from the definition of a “simplex” (plural simplexes or simplices). A k -simplex is the convex hull of $k+1$ independent points,

e.g., a segment is a 1-simplex, a triangle is a 2-simplex and a tetrahedron is a 3-simplex. By definition, a k -simplex mesh has a $(k+1)$ -simplex in each vertex. For example, a 1-simplex mesh is a contour in which each vertex and its two neighbors define a triangle (Fig. 2.1(a)). This property defines the connectivity of the mesh, i.e., the vertices of a k -simplex mesh have $k+1$ neighbors. The type of objects that these meshes can represent depends on this connectivity, e.g., a k -simplex with $k=1$ can represent a curve, $k=2$ a surface, $k=3$ a volume.

Another useful way to define a k -simplex is as a union of p -cells. Since these cells are p -simplex meshes, the definition of a cell is recurrent. Therefore, a 0-cell in \mathbb{R}^d is a point, a 1-cell is an edge, and so on. Similarly, if we follow the recurrence, a p -cell C (with $p \geq 2$) is the union of $(p-1)$ -cells in the following way:

- Each vertex belonging to C , belongs to p different $(p-1)$ -cells.
- The intersection of 2 $(p-1)$ -cells is empty or a $(p-2)$ -cell.
- Given two vertices of C , there exists a path that link them.

2.1.1.1 Simplex Meshes and Triangulations

A k -triangulation or k -simplicial complex in \mathbb{R}^d is a set of p -simplices ($1 \leq p \leq k \leq d$), also called p -faces of the triangulation. A p -face is a p -simplex; accordingly, the 0-faces are vertices, 1-faces are edges, and 2-faces are triangles. The intersection between p -faces is empty or a $(p-1)$ -simplex. An important feature of a k -simplex mesh is that it is the topological dual of a k -triangulation. Thus, the dual of the graph of a k -simplex mesh is the graph of a k -triangulation. For example, the 2-faces of a 2-triangulation are triangles, and each triangle is related to a vertex of the dual 2-simplex mesh, which are 0-cells (dark dots in Figure 2.1(b)). Conversely, each face of the 2-simplex mesh is related to a vertex of the 2-triangulation (white dots in Figure 2.1(b)).

A topological transformation between a k -simplex and a k -triangulation can be defined (Figure 2.1). Basically, this dual transformation associates a p -face of a k -triangulation with a $(k-p)$ -cell of a simplex mesh (Table 2.1). But the transformation is different for cells or faces belonging to the borders of a triangulation or simplex mesh. Tables 2.1 and 2.2 show this relation for k -simplex meshes with $k=1$ or 2.

On one hand, a k -simplex mesh and a k -triangulation are not geometrical duals. This can be easily proved because the geometry of a k -simplex mesh and a k -triangulation is determined by the coordinates of its vertices. However, for

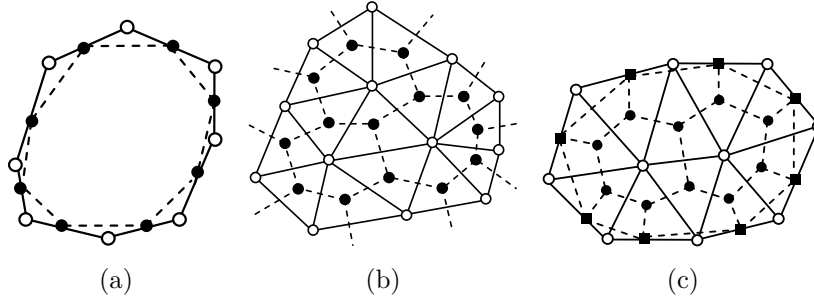


Figure 2.1: A simplex mesh is the topological dual of a triangulation. The dark dots in the figure form a simplex mesh, and the white dots form a triangulation. Figure (a) shows a 1-simplex mesh. Figures (b) and (c) show two 2-simplex meshes, with and without the borders of the simplex mesh. The duals of the borders are represented as black rectangles in figure (c). Table 2.1 shows the duality between the internal p -faces of the k -triangulations and the $(k-p)$ -cells of the dual k -simplex meshes that are shown in the figure. Table 2.2 shows the relation for the boundary faces.

Table 2.1: Duality between a k -triangulation and a k -simplex mesh, for internal faces and with $k=1$ and 2. The relation between the p -faces of the triangulation and the $(k-p)$ -cells of the simplex mesh are indicated. [Delingette 1999]

p -face of the triangulation	1-Tr \Leftrightarrow 1-SM	2-Tr \Leftrightarrow 2-SM
$p=0$	vertex \Leftrightarrow edge	vertex \Leftrightarrow face
$p=1$	edge \Leftrightarrow vertex	edge \Leftrightarrow edge
$p=2$		triangle \Leftrightarrow vertex

$k > 1$ the number of vertices V_{SM} of a k -simplex mesh is different from the number of vertices V_{Tr} of its dual k -triangulation. This is easy to prove for $k = 2$ and a triangulation without holes, using the Euler relation we have:

$$V_{Tr} - \frac{V_{SM}}{2} = 2(1 - g), \quad (2.4)$$

where g is the genus of the mesh, which characterizes the topology of the surface and corresponds to the number of handles. Because $V_{Tr} \neq V_{SM}$, we cannot build a homomorphism between the set of coordinates of a simplex mesh and the set of coordinates of its dual triangulation. Therefore, k -simplex meshes and k -triangulations are topologically, but not geometrically, equivalent.

Since 3D surface meshes have to be considered in this work, we use only 2-simplex meshes and from now on, we will refer to 2-simplex meshes simply as

Table 2.2: Duality between a k -simplex mesh and a k -triangulation, for boundary faces and with $k=1$ and 2. The relation between the p -faces of the triangulation and the cells of the simplex mesh, or between the p -cells of the simplex mesh and the faces of the triangulation are indicated. The word “*null*” indicates that there is no related face/cell in the dual mesh. [Delingette 1999]

p -face or p -cell	1-SM \Rightarrow 1-Tr	2-SM \Rightarrow 2-Tr	1-Tr \Rightarrow 1-SM	2-Tr \Rightarrow 2-SM
$p=0$	vertex \Rightarrow <i>null</i>	vertex \Rightarrow <i>null</i>	vertex \Rightarrow edge vertex \Rightarrow vertex	vertex \Rightarrow face vertex \Rightarrow edge
$p=1$		edge \Rightarrow <i>null</i>		edge \Rightarrow edge edge \Rightarrow vertex

simplex meshes.

2.1.1.2 Local Geometry of 2-Simplex Meshes

Each vertex of these meshes has three neighbors, and these four points define a tetrahedron $[P_i, P_{N1(i)}, P_{N2(i)}, P_{N3(i)}]$ (Fig. 2.2(a)). As explained in section 2.1.1.1, simplex meshes are topologically dual of triangulations (meshes of triangles), which allows to obtain a simplex mesh by applying a dual operation to a triangulation, and vice versa (Fig. 2.1(b)). This property is of great interest as it is sometimes more convenient to represent a surface with a triangulation for some tasks, e.g., rendering, calculation of intersections, or construction of volumetric meshes.

Now, we will give a brief explanation on the local geometry of a simplex mesh. As mentioned above, each vertex P_i of a simplex mesh has three neighbors, positioned at $P_{N1(i)}, P_{N2(i)}, P_{N3(i)}$. Thus, the vertex and its neighbors form a tetrahedron (see Fig. 2.2(a)). These neighbors define a plane π_i , and the unit normal vector to this plane is:

$$\vec{N}_i = \frac{P_{N1(i)} \times P_{N2(i)} + P_{N2(i)} \times P_{N3(i)} + P_{N3(i)} \times P_{N1(i)}}{\|P_{N1(i)} \times P_{N2(i)} + P_{N2(i)} \times P_{N3(i)} + P_{N3(i)} \times P_{N1(i)}\|}. \quad (2.5)$$

Also, we can calculate the sphere circumscribed to the tetrahedron, which center is $O_i = [x_{O_i}, y_{O_i}, z_{O_i}]$ and radius $R_i = \|P_i - O_i\|$. The center O_i of this

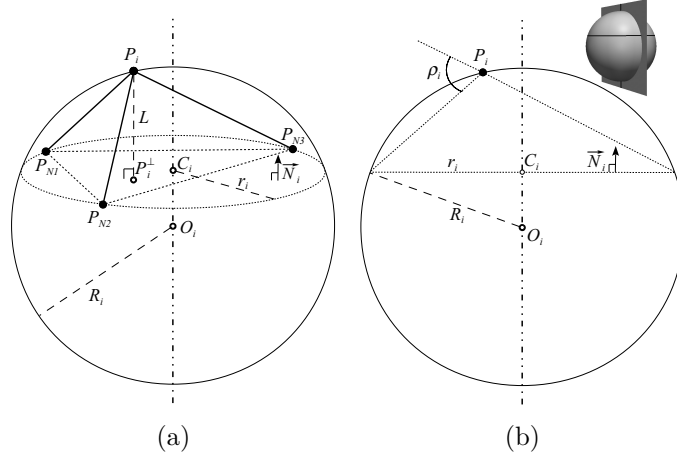


Figure 2.2: (a) Local geometry of a 2-simplex mesh. The tetrahedron formed by a vertex P_i and its 3 neighbors $P_{N1(i)}, P_{N2(i)}, P_{N3(i)}$ is illustrated. These four points (vertex P_i and its neighbors) define the sphere of center O_i and radius R_i circumscribed to the tetrahedron. Moreover, the three neighbors define the plane π_i and the circle of center C_i and radius r_i in this plane. (b) Simplex angle ρ_i shown in the cut passing through the vertex P_i and the axis of the sphere. The image shows the lines connecting P_i to the intersection between the plane π_i and the sphere in the cutting plane.

sphere can be found by solving the determinant:

$$\begin{vmatrix} x_{O_i}^2 + y_{O_i}^2 + z_{O_i}^2 & x_{O_i} & y_{O_i} & z_{O_i} & 1 \\ x_i^2 + y_i^2 + z_i^2 & x_i & y_i & z_i & 1 \\ x_{N1(i)}^2 + y_{N1(i)}^2 + z_{N1(i)}^2 & x_{N1(i)} & y_{N1(i)} & z_{N1(i)} & 1 \\ x_{N2(i)}^2 + y_{N2(i)}^2 + z_{N2(i)}^2 & x_{N2(i)} & y_{N2(i)} & z_{N2(i)} & 1 \\ x_{N3(i)}^2 + y_{N3(i)}^2 + z_{N3(i)}^2 & x_{N3(i)} & y_{N3(i)} & z_{N3(i)} & 1 \end{vmatrix} = 0. \quad (2.6)$$

Moreover, the three neighbors of P_i define a circle with center:

$$C_i = O_i + \vec{N}_i \left(\overrightarrow{O_i P_{N1(i)}} \cdot \vec{N}_i \right), \quad (2.7)$$

and radius $r_i = \left\| P_{N1(i)} - C_i \right\|$. This circle is the intersection between the sphere of center O_i and the plane π_i . With these definitions, the first of the geometric entities that control the mesh deformation can be presented, the simplex angle

ρ_i (see Fig. 2.2(b)):

$$\begin{aligned} \rho_i &\in [-\pi, \pi] \\ \sin(\rho_i) &= \frac{r_i}{R_i} \operatorname{sgn} \left(\overrightarrow{P_i P_{N1(i)}} \cdot \vec{N}_i \right), \\ \text{or} \\ \cos(\rho_i) &= \frac{\|O_i C_i\|}{R_i} \operatorname{sgn} \left(\overrightarrow{O_i C_i} \cdot \vec{N}_i \right), \end{aligned} \quad (2.8)$$

where sgn is the *sign* function. Hence, the simplex angle ρ_i is defined for each vertex P_i through its neighbors $P_{N1(i)}, P_{N2(i)}, P_{N3(i)}$, and it does not depend on the position of the neighbors within the circle they define. The simplex angle and the height L (Fig. 2.2(a)) of P_i over the plane π_i defined by its neighbors are related by:

$$\begin{aligned} L(r_i, d_i, \rho_i) &= \frac{(r_i^2 - d_i^2) \tan(\rho_i)}{\chi \sqrt{r_i^2 + (r_i^2 - d_i^2) \tan^2(\rho_i)} + r_i}, \\ \chi &= \begin{cases} 1 & \text{if } |\rho_i| < \pi/2 \\ -1 & \text{if } |\rho_i| > \pi/2 \end{cases}, \end{aligned} \quad (2.9)$$

where $d_i = \|C_i P_i^\perp\|$, and P_i^\perp is the projection of P_i over the plane π_i (Fig. 2.2(a)). Since the simplex angle is scale-invariant, it can be considered as a local and scale-invariant measure of the height L of P_i over the plane π_i .

The simplex angle is related with the surface curvature at P_i . The *mean curvature* of a continuous surface can be calculated at point P_i by:

$$H_i = \frac{k_1 + k_2}{2}, \quad (2.10)$$

where k_1 and k_2 are the *principal curvatures* (the maximum and minimum of the normal curvature) at P_i . This *mean curvature* can also be obtained locally by approximating the surface by a sphere [Delingette 1994]. The sphere that best fits the surface at point P_i is called the “minimum sphere” and its curvature is also the main curvature of the surface at P_i . If the radius of this sphere is R_i , the main curvature at P_i is:

$$H_i = (1/R_i). \quad (2.11)$$

This “minimum sphere” can be obtained at any point P_i on a simplex mesh by using the neighbors $P_{N1(i)}, P_{N2(i)}, P_{N3(i)}$ of P_i , as it is defined as the sphere

circumscribed to the tetrahedron formed by the four points (Fig. 2.2(a)). Thus, the equation of the mean curvature (2.11) at point P_i can be expressed in terms of the simplex angle [Delingette 1999] using the equation (2.8) to replace R_i , obtaining:

$$H_i = \frac{\sin(\rho_i)}{r_i} . \quad (2.12)$$

Other important geometric entities that can be used to control the mesh deformation are the metric parameters $\varepsilon_{1i}, \varepsilon_{2i}, \varepsilon_{3i}$. These parameters are the barycentric coordinates, with respect to the triangle defined by the neighbors of P_i , of the projection P_i^\perp of the vertex P_i on the plane π_i (Fig. 2.2(a)):

$$\begin{aligned} P_i^\perp &= \varepsilon_{1i}P_{N1(i)} + \varepsilon_{2i}P_{N2(i)} + \varepsilon_{3i}P_{N3(i)} , \\ \varepsilon_{1i} + \varepsilon_{2i} + \varepsilon_{3i} &= 1 . \end{aligned} \quad (2.13)$$

We know the position of a vertex projection on the plane defined by its neighbors by equation (2.13), and the height of the vertex over this plane by equation (2.9). Therefore, the metric parameters and the simplex angle completely determine the position of the vertex as follows:

$$P_i = \varepsilon_{1i}P_{N1(i)} + \varepsilon_{2i}P_{N2(i)} + \varepsilon_{3i}P_{N3(i)} + L(r_i, d_i, \rho_i)\vec{N}_i . \quad (2.14)$$

2.1.1.3 Local Geometry of Contours in 2-Simplex Meshes

The contours on simplex meshes can be used as boundary conditions of the deformation. They can be controlled independently of the surface, and thus the mesh deformation may be restricted by the positions of its boundaries.

Contours in 2-simplex meshes are 1-simplex meshes in \mathbb{R}^3 , i.e., a chain of vertices P_i with $i = \{0, 1, 2, \dots\}$ in 3D space. The definition of the geometric entities that control the geometry of a 1-simplex mesh is analogous to the previous case of 2-simplex meshes. Each vertex P_i of the contour and its two neighbors P_{i-1}, P_{i+1} define a triangle or 2-simplex (Fig. 2.3(a)). These vertices also define the circle with center O_i and radius $R_i = \|P_i - O_i\|$ circumscribed to the triangle. The neighbors of P_i define a line segment with center $C_i = (P_{i-1} + P_{i+1})/2$. Over this line, half of the distance between P_{i-1} and P_{i+1} equals to $r_i = \|P_{i-1} - P_{i+1}\|/2$.

The vectors tangent \vec{T}_i , binormal \vec{B}_i and normal \vec{N}_i of the contour are defined as:

$$\vec{T}_i = \frac{P_{i+1} - P_{i-1}}{\|P_{i+1} - P_{i-1}\|}, \quad (2.15)$$

$$\vec{B}_i = \frac{(P_i - P_{i-1}) \times (P_{i+1} - P_i)}{\|(P_i - P_{i-1}) \times (P_{i+1} - P_i)\|}, \quad (2.16)$$

$$\vec{N}_i = \vec{T}_i \times \vec{B}_i. \quad (2.17)$$

The simplex angle ρ_i at P_i is defined by (Fig. 2.3(a)):

$$\rho_i = \arccos \left(\frac{P_i - P_{i-1}}{\|P_i - P_{i-1}\|} \cdot \frac{P_{i+1} - P_i}{\|P_{i+1} - P_i\|} \right). \quad (2.18)$$

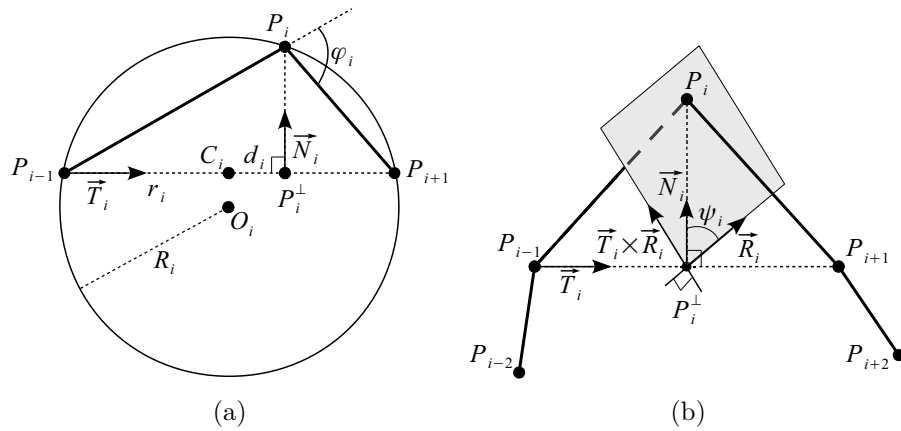


Figure 2.3: Local geometry of a 1-simplex mesh. Contours on a 2-simplex mesh are 1-simplex meshes. In 1-simplex meshes each vertex P_i has two neighbors: P_{i-1} , P_{i+1} . These vertices form a triangle (a), and define the circumscribed circle, of center O_i , to the triangle. Figure (a) shows the simplex angle ρ_i in these meshes. Figure (b) shows the angle ψ_i between the normal vector \vec{N}_i and \vec{R}_i (2.20). The plane orthogonal to \vec{T}_i and defined by vectors \vec{R}_i and $\vec{T}_i \times \vec{R}_i$ is showed in Figure (b). The normal vector \vec{N}_i lies in this plane.

In 1-simplex meshes, there are 2 metric parameters ε_{1i} , ε_{2i} . If P_i^\perp is the orthogonal projection of P_i on the line defined by its two neighbors, the metric parameters are the barycentric coordinates of P_i^\perp along the line:

$$\begin{aligned} P_i^\perp &= \varepsilon_{1i} P_{i-1} + \varepsilon_{2i} P_{i+1}, \\ \varepsilon_{1i} + \varepsilon_{2i} &= 1. \end{aligned} \quad (2.19)$$

Another metric parameter is defined for each vertex of a 1-simplex 3D mesh: the angle ψ_i (Fig. 2.3(b)). This angle is computed by using the vector:

$$\vec{R}_i = \frac{T_i \times ((P_{i-1} - P_{i-2}) \times (P_{i+2} - P_{i+1}))}{\|T_i \times ((P_{i-1} - P_{i-2}) \times (P_{i+2} - P_{i+1}))\|}. \quad (2.20)$$

The angle ψ_i is defined as the angle between \vec{R}_i and \vec{N}_i . Therefore ψ_i can be computed by:

$$\psi_i = \arccos(\vec{R}_i \cdot \vec{N}_i) \operatorname{sgn}(\vec{N}_i \cdot (\vec{T}_i \times \vec{R}_i)). \quad (2.21)$$

A normal plane orthogonal to \vec{T}_i is defined by vectors \vec{R}_i and $\vec{T}_i \times \vec{R}_i$. Figure 2.3(b) shows the position of this plane, and the direction of vectors \vec{R}_i and $\vec{T}_i \times \vec{R}_i$. Because the normal vector lies in the above defined plane, it can be expressed as:

$$\vec{N}_i = \cos(\psi_i) \vec{R}_i + \sin(\psi_i) (\vec{T}_i \times \vec{R}_i). \quad (2.22)$$

The position of every vertex P_i of a 1-simplex mesh can be determined similarly to the case of 2-simplex meshes. The position of P_i can be defined by the simplex angle, the metric parameters and the ψ_i angle:

$$P_i = \varepsilon_{1i} P_{i-1} + \varepsilon_{2i} P_{i-2} + L(r_i, d_i, \rho_i) \cos(\psi_i) \vec{R}_i + L(r_i, d_i, \rho_i) \sin(\psi_i) (\vec{T}_i \times \vec{R}_i), \quad (2.23)$$

where $d_i = |P_i^\perp - C_i| = |2 \varepsilon_{1i} - 1| r_i$, and $L(r_i, d_i, \rho_i)$ is defined by equation (2.9).

2.1.2 Mesh Deformation

The deformation of a simplex mesh can be controlled by internal and external forces. External forces are computed from the image, and aim to push the mesh to the desired borders. These forces can be computed in many ways. For example, the external force can be represented by a vector field computed using a potential $\vec{F}_{ext} = -\nabla \mathcal{P}$ [Delingette 1997]. If the potential \mathcal{P} is computed using the image gradient $\mathcal{P} = -\|\nabla I\|^2$, the vector field pushes the mesh toward areas of high image gradient which usually represent the borders of an object. Also, the external force can be computed using rules over the image gray level or the distance to some target point (sec. 2.1.4). Internal forces are issued from the mesh, control the smoothness of the deformation and avoid the mesh to lose its geometric regularity. In this work, these forces are locally computed using the properties of simplex meshes (sec. 2.1.3). The dynamic of the model can be controlled by means of a Newtonian law of motion [Delingette 1997]:

$$m \frac{\partial^2 P_i}{\partial t^2} = -\gamma \frac{\partial P_i}{\partial t} + \vec{F}_{int_i} + \vec{F}_{ext_i}, \quad (2.24)$$

where m is the mass unit of a vertex (usually 1), $\gamma \in [0, 1]$ is a damping factor to prevent oscillations, P_i is the position of vertex i , $\overrightarrow{F_{int_i}}$ and $\overrightarrow{F_{ext_i}}$ represent respectively the internal and external forces at vertex i . Considering discrete time, using finite differences, and considering $m = 1$:

$$P_i^{t+1} = P_i^t + (1 - \gamma) (P_i^t - P_i^{t-1}) + \overrightarrow{F_{int_i}} + \overrightarrow{F_{ext_i}}. \quad (2.25)$$

The choice of γ is a compromise between model efficiency and stability. When γ increases, the convergence becomes more stable but convergence gets slower. In the extreme case, when $\gamma = 1$, the speed of P_i is equal to sum of the forces, and it is not affected by the acceleration. On the other hand, if γ decreases, the effect of the acceleration increases. In the extreme case, when $\gamma = 0$, the model behaves as a perfect oscillator. The importance of internal and external forces are explained in the following sections.

2.1.3 Internal Forces

The internal force applied to the mesh can be decomposed into a tangential and a normal part. The normal force $\overrightarrow{F_{norm_i}}$ controls the height of vertex P_i with respect to the plane π_i (Fig. 2.2); in other words, it allows to control the curvature of the surface. The tangential force $\overrightarrow{F_{tang_i}}$ controls the position of the vertex P_i in the plane defined by its neighbors, i.e., it monitors the position of the projection P_i^\perp . The tangential force may be used to control the accumulation of vertices in different zones, for example, in zones with high curvature where more information is required to obtain an acceptable surface description. Thus, the internal force of the mesh is:

$$\overrightarrow{F_{int_i}} = \lambda (\overrightarrow{F_{tang_i}} + \overrightarrow{F_{norm_i}}), \quad (2.26)$$

where λ is a weight for the internal force. The tangential force pushes each vertex P_i to move P_i^\perp to an ideal position. This position is defined by target metric parameters $(\varepsilon_{1i}^*, \varepsilon_{2i}^*, \varepsilon_{3i}^*)$ (Eq. 2.13). Thus, the tangential force at vertex P_i is defined as:

$$\overrightarrow{F_{tang_i}} = (\varepsilon_{1i}^* - \varepsilon_{1i})P_{N1(i)} + (\varepsilon_{2i}^* - \varepsilon_{2i})P_{N2(i)} + (\varepsilon_{3i}^* - \varepsilon_{3i})P_{N3(i)}. \quad (2.27)$$

As mentioned before, the tangential force can be used to concentrate vertices in particular zones, for example, to have a better definition of the surface. Nevertheless, this feature is not used in the present work, and all the target metric parameters are set as $\varepsilon_{ji}^* = 1/3$, to obtain a homogeneous mesh.

The normal force controls the local curvature by the simplex angle, and is defined as:

$$\overrightarrow{F}_{norm_i} = (L(r_i, d_i^*, \rho_i^*) - L(r_i, d_i, \rho_i)) \overrightarrow{N}_i, \quad (2.28)$$

where ρ_i^* is the target simplex angle, and $d_i^* = \|C_i P_i^{\perp*}\|$ is computed with the vertex projection $P_i^{\perp*}$ calculated using the target metric parameters (Eq. 2.13). The target simplex angle in each vertex can have a fixed value, defining the mesh curvature, or can be computed to follow the mean curvature in a neighborhood:

$$\begin{aligned} \rho_i^* &= \arcsin \left(r_i \sum_{j \in Q^{S_i}(i)} \chi_{ij} \frac{\sin(\rho_j)}{r_j} \right), \\ \sum_{j \in Q^{S_i}(i)} \chi_{ij} &= 1, \quad 0 < \chi_{ij} < 1, \end{aligned} \quad (2.29)$$

where $Q^{S_i}(i)$ is a neighborhood of size S_i around P_i . In this way, ρ_i^* is obtained by computing the weighted average of the mean curvature of the vertices belonging to the neighborhood $Q^{S_i}(i)$. This neighborhood is defined recursively, so that the neighborhood $Q^{S_i}(i)$, with $S_i > 1$, is the combination of the neighborhood $Q^{S_i-1}(i)$ with the vertices that have any neighbor vertex on $Q^{S_i-1}(i)$ (Fig. 2.4).

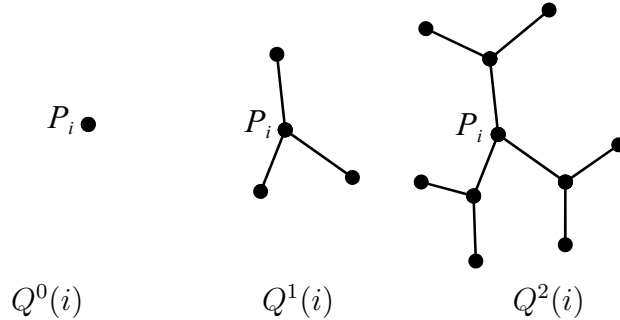


Figure 2.4: Neighborhood $Q^{S_i}(i)$ around of vertex P_i . [Delingette 1997].

S_i corresponds to the notion of rigidity. If a large neighborhood is defined, the mesh tends to keep the curvature in large zones, thus an external force will cause a small deformation but in a large zone. On the other hand, a small neighborhood allow deformations in small zones of the mesh without affecting the rest of the mesh.

2.1.3.1 Internal Forces on a Contour

The contour deformation is independent of the surface deformation, and therefore, the contour acts as boundary conditions for the surface deformation. This feature is particularly important for the deformation of open surfaces used in our study. For example, when the internal membranes of the brain are segmented (sec. 2.3.7), their boundaries are restricted to slide over other structures. In this way, the mesh surface is deformed to segment the membrane and the mesh borders keep the anatomical joint with the neighboring structures.

As for the surface case, the internal force on the contour can be divided into a normal $\overrightarrow{F_{norm_i}}$ and tangential $\overrightarrow{F_{tang_i}}$ force:

$$\overrightarrow{F_{int_i}} = \lambda \left(\overrightarrow{F_{tang_i}} + \overrightarrow{F_{norm_i}} \right), \quad (2.30)$$

where λ is the weight for the internal force of the contour. The tangential force controls the position of the plane orthogonal to $\overrightarrow{T_i}$ passing through P_i (plane defined by vectors $\overrightarrow{R_i}$ and $\overrightarrow{T_i} \times \overrightarrow{R_i}$ in Figure 2.3(b)). The target position of this plane is defined by two target metric parameters ε_{1i}^* and ε_{2i}^* , which were set to 1/2 in this work to obtain homogeneous contours. Thus, the tangent force is computed as follows:

$$\overrightarrow{F_{tang_i}} = (\varepsilon_{1i}^* - \varepsilon_{1i})P_{i-1} + (\varepsilon_{2i}^* - \varepsilon_{2i})P_{i+1}. \quad (2.31)$$

The normal force $\overrightarrow{F_{norm_i}}$ controls the contour curvature. The target curvature of the contour is defined by a target simplex angle ρ_i^* , and a target angle ψ_i^* . The target simplex angle controls the height of P_i over the line defined by its two neighbors, i.e., the contour curvature. The target angle ψ_i^* controls the direction of the contour normal at P_i with respect to the contour normal in the neighborhood of the simplex (triangle) at P_i , both measured around the contour tangent vector $\overrightarrow{T_i}$. The normal force is computed as:

$$\begin{aligned} \overrightarrow{F_{norm_i}} = & (L(r_i, d_i^*, \rho_i^*) \cos(\psi_i^*) - L(r_i, d_i, \rho_i) \cos(\psi_i)) \overrightarrow{R_i} \\ & + (L(r_i, d_i^*, \rho_i^*) \sin(\psi_i^*) - L(r_i, d_i, \rho_i) \sin(\psi_i)) \left(\overrightarrow{T_i} \times \overrightarrow{R_i} \right), \end{aligned} \quad (2.32)$$

where $d_i^* = \|C_i P_i^{\perp*}\|$ is computed with the vertex projection $P_i^{\perp*}$ calculated using the target metric parameters (Eq. 2.19).

2.1.4 External Forces

External forces applied to the deformable model are computed from the image, in order to push the mesh towards the edges of the structures that we want to

segment. These edges are usually characterized by a high image gradient. In this work, the computation of the external forces of the mesh is usually achieved by using the normal profile to each vertex, in a similar way to Active Shape Models [Cooper 1995, Weese 2001]. However, an elastically deformable model has been used in our case, avoiding the need of a training set. A set of sampling points is defined over each normal profile of length $2l$ as:

$$x_{i,j} = P_i + j\delta\vec{N}_i, \quad (2.33)$$

where δ is a sampling distance, and $j = \{-l/\delta, [-l/\delta] + 1, \dots, [l/\delta] - 1, [l/\delta]\}$. Figure 2.5 shows the normal profiles for a specific mesh. A target point x_i^{target} is computed for every profile using different rules for each anatomical structure. These rules can involve gray level, image gradient, position of other meshes, etc. Then, the vertices are pushed toward their target points by the external force. To accomplish this, the external force, \vec{F}_{ext_i} is computed using the target points, including an exponential decay if the target point is farther than a distance, D_F :

$$\vec{F}_{ext_i} = (x_i^{target} - P_i) \beta, \quad (2.34)$$

where,

$$\beta = \begin{cases} 1, & \text{if } \|x_i^{target} - P_i\| < D_F \\ \frac{1}{\exp(\|x_i^{target} - P_i\| - D_F)}, & \text{if } \|x_i^{target} - P_i\| \geq D_F \end{cases}. \quad (2.35)$$

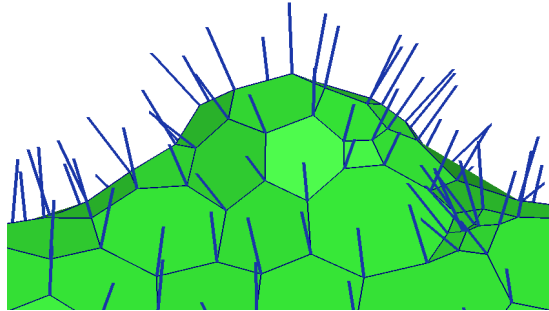


Figure 2.5: Search profiles on a simplex mesh. The profiles are in the direction of the normal vector to each vertex. Measurements of the image are taken on these profiles to guide the mesh deformation.

2.1.4.1 External Forces on a Contour

Some open meshes are used in this work to segment the internal membranes of the brain (Appx. B.4.1). The normal profiles to compute the external forces of the border vertices of the open meshes must be computed in a different way than for the vertices laying on the surface. The sampling points in a profile of length $2l$ of a border vertex are defined as:

$$x_{i,j} = P_i + j\delta\vec{M}_i, \quad (2.36)$$

where δ is a sampling distance, $j = \{[-l/\delta], [-l/\delta] + 1, \dots, [l/\delta] - 1, [l/\delta]\}$, and \vec{M}_i is computed as follows. Let \vec{N}_{SNi} be the normal vector to the surface at the neighbor vertex of P_i that lies in the surface of the mesh, and \vec{T}_i the tangent vector to the mesh border (sec. 2.1.3), \vec{M}_i is defined as (Fig. 2.6):

$$\vec{M}_i = \vec{N}_{SNi} \times \vec{T}_i. \quad (2.37)$$

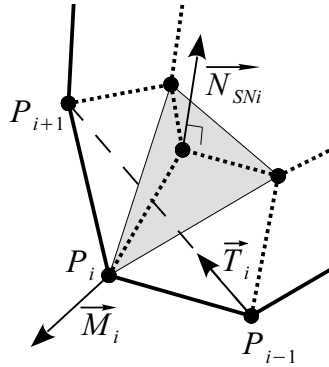


Figure 2.6: Scheme of the computation of vector \vec{M}_i used to define the sampling points of the contour vertices. Edges in the surface of the mesh are represented by dotted lines. Edges in the external contour of the mesh are represented by continuous lines.

The vector used to define the profiles of border vertices (Eq. 2.37) is computed by using the surface normal because the position of the searched structures is related with the surface normal and not with the contour normal defined in section 2.1.1.3. A target point x_i^{target} is also computed in each profile and the border vertices are pushed over these target points using the same definition of the external force employed for the surface vertices (Eq. 2.34).

2.2 Transformation Between Triangulations and Simplex Meshes

All the basic concepts related to simplex meshes have been introduced in the previous section. However, as explained in the section 1.4, the method developed in this work also uses triangle meshes. The relation between these two dual types of meshes was explained in section 2.1.1.1. In the following section, a new and direct method developed in this thesis for transforming between simplex meshes and triangulations is explained.

Simplex meshes have good properties for being used on deformable models, nevertheless triangle meshes are better for some other tasks. In this work, some of them are required, such as computation of intersections (Fig. 2.36) or construction of volumetric meshes. Therefore, a method to transform a simplex meshes into its dual triangulation is needed, with minimal geometric deterioration. A new method to perform these meshes transformations, is explained below, for both directions.

As explained in section 2.1.1.1, a simplex mesh can be seen as the topological dual of a triangulation, each vertex of the simplex mesh corresponds to a triangle in the related dual triangulation (Fig. 2.1). However, simplex meshes and triangulations are not geometrically duals (sec. 2.1.1.1). Their geometry is determined by the coordinates of their vertices, however the number of vertices of a simplex mesh V_{SM} and the number of vertices of its dual triangulation V_{TM} are different (Eq. 2.4). Therefore, it is not possible to build a homeomorphism between each set of coordinates. Consequently, there is loss of information and geometry deterioration whenever a transformation between these meshes takes place. Currently, the most common way to perform this transformation is to determine the set of vertices for the final mesh as the gravity center of each face of the initial mesh (Fig. 2.7(a)), e.g., [Delingette 1997, ITK]. This technique is very fast, but unfortunately in this case, mesh smoothing is generally very high; original shape (curvature) and volume is far to be accurately respected. An alternative is to compute the gravity center of each face and next insert this point in the mesh before triangulation, as shown in Figure 2.7(b). Although this method reduces the geometry deterioration, the resulting mesh is not dual to the initial simplex mesh, and moreover, the number of points will rises considerably. It is also possible to consider only the face vertices, but the resulting mesh will either not be topologically dual. Moreover, the converse process to obtain a simplex mesh from a triangulation is not straightforward. In [de Putter 2006], the authors

2.2. Transformation Between Triangulations and Simplex Meshes 45

show the importance of such a transformation, especially in medical applications where simplex meshes are of great use in the creation of the computational mesh based on the segmented geometry. They propose an iterative curvature correction algorithm for the dual triangulation of a two-simplex mesh. Their solution provide optimal error distribution between the two dual surfaces while preserving the geometry of the mesh, but at the price of an iterative global minimization over the whole meshes.

For all these reasons, it is essential to have an efficient method to perform transformations between these two types of meshes. In this thesis, a new technique is presented, achieving reasonable computation cost and minimal loss of geometric information.

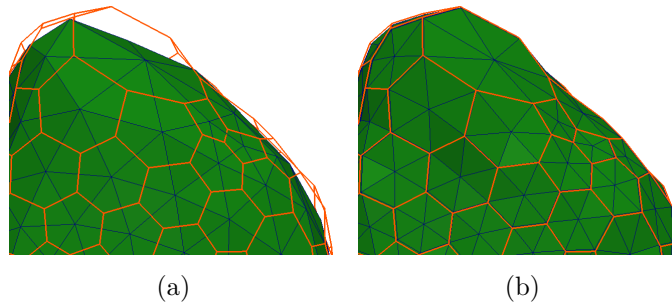


Figure 2.7: Two common ways to transform a simplex mesh into a triangulation. (a) Dual triangulation using the gravity center of each face. This type of transformation causes a geometrical degradation of the mesh. (b) Non-dual transformation in which the triangles are constructed for each face of the simplex mesh, creating edges between the gravity center and the vertex of the face. This transformation reduces the geometrical deterioration; nevertheless the number of points rise, and the converse process starting from any simplex mesh is not straightforward.

From a geometric point of view, the problem can be reduced to find an interpolation of the center of each face, and to build the dual mesh accordingly to these points. Subdivision, variational surfaces, traditional splines or implicit surfaces are among the most used techniques to find interpolating points in a mesh. As the requirement here is to get a simple and straightforward method, we propose to use a geometric interpolation, based on the distance to the tangent planes of the vertices of each face. A similar measure has been successfully used in [Ronfard 1996] to compute a local geometric error based on the maximal distance to a set of planes, in order to perform triangle mesh simplifications. An equivalent measure has been employed, using this time a summation to obtain a quadratic error [Garland 1997, Heckbert 1999]. In a more recent work, a method

for refining triangulations has been developed [Yang 2005]. It is based on face splitting and interpolation using distance minimization over the neighboring triangles planes. Here, it is worth to point out that our global objective is to perform a transformation between meshes, and not to refine them. However, we mainly got inspiration from this last work, but in our case the error measurement is applied to find the vertices of a dual mesh, to permit conversion between simplex meshes and triangulations, and conversely.

To perform transformations in any direction between these two types of dual meshes, we have to find an associated vertex q_u of the dual mesh M_2 for each face f_u of the initial mesh M_1 . When dealing with triangulations, faces are triangles; and conversely for simplex meshes, faces are polygons whose vertices are generally not coplanar. The resulting mesh M_2 should have a regular shape and preserve the geometry defined by M_1 , what is far from being straightforward. For trying to maintain the geometry, we can impose that q_u remains close to the tangent planes π_i of each vertex p_i defining the face f_u . Constraining M_2 to have a regular shape, can be achieved by choosing q_u close to the center of the face f_u , i.e., minimize the distance between q_u and all p_i . Therefore, we must minimize the distance between a point q_u and a set of points and planes. Accordingly, the purpose of the present method is to compensate the lack of existing techniques on these aspects. A technique to perform the above mentioned goal is explained in the next section.

2.2.1 Interpolation Based on Tangent Planes

The equation of a plane π can be denoted as $A \cdot p = 0$, where $A = [a, b, c, d]$ and $P = [x_p, y_p, z_p, 1]^T$ is a point lying in the plane. The coefficients a, b, c are the components of the unit vector \vec{N} normal to the plane π , and $d = -\vec{N} \cdot p$. Using the above definition, the distance between an arbitrary point q in the space and the plane π , is $|A \cdot q|$.

Considering now a set of planes π_i represented by $A_i \cdot P = 0$ with $i = \{1, \dots, L\}$, the distance between any point $q = [x, y, z, 1]^T$ to each plane π_i is $|A_i \cdot q|$. On the other hand, consider a set of points $P_j = [x_j, y_j, z_j, 1]^T$ with $j = \{1, \dots, M\}$. If we want to find the point q minimizing its distance to planes π_i and points p_j , the function to be considered follows:

$$D(q) = \sum_{i=1}^L \alpha_i |A_i \cdot q|^2 + \sum_{j=1}^M \beta_j |q - P_j|^2, \quad (2.38)$$

2.2. Transformation Between Triangulations and Simplex Meshes 47

where α_i and β_j are the weights for the distance to the planes (in order to respect geometry and curvature) and points (controlling shape regularity), respectively. Equation (2.38) can be rewritten in matrix form as:

$$D(q) = q^T Q q , \quad (2.39)$$

where

$$Q = \sum_{i=1}^L \alpha_i A_i^T A_i + \sum_{j=1}^M \beta_j Q_j , \quad (2.40)$$

and

$$Q_j = \begin{bmatrix} 1 & 0 & 0 & -x_j \\ 0 & 1 & 0 & -y_j \\ 0 & 0 & 1 & -z_j \\ -x_j & -y_j & -z_j & x_j^2 + y_j^2 + z_j^2 \end{bmatrix} . \quad (2.41)$$

Since Q_j and $A_i^T A_i$ are symmetric matrices, then Q is also symmetric and can be written as:

$$Q = \begin{bmatrix} q_{11} & q_{12} & q_{13} & q_{14} \\ q_{12} & q_{22} & q_{23} & q_{24} \\ q_{13} & q_{23} & q_{33} & q_{34} \\ q_{14} & q_{24} & q_{34} & q_{44} \end{bmatrix} . \quad (2.42)$$

To minimize the quadratic form of equation (2.39), let's solve the following system of equations:

$$\frac{\partial D(q)}{\partial x} = 0, \quad \frac{\partial D(q)}{\partial y} = 0, \quad \frac{\partial D(q)}{\partial z} = 0 . \quad (2.43)$$

Taking the partial derivatives of:

$$\begin{aligned} q^T Q q &= q_{11}x^2 + 2q_{12}xy + 2q_{13}xz + 2q_{14}x + q_{22}y^2 \\ &\quad + 2q_{23}yx + 2q_{24}y + q_{33}z^2 + 2q_{34}z + q_{44} , \end{aligned} \quad (2.44)$$

it can be noticed that the system in equation (2.43) can be rewritten in a matrix form as:

$$\begin{bmatrix} q_{11} & q_{12} & q_{13} & q_{14} \\ q_{12} & q_{22} & q_{23} & q_{24} \\ q_{13} & q_{23} & q_{33} & q_{34} \\ 0 & 0 & 0 & 1 \end{bmatrix} \begin{bmatrix} x \\ y \\ z \\ 1 \end{bmatrix} = \begin{bmatrix} 0 \\ 0 \\ 0 \\ 1 \end{bmatrix} . \quad (2.45)$$

2.2. Transformation Between Triangulations and Simplex Meshes 48

Finally, the solution of equation (2.45) follows:

$$\begin{bmatrix} x \\ y \\ z \end{bmatrix} = \begin{bmatrix} q_{11} & q_{12} & q_{13} \\ q_{12} & q_{12} & q_{23} \\ q_{13} & q_{23} & q_{33} \end{bmatrix}^{-1} \begin{bmatrix} -q_{14} \\ -q_{24} \\ -q_{34} \end{bmatrix}, \quad (2.46)$$

where $q = [x, y, z]^T$. This system always has a unique solution (i.e., the matrix is invertible) because function (2.38) is strictly convex and therefore has no more than one minimum.

A way to minimize equation (2.38) was explained above, but we have not mentioned how to choose the values for the weights α_i and β_j . The weights α_i should reflect the importance of each plane to the interpolation, a way for computing their values is explained to transform triangulations into simplex meshes (sec. 2.2.2) or vice-versa (sec. 2.2.3). The weights β_j reflects how the positions of points P_j are considered in the interpolation. A technique to compute these weights β_j is introduced in the next section.

2.2.1.1 Weights Computation

The solution of equation (2.38) can be understood as an affine combination of the generalized intersection of all planes π_i (first term) and the average of all points P_j (second term). This affine combination is controlled by the weights α_i and β_i . For example, let's consider points P_1, P_2 and planes π_1, π_2 as shown on Figure 2.8. Planes intersect at point P_α , and the average of the points (for $\beta_i = \beta$) is P_β . The weights α_i should reflect the importance of each plane to the interpolation; and this importance will be estimated in a different way for triangulations or simplex meshes, as this will be detailed in the next sections.

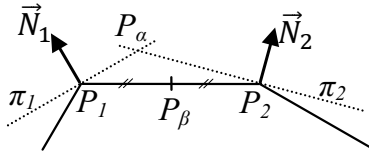


Figure 2.8: Solution of equation (2.38) as the affine combination of the generalized intersection of planes π_i (P_α) and the average of all points p_i (P_β , for $\beta_i = \beta$).

The weights β_i can be calculated using an analogue method to the one used for mesh refinement in [Yang 2005]. We are looking for an interpolated point q at the center of each face. Assuming that points P_i define a face, and \vec{N}_i are the

2.2. Transformation Between Triangulations and Simplex Meshes 49

unit normal vectors to the mesh at P_i , then we can estimate the position for q as:

$$\bar{q} = c_u + w \sum_{i=1}^L ((P_i - c_u) \cdot \vec{N}_i) \vec{N}_i, \quad (2.47)$$

where w is a free positive parameter controlling the smoothness of the interpolation, and where:

$$c_u = \frac{1}{L} \sum_{i=1}^L P_i. \quad (2.48)$$

Substituting q with its estimation \bar{q} in equation (2.45), it follows:

$$\begin{bmatrix} q_{11} & q_{12} & q_{13} & q_{14} \\ q_{12} & q_{22} & q_{23} & q_{24} \\ q_{13} & q_{23} & q_{33} & q_{34} \\ 0 & 0 & 0 & 1 \end{bmatrix} \begin{bmatrix} \bar{x} \\ \bar{y} \\ \bar{z} \\ 1 \end{bmatrix} = \begin{bmatrix} \delta_x \\ \delta_y \\ \delta_z \\ 1 \end{bmatrix}. \quad (2.49)$$

Now, the weights β_i that minimize the residues δ (ep. (2.49)) should be found such that \bar{q} approaches the solution of equation (2.49). Because q should lie close to the face center, the same weight can be assigned to all points, i.e., $\beta_i = \beta$. Then, using the notation $\pi_i = A_i \cdot P_i$ to express the planes, the residues δ can be written as:

$$\begin{aligned} \delta_x &= \sum_{i=1}^L \alpha_i a_i (A_i \cdot \bar{q}) + \beta \left(L\bar{x} - \sum_{i=1}^L x_i \right), \\ \delta_y &= \sum_{i=1}^L \alpha_i b_i (A_i \cdot \bar{q}) + \beta \left(L\bar{y} - \sum_{i=1}^L y_i \right), \\ \delta_z &= \sum_{i=1}^L \alpha_i c_i (A_i \cdot \bar{q}) + \beta \left(L\bar{z} - \sum_{i=1}^L z_i \right). \end{aligned} \quad (2.50)$$

Then, finding the weight β can be achieved by minimizing $\delta_x^2 + \delta_y^2 + \delta_z^2$. The solution of $\partial(\delta_x^2 + \delta_y^2 + \delta_z^2)/\partial\beta = 0$ leads to:

$$\beta = \frac{TB}{B^2}, \quad (2.51)$$

where:

$$\begin{aligned} T &= \sum_{i=1}^L \alpha_i (A_i \cdot \bar{q}) \vec{N}_i, \\ B &= \sum_{i=1}^L (p_i) - L\bar{q}. \end{aligned} \quad (2.52)$$

2.2. Transformation Between Triangulations and Simplex Meshes 50

To avoid a negative or zero value of β , and to keep a regular surface, $\beta = \min(\max(TB/B^2, 0.1), 2)$.

2.2.2 From Triangulation to Simplex Mesh

In this section, we will see the first case, i.e., when performing the mesh transformation from a triangulation to a simplex mesh. In this case, an appropriate point q_u in the new simplex mesh must be calculated for each triangular face t_u . Then, we need information for each triangle t_u about the curvature of the mesh. Let us consider the tangent planes to the vertices P_i ($i = 1, 2, 3$) composing triangle t_u ; these planes π_i can be written as $A_i \cdot P_i = 0$ as defined previously. Moreover, the normal vectors that define these planes can be calculated as:

$$\vec{N}_i = \frac{\sum_{k=1}^{L_i} \phi_k \vec{N}_k}{\left\| \sum_{k=1}^{L_i} \phi_k \vec{N}_k \right\|}, \quad (2.53)$$

where \vec{N}_k ($k = 1, \dots, L_i$) are the normals of the triangles t_k to which the vertex P_i belongs, and ϕ_k is the angle of the triangle t_k at vertex P_i (Fig. 2.9).

To approximate the surface, the distance between the new point q_u and planes π_i is minimized. Again, q_u should not lie too far from the center of triangle t_u to preserve a regular shape, therefore q_u should minimize its distance to vertices P_i . The direct minimization of equation (2.38) will provide us with an appropriate q_u .

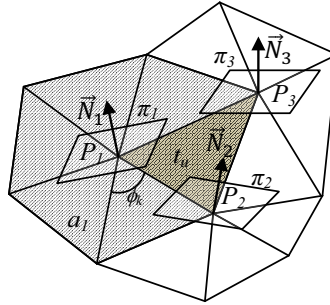


Figure 2.9: Scheme of the geometric entities of a triangle mesh, used to compute the vertex q_u of the dual simplex mesh. The triangle t_u related to the vertex q_u (dual relation) is colored in dark gray, and the area a_1 corresponding to the vertex P_1 (Eq. 2.54) is colored in light gray.

2.2. Transformation Between Triangulations and Simplex Meshes 51

Each weight α_i is calculated based on the area a_i corresponding to the sum of the areas of all triangles t_k sharing P_i (Fig. 2.9):

$$\alpha_i = \frac{a_i}{\sum_{j=1}^3 a_j} . \quad (2.54)$$

This way, the distance to each plane is weighted according to the area of triangles that were used to calculate it. The weights β_i are calculated with equation (2.51).

2.2.3 From Simplex Mesh to Triangulation

In this section, we are dealing now with the converse case. A vertex q_u of the triangulation must be calculated for each face f_u of the simplex mesh. However, faces of a simplex mesh do not have a fixed number of vertices P_i ($i = 1, \dots, N_u$), and moreover they are generally not coplanar. The distance between q_u and the planes π_i tangent to the vertices P_i , is minimized to maintain the geometry of the mesh. These planes are defined by the vertices P_i and the normal vector at each vertex. In a simplex mesh, normals are defined by the plane containing the three neighbors $P_{N1(i)}, P_{N2(i)}, P_{N3(i)}$ (Fig. 2.2) of the considered vertex P_i [Delingette 1999]. As in the inverse case, q_u should lie close to the center of the face f_u to preserve a regular shape. Figure 2.10 illustrates these planes and vertices. As previously, equation (2.38) can be used to calculate q_u by minimizing the distance to planes π_i and vertices p_i .

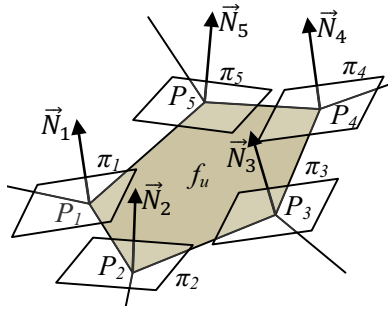


Figure 2.10: Scheme of the geometric entities of a simplex mesh, used to compute the vertex q_u of the dual triangle mesh. The face f_u related to the vertex q_u (dual relation) is colored in gray.

The surface of the circle defined by the neighbors at each vertex P_i is a good estimation of the importance the plane π_i has within the mesh, thus its radius r_i

is used to calculate the weights α_i for equation (2.38) (Fig. 2.2). It follows:

$$\alpha_i = \frac{r_i^2}{\sum_{j=1}^{N_u} r_j^2}. \quad (2.55)$$

Again, in this case, weights β_i are calculated using the same technique described in section 2.2.1, equation (2.51).

Results of the implemented method are shown in section 2.2.4.

2.2.4 Transformation Results

In section 2.2, a method for transforming between triangulations and simplex meshes was introduced. In the present section, some results of this method will be shown.

When performing a transformation between simplex meshes and triangulations (and conversely), a similar mesh to the original one is expected, to result in a minimal geometric perturbation. To measure the quality of the transformations in both directions, the set of successive transformations ($TM_1 \rightarrow SM_1 \rightarrow TM_2 \rightarrow \dots \rightarrow TM_k \rightarrow SM_k \rightarrow TM_{k+1} \rightarrow \dots \rightarrow TM_N \rightarrow SM_N$) is performed, where TM_k is a triangulation and SM_k a simplex mesh, with ($k = 1, \dots, N$). It is obvious that such back and forth conversion will never be required by any application, but successive transformations permit to magnify, and thus pointing out, incorrect behaviors of a technique.

The present technique has been compared to the most commonly used at this time, i.e., using the Center of Mass of each face to compute the corresponding point of the dual mesh [Delingette 1999]. Since all meshes T_k and S_k have respectively the same number of vertices, we have considered that the most appropriate measure is a simple vertex-to-vertex distance computation after each transformation cycle. In this way, each triangulation is compared at each step to the first triangulation; and correspondingly, each simplex meshes is considered accordingly to the first simplex mesh obtained.

Figure 2.11 shows the distance graph measured for the surface of cerebral ventricles (1360 vertices/simplex faces, 2728 triangles/vertices), for 150 iterations. The vertex-to-vertex mean distances are expressed as a percentage of the bounding box diagonal of TM_1 or SM_1 for the triangulation or simplex mesh, respectively. Curve 2.11(a) shows results using the *Center of Mass* technique, while 2.11(b) draws results with our original technique. If we compare the results for a set of meshes, the *Center of Mass* technique produces high degeneration in

2.2. Transformation Between Triangulations and Simplex Meshes 53

some parts of the mesh (Fig. 2.12(b), (c) and (d)), losing most of the details present in the initial geometry. However, using an interpolation based on the tangent planes, the initial geometry is much better preserved, as it is shown in Figure 2.12(e), (f) and (g).

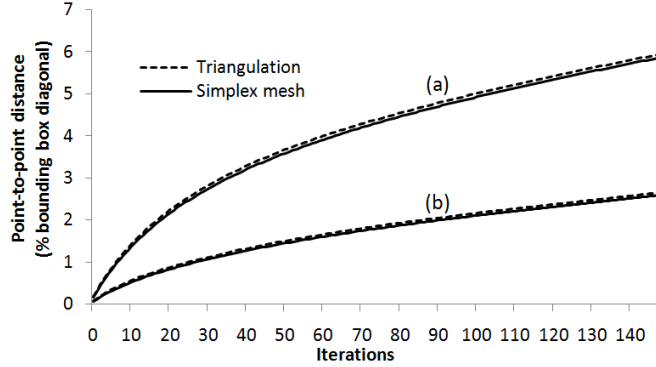


Figure 2.11: Curves of the mean error of the successive transformations of a cerebral ventricles surface (a) Transformation based on the faces center of mass. (b) Interpolation based on tangent planes.

As a complementary result, the Hausdorff distance was also measured between initial and transformed meshes by using the *Metro* [Cignoni 1998] tool that adopts a surface sampling approach. This tool is integrated in the free software *Meshlab* [Meshlab] (GNU license). The *Prism* (92 vertices, 180 triangles; from the AIM@SHAPE Shape Repository [AIM@SHAPE]), *Block* (2132 vertices, 4272 triangles; from AIM@SHAPE), *Horse* (48485 vertices, 96966 triangles; from Cyberware, Inc [Cyberware]), and *Bunny* (34834 vertices, 69451 triangles; from the Stanford 3D Scanning Repository [StanfordRep]) meshes have been considered; and the distance was measured after a cycle of transformations, i.e., swapping to simplex mesh and back to triangulation. Figure 2.13 shows the initial mesh with coloration according to its distance to the resulting one, and Table 2.3 shows the well known ratio between measured distances and the bounding box diagonal of the original mesh. The mean and Root Mean Square (RMS) distances between two surfaces M_1 and M_2 are defined as:

$$\text{Mean distance}(M_1, M_2) = \frac{1}{|M_1|} \int_{p \in M_1} \text{HD}(p, M_2) ds ,$$

$$\text{RMS distance}(M_1, M_2) = \sqrt{\frac{1}{|M_1|} \int_{p \in M_1} \text{HD}(p, M_2)^2 ds} ,$$

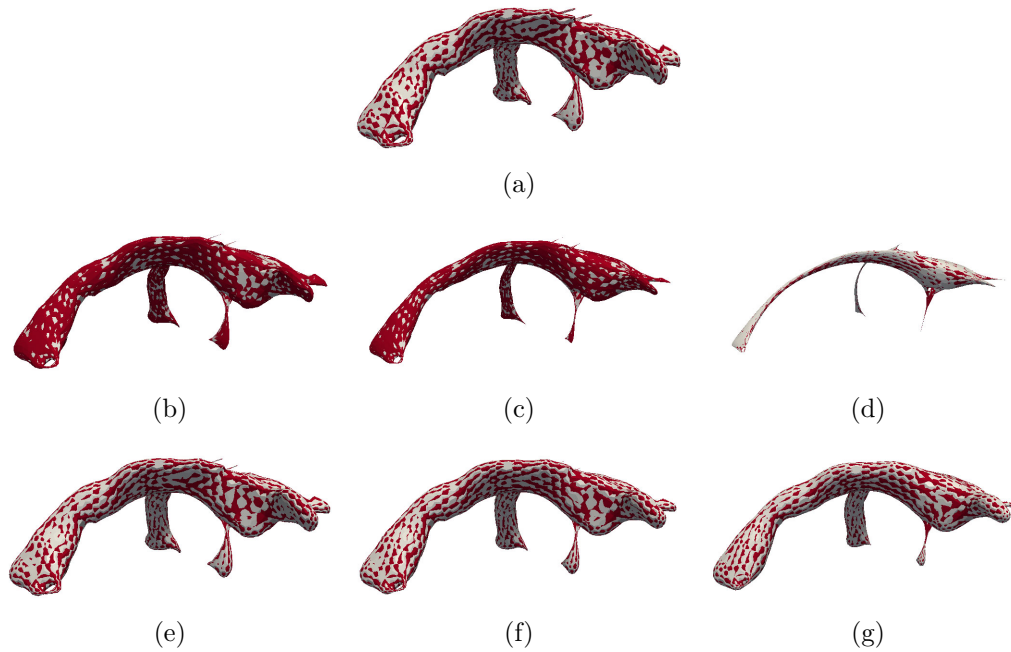


Figure 2.12: Cerebral ventricles mesh (a) after successive transformations between simplex (lighter) mesh and triangulation (darker). Middle row: meshes obtained by using the technique based on the mass center of the faces, after (b) 5, (c) 15 and (d) 50 cycles. Bottom row: meshes obtained using our technique, after (e) 5, (f) 15 and (g) 50 cycles.

were $\text{HD}(p, M)$ is the Hausdorff distance between point p and surface M , and $|M|$ is the area of M . The computation time was multiplied by approximately 30 with our method; e.g., the computation time for the prism mesh was 7.161 ms with the center of mass and 0.27 seconds with our method ¹. As it can be expected, in both cases, the main error is concentrated in high curvature areas. But, as previously seen, the error dramatically decreases with our technique (Fig. 2.13, bottom row) compared to the *Center of Mass* (Fig. 2.13, upper row).

Figure 2.14 shows a comparison between the initial (darker) and the resulting (lighter) meshes, using both methods. Errors are significantly lower in our case (b) than for the *Center of Mass* technique (a). Moreover, the resulting mesh tends to be inside (resp. outside) the initial mesh in areas with positive (resp. negative) curvature for the classic technique, while our technique avoids this construction artifact, thanks to the introduction of an appropriate weighting between element regularity and surface smoothness. Moreover, from exam-

¹developed in Python Language on AMD Athlon 62x2 Dual, 2GHz, 1Gb RAM

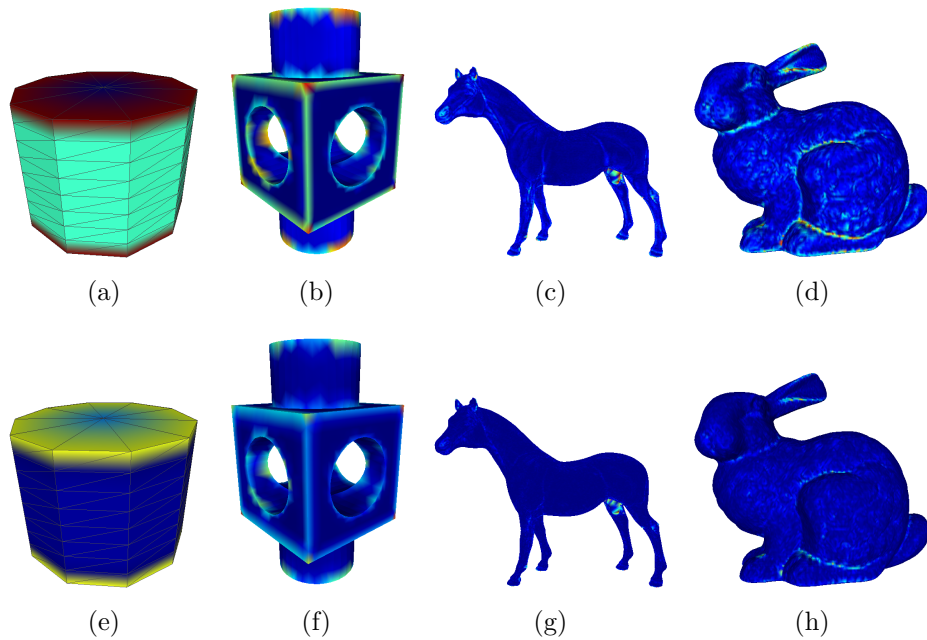


Figure 2.13: *Prism, Block, Horse* and *Bunny* meshes colored according to the Hausdorff distance between the initial and final triangle meshes after a cycle of transformations (triangle mesh \rightarrow simplex mesh \rightarrow triangle mesh). The blue-green-red (or black-white) color scale is used, where red (white) represents the largest value. 1) Upper figures (a), (b), (c) and (d) using the *Center of Mass*. 2) Lower figures (e), (f), (g) and (h) using our method based on the *Distance to the tangent planes*.

ining equation (2.38), the question of the topological validity of the resulting mesh may arise. The solution is an equilibrium between shape preservation and mesh smoothing, that behaves properly (i.e., the point lays inside the triangle). However, for extreme cases like spiky meshes with high curvature areas, some additional feature preserving process may be required.

Discussion on Our Conversion Method. A method to carry out transformations between triangulations and simplex meshes has been presented. Compared to the ones proposed in the literature, our method is straightforward and does not require any iteration. It is intuitively based on the interpolation of the initial mesh to find the corresponding vertices of the dual mesh. The interpolation is based on a direct and local minimization of the distance to tangent planes, and vertices of each face. Our transformation technique was compared to the most frequently used method, which is based on placing the dual vertices

2.2. Transformation Between Triangulations and Simplex Meshes 56

Table 2.3: Hausdorff distances.

		Center of Mass	Distance to Planes	Gain [%]
Prism Mesh	min	0,003537	0,000016	99,54
	max	0.060099	0.037205	38.09
	mean	0.033701	0.014088	58.20
	RMS	0.036620	0,018715	48,89
Block Mesh	min	0.0	0.0	0.0
	max	0.019153	0.014321	25.23
	mean	0.002397	0.001820	24.07
	RMS	0.003855	0.002840	26.34
Horse Mesh	min	0.0	0.0	0.0
	max	0.004596	0.003873	15.74
	mean	0.000126	0.000047	62.50
	RMS	0.000205	0.000107	48.08
Bunny Mesh	min	0.0	0.0	0.0
	max	0.003321	0.002761	16.85
	mean	0.000220	0.000096	56.36
	RMS	0.000324	0.000160	50.62

at the center of mass of the initial faces, and the weaknesses of this latter have been illustrated. The performance of the proposed method was measured using a vertex-to-vertex distance between both triangulations and simplex meshes, after performing a chain of successive transformations. Moreover, we measured the Hausdorff distance between meshes after performing a cycle of transformations, i.e., after carrying out a transformation to simplex mesh and back to triangulation. The performance of our method was satisfactory, providing a significant reduction of the error, of nearly 50%, at reasonable linear time. The computation time was multiplied by approximately 30 with our method compared to the center of mass. The computational time is linear according to the number of vertices of the mesh because our method is direct and performed locally for each vertex. From the results we obtain, we believe it is worth paying an extra (but limited) amount of computation to drastically improve the final quality of the dual mesh

Thus, the method has proven to be adequate to be used in any application requiring topological mesh transformation while preserving geometry, and without increasing complexity. Our method was presented in [Galdames 2012].

In the next section (sec. 2.3), the segmentation method itself is explained. And we will see how our conversion method can be used adequately to take advantage of simplex or triangle formulations for meshes. Of course, this conversion is just a

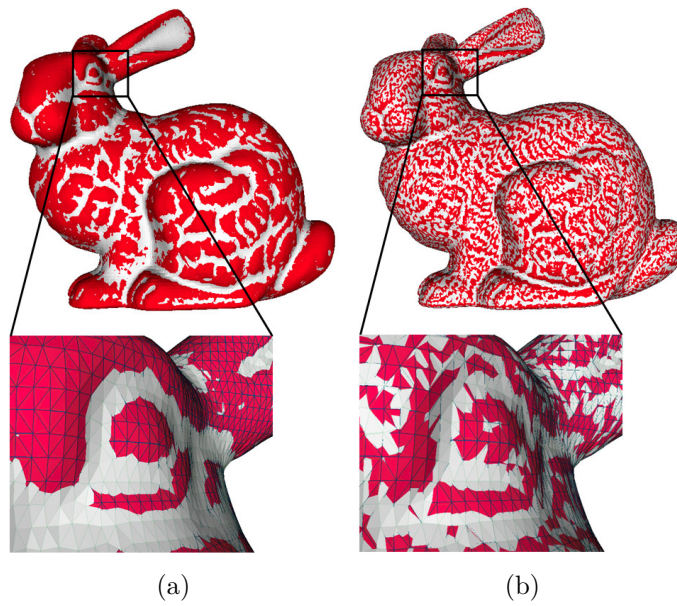


Figure 2.14: Comparison between the *bunny* original mesh (darker) and after a cycle of transformations (lighter) using two different methods. The figure shows the original and transformed meshes superimposed, and a zoom of the area around the eye. (a) Using *Center of Mass*. (b) Using our distance to the tangent planes.

tool, and the main segmentation steps are fully detailed in the following sections.

2.3 MRI Segmentation

In this section, our original method to segment a particular MRI brain image is presented. Figure 2.15 shows a flow diagram of the method. The result of this method is a patient-specific anatomical model of the brain suitable for mechanical modeling. Evaluations of the different steps of the method are presented in Chapter 3.

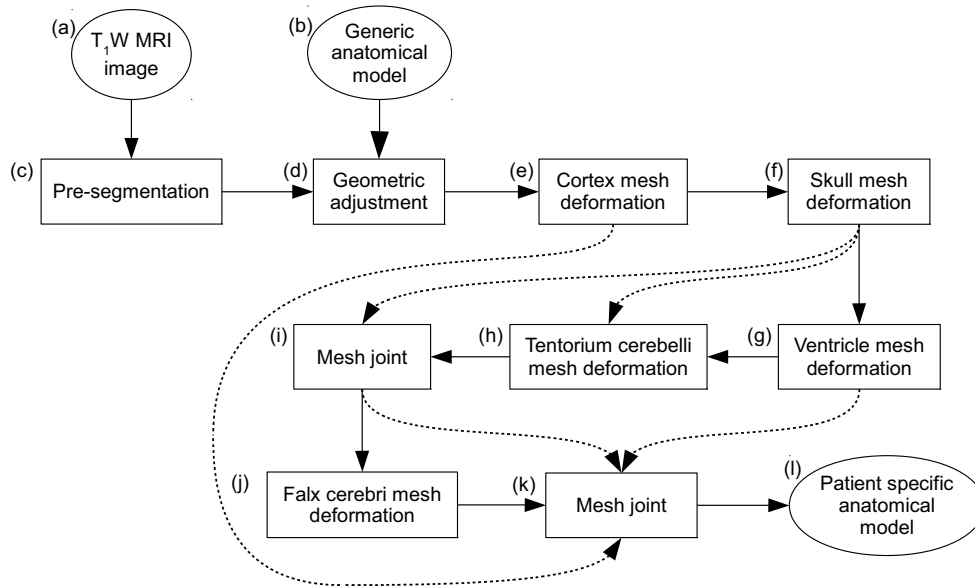


Figure 2.15: Flow diagram of the segmentation method. Continuous lines represent the direction of the process and dashed lines represent information that is passed from one part of the process to another. The original T_1W MRI image (a) is first pre-segmented (c). Then, a generic anatomical model of the brain (b) is geometrically adjusted to the pre-segmentation (c). After that, the meshes that conform to this anatomical model are independently deformed. The cortex mesh is the first to be deformed (e). Then, the skull mesh is deformed using the deformed cortex mesh (f). Next, the ventricle mesh is deformed (g). The deformation of the tentorium cerebelli mesh (h) is based on the deformed skull mesh, and after its deformation both meshes are then joined (i) to control the deformation of the falx cerebri mesh (j). Finally, the previously joined skull and tentorium meshes are joined with the falx cerebri, ventricle and cortex meshes (k) obtaining a patient specific anatomical model (l).

Our segmentation method can be divided into A) a pre-segmentation (Fig. 2.15(c)) based on thresholds, histogram analysis and morphological operators (sec. 2.3.1); and B) a segmentation based on deformable models. The pre-segmentation is designed to eliminate most of non-brain tissue. This pre-segmentation permits to get rid of initialization hazard, for which all

deformable model methods are known to be very sensitive to. Moreover, the brain tissue lost in the pre-segmentation will be recovered in this segmentation step.

A) The pre-segmentation includes three main steps:

1. Background elimination (sec. 2.3.1.1) with Otsu threshold [Otsu 1979].
2. Brain identification (sec 2.3.1.2): Application of a threshold computed using the image histogram and a model mask of the brain. The brain tissue is selected using morphological operators and 3D Connected Component Analysis.
3. Modeling by Gaussians (sec 2.3.1.3): Application of thresholds computed using a Gaussian model of the image histogram. The brain tissue is selected similarly as in the previous step.

B) In the segmentation by deformable models, a generic model of the brain anatomy (sec. 2.3.2) is deformed to match the particular anatomy of the patient. Each structure of the brain anatomy is represented by an independent mesh of the generic model. The segmentation can be divided into the following steps:

1. Geometric adjustment (sec. 2.3.3): The adjustment of the model is performed by using the pre-segmentation, and the cortex and ventricle meshes, because the edges of these structures are explicitly defined in the pre-segmentation (Fig. 2.15(d)).
2. Cortex segmentation (sec. 2.3.4): Due to its numerous convolutions, this is the most complex structure of the model (Fig. 2.15(e)). The deformation of the mesh is divided as follows:
 - (a) First deformation (sec. 2.3.4.1): The cortex mesh is adjusted to the pre-segmentation by using deformable models techniques. This deformation allows to use the pre-segmentation as the starting point of the segmentation.
 - (b) Second deformation (sec. 2.3.4.2): The mesh is deformed to reach the GM-CSF interface. This deformation is designed to correct the mesh in areas where the pre-segmentation has eliminated part of the brain parenchyma.

- (c) Third deformation (sec. 2.3.4.3): The mesh is more carefully adjusted to segment the cortical surface and to eliminate parts of cerebrospinal fluid that may remain at the brain surface. The result of this final deformation is an accurate segmentation that includes all the brain tissue whereas it eliminates the CSF.
3. Skull segmentation (sec. 2.3.5): The skull mesh is deformed to segment the internal surface of the skull. This deformation is also guided by the deformed cortex mesh (Fig. 2.15(f)).
 4. Ventricles segmentation (sec. 2.3.6): The ventricle mesh is deformed using the original image (Fig. 2.15(g)).
 5. Tentorium cerebelli segmentation (sec. 2.3.7.1): The tentorium cerebelli membrane is segmented by the corresponding open mesh. The deformed skull mesh is also used to guide the segmentation, since this membrane is joined to the skull and this anatomical relation must be respected (Fig. 2.15(h)).
 6. Falx cerebri segmentation (sec. 2.3.7.2): The falx cerebri membrane is segmented using the corresponding mesh. To guide the deformation, the skull and tentorium meshes are also used, because the falx cerebri is related with these two structures (Fig. 2.15(j)).
 7. Obtaining the final mesh (sec. 2.3.8): All deformed meshes are integrated into a final mesh representing the patient's brain anatomy (Fig. 2.15(k)).

Each step of the segmentation method is explained in details in the following sections.

2.3.1 Pre-segmentation

To perform this preliminary step, a method based on thresholds, morphological operators, and modeling by Gaussian function, has been used. This type of methods are fast, robust and based on the fact that the brain is the largest connected structure inside the head [Shan 2002, Kovacevic 2002, Dogdas 2005, Chiverton 2007]. In the following, we propose an extension of such approaches, by defining an adaptive threshold based on the image data. Figure 2.16 shows a flow diagram of the proposed pre-segmentation. Since the result will only be used as an optimal starting point for the segmentation step, we do not need here to

perform a precise Skull Stripping. Our goal here is to eliminate all tissues except the brain, which it is composed mainly of white and gray matter. At this point, no matter whether the quality of the discrimination is not perfect, as it will be greatly improved in the next steps to achieve a proper segmentation.

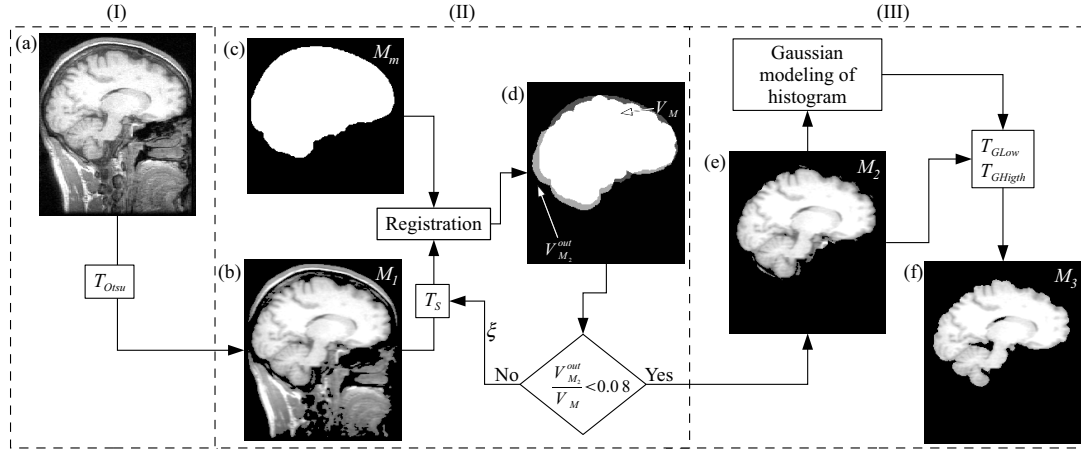


Figure 2.16: Flow diagram of the pre-segmentation method. The method can be divided into 3 steps. In step (I), an Otsu threshold T_{Otsu} is applied to the original image (a) to eliminate background, obtaining a masked image (b). In step (II), a threshold T_s and morphological operators are applied to the masked image (b), obtaining a mask M_2 (white and light gray in (d)). The threshold T_s is adjusted by comparing the mask M_2 with a model mask M_m (c) [Rex 2003]. To perform the comparison, M_2 and the model mask are registered. Figure (d) shows the registration: white represents M_m and M_2 ; dark gray represents only M_m ; and light gray represents only M_2 . Then, if the volume $V_{M_2}^{out}$ (light gray in (d)) of M_2 that lies outside the model mask is inferior to 8% of the model mask volume V_M (dark gray and white in (d)), the image masked with M_2 (e) is used in the next step (III). Otherwise, T_s is modified to eliminate more non-brain tissue. In step (III), the gray levels of different tissues are modeled using Gaussian functions. This modeling is used to compute two thresholds T_{GLow} and T_{GHigh} which are used, together with morphological operators, in the image (e). The result of this final step is a pre-segmented image (f).

To compute the thresholds, the image histogram $p(i)$ is seen as a probability density function of the image gray levels:

$$p(i) = \frac{n_i}{N}, \quad (2.56)$$

where n_i is the number of voxels with gray level $i = \{0, 1, 2, \dots, W - 1\}$, and N is the number of voxels in the image, i.e., $p(i)$ is the probability for a voxel to get intensity i . Usually the number of gray levels may change depending on the image, but using a fixed number of bins W will allow standardizing our analysis. We

used $W = 256$ as in [Shan 2002], because no significant improvement is reached when more levels are used.

2.3.1.1 Background Elimination

First, a threshold is used in order to remove the image background. This threshold T_{Otsu} is computed using the Otsu method [Otsu 1979] that is based on the binarization of the image into two classes: C_B and C_F . Class C_B represents the image background, which in our case consists of air, bone and part of the cerebrospinal fluid. Class C_F represents the foreground, which is composed of other tissues including the GM and WM of the brain. The classes are defined using a threshold T : $C_B = \{0, 1, 2, \dots, T - 1\}$, $C_F = \{T, T + 1, \dots, W - 1\}$.

The Otsu method calculates the optimal threshold T_{Otsu} minimizing the dispersion within each class. Thus, T_{Otsu} should minimize the weighted sum of the variances of each class, this sum is called the *within-class variance*:

$$\sigma_{within}^2(T) = n_B(T)\sigma_B^2(T) + n_F(T)\sigma_F^2(T), \quad (2.57)$$

where $\sigma_B^2(T)$ and $\sigma_F^2(T)$ are the variances of background and foreground voxels, respectively, and:

$$\begin{aligned} n_B &= \sum_{i=0}^{T-1} p(i), \\ n_F &= \sum_{i=T}^{W-1} p(i). \end{aligned} \quad (2.58)$$

To find the minimum, the value of the within-class variance should be computed for each possible threshold. But this calculation can be performed in a more efficient way. If the within-class variance is subtracted from the total variance of the image, the *between-class variance* is obtained:

$$\begin{aligned} \sigma_{between}^2(T) &= \sigma^2 - \sigma_{within}^2(T) \\ &= n_B(T) [\mu_B(T) - \mu]^2 + n_F(T) [\mu_F(T) - \mu]^2, \end{aligned} \quad (2.59)$$

where σ^2 is the total variance and μ is the overall image mean. The between-class variance can be viewed as an indicator of the distance between the class means. Substituting $\mu = n_B(T)\mu_B(T) + n_F(T)\mu_F(T)$ and simplifying, we get:

$$\sigma_{between}^2(T) = n_B(T)n_F(T) [\mu_B(T) - \mu_F(T)]^2. \quad (2.60)$$

This avoid to calculate differences between individual intensities and the class means. The optimal threshold T_{Otsu} is the one that maximizes the between-class variance (or, conversely, minimizes the within-class variance). To optimize the computation, the values of $n_B(T)$, $n_F(T)$, $\mu_B(T)$ and $\mu_F(T)$ can be updated at every increase of T using recurrence relations:

$$\begin{aligned} n_B(T+1) &= n_B(T) + n_T, \\ n_F(T+1) &= n_F(T) - n_T, \\ \mu_B(T+1) &= \frac{\mu_B(T)n_B(T) + n_T T}{n_B(T+1)}, \\ \mu_F(T+1) &= \frac{\mu_F(T)n_F(T) + n_T T}{n_F(T+1)}. \end{aligned} \tag{2.61}$$

After calculating the threshold T_{Otsu} , the original image 2.17(a) is masked, i.e., all voxels with lower gray value are ignored, leading to the mask, M_1 , (see Fig. 2.16(b)). Figure 2.17(b) shows the image and its histogram after applying the Otsu threshold. In this image the air, bone, and most of the cerebrospinal fluid have been removed. The removal of very low intensity voxels (background) allows focusing the processing on the tissues of interest (foreground). Next, the brain can be identified as the largest structure inside the head.

2.3.1.2 Brain Identification

The brain is first separated from other tissues by applying a threshold, T_s based on an image histogram, and a brain model mask as will be explained in this section.

Since the brain is the largest organ in the head, and is formed primarily of white and gray matter, we can infer that the two peaks in the histogram of the image masked with M_1 (Figure 2.16(b) in flow diagram) are the mean gray level of the GM μ_{gm} , and WM μ_{wm} , respectively. Figure 2.17(b) shows these peaks. The threshold for separating the brain is defined as:

$$T_s = T_{Otsu} + \xi(\mu_{gm} - T_{Otsu}). \tag{2.62}$$

This definition is similar to the one proposed by Shan in [Shan 2002], where ξ is fixed to 0.7. We have extended this definition, leading to a more flexible

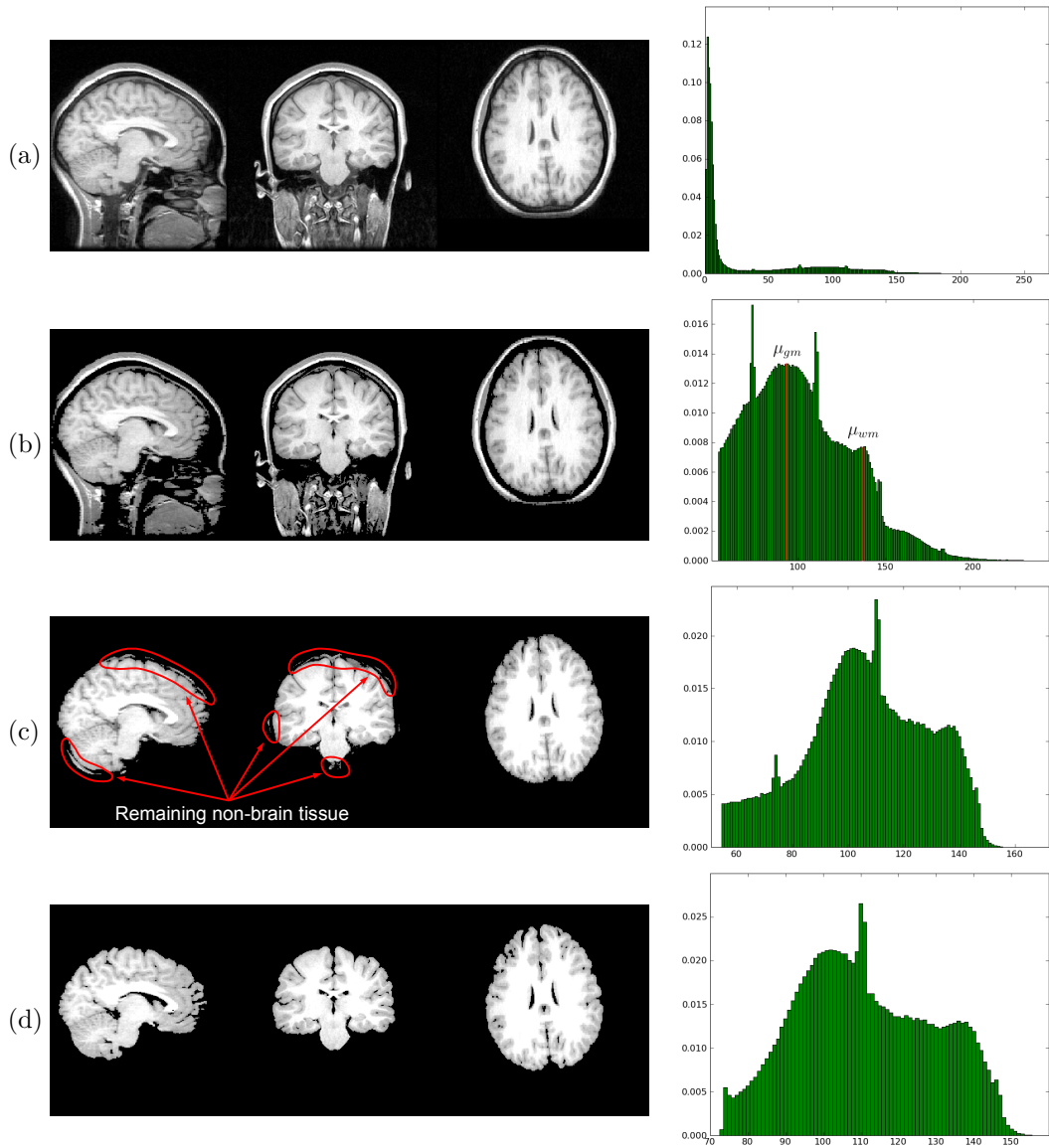


Figure 2.17: Skull Stripping of MRI. The MRI image (left) and its histogram (right) are shown at different steps of the skull stripping process. The histograms are represented as probability density functions of the gray levels of the images (Eq. (2.56)). (a) Original MRI image and its histogram. (b) Result of applying the Otsu threshold T_{Otsu} . The background of the image is removed. Peaks formed by gray μ_{gm} and white μ_{wm} matter are shown in the histogram. (c) Result after applying threshold T_s and identify the brain. Most of the non-brain tissue is removed, remaining only some tissue of the meninges which is highlighted in the figure. (d) Skull stripping image after the final step based on the modeling of the image gray level by Gaussian functions. All the non-brain tissue is removed.

threshold that can be adjusted depending on the image. ξ must be high enough to separate the brain from other tissues, while preserving the removal of brain tissue. To achieve this, the ideal T_s for each image is estimated applying thresholds computed with increasing values of ξ as follows:

Given a value of ξ , the threshold T_s is computed using (2.62). Then, T_s is applied to the image masked with M_1 (Fig. 2.16(b)), and the resulting image is binarized. In this binarized image, small connections between brain and surrounding tissue may still remain. To eliminate them, a binary opening is applied 2 times to the mask, using a 3D spherical structural element with a 3 mm radius. Next, the mask, M_2 (Fig. 2.16(d)), is obtained by performing a 3D connected component analysis using a square connectivity equal to one, and keeping the largest element. To recover some tissue removed by the binary opening, a binary dilatation is applied 2 times to M_2 using the same structural element. As M_2 has to be brain-shaped, this idea is used to evaluate whether enough tissue has been removed. For this, a fast and simple method is used: the resulting volume is compared with a brain model mask. The model used is a binary mask of the ICBM452 5th-order warp atlas from the Lab. of Neuro Imaging at UCLA [Rex 2003] (Fig. 2.16(c)). The model mask is registered to the mask, M_2 before the comparison. Assuming the model mask and M_2 have the same orientation, a simple and direct transformation with 6 parameters is used for the registration; 3 translations and 3 scaling operations. In the coordinate axis, the transformation matches the limits of the upper part of the brain. Because usually there are tissue remnants that can cause errors when simply the “bounding box” (limits of the whole volume in the three coordinate axis) of M_2 is used, a careful selection of the limits is performed as follows:

Upper Limit: The rules to find the connected volume representing the brain are designed to ensure that the head will always be recognized; hence the upper reference limit is the top of the mask in the axial direction (sagittal and coronal cuts in Figure 2.18(a)(b)).

Lower Limit: The lower reference limit is defined as the axial position, L_{bottom} , of the bottom of the frontal lobe (sagittal cuts in Figure 2.18(a)(b)). To identify this landmark, a set of sagittal slices in the center of the skull is analyzed, because remaining non-brain tissue may be in the lateral parts of the head (e.g., the eyes). The center of the bounding box of the brain mask M_2 is considered to be the center of the skull; and the slices at a distance from the center less than $1/30$

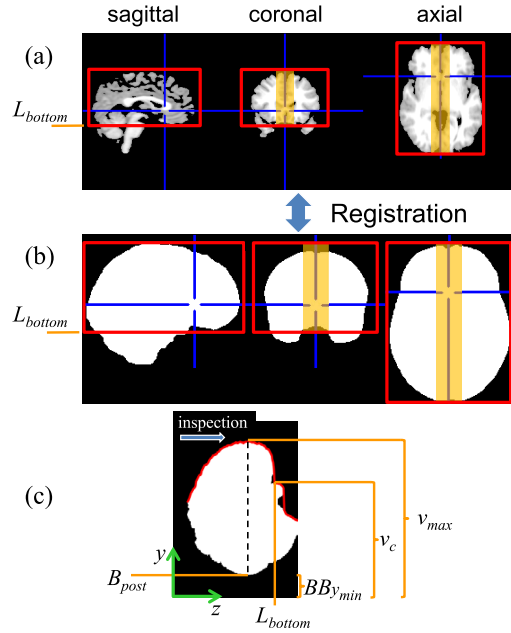


Figure 2.18: References used to register (a) the pre-segmentation Mask M_2 , and (b) the Model Mask. This registration is used to estimate the value of ξ in the computation of threshold, T_s . The limits used to compute the registration are marked as red/gray boxes. The bottom of the frontal lobe, L_{bottom} , is used as the caudal limit, which is found using the central sagittal slices marked in coronal and axial cuts (a)(b). (c) A frontal profile of the lateral projection of the central slices is used to identify the bottom of the frontal lobe. This frontal profile is represented as a red/gray line in the border of the projection shown in Figure(c). The bottom of the frontal lobe is defined as the first axial slice where $v_c < v_{max} - (v_{max} - BB_{y_{min}})0.2$, if the profile is inspected in the direction shown in Figure (c) (see text in paragraph “Lower limit” in page 65).

of the bounding box’s lateral length are selected (Fig. 2.18(a)(b)). The bottom of the frontal lobe is identified in a profile constructed by projecting the selected slices laterally (Fig.2.18(c)). The profile is inspected in a caudal direction, z -axis, starting from the top of the head, i.e., each step corresponds to an axial slice. Figure 2.18(c) shows the profile as a red line in the border of the brain mask. At each step, the position v_c of the profile is measured in the y -axis and compared with the maximum value found in the previous steps, v_{max} . We estimate that the axial position L_{bottom} of the bottom of the frontal lobe is the first axial slice where the current profile value, v_c , has a significant difference from the maximum value of the previous steps, v_{max} . An appropriate difference is 20% of the skull length in the posterior-anterior direction. To estimate the length of the skull,

v_{max} is taken as the anterior limit, and BBy_{min} , the posterior bound of the mask bounding box, is taken as the posterior limit. Therefore, L_{bottom} (Fig. 2.18(c)) is reached in the first slice where:

$$v_c < v_{max} - (v_{max} - BBy_{min})0.2 . \quad (2.63)$$

Anterior and Posterior Bounds: The anterior reference limit for the registration is v_{max} . The posterior reference limit is the posterior limit, B_{post} , of the projection of the central slices at the slice where v_{max} was found (Fig. 2.18(c)).

Lateral Limit: The lateral reference limits are the bounding box lateral limits of the upper part of the mask, from the top of the head to the bottom of the frontal lobe, L_{bottom} (axial cuts in Figure 2.18(a) and (b)).

After registration, M_2 is compared to the model mask (see Fig. 2.16(d)) to check whether the non-brain tissue has been properly removed. If the volume (number of voxels) of M_2 lying outside the model mask, $V_{M_2}^{out}$ (light gray in Figure 2.19), is small enough compared to the volume of the model mask, V_M (dark gray and white in Figure 2.19), it is assumed that the tissue removal is successful. Therefore, an empirical threshold of 0.08 is used, and the following condition should be satisfied to accept the tissue removal:

$$\frac{V_{M_2}^{out}}{V_M} < 0.08 . \quad (2.64)$$

Equation (2.64) determines whether enough non-brain tissue has been removed to proceed with the histogram analysis. The volume of mask M_2 that lies outside the model after registration, $V_{M_2}^{out}$, is an estimate of the non-brain tissue. When $V_{M_2}^{out}$ is large compared to the model's volume V_M , a significant part of non-brain tissue is present in the mask M_2 . Figure 2.19 shows an example in which the volume $V_{M_2}^{out}$ is large because the mask M_2 includes non-brain tissue. This non-brain tissue must be removed before performing the next step of our method. To remove the tissue, the threshold T_s is increased in equation (2.62) by using a higher value of ξ in the set $\xi = \{0.1, 0.2, \dots, 0.9\}$. If (2.64) is satisfied, no more values of ξ are tested and the current mask M_2 is used in the next step of the pre-segmentation (Fig. 2.16(e)). Figure 2.17(c) shows the image masked by M_2 and its histogram. Note that there are some voxels with gray value under T_{otsu} in the histogram, this is caused by the dilation of the mask that included some voxels ignored in the first step. The first value of T_s is lowest to avoid

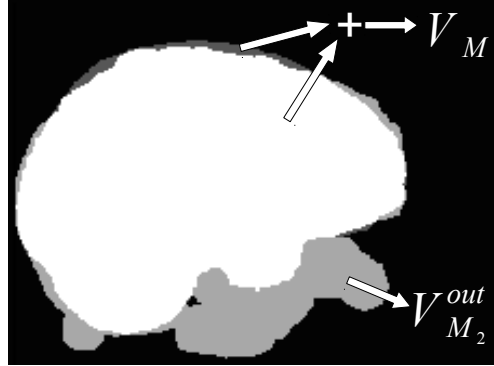


Figure 2.19: Example of non-brain tissue in mask M_2 . A large volume of M_2 lies outside the model. This volume $V_{M_2}^{out}$ is represented in light gray and corresponds to non-brain tissue that must be removed. The volume, V_M , of the model mask is represented in dark gray (only model mask) and white (model mask overlapped with M_2). In this case, equation (2.64) is not satisfied, therefore the threshold T_s must be increased by using a higher value of ξ in equation (2.62).

removing brain tissue. Moreover, if some brain tissue is removed in this step, it is recovered in the second deformation of the mesh as is explained in section 2.3.4.2.

After the brain identification described in this section, some parts of other tissues, such as dura, still remain around the brain. Thus, other thresholds are required, and they are computed by assuming that those tissues belong to a class depending on their gray levels. The classes are modeled by Gaussian functions, and the resulting model is used to compute the new thresholds (sec. 2.3.1.3) and as part of the information to guide the deformable model (sec. 2.3.4).

2.3.1.3 Modeling by Gaussians

Elimination of non-brain tissue is performed in this stage by the application of thresholds computed using a Gaussian approximation of the image histogram. The brain tissue is also selected using morphological operators and 3D connected component analysis (Fig. 2.16(III)).

As explained in Appendix C, there are different types of MR images and the gray level of the tissues is different in each one of them. Figure C.6 (p. 181) shows the approximate gray level of the tissues in the T_1 -weighted MR images used in this thesis. Based on the above mentioned gray levels, it can be assumed that image tissues belong to four classes that follow normal distribution [Shan 2002, Kovacevic 2002, Chiverton 2007] (Fig. 2.20):

- C_1 : Background noise, cerebrospinal fluid and dura. It may form a peak in the histogram, but often does not (green line in Fig. 2.20(a)).
- C_2 : Gray matter. It forms the central peak in the histogram (yellow line in Fig. 2.20(a)).
- C_3 : White matter. It forms the peak at the right side of the histogram (blue line in Fig. 2.20(a)).
- C_4 : Other tissues with high gray value. Consist of very few voxels and never forms a peak.

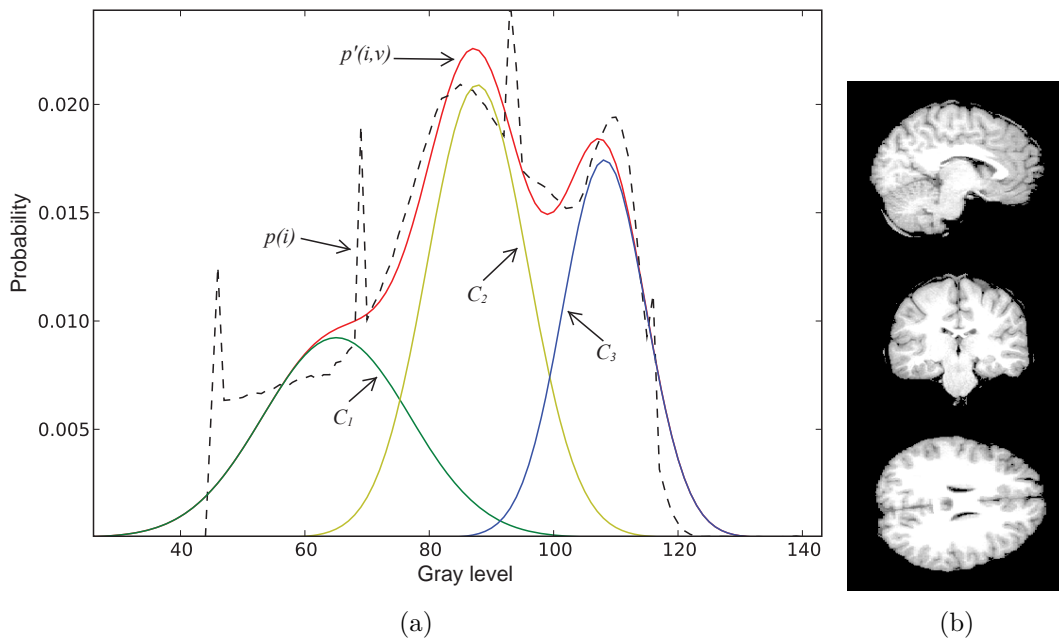


Figure 2.20: (a) Histogram as a probability density function and approximated by Gaussian functions. The black dashed line represents the real image histogram, $p(i)$, and the red line is the approximated histogram, $p'(i, v)$. The approximated histogram is the sum of the estimated normal distributions of the gray levels of classes C_1 (green line, left), C_2 (yellow line, center) and C_3 (blue line, right) (sec. 2.3.1.3). (b) MRI image used to compute the histogram.

An approximated histogram is constructed modeling these classes with Gaussians. Because class C_4 has very few voxels, only classes C_1 , C_2 , and C_3 are modeled. Figure 2.20(a) shows the approximated histogram and classes. There-

fore, the approximated histogram is:

$$p'(i; v) = \sum_{k=1}^3 p_k \exp\left(-\frac{1}{2} \left[\frac{i - \mu_k}{\sigma_k}\right]^2\right), \quad (2.65)$$

where i is a gray level, μ_k is the mean gray level of class $k = \{1, 2, 3\}$, p_k is the probability for a voxel of class k to obtain intensity μ_k , σ_k is the standard deviation of the Gaussian function that represents the class k , $v = (\mu_k, \sigma_k, p_k)$ is the vector of parameters of the Gaussian functions, and $p'(i; v)$ is the probability that a voxel has intensity, i , using the vector of parameters, v . Thus, the values, μ_k , should correspond to the main peaks in the image histogram. The parameters of the Gaussian functions are adjusted such that $p'(\cdot; v)$ fits the image histogram. Therefore, the vector of optimal parameters $v^* = (\mu_k^*, \sigma_k^*, p_k^*)$ is:

$$v^* = \underset{v}{\operatorname{argmin}} \sum_{i=0}^{W-1} [p(i) - p'(i; v)]^2, \quad (2.66)$$

where W is the number of gray levels or bins in the histogram. This minimization is performed using the Levenberg-Marquardt algorithm [Moré 1978], which is especially suitable for minimizing functions that can be expressed as a sum of squared residuals. The initial vector of parameters for the minimization is computed as follows.

Kernel Density Estimation The initial vector of parameters for the minimization of equation (2.66) is computed using a non-parametric smoothing method. This method is based on *kernel density estimation* [Rosenblatt 1956] which is a technique used to estimate the probability density function of a random variable. In our case, this variable is the image histogram, $p(i)$. Thus, the kernel density estimation is:

$$\hat{p}(i; h) = \frac{1}{Nh} \sum_{j=0}^{W-1} K\left(\frac{i-j}{h}\right), \quad (2.67)$$

where K is the kernel function, h is the bandwidth parameter of the kernel (Eq. (2.68)), and j is the internal variable of the summation over all the W gray levels. The commonly used normal distribution with mean 0 and variance 1 is used as the kernel function:

$$K\left(\frac{i-j}{h}\right) = \frac{p(j)}{\sqrt{2\pi}} e^{-\frac{(i-j)^2}{2h^2}}. \quad (2.68)$$

In this way, the variance is controlled indirectly through parameter h . This parameter controls the amount of smoothing of $\hat{p}(i; h)$, i.e., when h is high, $\hat{p}(i; h)$ will be smoother. Since the image histogram is seen as a probability density function, the peaks of each class correspond to main function modes (the more likely or more repeated values). In order to localize the modes of the function, the parameter, h , is adjusted to obtain a smooth function whose number of peaks, \hat{m} , is equal to the number of modes, m , we want to identify. Figure 2.21 shows the kernel density estimation of the histogram using different values of h . The larger the value of h , the smoother the estimation $\hat{p}(i; h)$ and the fewer the number of local maxima. The adjustment of h to obtain a desired number of local maxima, m , is explained as follows.

First, two limit values for h are fixed: h_{high} and h_{low} . Since m modes should be found, h_{high} must be high enough to obtain $\hat{m} < m$ modes when it is used in the estimation, and h_{low} must be low enough to obtain $\hat{m} > m$ modes. Then, h is adjusted iteratively, providing a value, h_t at each iteration, t , starting with $h_0 = (h_{high} + h_{low})/2$:

1. Compute $\hat{p}(\cdot; h_t)$ (Eq. (2.67))
2. Calculate the number of modes \hat{m} in $\hat{p}(\cdot)$
3. **if** $\hat{m} \leq m$ **then**
 $h_{high} = h_t$
else
 $h_{low} = h_t$
end if
4. Compute $h_{t+1} = \frac{h_{high} + h_{low}}{2}$.
5. **if** $\hat{m} = m$ and $|h_t - h_{t+1}| < \varepsilon$ **then**
return $\hat{p}(\cdot; h_{t+1})$
else
go to step 1.
end if

Now, we get back to the computation of the initial vector of parameters to adjust the Gaussian functions. The class C_1 does not always show a peak. Therefore, to compute the initial vector of parameters to adjust $p'(i; v)$, the best method is to find the peaks of classes C_2 and C_3 . Because μ_2 and μ_3 are the highest peaks in the histogram, they can be located using the algorithm described above. Figure 2.21(e) shows a histogram smoothed using $h = 2.865$,

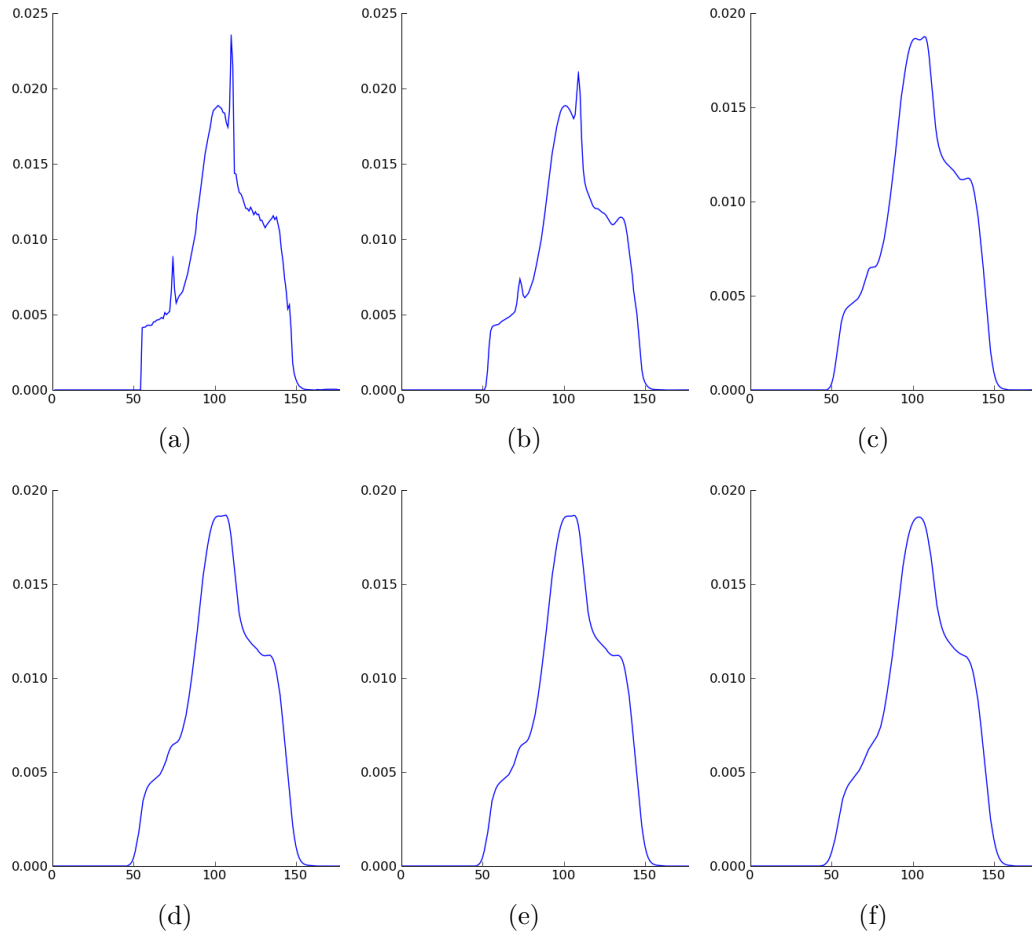


Figure 2.21: Histogram smoothing using “kernel density estimation”. Examples with different values of h and local maximum (LM), are showed. The values of h were selected to show how the number of LM change. (a) Original histogram, (b) $h = 1.0$, $\text{LM} = [73, 101, 109, 135]$. (c) $h = 2.507$, $\text{LM} = [75, 102, 107, 134]$. (d) $h = 2.819$, $\text{LM} = [102, 106, 133]$. (e) $h = \mathbf{2.865}$, $\text{LM} = [\mathbf{106}, \mathbf{133}]$. Minimum value of h at which two LM were obtained. (f) $h = 3.756$, $\text{LM} = [104]$.

this histogram has two peaks $[106, 133]$ which correspond to μ_2 and μ_3 . Using these estimations of the mean gray levels, the initial vector of parameters $v = (\mu_k, \sigma_k, p_k)$ for the adjustment of the Gaussian functions (Eq. (2.66)) is obtained: $v = [\mu_2 \ 0.75, \mu_2, \mu_3, W/6, W/6, W/6, \hat{p}(\mu_2 \ 0.75), \hat{p}(\mu_2), \hat{p}(\mu_3)]$, where W is the number of gray levels. The mean gray level $\hat{\mu}_1$ of class C_1 is estimated using $\hat{\mu}_2$ because class C_1 usually does not present a peak, and the value 0.75 was empirically selected based on the typical form of the histogram. This initial

vector is used in the Levenberg-Marquardt algorithm to perform the minimization of equation (2.66), and obtain the optimal vector of parameters v^* for the approximated histogram, $p'(\cdot, v)$ (Eq. (2.65)). Figure 2.20 shows the image histogram, $p(i)$ (black dashed line), and the approximated histogram, $p'(i; v^*)$ (red line) formed by the sum of the Gaussian functions representing the gray level distributions of classes C_1 (green line), C_2 (yellow line), and C_3 (blue line). Because class C_2 represents the gray matter and class C_3 the white matter, it can be assumed that the mean value and standard deviation of the GM and WM gray level are, $\mu_{gm} = \mu_2$, $\sigma_{gm} = \sigma_2$; and $\mu_{wm} = \mu_3$, $\sigma_{wm} = \sigma_3$, respectively.

Two final thresholds, T_{GLow} and T_{GHigh} , are computed using the estimated gray level distribution of the tissues [Shan 2002]:

$$\begin{aligned} T_{GLow} &= \mu_{gm} - 2.5\sigma_{gm} , \\ T_{GHigh} &= \mu_{wm} + 2.5\sigma_{wm} . \end{aligned} \quad (2.69)$$

A new mask is computed using these thresholds (Fig. 2.16(f)). The mask is composed of all voxels, in the image masked with M_2 (Fig. 2.17(c)), having a gray level, i , that satisfies: $T_{GLow} \leq i \leq T_{GHigh}$. With the purpose of disconnecting the remaining tissues with gray levels similar to the brain, a binary opening is used in the mask. The opening operator is applied once, using a 3D spherical structural element with a radius of 4 mm. Then, to identify the brain, a 3D connected component analysis is performed in the mask, using a square connectivity equal to one. The largest element is kept, and it forms the mask, M_3 . The original image masked by M_3 is the final pre-segmentation of the brain. Figure 2.22 shows two orthogonal slices of the MRI pre-segmentation, in which tissues have been eliminated, except for the cerebral parenchyma (Fig. 2.22(c)). Figure 2.17(d) shows a segmented image and its histogram.

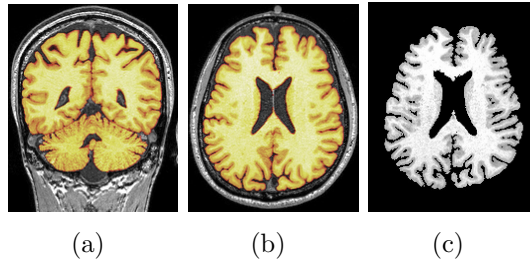


Figure 2.22: (a) Coronal and (b) Axial slice of the MRI. (c) Extraction of the cerebral parenchyma by the pre-segmentation method.

2.3.2 Initial Generic Meshes

Addressing the problem of validating the techniques of quantitative analysis of MR images, an anatomical model of the brain was developed at the Montréal Neurological Institute (*BrainWeb* [Cocosco 1997, Kwan 1999]). The model is composed of a set of digital phantoms. Each phantom is defined by a set of 3D fuzzy tissue membership volumes, which are next used to synthesize MR images (Fig. 2.23(b)), and an associated discrete anatomical model (Fig. 2.23(a)). This discrete model consists in a class label associated to each voxel, representing the tissue with the largest contribution. We have slightly adapted it in order to construct an initial generic mesh corresponding to the structures we want to take into account. This adaptation consists, for example, in the edition of the ventricular cavities as they appear as open structures in *BrainWeb* models (containing fuzzy information, and certainly not a structured segmentation). Next, meshes have been created using the well known marching cubes algorithm [Lorenson 1987] and proper image segmentation techniques. The final model consists of five meshes reconstructed from the same discrete model extracted from a BrainWeb synthetic model:

1. Three closed meshes:
 - (a) Cortex, \mathcal{M}_C .
 - (b) Skull, \mathcal{M}_S .
 - (c) Ventricles, \mathcal{M}_V .
2. And two inner membranes:
 - (a) Tentorium cerebelli, \mathcal{M}_T .
 - (b) Falx cerebri, \mathcal{M}_F .

Since the inner membranes are not specifically identified within the *BrainWeb* model, they need to be marked before creating the meshes. As this operation has to be performed only once for the generic mesh, there is no major restriction in achieving this manually. The closed surfaces have genus 0 and, for simplification, \mathcal{M}_C does not include *sulci* or *gyri* in details.

Finally, all these meshes can be joined together, resulting in a complete brain anatomy (Fig. 2.24). Of course, depending on the aimed application, any partial combination of the meshes is available, at any resolution.

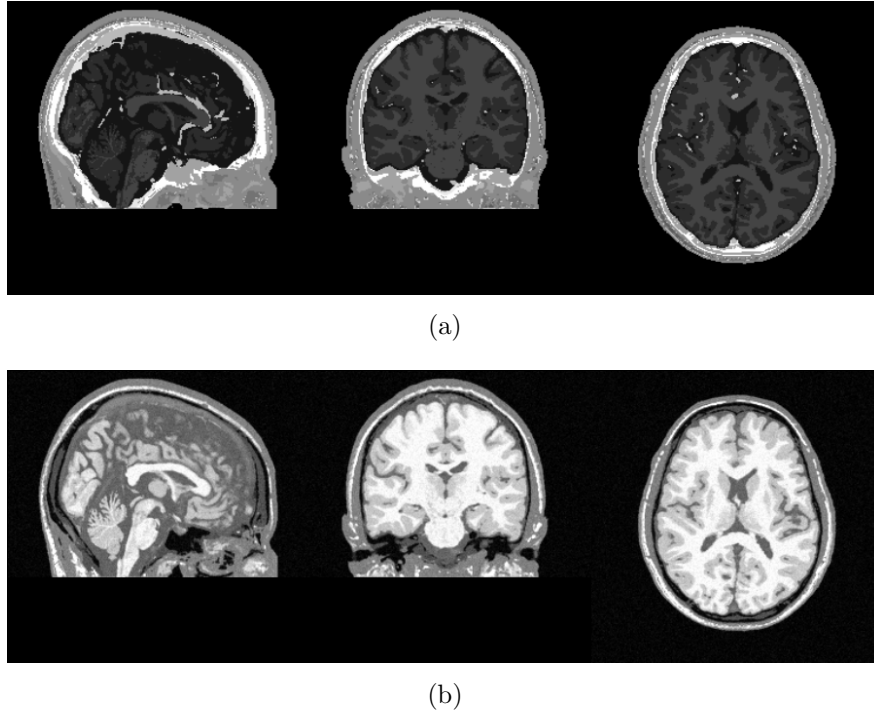


Figure 2.23: Example of a BrainWeb's model. (a) Discrete anatomical model which consists of 11 types of tissues. The gray level of each voxel in the model is a label to the tissue type. (b) Synthetic image created using the model shown in (a).

After adjusting the simplex meshes to the patient's anatomy, they can be easily shifted to a triangulation (sec. 2.2). This allows performing junction between the different meshes [Lo 2005], each one representing a part of the whole cerebral structure. The resulting triangle mesh is defined adequately to be integrated in a three-dimensional volume mesh generator. Thus, tetrahedral or hexahedral meshes can be built, and next used for simulation purposes. As stated previously, the main advantage of our technique is to produce compliant volume meshes where inner structures have been well identified and marked with different domain labels, which will help, for example, to define the boundary conditions for a Finite Elements resolution method.

2.3.3 Geometric Adjustment of the Meshes

After pre-segmentation, a global matching of the generic meshes (\mathcal{M}_C , \mathcal{M}_S , \mathcal{M}_V , \mathcal{M}_T , \mathcal{M}_F), is carried out using geometric transformations. The mesh \mathcal{M}_C

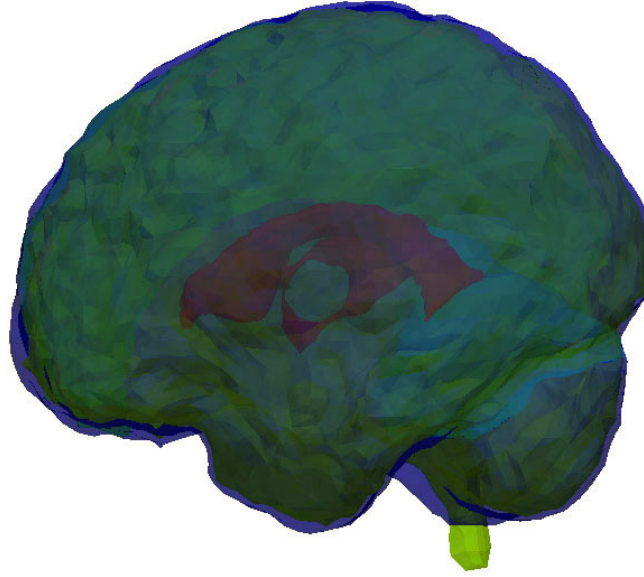


Figure 2.24: External and semitransparent view of our generic mesh of the brain anatomy, integrating outer and inner structures.

represents the structure segmented in the pre-segmentation (brain), consequently this mesh is used to compute the first geometric adjustment. First, \mathcal{M}_C is scaled and translated to match the pre-segmented MRI. The references used to carry out this transformation are found in the same way as the estimation of threshold T_s that is described in section 2.3.1.2. The caudal limit of the frontal lobe and the bounding box of the upper part of the brain in \mathcal{M} are matched with the same references in the pre-segmented image. Then, this transformation computed using \mathcal{M}_C is used on all the meshes: $\mathcal{M}_C, \mathcal{M}_S, \mathcal{M}_V, \mathcal{M}_T, \mathcal{M}_F$.

Next, an affine transformation is carried out minimizing the sum of the square distances among the vertices of \mathcal{M}_C and the pre-segmented MRI edges. The optimal transformation parameters are found using the Levenberg- Marquardt minimization method. The distances in the pre-segmented MRI image are pre-computed using the distance transformation on the edges of the MRI segmentation after binarization. Figure 2.25(a) shows the cortex mesh after the affine transformation. Then, this affine transformation is also applied to the other meshes: $\mathcal{M}_C, \mathcal{M}_S, \mathcal{M}_V, \mathcal{M}_T, \mathcal{M}_F$.

The pre-segmentation has removed the CSF inside the brain, therefore the ventricles are represented by holes. They are used to perform another geometric adjustment of \mathcal{M}_V . In the same way as for \mathcal{M}_C , the sum of the square distances

between the vertices of \mathcal{M}_V and the pre-segmented MRI edges is minimized using an affine transformation. The distance transformation and Levenberg-Marquardt minimization method are also used to find the optimal transformation parameters.

The mesh resulting from this step is close enough to its final position to be transmitted as input to a more local deformable model technique. The deformation of each mesh that represents an anatomical structure (cortex, skull, ventricles, tentorium cerebelli and falx cerebri) is described in the following sections.

2.3.4 Cortical Surface Segmentation

2.3.4.1 First Mesh Deformation

After the geometric adjustment (sec. 2.3.3), the mesh, \mathcal{M}_C , is deformed in order to match the pre-segmentation borders more accurately. This deformation allows a better initialization by using the pre-segmentation. In equation (2.24), the external force definition is important as it will drive the mesh to the image's natural edges. To compute the external force, a target point x_i^{target} is searched on the normal profile of each vertex, defined in section 2.1.4 (Eq. 2.33). The target point, x_i^{target} , defined as the first point inside the mask, M_3 , is searched in each profile, starting from l to $-l$. Thus, using the target point, the external force, $\overrightarrow{F_{ext_i}}$ is defined in each vertex a:

$$\overrightarrow{F_{ext_i}} = \left[\frac{\nabla M_3(x_i^{target})}{\|\nabla M_3(x_i^{target})\|} \cdot (x_i^{target} - P_i) \right] \overrightarrow{N_i}, \quad (2.70)$$

where $\nabla M_3(x_i^{target})$ is the gradient of M_3 at x_i^{target} , i.e., the gradient of the mask border. In this way, the vertex is pushed to the pre-segmentation border more strongly if the normal of the mask border is in the same direction as the mesh normal.

Because an affine transformation was used in the previous mesh geometric adjustment, it can be assumed that the mesh did not lose its general shape. Therefore, to avoid an excessive mesh deformation if there are errors in the pre-segmentation, the initial simplex angles of the mesh are preserved as target simplex angles, ρ_i^* during the deformation. Thus, the simplex angle of every vertex, ρ_i is computed after the geometric adjustment and used in this deformation as ρ_i^* (Eq. 2.28). An example of the adjustment result to the pre-segmentation is shown in Figure 2.25(b).

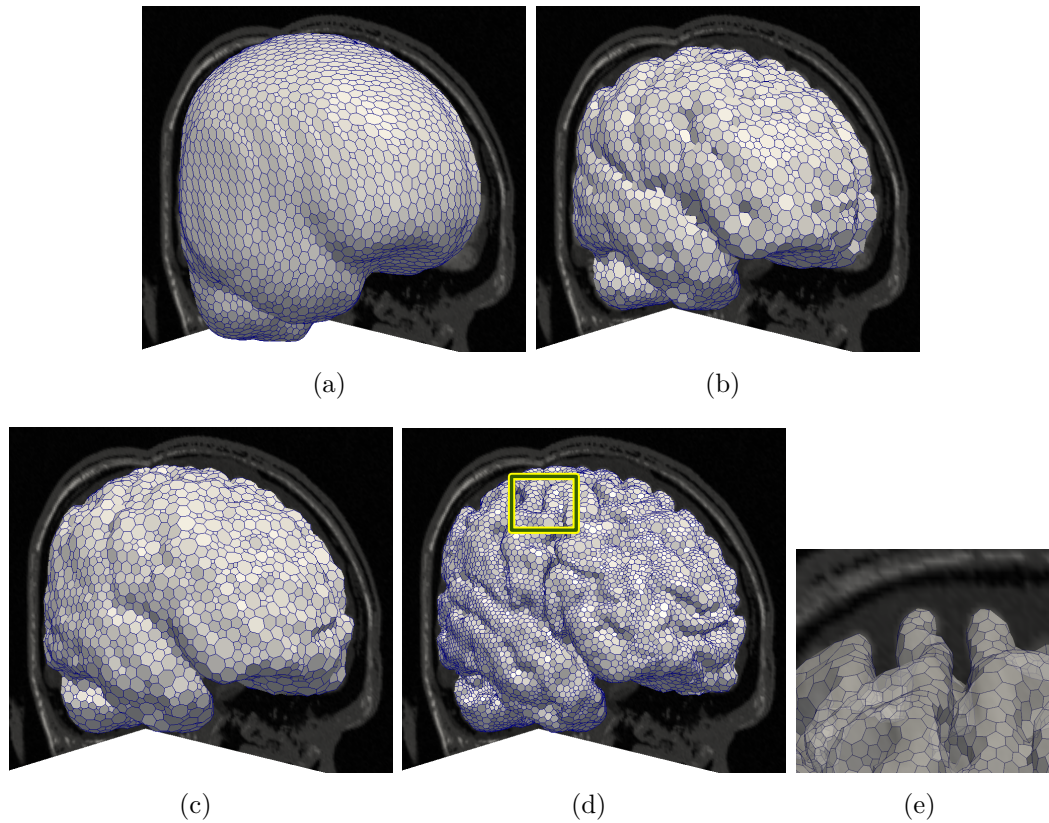


Figure 2.25: Examples of deformation steps with the simplex mesh: (a) After geometric adjustment by affine transformations (sec. 2.3.3). (b) After a first deformation to match the pre-segmentation (sec. 2.3.4.1). (c) After a coarse second deformation to roughly match the cortical surface. (sec. 2.3.4.2). (d) After a third and final refined deformation to match the sulci and gyri (sec. 2.3.4.3). (e) Zoom image of the final deformation showing how the mesh can follow the sulci and gyri.

After this first deformation, the mesh matches the pre-segmented image borders. Because the pre-segmentation is designed to remove most of the non-brain tissue, the mesh lies mainly in the WM or near the GM-CSF interface.

2.3.4.2 Second Mesh Deformation

The second deformation is computed using the original MRI, and the goals are to find the GM-CSF interface, and correct the mesh in those areas where the pre-segmentation eliminated brain tissue. Therefore, the mesh moves mainly inside the WM or near the GM-CSF interface in this deformation.

In a similar manner to the first deformation, a target point, x_i^{target} is computed in each vertex profile. (See Eq. (2.33)). To compute the target point, rules based on the image gray level are applied, as will be explained later in this section (Fig. 2.26). In each iteration, the vertices are pushed toward their target points by the external force, as explained in section 2.1.4.

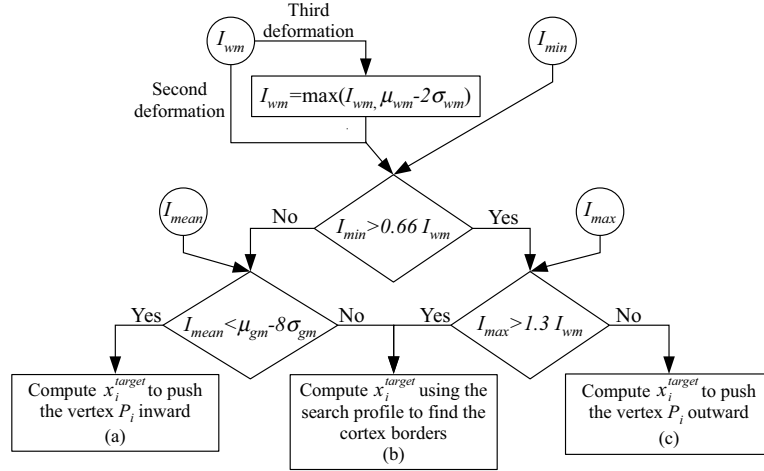


Figure 2.26: Flow diagram of the rules to compute the simplex mesh external forces. The inputs, represented by circles, are measures of the image gray levels taken over the normal profile of each vertex P_i (Fig. 2.5). The outputs, at the end of the scheme, are the equations used to compute the target point x_i^{target} of each vertex: (a) Equation (2.74) is used to push the vertex toward the brain. (b) Equation (2.75) is used to push the vertex toward the cortex border. (c) Equation (2.77) is used to push the vertex outward the brain.

Figure 2.26 shows a flow diagram of the rules employed to compute the target points. First, whether the vertex P_i is outside the WM is estimated. This is carried out by computing two values: an estimation of the WM gray value in each profile

$$I_{wm}(i) = \max_{j=[-l/\delta], \dots, 0} I(x_{i,j}), \quad (2.71)$$

and the minimum gray level value over a distance, d_{min} in the direction, $-\vec{N}_i$:

$$I_{min}(i) = \min_{j=[-d_{min}/\delta], \dots, 0} I(x_{i,j}). \quad (2.72)$$

If $I_{min}(i) \leq 0.66 I_{wm}(i)$, it is assumed that the vertex, P_i is in the CSF or the GM. The threshold for this comparison was selected based on the typical gray level values of the MR images used in this thesis (see section 3.1). In this case,

another measurement is made over a distance d_{mean} in the direction, $-\vec{N}_i$:

$$I_{mean}(i) = \frac{\sum_{j=[-d_{mean}/\delta]}^0 I(x_{i,j})}{[d_{mean}/\delta] + 1}. \quad (2.73)$$

Using $I_{mean}(i)$, it is possible to determine whether the vertex, i , is near the GM. If $I_{mean}(i)$ has a low value, the vertex, i , is in the CSF far from the GM. In this case, P_i must be pushed to reach the GM. $I_{mean}(i)$ is analyzed using the mean value μ_{gm} and standard deviation σ_{gm} of the GM gray level computed in section 2.3.1.3. Accordingly, if $I_{mean}(i) < \mu_{gm} - 8\sigma_{gm}$, the vertex is pushed inward. Since each vertex is pushed over its target point, the target point is defined as:

$$x_i^{target} = P_i - d_p \vec{N}_i, \quad (2.74)$$

where d_p is a distance that controls the applied force. Otherwise, if $I_{mean}(i) \geq \mu_{gm} - 8\sigma_{gm}$, it is assumed that the vertex is near the interface between the GM and CSF, and must be pushed into it. This interface can be detected looking for a high gradient in the search profile. A function, \mathcal{F} , based on both image and mesh, is defined as $\mathcal{F}_i(x) = -\vec{N}_i \cdot \nabla I(x)$, where $I(x)$ is the gray value of the image normalized between the values [0,1] at point x , and ∇ is the gradient operator. Then, the target point [Weese 2001] is defined as:

$$x_i^{target} = P_i + \arg \max_{j=[-l/\delta], \dots, [l/\delta]} [\mathcal{F}_i(x_{i,j}) - Dj^2\delta^2] \delta \vec{N}_i, \quad (2.75)$$

where D is a weight to give less importance to points that are far from P_i . In contrast, if $I_{min}(i) > 0.66 I_{wm}(i)$, it is assumed that the vertex P_i is inside the WM. In this case, another measure is performed over a distance, d_{max} , in the profile:

$$I_{max}(i) = \max_{j=0, \dots, [d_{max}/\delta]} I(x_{i,j}). \quad (2.76)$$

The purpose of $I_{max}(i)$ is to determine whether the eyes are in front of $P(i)$. An area with high gray level values characterizes the region behind the eyes, where the optic tracts are located. We estimated a threshold for $I_{max}(i)$ to be 130% of the WM intensity. If $I_{max}(i) > 1.3 I_{wm}$, it is assumed that the eyes are in front of P_i , and the GM border is found using (2.75); otherwise, the vertex P_i is inside the WM and must be pushed to reach the GM and the GM-CSF interface. The vertex is pushed defining the target point x_i^{target} as:

$$x_i^{target} = P_i + d_p \vec{N}_i. \quad (2.77)$$

In the second deformation, the mesh should be adjusted more precisely. Therefore, more freedom is allowed in the deformation by computing the target simplex angle, ρ_i^* , using a curvature continuity constraint [Delingette 1999] computed over a neighborhood, $Q^S(i)$, of size, S , around each vertex. The neighborhood, $Q^S(i)$, is defined as all the vertices that can be connected to P_i by a path formed with S edges. Figure 2.25(c) shows an example of the mesh obtained after the second deformation.

The pre-segmentation is designed to eliminate the non-brain tissue enabling to identify landmarks in order to register the generic mesh, \mathcal{M}_c , with the image (sec. 2.3.3), but in some cases part of the brain is also removed. Therefore, the purpose of the second deformation, in addition to reaching the GM-CSF interface, is to correct the mesh in those areas where the pre-segmentation eliminated brain tissue. Figure 2.27 shows an example in which part of the brain was removed in the pre-segmentation and recovered in the second deformation.

2.3.4.3 Third Mesh Deformation

A final deformation is carried out removing parts of the CSF that may remain outside the cortex or in the sulci, by mesh refinement, and using similar forces to those described in the previous section. There are many well-known algorithms to refine triangulations. Therefore, the simplex mesh is first transformed into a triangulation using the method described in section 2.2. This method is based on the computation of the dual mesh vertices by an interpolation that uses a direct minimization of the distance to both vertices of each face and the tangent planes in these vertices. After the dual transformation, the triangulation is refined using the butterfly scheme [Zorin 1996], and re-transformed into a simplex mesh (sec. 2.2). To improve this step, and avoid to perform a mesh conversion back and forth, similar techniques as in [Gilles 2010] for simplex mesh adaptation can be implemented. Nevertheless, since the results are similar, we preferred to use our transformation method and a refinement method well validated in the literature.

To deform the refined mesh, similar forces to those described in the previous section (sec 2.3.4.2) are utilized. The difference is that the value of $I_{wm}(i)$ is modified if it is very different from the estimation of the WM gray level in the pre-segmentation stage. The objective of this correction is to make sure that vertices over sulci will be pushed into the sulci. There are cases in which the estimation of the WM local gray level $I_{wm}(i)$ is excessively low when the vertex is over a large sulcus, especially over the sagittal sinus. Moreover, in this stage

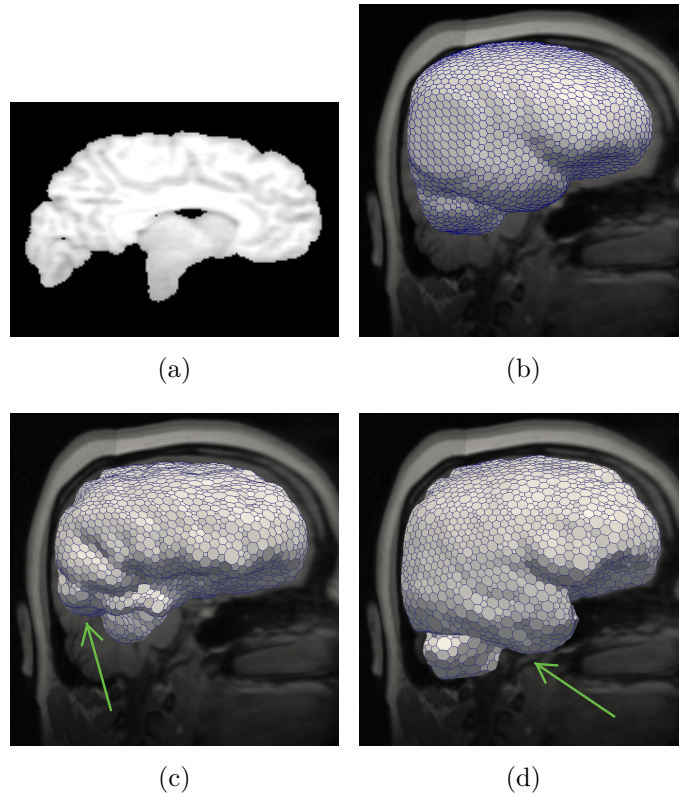


Figure 2.27: Example of brain tissue recovery by the second deformation. (a) The pre-segmentation of an image in which the cerebellum has been removed because of a bias problem in the image. (b) Mesh registered with the pre-segmentation by geometric transformations. (c) Mesh deformed using the pre-segmented image. This first deformation removes a great part of the cerebellum because it is based in the pre-segmentation (see the arrow). (d) Mesh after the second deformation. This deformation recovers the cerebellum because the external forces push the vertices if they are inside the brain tissue (see the arrow).

the mesh has reached the cortex as a result of the second deformation; therefore, it is more important to push the vertices into the sulcus. If $I_{wm}(i) < \mu_{wm} - 2\sigma_{wm}$, its value is replaced by $I_{wm}(i) = \mu_{wm} - 2\sigma_{wm}$. Figures 2.25(d) and (e) show an example of the final segmentation.

2.3.4.4 Mesh Self-intersection Control

Mesh deformations following complex shapes, such as cortex sulci and gyri, may generate errors due to mesh self-intersections. A self-intersection may cause the surface normal vector to point toward inside the mesh instead of outward. This

error in the normal vector causes the mesh to be pushed in the wrong direction, because the forces that deform the mesh depend on the surface normal vector. The mesh internal forces avoid these intersections to some degree, but in some cases they are not sufficient. For example, if two neighboring surfaces get too close, but without causing a significant change in the mesh curvature, the internal forces will not prevent an intersection to happen. Also, if the mesh deforms too quickly in a zone, causing the surface to fold over itself, the internal forces may not be able to correct the problem properly. To prevent these auto-intersections, we check and correct their occurrence every 10 iterations.

Meshes are defined by their vertices and edges, but if we want to detect intersections in the surface defined by a mesh, an unambiguous definition of the surface is needed. The vertices that form a face of a simplex mesh are not in a single plane, unlike as in triangle meshes where the vertices of each triangle unambiguously define a plane. Therefore, a surface cannot be defined in a simplex mesh by using one plane in each face. Other definitions of the surface can be given by a set of equations based on the vertices; however using planar faces is the easiest and direct method to compute intersections. Consequently, the simplex mesh is first transformed into its dual triangulation (sec. 2.2) to have a mesh formed by planar faces (Fig. 2.28(b)). Then, the intersections between triangles can be computed easily. Because the topological dual triangulation is used, each triangle corresponds to a vertex of the simplex mesh (Fig. 2.1(b)). Therefore, if an intersection is detected in a triangle, the position of the corresponding simplex mesh vertex must be corrected. After all triangles with intersections have been detected (Fig. 2.28(c)), areas enclosed by these triangles are computed (Fig. 2.28(d)). The triangles of these areas have no intersections because they have completely crossed from one side of the surface to the other. Therefore, the position of the simplex mesh vertices related to triangles in the enclosed areas must also be corrected.

Consequently a set, \mathcal{G} , is formed with the vertices related to intersected triangles and triangles enclosed by intersections. To correct the intersections, a Laplacian smoothing is applied to the vertices of \mathcal{G} and to a neighborhood around them. The smoothing is applied in stages $k = \{1, 2, \dots\}$ to make sure of the self-intersection problem correction, while changing the rest of the mesh as little as possible. In each stage, the Laplacian smoothing is applied 50 times or until the mean displacement of the vertices is less than 0.001. Because in a simplex mesh each vertex P_i has 3 neighbors, the Laplacian smoothing is performed assigning

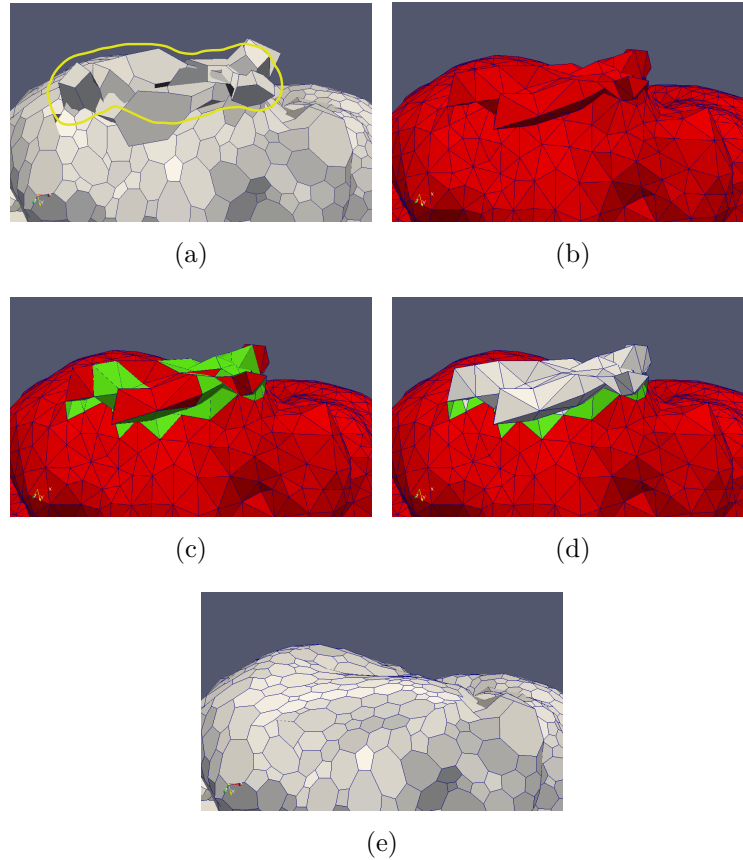


Figure 2.28: Example of self-intersections control. When the mesh is deformed around complex shapes, self-intersections may appear, such as those marked by a contour in Figure (a). The easiest method to detect intersections in a surface is by defining the surface as a set of planar faces. Nevertheless, the vertices that form a face of a simplex mesh are not in a single plane, so the surface of a face cannot be defined by a plane. In order to detect the intersections in a simplex mesh, it is better to transform the mesh into a triangle mesh, which have planar faces. The dual transformation (sec. 2.2) of the simplex mesh is used to compute the triangulation (b). In the triangulation, the triangles with intersections can be easily detected (green triangles in Figure (c)). Some triangles may have crossed from one side of the surface to the other (of another part of the mesh). These triangles don't have intersections, but must be corrected. To detect these triangles, zones enclosed by intersections must also be detected (white triangles in Figure (d)). In the dual triangulation of a simplex mesh, each triangle correspond to a vertex of the simplex mesh. To correct the self-intersections, a Laplacian smoothing is applied to vertices of the simplex mesh that correspond to triangles with intersection or triangles enclosed by them. Figure (e) shows the simplex mesh smoothed and without self-intersection.

to each vertex the mean position of its neighbors:

$$P_i = \frac{P_{N1(i)} + P_{N2(i)} + P_{N3(i)}}{3}. \quad (2.78)$$

Another detection of self-intersections and enclosed areas is performed at the end of each stage. If there are still self-intersections, another set \mathcal{G} , is formed in the next stage and a Laplacian smoothing is carried out. The neighborhood around \mathcal{G} depends on the stage, k , defining increasing neighborhoods to provide more freedom if the intersections were not corrected in the previous stage. Thus, in a stage k , the neighborhood $Q^S(\mathcal{G})$ of \mathcal{G} is of size $S = k$, where $Q^S(\mathcal{G})$ is defined as all the vertices that can be connected to any vertex of \mathcal{G} by a path formed with S edges. Figure 2.28(a) shows a mesh with self-intersections, which are corrected in Figure 2.28(e).

2.3.4.5 Cortical Surface Segmentation as a Skull Stripping Method

As explained in section 1.2.4.1, the brain segmentation obtained with the cortex mesh can be seen as a *Skull Stripping* or brain extraction process. The Skull Stripping eliminates the non-brain tissue present in the image, which is a preliminary step for many methods, mandatory before employing these images in medical or research application. Accordingly, the voxels in the image are classified as brain or non-brain tissue. To perform this classification, a binary mask is built using the final deformed cortex mesh. In this mask, voxels inside the mesh are classified as brain tissue and as non-brain tissue those voxels outside the mesh. The resolution of the mesh is sufficient to obtain a satisfactory result for building a mechanical model. Nevertheless, some voxels in the surface of the mask can be misclassified because the mesh has no sub-voxel resolution to perform an efficient deformation. To refine the classification of the aforementioned voxels, *conditional morphological operators* are applied to the mask as follows.

The conditional morphological operators employ thresholds computed using the statistical gray level model built in the pre-segmentation (sec. 2.3.1.3) and gray level estimates in the neighborhood of the voxel. Moreover, the structural element used in the morphological operators has $3 \times 3 \times 3$ voxels, because the misclassified voxels are only at the surface of the mask. First, a conditional erosion is performed two times in the brain mask. This operation applies a classical erosion [Russ 2011], but only if the gray value of the voxel is below a threshold in the original image. The threshold is the same employed in the mesh deformation (Fig. 2.26), thus the voxels with gray levels in the original image

$i \leq \mu_{gm} - 8\sigma_{gm}$, can be eroded in the binary mask. This erosion removes voxels of CSF that were misclassified as brain. Then, a conditional dilation is performed one time in the binary mask using the same structural element. The conditional dilation is a classical binary dilation that is performed only if the gray value of the voxel where the operator is applied, is above a threshold in the original image. The threshold is determined using the maximum gray level in the original image of the voxels inside the structural element: I_{max}^{se} . The value of I_{max}^{se} is an estimate of the gray level value of the brain parenchyma in the neighborhood of the voxel. If the voxel is far from the parenchyma (e.g., in a sulcus) the threshold of the conditional erosion is used. Then, the voxel may be dilated if its gray level $i > \max(I_{max}^{se} - 5\sigma_{gm}, \mu_{gm} - 8\sigma_{gm})$. This dilation recovers misclassified voxels of brain tissue. Figure 2.29 shows the correction performed in the binary mask.

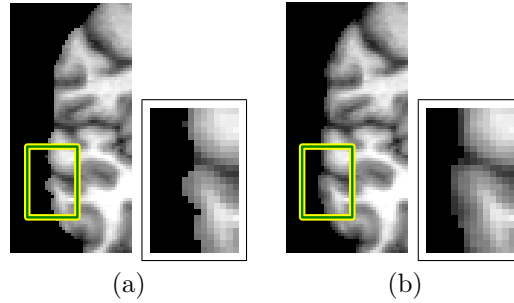


Figure 2.29: Correction performed in the binary mask. (a) Image masked by the binary mask built using the final deformed mesh. The image includes a zoom of the marked rectangular area. (b) Image masked by the mask after correction by conditional morphological operators. Misclassified voxels in the surface of the mask are corrected by the conditional morphological operators.

2.3.5 Skull Mesh Deformation

After the deformation of cortex mesh \mathcal{M}_C (sec. 2.3.4), the skull mesh \mathcal{M}_S must be deformed to follow the internal surface of the skull. The starting point for the deformation is the skull mesh after the geometric adjustment explained in section 2.3.3 (Fig. 2.30(a)). The deformation of this mesh is based on the image and on the position of the cortex mesh after deformation. The deformation is controlled to avoid intersections between these two meshes (cortex and skull) and to ensure a minimal distance between them. Figure 2.31 shows a flow diagram of the rules used to compute the external forces of the mesh.

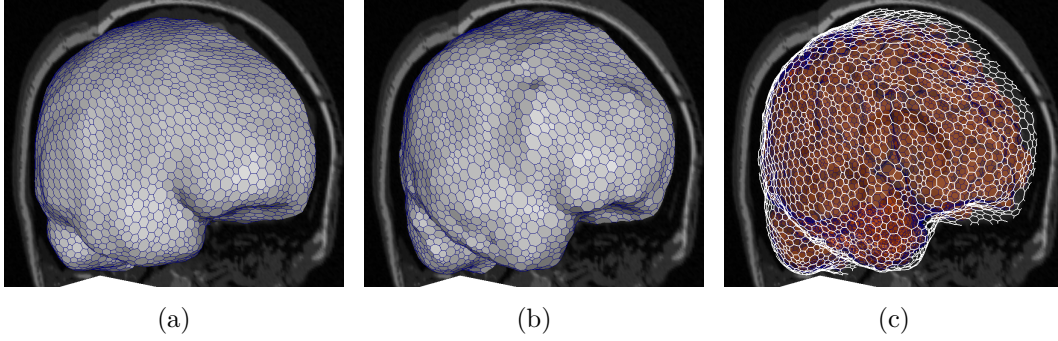


Figure 2.30: Examples of deformation steps with the skull simplex mesh: (a) After geometric adjustment by affine transformations (sec. 2.3.3). (b) After deformation to match the skull inner borders. (c) After deformation and with the cortex mesh inside it. The skull mesh deformation has constraints to maintain a minimum distance from the cortex mesh.

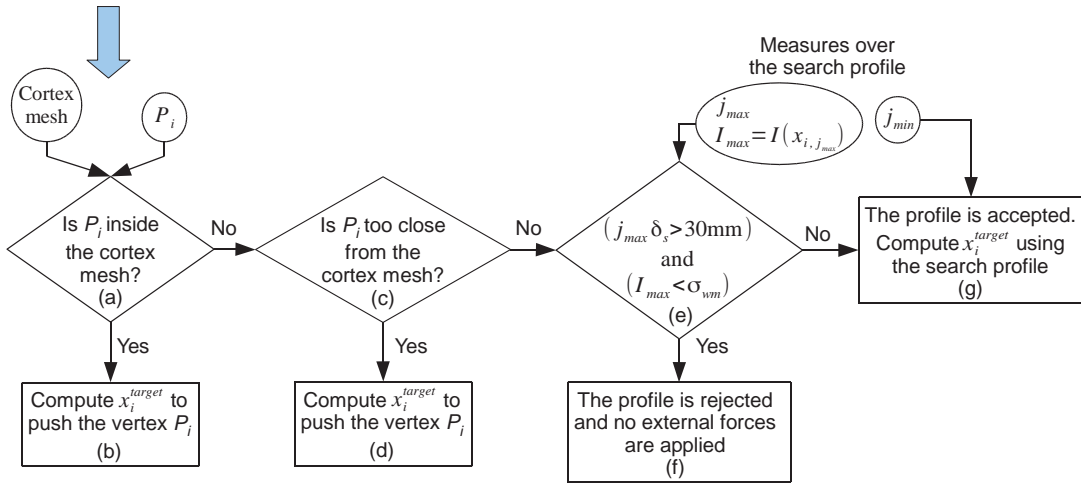


Figure 2.31: Flow diagram to compute the simplex mesh external forces to deform the skull mesh. The external force is computed using the target point x_i^{target} , therefore this point is computed in different ways depending the position of the vertex P_i . (a) First, if P_i is inside the cortex mesh (see Eq. (2.79)), x_i^{target} is computed (b) using Eq. (2.80) to push P_i outwards. (c) If P_i is outside the cortex mesh but too close from it (see Eq. (2.81)), x_i^{target} is computed (d) using Eq. (2.83) to push P_i sufficiently far away from the cortex mesh. (e) If P_i is outside the cortex mesh and sufficiently far away from it, the search profile is subject to a validation. (f) If the profile is rejected no external force are applied to the vertex P_i . (g) If the search profile is accepted, x_i^{target} is computed using Eq. (2.86) over the profile to find the skull border.

To make sure that the skull mesh does not intersect the cortex mesh, the following procedure is performed. First, as simplex faces are not flat, the de-

formed \mathcal{M}_C is transformed in its dual triangulation (section 2.2). Then, for each vertex P_i of \mathcal{M}_S , the closest point $P_{i,cortex}$ in the surface defined by the cortex mesh is computed. The point $P_{i,cortex}$ is used to check whether P_i is inside the cortex mesh. The point $P_{i,cortex}$ is in the surface defined by the cortex mesh, and therefore is associated with a triangle T_i of \mathcal{M}_C . $P_{i,cortex}$ can be in the surface of T_i , nevertheless if $P_{i,cortex}$ is in a vertex or an edge, any triangle formed by the vertex or the edge can be taken as T_i . To check if P_i is inside the cortex mesh, the following expression is used:

$$\|(P_{i,cortex} - P_i) \cdot \vec{N}_{T_i}\| \begin{cases} > 0 \Rightarrow P_i \text{ is inside the cortex mesh} \\ \leq 0 \Rightarrow P_i \text{ is outside the cortex mesh} \end{cases}, \quad (2.79)$$

where \vec{N}_{T_i} is the unit normal vector of the triangle T_i . If P_i is inside the cortex mesh, the equation (2.34) is used to push P_i outward by defining the target point x_i^{target} as:

$$x_i^{target} = P_i + \|(P_{i,cortex} - P_i)\| \vec{N}_i. \quad (2.80)$$

Using equation (2.80), P_i is pushed in the direction normal to the mesh, and therefore the mesh deforms without affecting the parametrization. Moreover, the force applied to P_i is proportional to its distance to the cortex mesh, and when P_i will be close enough to the cortex mesh the direction of $(P_{i,cortex} - P_i)$ and \vec{N}_i will be similar.

The cortex and the skull mesh must not intersect, and furthermore there must be a minimum space between them. This space is used in the mechanical modeling and is full of CSF. Therefore, after confirming that P_i is outside the cortex mesh (eq 2.79), it is checked whether P_i is sufficiently far away from the cortex mesh using:

$$\|P_{i,cortex}^\perp - P_i\| \begin{cases} \geq L_{min} \Rightarrow P_i \text{ is far enough from the cortex mesh} \\ < L_{min} \Rightarrow P_i \text{ is too close from the cortex mesh} \end{cases}, \quad (2.81)$$

where L_{min} is the minimum distance allowed between the two meshes, that in our case is $L_{min} = 1$ mm, and

$$P_{i,cortex}^\perp = P_i + ((P_{i,cortex} - P_i) \cdot \vec{N}_i) \vec{N}_i. \quad (2.82)$$

Using the point $P_{i,cortex}^\perp$ to measure the distance between the two meshes, it is possible to maintain a constant minimum distance although P_i may be over a

sulcus (see Fig. 2.32). If P_i is too close from the cortex mesh, the target point is defined as:

$$x_i^{target} = P_{i,cortex}^\perp + L_{min} \vec{N}_i. \quad (2.83)$$

If P_i is outside the cortex mesh (2.79) and is sufficiently far away from it (2.81), a set of measures are taken in search profiles normal to the mesh to localize the skull border. In this case, the search profiles are defined differently than in our general definition presented in section 2.1.4. Each profile of length l_s starts near the surface of the cortex mesh and is normal to skull mesh. The sampling points over the profiles are defined by:

$$x_{i,j} = P_{i,cortex}^\perp + j\delta_s \vec{N}_i, \quad (2.84)$$

where δ_s is a sampling distance, and $j = \{0, 1, \dots, [l_s/\delta_s] - 1, [l_s/\delta_s]\}$. In this way, the search profiles are defined by the normal vector \vec{N}_i and start near the cortical surface but not into a sulcus. Figure 2.32 shows a scheme of the search profiles.

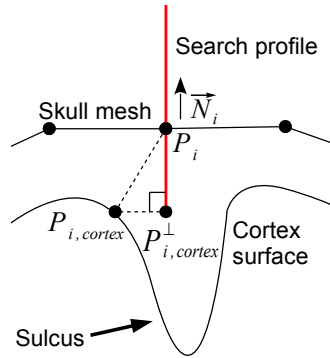


Figure 2.32: Search profile to compute the target points in the skull mesh. To define the search profiles, the surface defined by the cortex mesh is used. By defining $P_{i,cortex}^\perp$ (Eq. 2.82) as the beginning of the profile, it is possible to maintain a constant minimum distance between the skull mesh and the cortex mesh, although P_i may be over a sulcus.

The first measurement taken over the search profile is the position j_{max} of the maximum gray level $I_{max} = I(x_{i,j_{max}})$:

$$j_{max} = \arg \max_{j=0, \dots, [l_s/\delta_s]} I(x_{i,j}). \quad (2.85)$$

The value of j_{max} is an estimation of the scalp position, outside the skull. In this area, the subcutaneous tissue got high gray level intensity in the MRI image. To make sure that j_{max} is actually the scalp position, two comparisons are used:

1. If $j_{max}\delta_s > 30$ mm, it is considered that the position is too far, and maybe corresponds to the lower part of the skull. Therefore, the search profile is rejected.
2. If $I_{max} < \sigma_{wm}$, it is considered that the gray intensity I_{max} is too low, and therefore j_{max} cannot be considered a reliable estimation of the scalp position. The mean value of the WM intensity σ_{wm} computed in section 2.3.1.3 is used in this comparison.

If the two comparisons are negative and hence the profile is not rejected, another measurement is taken. Starting from 0 to j_{max} , the first position j_{min} in which $I(x_{i,j_{min}}) < 0.5 \sigma_{gm}$ is searched, where σ_{gm} is the mean value of the GM intensity computed in section 2.3.1.3. This position should correspond to CSF or bone, because both have a low gray value in the MRI. Therefore, the bone-CSF interface can be searched near of $x_{i,j_{min}}$. To search the interface, the image gradient is used. Because usually the gray value of the bone is lower than that of the CSF, the following equation is used to compute the target point x_i^{target} :

$$x_i^{target} = P_i + \arg \max_{j=0,\dots,[l_s/\delta_s]} \left[\mathcal{F}_i(x_{i,j}) - D(j - j_{min})^2 \delta_s^2 \right] \delta_s \vec{N}_i, \quad (2.86)$$

where D is a weight to give less importance to points that are far from $x_{i,j_{min}}$, $\mathcal{F}_i(x) = -\vec{N}_i \cdot \nabla I(x)$, and $I(x)$ is the gray value of the image normalized between the values $[0,1]$ at point x . Then the target point x_i^{target} , computed to push the mesh or to find the skull border, is used to calculate the external force applied to the mesh \vec{F}_{ext_i} (Eq. 2.34). Figure 2.30(b) shows an example of the skull mesh obtained after deformation, and Figure 2.30(c) shows the same mesh including the deformed cortex mesh inside it.

2.3.6 Ventricle Mesh Deformation

The ventricle mesh \mathcal{M}_V is inside the cortex mesh \mathcal{M}_C , and far away from it. Therefore, it is not necessary to measure the distance between these meshes, as for the skull mesh. To perform the deformation, local gray levels of the image and the statistical gray level model built in the pre-segmentation (sec. 2.3.1) are used. Search profiles (Eq 2.33), as explained in section 2.1.4, are used for each vertex to obtain measures of the local gray level. Then a target point is obtained and the external force is computed using equation (2.34).

Each vertex of \mathcal{M}_V can be in the cerebral parenchyma, or in the CSF into the ventricles. The cerebral parenchyma around the ventricles is composed of

WM, thalamus, basal ganglia and hippocampus. Therefore, the gray level of this tissue may vary, nevertheless the gray level of the CSF is always lower. First, a measure $I_{mean}(i)$ is taken over the profile to estimate the vertex position:

$$I_{mean}(i) = \frac{\sum_{j=[-d_{mean}/\delta], \dots, [+d_{mean}/\delta]} I(x_{i,j})}{[d_{mean}/\delta] + 1}. \quad (2.87)$$

To analyze $I_{mean}(i)$, the mean value μ_{gm} and standard deviation σ_{gm} of the GM gray level computed in section 2.3.1.3 are used. If $I_{mean}(i) < \mu_{gm} - 8\sigma_{gm}$, it is assumed that P_i is inside the CSF and must be pushed to reach the ventricle borders. Therefore, the target point is defined as:

$$x_i^{target} = P_i + d_p \vec{N}_i, \quad (2.88)$$

where d_p is a distance that controls the force applied. Otherwise, the ventricle border can be found looking for a high gradient. To find this high gradient, the target point x_i^{target} is defined as:

$$x_i^{target} = P_i + \arg \max_{j=[-l/\delta], \dots, [l/\delta]} [\mathcal{F}_i(x_{i,j}) - Dj^2\delta^2] \delta \vec{N}_i, \quad (2.89)$$

where D is a weight to give less importance to far points, and $\mathcal{F}_i(x) = \vec{N}_i \cdot \nabla I(x)$. Then the target point x_i^{target} , computed to push the mesh or to find the ventricle border, is used to calculate the external force applied to the mesh \vec{F}_{ext_i} . Figure 2.33(b) shows an example of the ventricle mesh obtained after deformation.

2.3.7 Open Meshes

The *falx cerebri* \mathcal{M}_F , and *tentorium cerebelli* \mathcal{M}_T meshes represent membranes, and must be treated as open meshes. It must also be considered that a part of these membranes is attached to the skull, or slides over other structures (Fig. 2.34). Therefore, a special deformation control of the points belonging to the external borders of these meshes is necessary. Such points can be classified into two types:

Attached Vertices: Vertices belonging to the junction between the membrane's edge and another structure.

Free Vertices: Vertices belonging to the free border of the membrane.

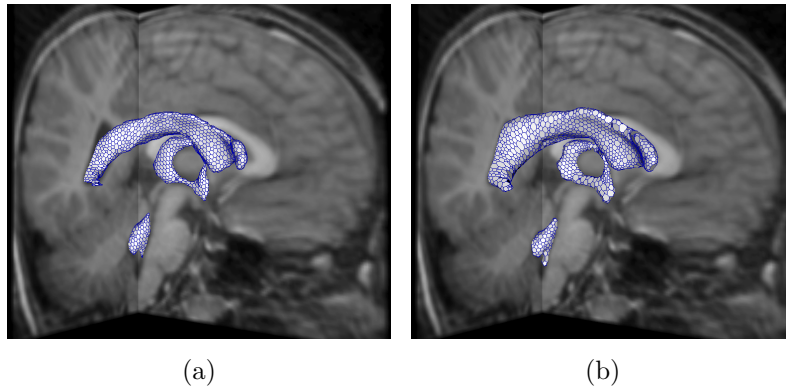


Figure 2.33: Examples of deformation steps with the ventricle simplex mesh: (a) After geometric adjustment by affine transformations (sec. 2.3.3). (b) After deformation to match the ventricle borders in the MRI image.

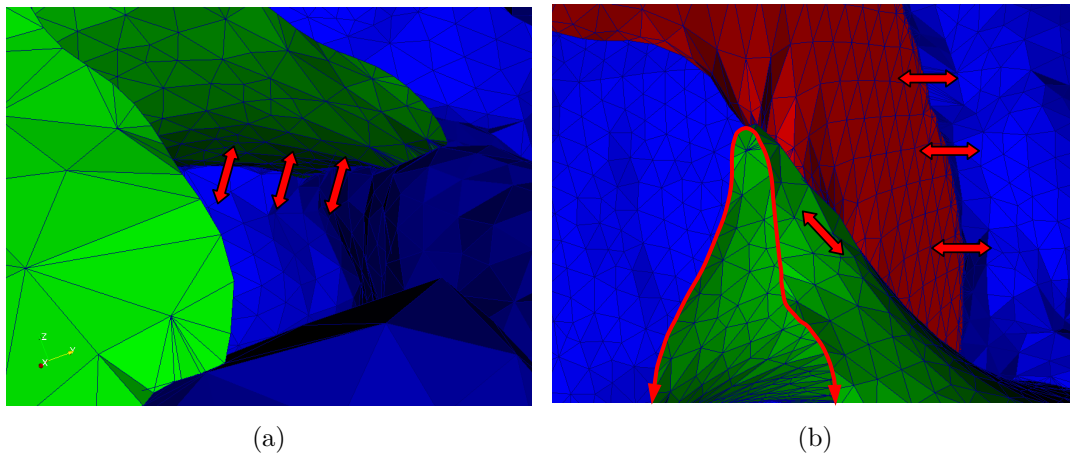


Figure 2.34: (a) Constraints on the *tentorium cerebelli* (green) border along the skull (blue). (b) Restriction on *falx cerebri* (red) borders and extremities along both *tentorium cerebelli* and skull.

Attached vertices P_i^{att} are restricted to move along the surface of another structure, \mathcal{S} . The attached vertices of the tentorium cerebelli move along the internal surface of the skull mesh; and the attached vertices of the falx cerebri move along both the internal surface of the skull mesh and the surface of the tentorium cerebelli (Fig. 2.34). To achieve this kind of movement, the position of the closest point to P_i^{att} , on the surface of \mathcal{S} is computed at each iteration of the deformation. This point C_i , on the surface of \mathcal{S} , is used to compute the external

force which is applied to P_i^{att} in order to keep it on the surface of \mathcal{S} . To obtain this external force, the point C_i is used as target point: $x_i^{target} = C_i$. In this way, the attached border of the mesh moves along the surface of \mathcal{S} , letting the rest of the mesh to fit freely the target structure.

The deformation of the two open meshes \mathcal{M}_F , and \mathcal{M}_T is explained in the following sections.

2.3.7.1 Tentorium Mesh Deformation

The tentorium mesh \mathcal{M}_T has to be considered first. In effect, due to the local deformation of the skull in the previous step (section 2.3.5), some parts of \mathcal{M}_T may intersect \mathcal{M}_S . This might cause problems during the deformation, and must be corrected. To compute the intersections, both simplex meshes are transformed into its dual triangle mesh (section 2.2). Then, the intersections are computed [Lo 2005], and the outer extension of \mathcal{M}_T is eliminated. After cutting \mathcal{M}_T , the mesh is shifted back into a simplex mesh, in order to be deformed.

The attached vertices P_i^{att} , in the border of the tentorium cerebelli mesh \mathcal{M}_T , lie on the junction between the inner skull surface and the tentorium cerebelli. The free vertices of \mathcal{M}_T lie between the brain and cerebellum (Fig. 2.34(a)). To differentiate between free and attached vertices, the distance between the border vertices of \mathcal{M}_T and the skull mesh \mathcal{M}_S surface is calculated. First, the distance threshold to differentiate free and attached vertices is set in such a way that 1/3 of the vertices are defined as free vertices, i.e., 1/3 of the vertices have a distance to the skull mesh larger than the threshold. Next, the largest section of the mesh border with consecutive free vertices is found, and all the vertices that are not in this section are considered attached vertices. Using this definition of the attached vertices, the surface will be folded if some vertices in the limits of the attached section of the border are pushed toward the surface defined by \mathcal{M}_S . Figure 2.35(a) shows an example of this situation, where the tentorium mesh will be folded if point P_2 is pushed toward the skull mesh. To avoid this fold, the classification is refined in the limits of the attached zone. Starting from the center of the attached section, it is searched the first point, P_{left} , to the left (left hemisphere) where the following expression is satisfied:

$$\vec{M}_i \cdot (C_i - P_i^{att}) \leq 0, \quad (2.90)$$

where \vec{M}_i is computed using the normal vector to the surface at the neighbor vertex of P_i^{att} that lies in the mesh surface \vec{N}_{SNi} and the tangent vector to the

mesh border \vec{T}_i (Eq. (2.37) in sec. 2.1.4.1):

$$\vec{M}_i = \vec{N}_{SNi} \times \vec{T}_i. \quad (2.91)$$

The same procedure is used in the right (right hemisphere), to find the point P_{right} . The attached section of the border is finally defined as all the vertices P_i^{att} between P_{right} and P_{left} . Figure 2.35 shows a scheme of the procedure to compute P_{right} and P_{left} .

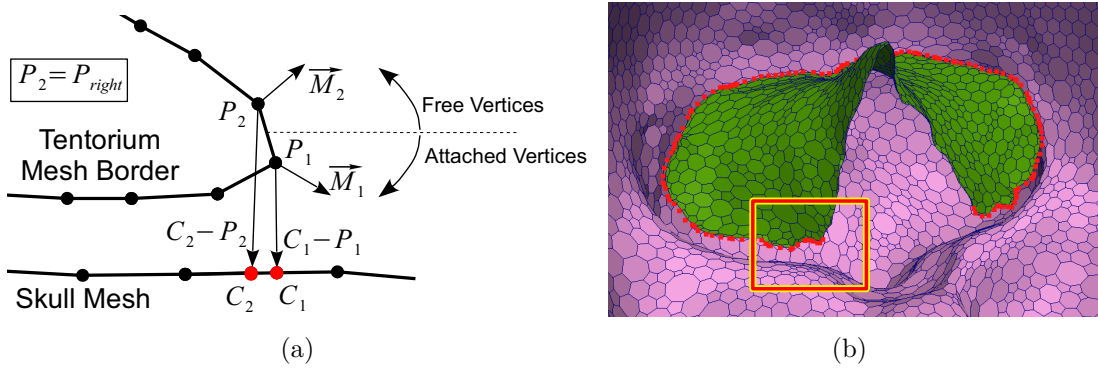


Figure 2.35: (a) Scheme of the attached vertices P_i^{att} selection. The right limit of the tentorium mesh border is shown. In this example, the first point P_i that satisfies equation (2.90) is P_2 . Therefore P_2 is considered as P_{right} . The mesh border (closed contour) can be divided into two sections by vertex P_{left} and its counterpart, P_{right} , in the right hemisphere. Vertices in the border section nearest the skull mesh \mathcal{M}_S are considered attached vertices P_i^{att} . (b) Tentorium mesh with vertices P_i^{att} highlighted. The marked rectangular area correspond to the scheme shown in (a).

The internal force \vec{F}_{int_i} applied to the vertices in the mesh surface is computed as in the case of closed meshes. Nevertheless, the internal force applied to contour vertices is computed as explained in section 2.1.3.1. The external force \vec{F}_{ext_i} is computed as follows.

To compute the external force applied to the surface vertices and free border vertices, some measures of the image gray level are taken over normal profiles. The normal profiles for the surface vertices are defined as explained in section 2.1.4 (Eq. 2.33), and for the border vertices as shown in section 2.1.4.1 (Eq. 2.36)

First, the position j_{min} of minimum gray value is computed in each profile:

$$j_{min} = \arg \min_{j=[-l/\delta], \dots, [l/\delta]} I(x_{i,j}). \quad (2.92)$$

The value of j_{min} is an estimation of the CSF position in the normal profile. The interface between the cerebellum and the brain contains CSF, therefore j_{min} is a first estimation of its position. Then, a target point x_i^{target} is computed to estimate the precise position of the interface. This target point is computed in a similar way to that used for the skull deformation:

$$x_i^{target} = P_i + \arg \max_{j=0, \dots, \lfloor l/\delta \rfloor} [\mathcal{F}_i(x_{i,j}) - D(j - j_{min})^2 \delta^2] \delta \vec{N}_i. \quad (2.93)$$

Nevertheless, the function $\mathcal{F}_i(x)$ to search the largest gradient is different in the present case. The interface between brain and cerebellum has lower gray value than both structures. Therefore, the function is defined as: $\mathcal{F}_i(x) = \|\vec{N}_i \cdot \nabla I(x)\|$.

The external force applied to the attached vertices P_i^{att} is designed to ensure that these vertices move on the skull mesh surface. Therefore the target point is computed as:

$$x_i^{target} = P_i^{att} + \min(\|C_i - P_i^{att}\|, d_{lim}) \frac{C_i - P_i^{att}}{\|C_i - P_i^{att}\|}, \quad (2.94)$$

where C_i is the closest point to P_i^{att} on the surface of \mathcal{M}_S , and $d_{lim} = 4$ mm is a threshold distance to restrict the force applied. The external force is computed using the target points as explained in section 2.1.4 (Eq. 2.34).

After deformation, \mathcal{M}_T is joined to the skull mesh \mathcal{M}_S . To join the two meshes, \mathcal{M}_T is transformed into its dual triangulation (sec. 2.2). Next, the free borders of \mathcal{M}_T are stretched in the \vec{M}_i direction to intersect both meshes. The intersection points are searched [Lo 2005] and the zone is remeshed. Finally, the part of \mathcal{M}_T which is outside the skull surface is discarded. The result of this union is the triangle mesh M_{ST} . Figure 2.36 shows the joining process. The mesh M_{ST} is used in the deformation of the falx mesh M_F .

2.3.7.2 Falx Mesh Deformation

After the tentorium mesh deformation, the falx mesh \mathcal{M}_F is deformed. This mesh is the second open mesh and its attached vertices must lie in the surface of the mesh \mathcal{M}_{ST} formed by the union of the skull mesh \mathcal{M}_S and tentorium mesh \mathcal{M}_T . Similar to the previous case, some parts of \mathcal{M}_F may intersect \mathcal{M}_{ST} , because the deformation. To correct this problem, \mathcal{M}_F is transformed into a triangulation (sec. 2.2), the intersection with \mathcal{M}_{ST} is computed [Lo 2005], and the outer extension of \mathcal{M}_F is discarded. After cutting \mathcal{M}_F , the mesh is shifted back into a simplex mesh, in order to be deformed.

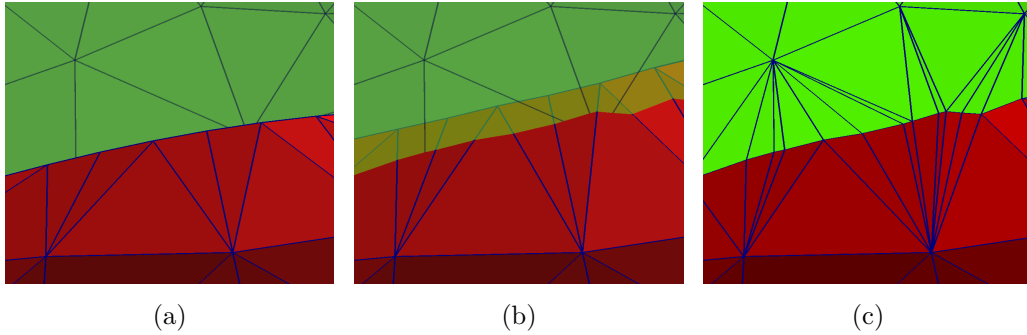


Figure 2.36: Joining process of two meshes, using to join the open meshes of the model. (a) Open mesh that has its border near the surface defined by another mesh. (b) The open mesh's border is stretched, and both meshes intersect. (c) The intersection points are computed and the zone is remeshed. The result is a new mesh which is the union of the two previous meshes. After remeshing, the part of the open mesh that lies beyond the other mesh can be discarded.

The falx cerebri is joined with two structures: the inner skull surface and the tentorium cerebelli. Therefore, the attached vertices P_i^{att} of \mathcal{M}_F lie in both junctions. The free vertices lie between the two cerebral hemispheres, around the *corpus callosum*. To differentiate between free and attached vertices, a similar approach to that used for the tentorium mesh is utilized. The distances between the border vertices in \mathcal{M}_F and the surface of \mathcal{M}_{ST} are computed. First, the free vertices are defined as the half of the edge vertices farthest to \mathcal{M}_{ST} . Next, the largest section of the mesh border with consecutive free vertices is found, and all the vertices that are not in this section are considered attached vertices. This definition of the vertices must be refined in the limits of the attached segment. In the more frontal limit, the mesh will be folded if some vertices are pushed toward the surface of \mathcal{M}_{ST} . To avoid this fold, the same technique used in the tentorium mesh is employed. Starting in anterior direction from the center of the attached section, it is searched the first vertex P_{ant} where the expression (2.90) is satisfied. P_{ant} is the anterior limit of the attached border segment. In the posterior limit of the attached segment the vertices lie in the tentorium surface, and the last vertex must lie in the border of the tentorium mesh (Fig. 2.34(b)). To define the best vertex to be attached to the mesh, the distances between vertices P_i^{att} , and the surface and border of the tentorium are computed. Let C_i be the closest point to P_i^{att} on the surface of \mathcal{M}_{ST} , and S_i the closest point to P_i^{att} in the border of \mathcal{M}_{ST} (Fig. 2.37(a)). Starting in anterior direction from the center of the attached section, it is searched the first border vertex P_{post} at which the

following expression is satisfied:

$$\|C_i - S_i\| < d_{Plim}, \quad (2.95)$$

where d_{Plim} is a threshold distance empirically defined as 1 mm. Note that C_i and S_i are not vertices, they are points of the surface and on the border of \mathcal{M}_{ST} ; therefore, they are searched by computing distances between vertices P_i^{att} and the surfaces or edges of the triangles that form \mathcal{M}_{ST} . Vertex P_{post} is the posterior limit of the attached border segment. All vertices between P_{ant} and P_{post} are defined as attached vertices P_i^{att} .

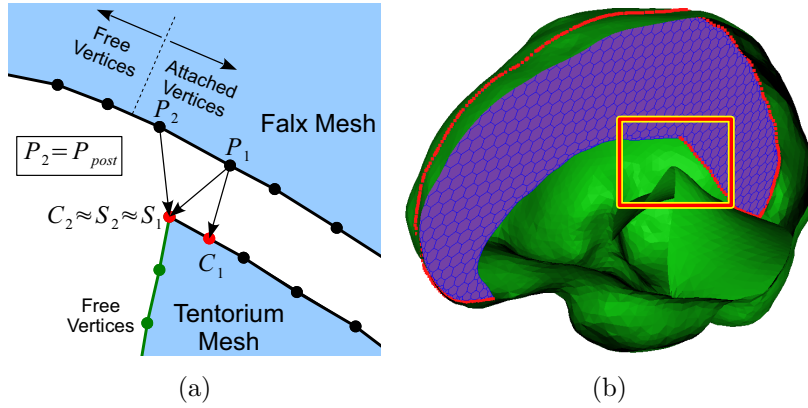


Figure 2.37: (a) Scheme of the attached vertices P_i^{att} selection in the falx mesh. The upper part of the tentorium cerebelli is shown. This area is marked with a rectangular frame in (b). In the example, the first point P_i that satisfies equation (2.95) is P_2 . Therefore P_2 is considered as P_{post} . The mesh border is divided into two segments by P_{ant} and P_{post} . (b) Falx cerebri mesh with vertices P_i^{att} highlighted.

The internal force $\overrightarrow{F_{int_i}}$ applied to the vertices in the mesh surface is computed as explained in the section 2.1.3, and for the vertices in the mesh border as explained in section 2.1.3.1.

The external force $\overrightarrow{F_{ext_i}}$ for the surface and border vertices is computed in the same way as for the tentorium mesh (sec 2.3.7.1). Nevertheless, the external force applied to P_{post} has a small difference. P_{post} is attached to the tentorium border (Fig. 2.34(b)), therefore, the target point of P_{post} is computed as:

$$x_i^{target} = P_{post} + \min(\|S_i - P_{post}\|, d_{lim}) \frac{S_i - P_{post}}{\|S_i - P_{post}\|}. \quad (2.96)$$

Figure 2.38(a) shows the deformed falx mesh, \mathcal{M}_F , with the tentorium mesh in an MRI image. After deformation, \mathcal{M}_F is joined to \mathcal{M}_{ST} using the same tech-

nique employed for the tentorium mesh (Figure 2.36). The result is a mesh \mathcal{M}_{STF} which includes the skull, tentorium cerebelli and falx cerebri. These meshes must be joined because both membranes are attached to the skull. Figure 2.38(b) shows the deformed falx mesh inside the mesh \mathcal{M}_{ST} . Figures 2.38(c) and (d) show the mesh \mathcal{M}_{STF} .

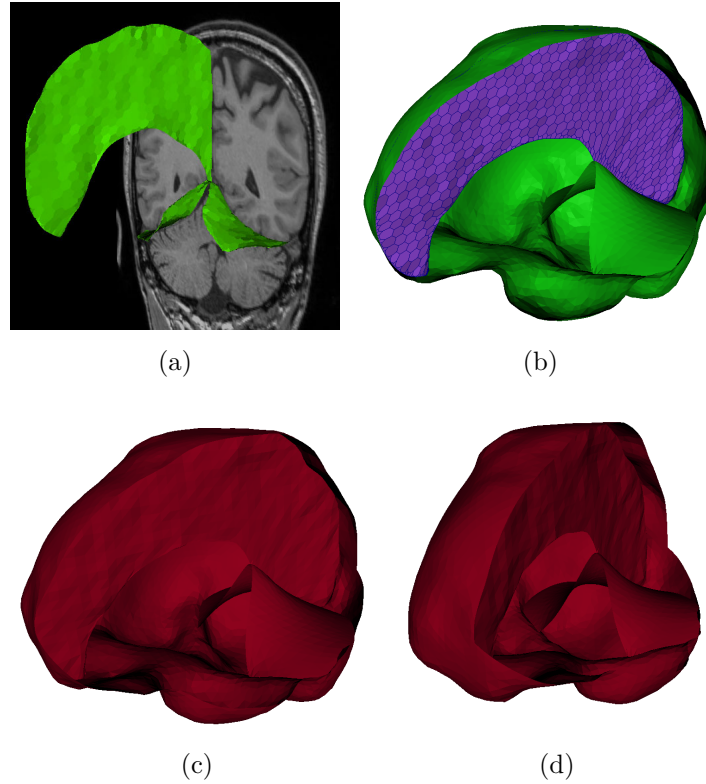


Figure 2.38: (a) Tentorium and falx mesh deformed in an MRI image. (b) Falx mesh deformed inside the mesh \mathcal{M}_{ST} (green). Mesh \mathcal{M}_{ST} is cut to allow visualization. (c) Falx mesh transformed into a triangulation and joined with \mathcal{M}_{ST} . (d) Same mesh from another point of view.

2.3.8 Final Mesh

After all meshes have been deformed, a final mesh is built combining all the surfaces. The cortex mesh \mathcal{M}_C and ventricles mesh \mathcal{M}_V are transformed into their dual triangulations (sec. 2.2); and then they are joined with \mathcal{M}_{STF} . The intersection points between \mathcal{M}_C and other meshes are computed and the zone

is remeshed [Lo 2005]. In this way, the final model is a complex mesh that includes all relevant anatomical structures for mechanical modeling. Moreover, there are no intersecting faces and a 3D meshing algorithm can be used to obtain a volumetric mesh suitable for finite element modeling. One may notice that each mesh is labelled separately, that will help in the further definition of specific border conditions in the simulation. Figure 2.39 shows the deformed final mesh.

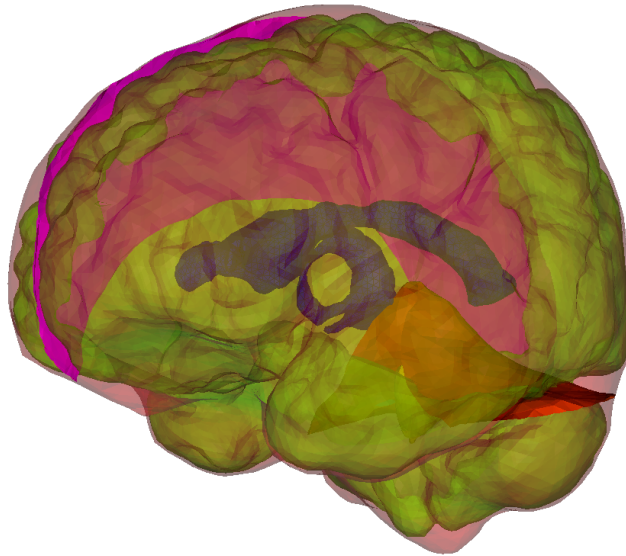


Figure 2.39: Final deformed mesh. The cortex and ventricle meshes are transformed into their dual triangulations and then are joined with the \mathcal{M}_{STF} mesh. The intersections between the cortex mesh and \mathcal{M}_{STF} are computed and the intersection zone is remeshed, obtaining a final mesh without self-intersections. This final mesh is suitable for obtaining a volumetric mesh, such as a tetrahedral meshes, by using a meshing algorithm. Then, the volumetric mesh can be used for 3D finite element modeling.

Evaluations of each step of the method explained in this chapter are presented in the next chapter.

Experiments and Results

Contents

3.1 Databases and Performance Measurements	100
3.1.1 Evaluation of Closed Meshes Segmentation	102
3.1.2 Evaluation of Open Meshes Segmentation	106
3.2 Segmentation Results	108
3.2.1 Cortical Surface Segmentation	108
3.2.2 Skull Segmentation	114
3.2.3 Ventricles Segmentation	116
3.2.4 Tentorium Cerebelli and Falx Cerebri Segmentation	118

In this chapter, our proposed method is assessed on international databases. First, the online databases, indices to measure the performance, and methods used for comparison are introduced in section 3.1. Then, results for the segmentation are shown in section 3.2. The segmentation of each anatomical structure is evaluated separately: cortex (sec. 3.2.1), skull (sec. 3.2.2), ventricles (sec. 3.2.3) and membranes (sec. 3.2.4).

3.1 Databases and Performance Measurements

To evaluate the performance of the proposed method, databases available online were used. By using these commonly used databases, it is possible to compare the method with other ones found in the literature. For the same reason, the most common performance indices were used in this assessment.

T₁W MRI Online Databases. A review of online available databases, used for the evaluation of our segmentation method, follows:

- 20 simulated T₁W MR images from the BrainWeb website [Cocosco 1997, Aubert-Broche 2006] (Fig. 3.1(a)), with 1 mm isotropic voxel size. This database includes Ground Truth segmentations available for 11 tissue types, including GM, WM and CSF (Fig. 3.1(b)). Table 3.1 shows those labels.

Table 3.1: BrainWeb Labels of Ground Truth segmentations.

0=Background	6=Muscle/Skin
1=CSF	7=Skull
2=Gray Matter	8=Vessels
3=White Matter	9=Around fat
4=Fat	10 =Dura matter
5=Muscle	11=Bone marrow

- 18 real T₁W MR images from the Internet Brain Segmentation Repository (IBSR) [Center for Morphometric Analysis 1995] (Fig. 3.1(c)), slice thickness 1.5 mm. This database has two different types of available Ground Truth segmentations. The first one is a manual segmentation of three types of tissues (Fig. 3.1(d)): GM, WM and CSF. The second one is a manual segmentation of 84 brain structures (Fig. 3.1(e)).
- 40 real T₁W MR images from the Segmentation Validation Engine (SVE) website, with 1.5 mm slice thickness and in-plane voxel resolution of 0.86 mm (38 subjects) or 0.78 mm (2 subjects) [Shattuck 2009]. No Ground Truth segmentations are available for this data set. However, segmentation masks can be sent to the website for performing an online comparison with manually edited brain mask volumes.

The above databases were segmented by our method using the parameters shown in Table 3.2. Then, the segmentation of each structure was evaluated independently: cortical surface, skull, ventricles, tentorium cerebelli, falx cerebri. Nevertheless, the way to evaluate the segmentation of closed and open meshes is different, as explained in the following sections.

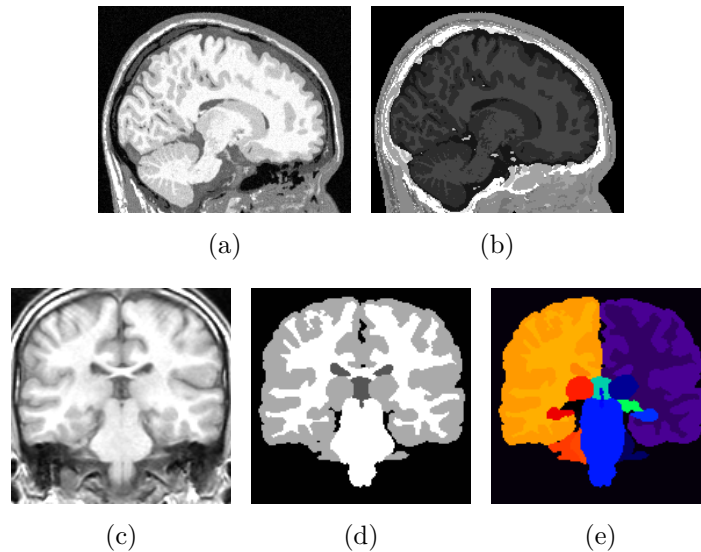


Figure 3.1: Examples of images from the BrainWeb and IBSR databases. (a) MRI image of the BrainWeb database. (b) Ground Truth segmentations of 11 tissue types available in the BrainWeb database. (c) MRI image of the IBSR database. (d) Ground truth segmentation of GM, WM and CSF available in IBSR database. (e) Ground Truth segmentation of 84 structures available in the IBSR database.

3.1.1 Evaluation of Closed Meshes Segmentation

As explained above, the segmentation of each structure was evaluated independently using the databases presented in the last section. The closed meshes were evaluated using volumetric measures (Dice, Jaccard, Sensitivity, Specificity) explained below in this section. To use these volumetric measures, voxels in the image must be classified as belonging or not to the segmented structure. Therefore, a binary mask of each structure was built using the final mesh after segmentation. The masks were built by classifying the voxels that lie inside a particular closed mesh as part of the structure represented by the mesh. However, the case of the cortex mesh is special. As explained in section 1.2.4.1, the segmentation obtained with the cortex mesh can be seen as a *Skull Stripping* process. Therefore, the segmentation of this structure was compared with the most popular Skull Stripping methods, and the binary mask was constructed as explained in section 2.3.4.5. The volumetric measures used in the evaluations are explained as follows.

Volumetric Measures for Evaluation. To measure the segmentation performance of the closed meshes, the two volumetric measures most used in the

Table 3.2: Parameters used to segment the databases. The anatomical structures, the section which explains the segmentation, and the equations where the parameters are used are indicated.

Cortex			
First deformation Section 2.3.4.1		Second and third deformation Sections 2.3.4.2 and 2.3.4.3	
Parameters	Eq.	Parameters	Eq.
$\lambda = 0.4$	(2.26)	$\lambda = 0.4$	(2.26)
$\gamma = 0.65$	(2.25)	$\gamma = 0.65$	(2.25)
$\delta = 0.5$	(2.33)	$\delta = 0.5$	(2.33), (2.75)
$l = 15$	(2.33)	$l = 8,$	(2.33)
$D_F = 10.$	(2.35)	$D_F = 1.$	(2.35)
		$S = 2$	(2.29)
		$d_{max} = 5$	(2.76)
		$d_{min} = 4$	(2.72)
		$d_{mean} = 2$	(2.73)
		$d_p = 0.5$	(2.74),(2.77)
		$D = 0.3$	(2.75)

Skull Section 2.3.5		Ventricle Section 2.3.6		Tentorium Section 2.3.7.1		Falx Section 2.3.7.2	
Parameters	Eq.	Parameters	Eq.	Parameters	Eq.	Parameters	Eq.
$\lambda = 0.4$	(2.26)	$\lambda = 0.4$	(2.26)	$\lambda = 0.4$	(2.26)	$\lambda = 0.4$	(2.26)
$\gamma = 0.65$	(2.25)	$\gamma = 0.65$	(2.25)	$\gamma = 0.9$	(2.25)	$\gamma = 0.9$	(2.25)
$\delta_s = 0.5$	(2.84) (2.86)	$\delta = 0.5$	(2.33) (2.89)	$\delta = 0.5$	(2.33) (2.36) (2.93)	$\delta = 0.5$	(2.33) (2.36) (2.93)
$l_s = 40$	(2.84)	$l = 8$	(2.33)	$l = 4$	(2.33) (2.36)	$l = 4$	(2.33) (2.36)
$D_F = 1$	(2.35)	$D_F = 1$	(2.35)	$D_F = 2$	(2.35)	$D_F = 2$	(2.35)
$S = 3$	(2.29)	$S = 2$	(2.29)	$\rho_i^* = 0.$	(2.28) (2.32)	$\rho_i^* = 0.$	(2.28) (2.32)
$D = 0.3$	(2.86)	$d_p = 0.2$	(2.88)	$\psi_i^* = 0.$	(2.32)	$\psi_i^* = 0.$	(2.32)

literature were employed: the **Jaccard** similarity [Jaccard 1912] and the **Dice** coefficient [Dice 1945]. These volumetric measures can be computed using the concepts of True Positive (TP), False Positive (FP), True Negative (TN) and False Negative (FN). In our case the TP and FP are defined as the number of voxels correctly and incorrectly classified as part of the segmented structure, respectively. Similarly, TN and FN are defined as the number of voxels correctly

and incorrectly classified as non-part of the structure, respectively. The Jaccard similarity, also termed the Tanimoto coefficient, measures the similarity of two sets S_1, S_2 , as the ratio of the size of their intersection divided by the size of their union:

$$J(S_1, S_2) = \frac{|S_1 \cap S_2|}{|S_1 \cup S_2|} = \frac{TP}{TP + FP + FN} . \quad (3.1)$$

The Dice coefficient measures the similarity of two sets S_1, S_2 , as the ratio of twice the size of their intersection divided by the sum of their sizes:

$$\kappa(S_1, S_2) = \frac{2|S_1 \cap S_2|}{|S_1| + |S_2|} = \frac{2TP}{2TP + FP + FN} . \quad (3.2)$$

The Dice coefficient is related to the Jaccard similarity by:

$$\kappa = \frac{2J}{J + 1} . \quad (3.3)$$

The sensitivity and specificity percentages were also computed, which show the percentage of brain and non-brain voxels recognized respectively:

$$\begin{aligned} \text{Sensitivity} &= \frac{TP}{TP + FN} , \\ \text{Specificity} &= \frac{TN}{TN + FP} . \end{aligned} \quad (3.4)$$

Methods for Comparison. As mentioned above, the cortex mesh segmentation has been compared with the most popular skull stripping methods. These methods are:

The Brain Extraction Tool (BET) [Smith 2002] that segments the brain using deformable models. The image is binarized using estimations of the minimum and maximum intensities of the brain. Next, the center of the head is estimated in the binarized image and the deformable model is initialized with a sphere shape in this position. The model is deformed using local adaptive forces. BET v2.1 is free and available in the FMRIB FSL software library [FMRIB]. The recommended default parameters were used for the evaluation: fractional intensity threshold = 0.5, threshold gradient = 0. BET v2 also performs skull segmentation [Jenkinson 2005, Pechaud 2006]. Although better skull segmentations can be obtained using registered T_1 and T_2 -weighted images, the algorithm also works using only a T_1 -weighted

image. To find the inner skull surface, a set of points are automatically detected in normals profiles from the first segmentation. Then, the deformed model is again adapted according to forces computed using the set of points. Because BET also performs this skull segmentation, it was used as a comparison to our technique.

The Brain Surface Extractor (BSE) [Shattuck 2001] uses Marr-Hildreth edge detection [Marr 1980] to identify the border of the brain. Before applying it, anisotropic diffusion filtering [Perona 1990] is used to de-noise the image. This spatially adaptive filter smoothes noisy regions while preserving edge boundaries. After applying the edge detection, the image is binarized using the computed edges, and the brain is found using morphological operators. Binary erosion is applied to eliminate narrow connections between the zones found by the binarization, and a 3D connected component analysis is carried out to identify the brain. Next, a morphological dilation is applied to the selected element (brain) to undo the effects of the erosion, and a closing operation is performed to close the small holes that may be in the volume. BSE is freely available as part of the BrainSuite of the Laboratory of Neuro Imaging (LONI) at the University of California, Los Angeles (UCLA) [BrainSuite]. Two sets of parameters were used in our evaluations: the default parameters (diffusion iterations = 3, diffusion constant = 25, edge constant = 0.64, erosion size = 1), and the parameters suggested by Hartley et al [Hartley 2006, Sadananthan 2010] (diffusion iterations = 3, diffusion constant = 35, edge constant = 0.62, erosion size = 2).

The Hybrid Watershed Algorithm (HWA) [Ségonne 2004] is a hybrid method that combines a watershed algorithm [Hahn 2000], and a deformable surface model [Dale 1999], which includes shape restrictions based on an atlas. First, a watershed algorithm that uses the concept of pre-flooding (the connectivity path between two points can contain a lower intensity than the darker of the two points up to a maximum difference) is used to segment the brain. Then, the deformable model is initialized with a balloon shape using the above segmentation. A first deformation of the model is carried out using the watershed segmentation and global parameter estimations. Next, an atlas is used to verify the resulting surface and correct it if there are errors. Finally, a deformation using estimations of local parameters is performed to find the brain borders. HWA v5 is included in the FreeSurfer software package [FreeSurfer] developed at the

Martinos Center for Biomedical Imaging at Harvard University, USA. The default parameters and the “-atlas” option to use basic atlas information to correct the result of the deformations, were used in our tests. The default parameters are: weight for the atlas = 0.85; probability of merging = 0.32; pre-flooding height = 10; seed points using atlas information; template deforming using atlas information; use of pre-weighting for the template deformation.

The method used to evaluate the segmentation of the open meshes is introduced in the next section.

3.1.2 Evaluation of Open Meshes Segmentation

The volumetric measures explained in the previous section cannot be used to evaluate the segmentation of open meshes, because the segmented structures are membranes. Moreover, the segmented internal membranes of the brain are not explicitly marked in the ground truths of the used databases. Nevertheless, their location can be deduced by using the segmentation of other structures. To measure the segmentation performance of the open meshes, we have computed the distance between the deformed mesh and the position where the corresponding membrane is expected to be based on to the position of other structures.

It can be assumed that the tentorium cerebelli lies between the cerebellum and the brain. Similarly, the falx cerebri is assumed to lie between both brain hemispheres. In the IBSR, the brain hemispheres and cerebellum can be identified using the available ground truth segmentations of 84 structures (Fig. 3.1(e)) in both brain hemispheres. Therefore, the IBSR is the only one among the used databases that can be employed to evaluate the segmentation of the membranes. The method to compute the distance between the deformed mesh and the estimated position of the membrane in the ground truth is explained in the following.

Distance Computation. To compute the distance between the deformed mesh and the estimated position of the membrane according to the ground truth segmentations, a sampling in profiles normal to the mesh was used. The normal profiles were defined by equation (2.33), in the same way as for the segmentation in section 2.3.7. The sampling distance was $\delta = 0.25$, and the nearest neighbor sampling method was used. Figure 3.2 shows a scheme of the sampling in the normal profile of a vertex P_i , and two voxels with centers V_A and V_B belonging to different structures A and B, respectively. The last sampling point inside the

structure A is represented by $x_{i,A}$, and the first sampling point inside the structure B is $x_{i,B}$. Thus, the distance d_i^{err} from the vertex P_i of the deformed mesh to the interface between structures is defined as:

$$d_i^{err} = \|P_i - x_i^{err}\|, \quad (3.5)$$

where

$$x_i^{err} = x_{i,A} + (x_{i,B} - x_{i,A}) \frac{\left(\frac{V_A + V_B}{2} - x_{i,A}\right) \cdot \hat{e}}{(x_{i,B} - x_{i,A}) \cdot \hat{e}},$$

$$\hat{e} = \frac{V_B - V_A}{\|V_B - V_A\|}. \quad (3.6)$$

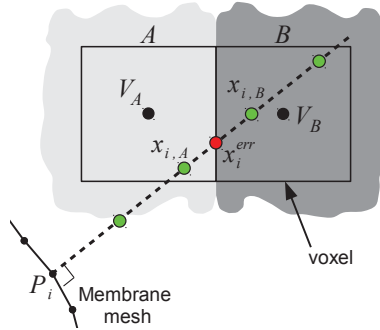


Figure 3.2: Scheme of the sampling points in the normal profile of a vertex P_i to find the midpoint between two structures A and B. The dashed line represents the normal profile, and $x_{i,A}$, $x_{i,B}$, are two sampling points in it. The gray value in the sampling points is computed using the nearest neighbor sampling method. The last sampling point inside the structure A is represented by $x_{i,A}$, and the first sampling point inside the structure B by $x_{i,B}$. V_A and V_B are the centers of voxels belonging to structures A and B, respectively. The point in the normal profile used to compute the error in the position of the membrane mesh is x_i^{err} . This point is considered as the position of the membrane between A and B and it is computed by equation (3.6).

The structures in the ground truth segmentations of the IBSR database were separated as belonging to: left brain hemisphere, right brain hemisphere, and cerebellum. Then, the above method was used to measure the distance between the vertices of the mesh representing the falx and the interface between both hemispheres. In the same way, the distance between the mesh representing the tentorium and the interface between the brain and the cerebellum was measured. Finally, a weighted mean distance was computed for every mesh. The distance d_i^{err} computed for every vertex P_i of the simplex mesh was weighted using the

radius r_i of the circle defined by the neighbors of P_i (Fig. 2.2, Eq. (2.7)). This weighting was used because the surface of the mentioned circle is a good estimation of the importance the vertex P_i has within the mesh. Therefore the weighted mean distance is:

$$\text{WMD} = \sum_{i=1}^N d_i^{\text{err}} \frac{r_i^2}{\sum_{j=1}^N r_j^2}, \quad (3.7)$$

where N is the number of vertices in the mesh.

The results of the segmentations of each structure in the corresponding databases are presented in the next section.

3.2 Segmentation Results

In this section, the segmentation results of the method are presented. The used databases and performance measurements were introduced in section 3.1. The segmentation of each structure is evaluated independently: cortical surface (sec. 3.2.1), skull (sec. 3.2.2), ventricles (sec. 3.2.3), and membranes (sec. 3.2.4).

3.2.1 Cortical Surface Segmentation

As was explained in section 1.2.4.1, the segmentation obtained with the cortex mesh can be seen as a *Skull Stripping* process. Therefore, this segmentation is compared to the most popular skull stripping methods, and using the most used publicly available databases (BrainWeb, IBSR, SVE) (sec. 3.1.1). To evaluate the cortex segmentation in the IBSR and BrainWeb databases, the ground truth was the union of GM and WM using the available segmentations. Because the IBSR database provides 2 types of segmentations, the one based on tissues (GM, WM and CSF) was used (Fig. 3.1(d)). Tables 3.3 and 3.4 show the performance of the different segmentation methods using the BrainWeb and IBSR databases, respectively. In the SVE database, the ground truth is not available, but the segmentation can be evaluated by an independent online assessment that provides all used volumetric measurements. Additionally, the performance of the other methods is available online for this database. Table 3.5 shows the performance of the methods in the SVE database. In addition to the segmentations using the methods default parameters, segmentation performances with different parameters can be found on the SVE website. The segmentation results with best reported performance for each method are also shown in Table 3.5 marked with an *.

Table 3.3: Performance Comparison among Different Methods using the set of 20 images of the BrainWeb database [Cocosco 1997, Aubert-Broche 2006]. The volumetric measures used for comparison, and the parameters used in the methods are presented in section 3.1.1. Two set of parameters was used for the BSE method: the default parameters and the parameters suggested by Hartley et al [Hartley 2006, Sadananthan 2010]. The best results are shown in bold.

Method	Jaccard mean (SD)	Dice mean (SD)	Sensitivity mean (SD)	Specificity mean (SD)
BET2.1	0.812 (0.020)	0.896 (0.012)	0.997 (0.002)	0.964 (0.004)
BSE (def.)	0.823 (0.091)	0.900 (0.061)	0.995 (0.003)	0.964 (0.027)
BSE (Hard.)	0.875 (0.049)	0.932 (0.031)	0.991 (0.004)	0.979 (0.012)
HWA	0.685 (0.017)	0.813 (0.012)	1.000 (0.001)	0.928 (0.005)
Our method	0.904 (0.011)	0.950 (0.006)	0.990 (0.003)	0.985 (0.002)

Table 3.4: Performance Comparison among Different Methods using the 18 images of the IBSR database [Center for Morphometric Analysis 1995]. The volumetric measures used for comparison, and the parameters used in the methods are presented in section 3.1.1. Two set of parameters was used for the BSE method: the default parameters and the parameters suggested by Hartley et al [Hartley 2006, Sadananthan 2010]. The best results are shown in bold.

Method	Jaccard mean (SD)	Dice mean (SD)	Sensitivity mean (SD)	Specificity mean (SD)
BET2.1	0.882 (0.092)	0.935 (0.060)	0.985 (0.012)	0.982 (0.019)
BSE (def.)	0.749 (0.152)	0.848 (0.101)	0.988 (0.011)	0.941 (0.049)
BSE (Hard.)	0.848 (0.065)	0.916 (0.038)	0.945 (0.072)	0.984 (0.014)
HWA	0.814 (0.036)	0.897 (0.022)	1.000 (0.000)	0.966 (0.012)
Our method	0.902 (0.030)	0.948 (0.017)	0.993 (0.009)	0.984 (0.010)

Figures 3.3 and 3.4 show a comparison among different segmentations of an IBSR and BrainWeb image, respectively. Figure 3.4 also includes an image of the ground truth segmentation, and a zoom of the cortex for better comparison. The HWA has a low specificity for both databases (see Table 3.4 and 3.5), nevertheless, the specificity of BSE is lower for the IBSR database when the default parameters are used (Fig. 3.3(d)). Also, the specificity of BET is low for the BrainWeb database (Fig. 3.4(d)) obtaining a low overall performance even though its sensitivity is good. The best performance was obtained by our method (Figs 3.3(f) and 3.4(g)), followed by BET2.1 for the IBSR database; and BSE.0.8b and BETv2.1 for the SVE database.

The BrainWeb database requires a special comment about the sensitivity index. The ground truths of the BrainWeb database are digital phantoms to syn-

Table 3.5: Performance Comparison among Different Methods using the 40 images of the SVE database [Shattuck 2009]. The results marked with * are the best on the website for each method, and the parameters used for these segmentations are given below the table. Best results are shown in bold.

Method	Jaccard mean (SD)	Dice mean (SD)	Sensitivity mean (SD)	Specificity mean (SD)
BETv2.1	0.892 (0.054)	0.942 (0.032)	0.986 (0.006)	0.980 (0.014)
BETv2.1*	0.940 (0.009)	0.969 (0.005)	0.962 (0.012)	0.996 (0.001)
BSEv08a (def.)	0.596 (0.207)	0.727 (0.150)	0.980 (0.014)	0.854 (0.094)
BSEv08b*	0.943 (0.028)	0.970 (0.016)	0.975 (0.033)	0.994 (0.002)
HWA3	0.851 (0.019)	0.919 (0.011)	0.999 (0.000)	0.969 (0.006)
HWA3*	0.854 (0.018)	0.921 (0.011)	0.999 (0.000)	0.969 (0.005)
Our method	0.946 (0.010)	0.972 (0.005)	0.987 (0.006)	0.992 (0.003)

parameters for BSEv08b*: -n 5 -d 15 -s 0.65 -p -noneck

parameters for BETv2.1*: -B

parameters for HWA3*: -less

thesize MR images instead of real segmentation of the brain structures. For the above reason, some tissue of other structures, such as meningeal membranes, is also included in the ground truth for the skull stripping evaluation if all the white and gray matter in the digital phantoms is considered as brain parenchyma. Therefore, a method with sensitivity close to 1 in this database means that there are many false positives in the segmentation. These are the cases of the methods shown in Table 3.3 which have a high sensitivity but a low specificity, such as the HWA.

Figure 3.5 is provided by the SVE website and shows the projections of FN and FP of the best result obtained by each method for the SVE database (methods marked with an * in Table 3.5). In the same way as with the other databases, the HWA has the lowest specificity with, a high number of FP (Fig. 3.5(b)). Conversely, the HWA has the highest sensitivity, with very few FN (Fig. 3.5(a)). It has the worst overall performance (Jaccard and Dice in Table 3.5). The best performance is obtained by our method (Figs. 3.5(g) and 3.5(h)).

An analysis of variance (ANOVA) and post-hoc comparisons were used to verify the statistical significance ($p < 0.05$) of the differences among the results (Jaccard and Dice) of our method and those of others. The Games-Howell method, that assumes that population variances may be different, was used for the post-hoc comparisons. Using the union of the results obtained in the IBSR and BrainWeb databases for comparison, our method exhibits a statistically significant difference with respect to the others. Also, the difference is statistically

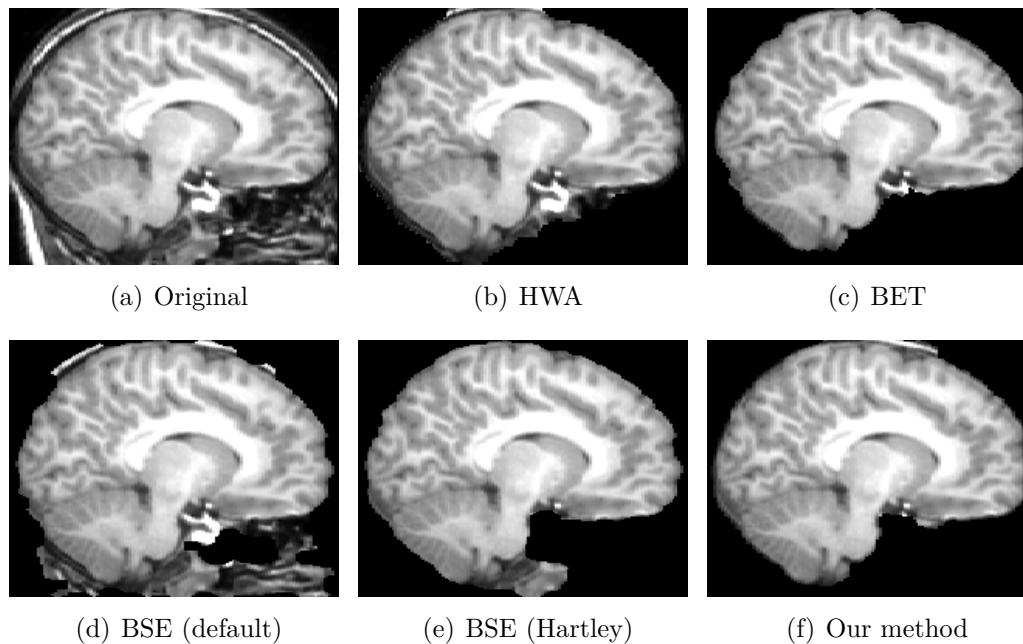


Figure 3.3: Comparison among different automated segmentations of an image from the IBSR database (a). The indices obtained with the full set of images are shown in Table 3.4. The BSE method has the lowest specificity when the default parameters are used (d). The HWA (b) also has a low specificity but its sensitivity is better, obtaining better overall performance (Table 3.4). Although the performance of BSE rises considerably when Hartley’s parameters are used (e), does not exceed the BET performance (c). Nevertheless, our method (f) has better performance than BET.

significant if the segmentation results in the IBSR and BrainWeb databases are used together with the results obtained with the default parameters in the SVE database. The difference is not statistically significant with only the BSEv0.8b* method if all the results for the SVE database are taken into account.

We compared the results of our method to those of recent methods in the literature that use the same publicly available databases:

- In [Park 2009], a region growing algorithm is presented, which obtains apparently better overall results than our method in the IBSR database: Jaccard index (J)=0.915 and Dice coefficient (κ)=0.955. Besides, its False Negative Rate ($FNR = FN/(TP + FN + FP)$) is 0.0620 and False Positive Rate ($FPR = FP/(TP + FN + FP)$) is 0.0229. The FNR and FPR of our method in the IBSR is 0.0079 and 0.087 respectively. Therefore, this method has more FN and less FP than our method. The mentioned differ-

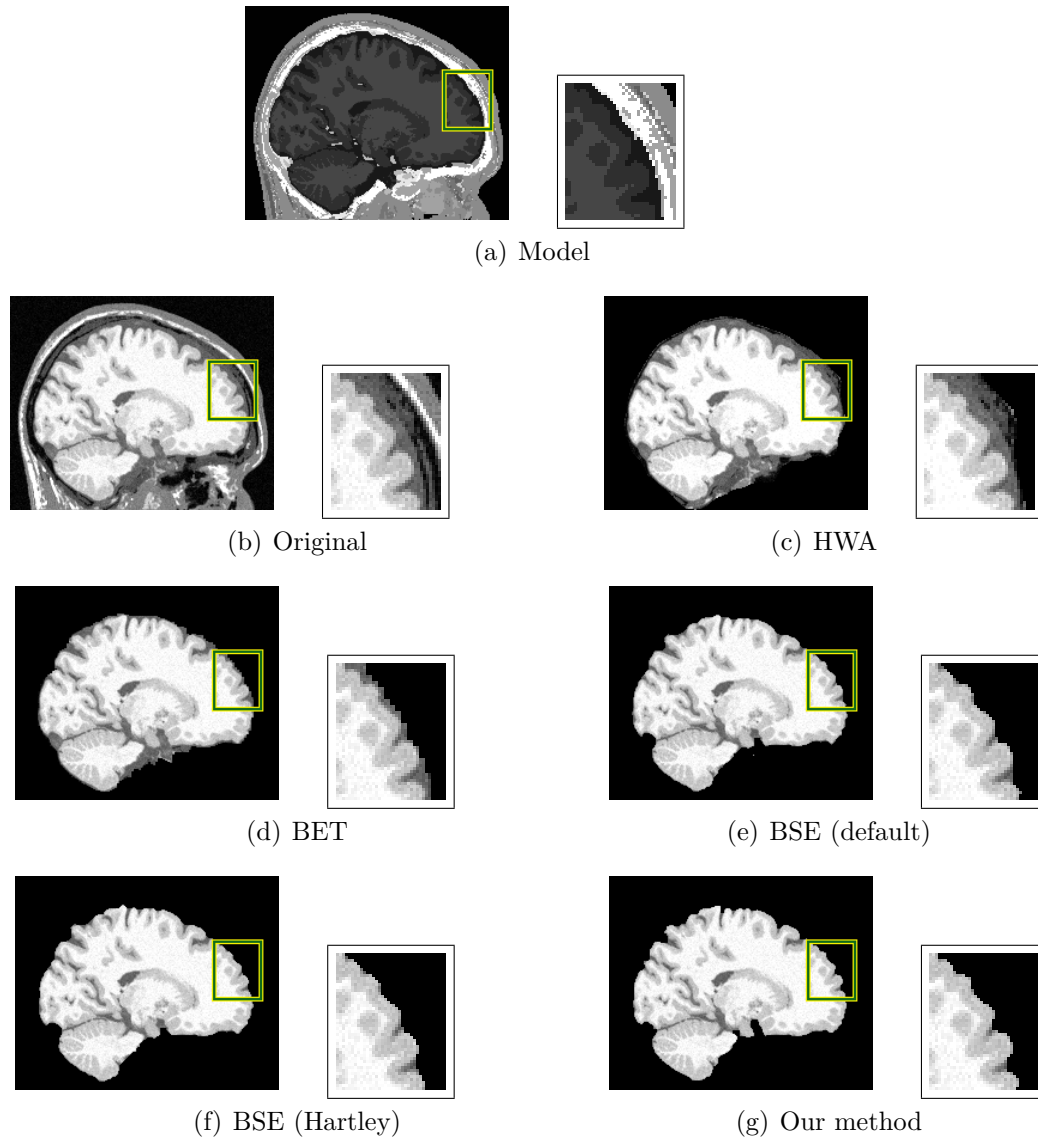


Figure 3.4: Comparison among different automated segmentations of an image from the Brain-Web database (b). The indices obtained with the full set of images are shown in Table 3.3. (a) Shows the digital phantom of the image with a marked zoom rectangular area. This phantom was used to obtain the ground truth segmentation. It can be seen that the HWA (c) is the method that remove less non-brain tissue, mainly CSF. For this reason the HWA has the lowest specificity among the methods (Table 3.3). The HWA has the highest sensitivity, because most of the brain tissue is included in the segmentation. Nevertheless, its overall performance (Jaccard and Dice) is lower than that of the other methods. The best performance was obtained by our method (g), which also has the highest specificity, followed by the BSE using Hartley's parameters.

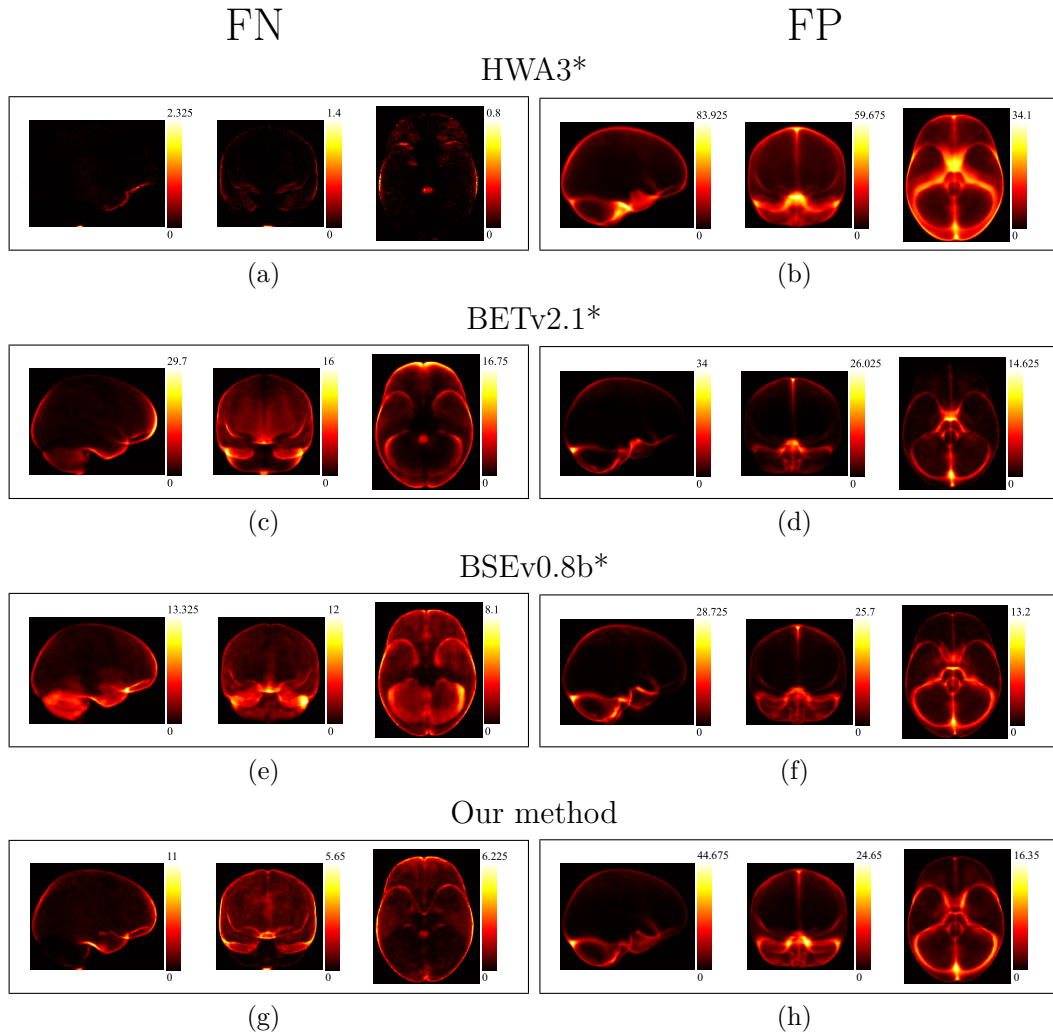


Figure 3.5: Projections of the FN (left) and FP (right) provided by the SVE website [Shattuck 2009]. The FN and FP projections of the different methods best segmentation results are shown (see Table 3.5). The methods shown in this figure are: HWA3*, BSEv0.8b*, BETv2.1*, and our method. The color scale represents the sum of the FN or FP along the direction orthogonal to the figure plane.

ence in the indices could be relativized to some extent because, as stated by many authors, it is more important to preserve the brain tissue than removing all the CSF.

- Another method that also uses the IBSR database is the Graph Cuts Skull Stripping (GCUT) presented in [Sadananthan 2010], which obtains: $J=0.84$ and $\kappa=0.91$.
- The Robust, Learning-Based Brain Extraction system (ROBEX) introduced in [Iglesias 2011] is evaluated using the SVE. The indices obtained by ROBEX are: $\kappa=96.6$, Sensitivity=95.6, Specificity=97.7.

Compared to the above mentioned methods, our method provides an accurate segmentation without removing brain tissue. On the other hand, there are methods with a higher performance than that of our method:

- The Brain Extraction based on nonlocal Segmentation Technique (BeaST) [Eskildsen 2012] is evaluated in the SVE database, obtaining $\kappa=0.9781$. This performance is better than that of ours. Nevertheless an advantage of our method is that no templates are required.
- The Multi-Atlas Propagation and Segmentation (MAPS) [Leung 2011] is also evaluated in the SVE database, obtaining $J=0.955$. This performance is also better than that of our method, nevertheless the MAPS method requires a template library and a long computational time (19 hrs compared with 57 minutes of our method).

These methods (BeaST and MAPS) with a higher performance than that of our method are based on comparisons with template libraries and require a large amount of computation, and obviously need suitable templates for the segmentation. Besides, our method is mainly based on deformable models and only uses a simple comparison with an atlas in the pre-segmentation. There are other methods published with results on non-public databases which cannot be compared. Moreover, some authors use different performance measures such as Hausdorff distance or mean symmetric surface-to-surface distance [Iglesias 2011].

3.2.2 Skull Segmentation

Not all databases can be used to evaluate the skull segmentation, because IBSR and SVE databases provide only data of brain segmentations. The BrainWeb

database proposes ground truth segmentations of the whole head, including skull and scalp. The union of GM, WM and CSF was considered as the skull ground truth segmentation. The vessels and the dura matter were not considered because of the shape of the digital phantoms. There are many voxels marked as vessels outside the skull, and the voxels marked as dura matter form complicate shapes with the vessels. Additionally, the dura matter is an almost rigid structure, and since the goal of our segmentation is to build a model suitable for mechanical modeling, we consider that this structure can be considered as part of the rigid internal surface of the skull. Table 3.6 shows the performance of BET and our skull segmentation method. Our method achieved the best performance in all indices but the sensitivity. Figure 3.6 shows a graph of Jaccard and Dice indices along all the subjects in BrainWeb database, and Figure 3.7 shows a comparison between a skull segmentation performed by BET and our method. To verify the statistical significance ($p < 0.001$) of the difference between the results, a paired t -test has been performed upon the four indices employed.

Table 3.6: Performance Comparison among BET and our skull segmentation method using the BrainWeb database [Cocosco 1997, Aubert-Broche 2006]. The best results are shown in bold.

Method	Jaccard mean (SD)	Dice mean (SD)	Sensitivity mean (SD)	Specificity mean (SD)
BET2.1	0.935 (0.016)	0.966 (0.009)	0.991 (0.003)	0.988 (0.004)
Our method	0.945 (0.015)	0.972 (0.008)	0.983 (0.008)	0.992 (0.003)

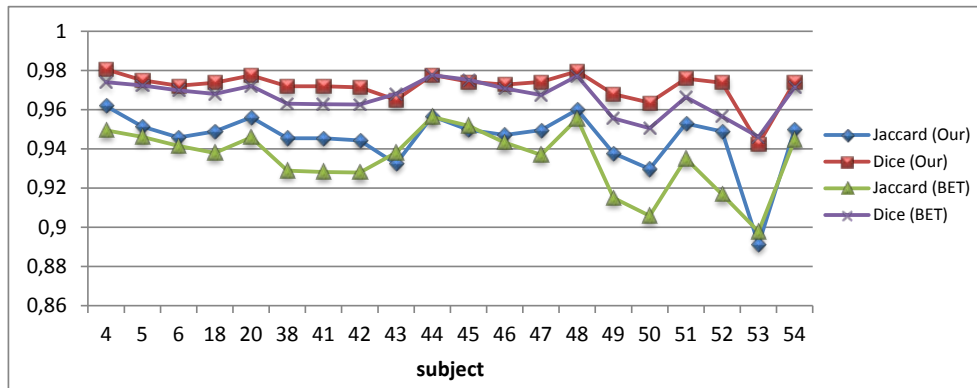


Figure 3.6: Graph of Jaccard and Dice indices of the Skull segmentation along all the subjects in the BrainWeb database. The number assigned to each subject corresponds to the number assigned in the online BrainWeb database. The BET and our method are shown.

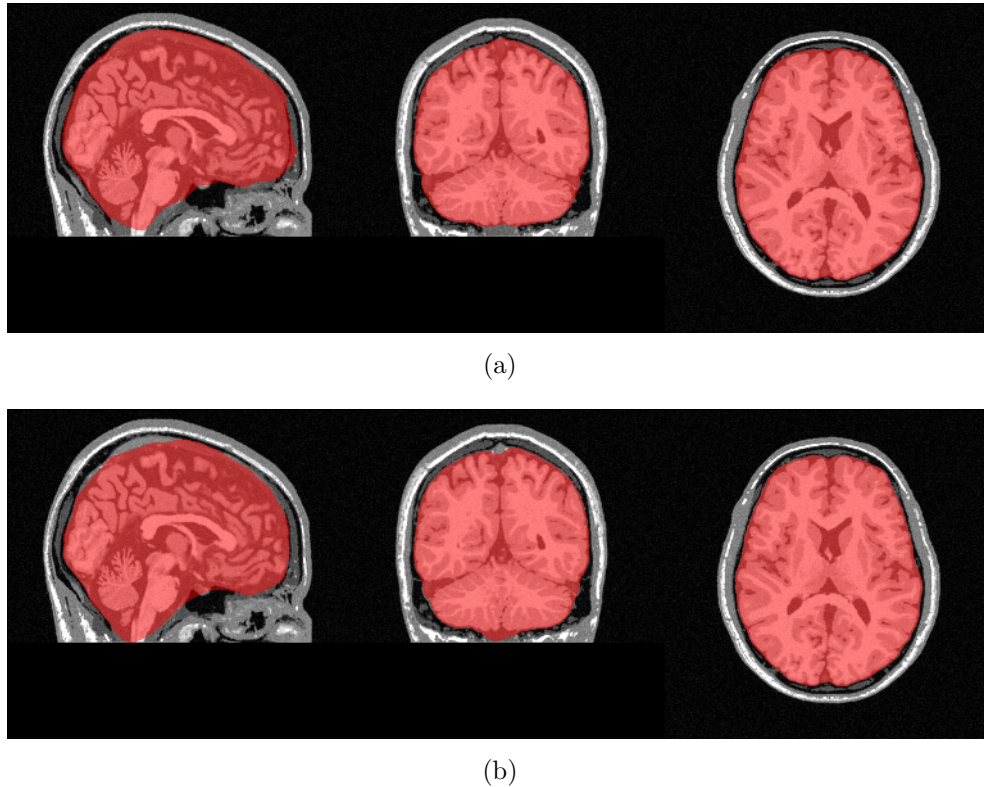


Figure 3.7: Comparison between BET (a) and our (b) skull segmentation of an image of the BrainWeb database. The segmented volume is marked in red. Our method has the best performance in all the indices except the sensitivity (see Table 3.6).

3.2.3 Ventricles Segmentation

Considering the IBSR, SVE and BrainWeb databases, only IBSR has ventricle ground truth segmentations available, as part of the manual segmentation of 84 structures in the IBSR (Fig. 3.1(e)). The structures corresponding to the ventricles in both hemispheres have been selected as ground truth. Table 3.7 shows the performance of the ventricle segmentation. Figure 3.8 shows a graph of Jaccard and Dice indices along all the subjects in IBSR database. Figure 3.9 shows an example of ventricle segmentation.

The performance of the ventricle segmentation of our method is lower than those obtained by our cortical surface and skull segmentation, due to its low sensitivity. The low sensitivity reflects the occurrence of false negatives. This false negatives occur because the ventricle mesh does not have as high resolution to capture every detail of the ventricular system, and does not include all its

structures neither. For example, the ventricle mesh does not include the *cerebral aqueduct*, the *central canal* (Appx. B.5.1) or other channels that are included in the ground truth of the IBSR database. These anatomical details were not included because they are not relevant for the mechanical modeling of the brain and to avoid adding complexity to the mesh.

Table 3.7: Performance of the ventricle segmentation in the IBSR database.

Method	Jaccard mean (SD)	Dice mean (SD)	Sensitivity mean (SD)	Specificity mean (SD)
Our method	0.623 (0.065)	0.766 (0.050)	0.757 (0.062)	1.000 (0.000)

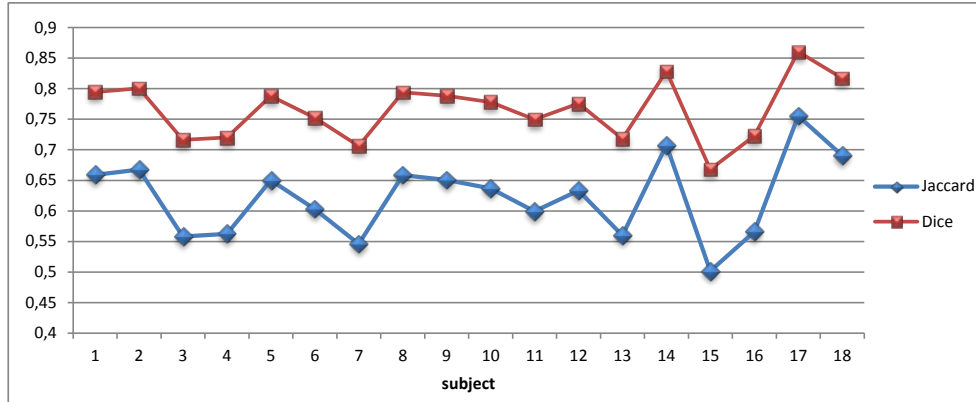


Figure 3.8: Graph of Jaccard and Dice indices of the ventricle segmentation along all the subjects in IBSR database.

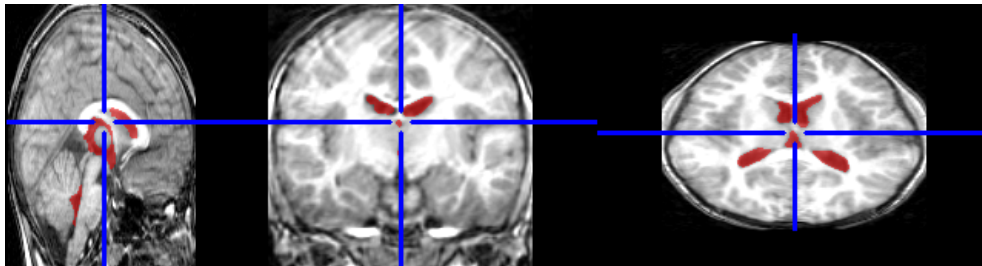


Figure 3.9: Example of a ventricle segmentation with our method in the IBSR database. The segmented volume is marked in red.

3.2.4 Tentorium Cerebelli and Falx Cerebri Segmentation

As explained in section 3.1.2, the distance between the estimated position of the membranes in the ground truth segmentations of the IBSR database, and the membrane meshes after deformation has been used to evaluate the segmentation of tentorium cerebelli and falx cerebri. Table 3.8 shows the mean distance (Eq. 3.7) achieved by the segmentations, and the graph in Figure 3.10 shows the distances along all subjects in the database. Figure 3.11 shows an example of deformed meshes colored according to their distance to the ground truth. The falx mesh obtained better performance in all segmentations, probably because the contrast in the interface between the cerebral hemispheres is usually larger than between the brain and cerebellum.

Table 3.8: Performance of the tentorium cerebelli and falx cerebri segmentations in the IBSR database.

Structure	Weighted Mean Distance (SD) (Eq. 3.7) [mm]
Tentorium Cerebelli	1.673 (0.758)
Falx Cerebri	0.745 (0.229)

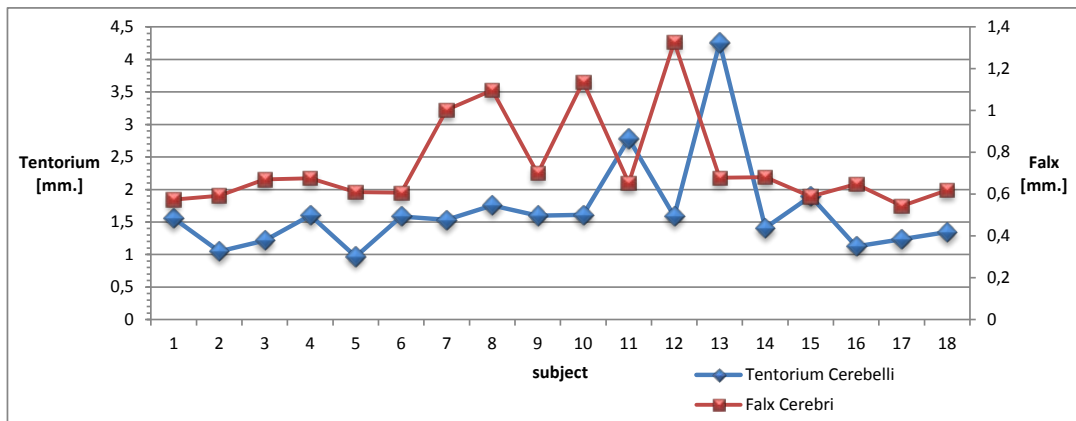


Figure 3.10: Graph of the weighted mean distances between all ground truth segmentations in the IBSR and both open meshes: falx cerebri and tentorium cerebelli.

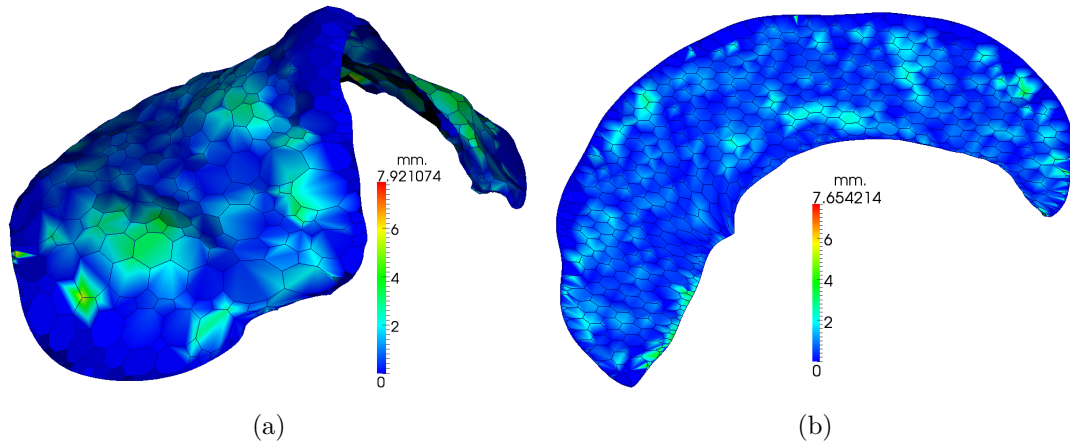


Figure 3.11: Meshes of the internal membranes of the brain colored according to their distance to the ground truth. (a) Tentorium cerebelli mesh. (b) Falx cerebri mesh.

Discussion and Conclusions

Contents

4.1 Discussion	121
4.2 Conclusion and Prospects	125
4.3 Publications	126

The aim of this work was to obtain an automated method to create a patient-specific anatomical model suitable for mechanical simulation. The particular motivation for the mechanical modeling was to simulate the brain shift phenomenon in future developments. The simulation of the brain shift can be used to update preoperative images, making them suitable for their use in the operating room (sec. 1.2.2).

The result of my work is an automated method that segments the relevant structures for the mechanical modeling of the brain. Particularly, the internal membranes of the brain were included. These structures are taken into account in very few publications, however it has been stated that they play a major (if not indispensable) role in the mechanical behavior of the brain. Moreover, they are usually segmented manually, or semi-manually in the best of cases. Our method was evaluated with the most common online databases, obtaining most of the time the best results.

In the future, we hope to improve the model including other characteristics relevant for the mechanical modeling, such as the anisotropy of the brain tissue, and the modeling of tissue cutting or extraction. Finally, we expect to obtain real images of the brain shift in the surgery to implement and assess a method for mechanical modeling which will include our anatomical model.

The conclusions and discussions of this thesis are presented in the next sections.

4.1 Discussion

A method to build a patient specific anatomical model of the brain has been proposed in this thesis. The method takes into account the main brain structures that play a role on the mechanical behavior of the brain: brain parenchyma, skull internal surface, ventricles, falx cerebri and tentorium cerebelli. The method is based on a generic model built from digital phantoms to generate synthetic MRI, which is next deformed to segment the specific anatomy of the patient. The patient's anatomy information is obtained from T_1 -weighted MRI images. This imaging modality is the most used in neurosurgery, as it provides high quality anatomical images of brain soft tissues.

Preoperative images are often used by the surgeon to plan the surgery, as well as a guide in the operating room. These images need to be registered with the position of the patient in the operating room in order to be employed as a reliable reference. Although a good initial registration may be obtained by rigid transformations, the brain is deformed during the surgery in a process called *brain shift* and, as a consequence, the registration loses validity. At this point, preoperative data becomes useless in the operating room, and the surgeon can only count on his experience. The motivation to build a mechanical model of the brain is that it can help to predict the brain deformation and then update the registration between the preoperative image and the position of the patient. This is important because of a realistic updated feedback is very useful for the surgeon during the surgery, reducing operation time and improving chances of success.

To build a mechanical model of the brain, a patient-specific anatomical model must be first obtained. In the literature, most of these anatomical models are obtained by manual segmentation, or using a mix of semi-manual methods, which in both case, is very time consuming and not routinely applicable. On the other hand, the internal membranes of the brain are usually not taken into account; and when considered, they are obtained using a manual segmentation [Dumpuri 2010, Garg 2010]. The method presented in this work is automatic and takes into account the internal structures: ventricles and membranes. Each anatomical structure is independently segmented. However, the segmentation follows a logical order, such that successive structure segmentations are guided by the position of the preceding ones. This segmentation scheme provides flexibility to the method. Even, a particular structure could be segmented by another method, and next be incorporated into the segmentation chain. Or conversely, one part of the segmentation can be used in other applications, for example, as

was explained in section 1.2.4.1, the surface cortex segmentation can be used as an excellent *Skull Stripping* method. Finally, all the specific structure segmentations are joined in a final segmentation of the whole brain anatomy.

On the Segmentation Method. The proposed segmentation method is based on a preliminary pre-segmentation, and specific segmentations of each structure by deformable models. The pre-segmentation (sec. 2.3.1) employs thresholds and morphological operators; it is based on previous work but incorporates new estimations of the optimal thresholds, based on comparisons with a brain atlas. Thus, this pre-segmentation makes it possible to find an optimal initialization for the deformable models, providing robustness to the segmentation. Moreover, a statistical model of the tissue gray level is obtained in the pre-segmentation stage and then used to drive the segmentation by deformable models.

- The cortical surface is the first structure to be segmented (sec. 2.3.4). The deformation of the cortex mesh combines 3 steps which make it possible: 1) to use the pre-segmentation to find the optimal starting point for the deformation; 2) to recover brain tissue missed in the pre-segmentation; and 3) to decrease the amount of CSF and sub-arachnoid space in the segmentation. The result of these steps is an accurate segmentation that minimizes the amount of non-brain tissue, without missing brain parenchyma.
- The internal surface of the skull is the second structure to be segmented (sec. 2.3.5). The deformation of the skull mesh is guided by the image gray levels, the statistical model built in the pre-segmentation, and the cortex mesh.
- The last closed mesh to be deformed is the ventricle mesh (sec. 2.3.6).
- Then, the open meshes, which correspond to the internal membranes of the brain, are segmented (sec. 2.3.7). The deformation of the tentorium cerebelli mesh (sec. 2.3.7.1) is guided by the image gray levels and the skull mesh, because the tentorium cerebelli is attached to the skull (Appx. B.4.1). Next, the falx cerebri mesh is deformed (sec. 2.3.7.2) using the skull and tentorium cerebelli meshes. The falx cerebri is attached to the skull and tentorium cerebelli; therefore, its deformation must be consistent with them.

On the Use of Simplex Meshes. Simplex meshes are a good option to implement deformable models; nevertheless, meshes of triangles are better for other tasks such as computing intersections, rendering or computing distances to the surface of the mesh. In our case, the intersections between the meshes must be computed before joining them. And computing intersections between triangulations is easier than with simplex meshes. Therefore, the simplex meshes used in the segmentation are transformed into their dual triangulations before joining them to form the final mesh representing the whole brain anatomy.

In order to cause minimal geometry degradation when simplex and triangle meshes are commuted one to another, a new method of transformation was developed (sec. 2.2). Our transformation method is straightforward and does not use iterations. This is achieved by applying an interpolation of the initial mesh to find the corresponding vertices of the dual mesh. The interpolation is based on a direct and local minimization of the distance to tangent planes, and points of each face.

In section 2.2.4, our mesh transformation technique was compared to the most frequently used method, which is based on placing the dual vertices at the center of mass of the initial faces, and the weaknesses of this latter method have been illustrated. The performance of the proposed transformation method was measured using a vertex-to-vertex distance between both triangulations and simplex meshes, after performing a set successive transformations between both representations. Moreover, we measured the Hausdorff distance between meshes after performing a cycle of transformations, i.e., after carrying out a transformation to simplex mesh and back to triangulation. The performance of our method was satisfactory, providing a significant reduction in the error of nearly 50% compared with the conventional method. Thus, our method has proven to be adequate to be used in any application requiring topological mesh transformation while preserving geometry, and without increasing complexity.

On Validating the Method. The segmentation method has been assessed using international MRI databases available online: the BrainWeb, the Internet Brain Segmentation Repository (IBSR), and the Segmentation Validation Engine (SVE). The segmentation of each structure has been evaluated independently. The performance of the segmentations by closed meshes has been measured by using the Jaccard Index (J) and Dice Coefficient (κ). The performance of the segmentations of open meshes has been evaluated by measuring the distance

between the deformed mesh and the estimated position of the structure in the ground truth.

- In order to evaluate the cortical surface segmentation, our method has been compared to three of the most popular *Skull Stripping* methods in the literature: the Brain Extraction Tool (BET), the Brain Surface Extractor (BSE), and the Hybrid Watershed Algorithm (HWA). Our method achieved the best performance and the difference was statistically significant ($p < 0.05$): $J=0.904$ and $\kappa=0.950$, for BrainWeb; $J=0.905$ and $\kappa=0.950$ for IBSR; $J=0.946$ and $\kappa=0.972$ for SVE. The obtained segmentations were accurate for all databases, with low performance variance. Also our results were compared to those of recent methods in the literature that use the same publicly available databases. Our method achieved better results than most of the others. The methods that achieved better results than ours require a larger amount of computation and templates libraries of segmented images.
- The performance of the skull internal surface segmentation was compared to BET v2.1. To evaluate the skull segmentation, the BrainWeb database was used because it is the only one with a ground truth including the skull. Our method achieved the best performance and the difference was statistically significant ($p < 0.05$): $J=0.945$ and $\kappa=0.972$.
- The ventricle segmentation was evaluated using the IBSR because the ground truth of this database includes the ventricles. The performance of our method was: $J=0.623$ and $\kappa=0.766$. The performance of this segmentation was lower than those obtained with the cortex and skull meshes due to the low sensitivity achieved. The low sensitivity is because the ventricle mesh does not have as high resolution to capture every detail of the ventricular system, and does not include all its structures neither. The structures and details that were not included are not relevant for mechanical modeling. Their inclusion only adds unnecessary complexity to the mesh, and were purposely excluded.
- The performance of membrane segmentations was evaluated using the IBSR because the ground truth of this database incorporates the segmentation of many structures in both hemispheres, allowing to estimate the position of the membranes. The mean distance measured for the tentorium cerebelli mesh was 1.673 mm, and for the falx cerebri mesh it was of 0.745 mm.

Therefore, our method provides a mesh-based anatomical model suitable for use in a 3D meshing method to obtain tetrahedral, hexahedral or other 3D volumetric mesh. This volumetric mesh can then be used in mechanical modeling.

4.2 Conclusion and Prospects

In this section, the relative weaknesses and possible improvements of the method are considered.

The union of triangle meshes is a part of the method that must be carefully addressed. When the meshes of different structures are joined, the remeshing may create triangles with irregular shapes in the intersection zone. If a volumetric tetrahedral mesh for mechanical modeling is built using this final triangle mesh, the irregular triangles can induce the construction of degenerated tetrahedra by the volumetric meshing algorithm. To solve this problem, the remeshing algorithm can be modified to ensure the quality of the new triangles. Another solution is to use a method to repair the mesh after performing the fusion of the different meshes. In a similar way, a method to improve the quality of the tetrahedral mesh and reduce the number of volumetric elements can be used. However, a better solution is to use only simplex meshes through the whole process. We expect to develop a method to compute intersections between simplex meshes in a simple way, avoiding the conversion into triangulations in this task. Additionally, the use of volumetric simplex meshes could be studied. The 3-simplex meshes are volumetric meshes formed by vertices with four neighbors, and their duals are the tetrahedral meshes. Therefore, an alternative is to use a 3-simplex mesh associated with a tetrahedral mesh; or to develop a method to directly incorporate simplex meshes in the Finite Element or Finite Volume method, or any other method for mechanical modeling.

Our anatomical model does not include information about the orientation of the tissue. If no orientation information is provided, it can be assumed that the tissue is an isotropic material. Nevertheless, it has been argued in the literature that brain tissue is anisotropic [Ferrant 2002, Warfield 2002], especially the white matter [Skrinjar 2002]. However, only a few works have addressed the problem [Prange 2002], usually using diffusion tensor MRI (DT-MRI) images to incorporate the anisotropy into a mechanical model [West 2002, Kemper 2003]. The proposed method should incorporate the tissue anisotropy in the future. As mentioned above, DT-MRI images may provide information about the preferred

direction of the fibers in each voxel. Even a representation of the fiber tracts or *tractography* can be obtained using DT-MRI.

Another improvement to be carried out in the future is the segmentation and incorporation of tumors. A large number of brain surgeries are performed to extract tumors. These tumors have particular mechanical properties, and therefore must be incorporated in the model [Dumpuri 2007, Wittek 2007, Joldes 2009], preferably by using an automated segmentation. The incorporation of intra-surgical information is also important. This information can be acquired, for example, by using spatial localized US [Pennec 2001], laser-range scanner [Sinha 2005] or stereopsis [Sun 2005].

To use the present method into a proper surgery simulation protocol, a way to simulate craniotomy, tissue extraction [Bailet 2011] and retraction [Vigneron 2009] would be very useful. Using an intraoperative method of simulation, the model could be updated during surgery to take into account the tissue manipulation. All the surgery could be simulated before performing it, to prevent errors and anticipate problems.

It is important to note that, although the method presented in this thesis was developed thinking in the brain shift problem, the proposed anatomical brain model can be used for other types of simulations as well. For example, mechanical impacts in the head [Horgan 2003, Belingardi 2005], or hydrocephalus [Dutta-Roy 2008].

The anatomical model obtained in the frame of this work has been used for modeling the interaction fluid(CSF)/structure(parenchyma) in [Araya 2007]. However, our model should be also tested using other methods of mechanical modeling. The anatomical model can be used to build a mechanical model by utilizing the Finite Element method or other methods for deformation and mechanical modeling, such as the Finite Volume method or mass-spring models.

4.3 Publications

The following publications resulted from the work of this thesis:

- Rodolfo Araya, Gabriel R. Barrenechea, **Francisco J. Galdames**, Fabrice Jaillet and Rodolfo Rodríguez. *Adaptive mesh and finite element analysis of coupled fluid/structure: application to brain deformations*. In Third International Conference SURGETICA 2007: Gestes médico-chirurgicaux assistés par ordinateur: outils et applications, pages 117–121, Chambéry, France, 19-20-21 September 2007.

-
- **Francisco J. Galdames**, Fabrice Jaillet. *From Triangulation to Simplex Mesh, and Vice-Versa, a Simple and Efficient Conversion*. In International Conference on Computer Graphics Theory and Applications - VISIGRAPP-GRAPP 2012, pages 151–156, Rome, Italy, 24-25-26 February 2012.
 - **Francisco J. Galdames**, Fabrice Jaillet, Claudio A. Perez. *An Accurate Skull Stripping Method Based on Simplex Meshes and Histogram Analysis for Magnetic Resonance Images*. *Journal of Neuroscience Methods*, vol. 206, no. 2, pages 103–119, May 2012.

Another publication which includes the whole process of construction and adaptation of the anatomical model is in perspective.

Bibliography

- [AccessExcell 2012] Access excellence® website.
http://www.accessexcellence.org/AE/AEC/CC/historical_background.php,
viewed in March 2012. 2012.
- [Acosta-Cabronero 2008] Julio Acosta-Cabronero, Guy B. Williams, João M. S. Pereira, George Pengas and Peter J. Nestor. *The impact of skull-stripping and radio-frequency bias correction on grey-matter segmentation for voxel-based morphometry*. NeuroImage, vol. 39, no. 4, pages 1654–1665, 2008.
- [AIM@SHAPE] AIM@SHAPE shape repository. <http://shapes.aim-at-shape.net/>, viewed in March 2012.
- [Akahn 2001] Z. Akahn, C. E. Acar and N. G. Gencer. *Development of realistic head models for electromagnetic source imaging of the human brain*. In 23rd Annual International Conference of the IEEE Engineering in Medicine and Biology Society, volume 1, pages 899–902, Istanbul, Turkey, 25-28 October 2001.
- [Akselrod-Ballin 2007] Ayelet Akselrod-Ballin, Meirav Galun, John Moshe Gomeri, Achi Brandt and Ronen Basri. *Prior knowledge driven multiscale segmentation of brain MRI*. In 10th International Conference on Medical Image Computing and Computer-Assisted Intervention (MICCAI), volume 4792 of *Lecture Notes in Computer Science*, pages 118–126, Brisbane, Australia, October 29 - November 2 2007.
- [Araya 2007] R. Araya, G. R. Barrenechea, F. J. Galdames, F. Jaillet and R. Rodríguez. *Adaptive mesh and finite element analysis of coupled fluid/structure: application to brain deformations*. In Third International Conference SURGETICA 2007: Gestes médico-chirurgicaux assistés par ordinateur: outils et applications, pages 117–121, Chambéry, France, 19-20-21 September 2007.
- [Ashburner 2000] John Ashburner and Karl J. Friston. *Voxel-Based Morphometry-The Methods*. NeuroImage, vol. 11, no. 6, pages 805–821, 2000.

- [Atkins 1998] M. Stella Atkins and Blair T. Mackiewicz. *Fully automatic segmentation of the brain in MRI*. IEEE Transactions on Medical Imaging, vol. 17, no. 1, pages 98–107, February 1998.
- [Atuegwu 2008] N. C. Atuegwu and R. L. Galloway. *Volumetric characterization of the Aurora magnetic tracker system for image-guided transorbital endoscopic procedures*. Physics in Medicine and Biology, vol. 53, no. 16, pages 4355–4368, Aug 2008.
- [Aubert-Broche 2006] Berengere Aubert-Broche, Alan C. Evans and Louis Collins. *A new improved version of the realistic digital brain phantom*. NeuroImage, vol. 32, no. 1, pages 138–145, Jun 2006.
- [Audette 2003a] Michel A. Audette, Hervé Delingette, Alexander Fuchs, Yoshihiko Koseki and Kiyoyuki Chinzei. *A procedure for computing patient-specific anatomical models for finite element-based surgical simulation*. In CARS 2003. Computer Assisted Radiology and Surgery. 17th Annual Conference of the International Society for Computer Aided Surgery (IS-CAS'03), volume 1256 of *International Congress Series*, London, UK, 25-28 June 2003.
- [Audette 2003b] Michel A. Audette, Kaleem Siddiqi, Frank P. Ferrie and Terry M. Peters. *An integrated range-sensing, segmentation and registration framework for the characterization of intra-surgical brain deformations in image-guided surgery*. Computer Vision and Image Understanding: CVIU, vol. 82, no. 2-3, pages 226–251, February 2003.
- [Babalola 2009] Kolawole Oluwole Babalola, Brian Patenaude, Paul Aljabar, Julia Schnabel, David Kennedy, William Crum, Stephen Smith, Tim Cootes, Mark Jenkinson and Daniel Rueckert. *An evaluation of four automatic methods of segmenting the subcortical structures in the brain*. NeuroImage, vol. 47, no. 4, pages 1435–1447, 2009.
- [Bailet 2011] Mathieu Bailet. *Interactive Modeling of Brain Tumor Resection*. Technical report, Grenoble INP – ENSIMAG, TIMC-IMAG Laboratory, 2011.
- [Baillard 2001] C. Baillard, P. Hellier and C. Barillot. *Segmentation of brain 3D MR images using level sets and dense registration*. Medical Image Analysis, vol. 5, no. 3, pages 185–194, 2001.

- [Bankman 2000] Isaac N. Bankman, editor. Handbook of medical imaging: Processing and analysis. Academic Press, 2000.
- [Barnett 2005] Gene H. Barnett, Robert Maciunas and David Roberts, editors. Computer-assisted neurosurgery. Informa Healthcare, 8 November 2005.
- [Basser 1994] P. J. Basser, J. Mattiello and D. LeBihan. *MR diffusion tensor spectroscopy and imaging*. Biophysical Journal, vol. 66, no. 1, pages 259–267, January 1994.
- [Beg 2005] Mirzal Faisal Beg, Michael I. Miller, Alain Trouvé and Laurent Younes. *Computing large deformation metric mappings via geodesic flows of diffeomorphisms*. International Journal of Computer Vision, vol. 61, no. 2, pages 139–157, 2005.
- [Belardinelli 2003] P. Belardinelli, A. Mastacchi and V. Pizzella G. L. Romani. *Applying a visual segmentation algorithm to brain structures MR images*. In First International IEEE EMBS Conference on Neural Engineering, pages 507–510, Capri Island, Italy, 20-22 March 2003.
- [Belingardi 2005] Giovanni Belingardi, Giorgio Chiandussi and Ivan Gaviglio. *Development and Validation of a New Finite Element Model of Human Head*. In 19th International Technical Conference on the Enhanced Safety of Vehicles, Washington D.C, USA, 6-9 June 2005.
- [Belliveau 1991] J. W. Belliveau, D. N. Kennedy Jr., R. C. McKinstry, B. R. Buchbinder, R. M. Weisskoff, M. S. Cohen, J. M. Vevea, T. J. Brady and B. R. Rosen. *Functional mapping of the human visual cortex by magnetic resonance imaging*. Science, vol. 254, no. 5, November 1991.
- [Benveniste 2005] Ronald J. Benveniste and Isabelle M. Germano. *Correlation of factors predicting intraoperative brain shift with successful resection of malignant brain tumors using image-guided techniques*. Surgical Neurology, vol. 63, pages 542–549, 2005.
- [Bertelsen 2010] Álvaro Bertelsen, Arrate Muñoz-Barrutia, Sonia Tejada, Carlos Ortiz de Solórzano and Diego Borro. *Segmentation of the Skull from MR T1 Images Using Label Fusion*. In 32nd Annual International Conference of the IEEE EMBS, pages 3121–3124, Buenos Aires, Argentina, 31 August - 4 September 2010.

- [Biot 1941] Maurice A. Biot. *General theory of three-dimensional consolidation*. Journal of Applied Physics, vol. 12, no. 2, pages 155–164, 1941.
- [Boesen 2004] Kristi Boesen, Kelly Rehm, Kirt Schaper, Sarah Stoltzner, Roger Woods, Eileen Lüders and David Rottenberg. *Quantitative comparison of four brain extraction algorithms*. NeuroImage, vol. 22, no. 3, pages 1255–1261, July 2004.
- [Böttger 2007] Thomas Böttger, Tobias Kunert, Hans P. Meinzer and Ivo Wolf. *Application of a New Segmentation Tool Based on Interactive Simplex Meshes to Cardiac Images and Pulmonary MRI Data*. Academic Radiology, vol. 14, no. 3, pages 319–329, March 2007.
- [BrainSuite] BrainSuite. Laboratory of Neuro Imaging (LONI), UCLA, USA, <http://www.loni.ucla.edu/Software/BrainSuite>, viewed in March 2012. March, 2012.
- [Buchholz 1997] Richard D. Buchholz, David D. Yeh, Jason Trobaugh, Leslie L. McDurmont, Christopher D. Sturm, Carol Baumann, Jaimie M. Henderson, Ari Levy and Paul Kessman. *The correction of stereotactic inaccuracy caused by brain shift using an intraoperative ultrasound device*. In CVRMed-MRCAS'97, Lecture notes in computer science, volume 1205, pages 459–466, Grenoble, France, 19-22 March 1997.
- [Carass 2011] Aaron Carass, Jennifer Cuzzocreo, M. Bryan Wheeler, Pierre-Louis Bazin, Susan M. Resnick and Jerry L. Prince. *Simple paradigm for extra-cerebral tissue removal: Algorithm and analysis*. NeuroImage, vol. 56, no. 4, pages 1982–1992, 2011.
- [Center for Morphometric Analysis 1995] Center for Morphometric Analysis. Massachusetts General Hospital, The Internet Brain Segmentation Repository (IBSR). <http://www.cma.mgh.harvard.edu/ibsr/>, viewed in March 2012). 1995.
- [Chen 2011] Ishita Chen, Aaron M. Coffey, Siyi Ding, Prashanth Dumpuri, Benoit M. Dawant, Reid C. Thompson and Michael I. Miga. *Intraoperative Brain Shift Compensation: Accounting for Dural Septa*. IEEE Transactions on Biomedical Engineering, vol. 58, no. 3, pages 499–508, 2011.

- [Chiverton 2007] John Chiverton, Kevin Wells, Emma Lewis, Chao Chen, Barbara Podda and Declan Johnson. *Statistical morphological skull stripping of adult and infant MRI data*. Computers in Biology and Medicine, vol. 37, pages 342–357, 2007.
- [Cignoni 1998] P. Cignoni, C. Rocchini and R. Scopigno. *Metro: Measuring error on simplified surfaces*. Computer Graphics Forum, vol. 17, no. 2, pages 167–174, June 1998.
- [Cinquin 2011] P. Cinquin. *How today's robots work and perspectives for the future*. Journal of Visceral Surgery, vol. 148, no. 5, pages e12–e18, 2011.
- [Ciofolo 2005] Cybèle Ciofolo and Christian Barillot. *Brain segmentation with competitive level sets and fuzzy control*. In 19th Conference on Information Processing in Medical Imaging, volume 3565 LNCS, pages 333–344, Glenwood Springs, CO, USA, 10-15 July 2005.
- [Clatz 2003] Olivier Clatz, Hervé Delingette, Eric Bardinet, Didier Dormont and Nicholas Ayache. *Patient specific biomechanical model of the brain: application to Parkinson's disease procedure*. In Proceedings of the 2003 international conference on Surgery simulation and soft tissue modeling, volume 2673 of Lecture Notes in Computer Science, pages 321–331, Juan-les-Pins, France, 12-13 June 2003.
- [Clatz 2005] Olivier Clatz, Hervé Delingette, Ion-Florin Talos, Alexandra J. Golby, Ron Kikinis, Ferenc A. Jolesz, Nicholas Ayache and Simon K. Warfield. *Robust Nonrigid Registration to Capture Brain Shift From Intra-operative MRI*. IEEE Transactions on Medical Imaging, vol. 24, no. 11, pages 1417–1427, November 2005.
- [Cocosco 1997] Chris A. Cocosco, Vasken Kollokian, Remi K.-S. Kwan and Alan C. Evans. *Brainweb: Online interface to a 3D MRI simulated brain database*. NeuroImage, vol. 5, no. 4, 19-23 May 1997. part 2/4 – Proceedings of 3rd International Conference on Functional Mapping of the Human Brain, Copenhagen, Denmark, S425.
- [Collins 1995] D. Louis Collins, C. J. Holmes, T. M. Peters and A. C. Evans. *Automatic 3-D model-based neuroanatomical segmentation*. Human Brain Mapping, vol. 3, no. 3, pages 190–208, 1995.

- [Conforto 1996] Silvia Conforto, Stefania Della Penna and Sergio Nicola Erne'. *Tissue segmentation of MRI of the head by means of a Kohonen map*. In 18th Annual International Conference of the IEEE Engineering in Medicine and Biology Society, pages 1087–1088, Amsterdam, The Netherlands, 31 October-3 November 1996.
- [Cooper 1995] D. H. Cooper, T. F. Cootes, C. J. Taylor and J. Graham. *Active shape models – their training and application*. *Computer Vision and Image Understanding : CVIU*, vol. 61, pages 38–59, 1995.
- [Coupé 2011] Pierrick Coupé, José V. Manjón, Vladimir Fonov, Jens Pruessner, Montserrat Robles and D. Louis Collins. *Patch-based segmentation using expert priors: Application to hippocampus and ventricle segmentation*. *NeuroImage*, vol. 54, no. 2, pages 940–954, 2011.
- [Cox 1996] Robert W. Cox. *AFNI: software for analysis and visualization of functional magnetic resonance neuroimages*. *Computers and Biomedical Research*, vol. 29, no. 3, pages 162–173, June 1996.
- [Cremers 2002] Daniel Cremers. *Statistical Shape Knowledge in Variational Image Segmentation*. PhD thesis, Universität Mannheim, 2002.
- [Cyberware] Cyberware, Inc. <http://www.cyberware.com/>, viewed in March 2012.
- [Dale 1999] Anders M. Dale, Bruce Fischl and Martin I. Sereno. *Cortical surface-based analysis: I. Segmentation and surface reconstruction*. *Neuroimage*, vol. 9, no. 2, pages 179–194, Feb 1999.
- [Daliri 2010] M. Daliri, H. Abrishami Moghaddam, S. Ghadimi, M. Momeni, F. Harirchi and M. Giti. *Skull Segmentation in 3D Neonatal MRI using Hybrid Hopfield Neural Network*. In 32nd Annual International Conference of the IEEE EMBS, pages 4060–4063, Buenos Aires, Argentina, 31 August - 4 September 2010.
- [Davatzikos 2001] Christos Davatzikos, Dinggang Shen, Ashraf Mohamed and Stelios K. Kyriacou. *A Framework for Predictive Modeling of Anatomical Deformations*. *IEEE Transactions on Medical Imaging*, vol. 20, no. 8, pages 836–843, 2001.

- [daVinciSurgi] da Vinci Surgical System. <http://www.davincisurgery.com/davincisurgery>, viewed in March 2012.
- [Davis 2006] G. B. Davis, M. Kohandel, S. Sivaloganathan and G. Tenti. *The constitutive properties of the brain paraenchyma, Part 2. Fractional derivative approach*. Medical Engineering & Physics, vol. 28, no. 5, pages 455–459, 2006.
- [de Boer 2010] Renske de Boer, Henri A. Vrooman, M. Arfan Ikram, Meike W. Vernooij, Monique M. B. Breteler, Aad van der Lugt and Wiro J. Niessen. *Accuracy and reproducibility study of automatic MRI brain tissue segmentation methods*. NeuroImage, vol. 51, no. 3, pages 1047–1056, 2010.
- [de Putter 2006] S. de Putter, F. Laffargue, M. Breeuwer, F. N. van de Vosse and F. A. Gerritsen. *Computational mesh generation for vascular structures with deformable surfaces*. International Journal of Computer Assisted Radiology and Surgery, vol. 1, no. 1, pages 39–49, 2006.
- [Delingette 1994] Hervé Delingette. *Simplex meshes: A general representation for 3-D shape reconstruction*. Technical Report 2214, I.N.R.I.A., Sophia-Antipolis, France, 1994.
- [Delingette 1997] Hervé Delingette. *General Object Reconstruction based on Simplex Meshes*. Technical Report 3111, I.N.R.I.A., Sophia-Antipolis, France, 1997.
- [Delingette 1999] Hervé Delingette. *General Object Reconstruction based on Simplex Meshes*. International Journal of Computer Vision, vol. 32, no. 2, pages 111–146, August 1999.
- [den Elsen 1993] P. A. Van den Elsen, E. J. D. Pol and M. A. Viergever. *Medical image matching: A review with classification*. IEEE Engineering in Medicine and Biology Magazine, vol. 12, no. 1, pages 26–39, 1993.
- [Dice 1945] Lee R. Dice. *Measures of the Amount of Ecologic Association Between Species*. Ecology, vol. 26, no. 3, pages 297–302, July 1945.
- [Dickhaus 1997] H. Dickhaus, K. A. Ganser, A. Staubert, M. M. Bonsanto, C. R. Wirtz, V. M. Tronnier and S. Kunze. *Quantification of Brain Shift Effects by MR-Imaging*. In 19th International Conference - IEEE/EMBS, pages 491–494, Chicago, IL, USA, 30 October - 2 November 1997.

- [Dogdas 2005] Belma Dogdas, David W. Shattuck and Richard M. Leahy. *Segmentation of Skull and Scalp in 3-D Human MRI Using Mathematical Morphology*. Human Brain Mapping, vol. 26, no. 4, pages 273–285, December 2005.
- [Dumpuri 2007] Prashanth Dumpuri, Reid C. Thompson, Benoit M. Dawant, A. Cao and Michael I. Miga. *An atlas-based method to compensate for brain shift: Preliminary results*. Medical Image Analysis, vol. 11, no. 2, pages 128–145, April 2007.
- [Dumpuri 2010] Prashanth Dumpuri, Reid C. Thompson, Aize Cao, Siyi Ding, Ishita Garg, Benoit M. Dawant and Michael I. Miga. *A Fast and Efficient Method to Compensate for Brain Shift for Tumor Resection Therapies Measured Between Preoperative and Postoperative Tomograms*. IEEE Transactions on Biomedical Engineering, vol. 57, no. 6, pages 1285–1296, 2010.
- [Dutta-Roy 2008] Tonmoy Dutta-Roy, Adam Wittek and Karol Miller. *Biomechanical modelling of normal pressure hydrocephalus*. Journal of Biomechanics, vol. 41, pages 2263–2271, 2008.
- [Ecabert 2003] O. Ecabert, T. Butz, A. Nabavi and J. P. Thiran. *Brain shift correction based on a boundary element biomechanical model with different material properties*. In 6th Medical Image Computing And Computer-Assisted Intervention (MICCAI), volume 2878 of *Lecture Notes in Computer Science*, pages 41–49, Montreal, Canada, 15-18 November 2003.
- [Eskildsen 2012] Simon F. Eskildsen, Pierrick Coupé, Vladimir Fonov, José V. Manjón, Kelvin K. Leung, Nicolas Guizard, Shafik N. Wassef, Lasse Riis Østergaard, D. Louis Collins and The Alzheimer’s Disease Neuroimaging Initiative. *BEaST: Brain extraction based on nonlocal segmentation technique*. NeuroImage, vol. 59, no. 3, pages 2362–2373, February 2012.
- [Fennema-Notestine 2006] Christine Fennema-Notestine, I. Burak Ozyurt, Camellia P. Clark, Shaunna Morris, Amanda Bischoff-Grethe, Mark W. Bondi, Terry L. Jernigan, Bruce Fischl, Florent Segonne, David W. Shattuck, Richard M. Leahy, David E. Rex, Arthur W. Toga, Kelly H. Zou, Morphometry Biomedical Informatics Research Network (BIRN) and Gregory G. Brown. *Quantitative Evaluation of Automated Skull-Stripping*

- Methods Applied to Contemporary and Legacy Images: Effects of Diagnosis, Bias Correction, and Slice Location.* Human Brain Mapping, vol. 27, no. 2, pages 99–113, 2006.
- [Ferrant 2001] Matthieu Ferrant, Arya Nabavi, Benoît Macq, Ferenc A. Jolesz, Ron Kikinis and Simon K. Warfield. *Registration of 3-D Intraoperative MR Images of the Brain Using a Finite-Element Biomechanical Model.* IEEE Transactions on Medical Imaging, vol. 20, no. 12, pages 1384–1397, 2001.
- [Ferrant 2002] Matthieu Ferrant, Arya Nabavi, Benoît Macq, P.M. Black, Ferenc A. Jolesz, Ron Kikinis and Simon K. Warfield. *Serial registration of intraoperative MR images of the brain.* Medical Image Analysis, vol. 6, pages 337–359, 2002.
- [Fischl 2002] Bruce Fischl, David H. Salat, Evelina Busa, Marilyn Albert, Megan Dieterich, Christian Haselgrove, Andre van der Kouwe, Ron Killiany, David Kennedy, Shuna Klaveness, Albert Montillo, Nikos Makris, Bruce Rosen and Anders M. Dale. *Whole brain segmentation: automated labeling of neuroanatomical structures in the human brain.* Neuron, vol. 33, no. 3, pages 341–355, 2002.
- [Fischl 2004] Bruce Fischl, David H. Salat, André J.W. van der Kouwe, Nikos Makris, Florent Ségonne, Brian T. Quinn and Anders M. Dale. *Sequence-independent segmentation of magnetic resonance images.* NeuroImage, vol. 23, no. Suppl 1, pages S69–S84, 2004.
- [FMRIB] Software library of the Oxford Centre for Functional MRI of the Brain (FMRIB). University of Oxford, <http://www.fmrib.ox.ac.uk/fsl/>, viewed in March 2012.
- [Franceschini 2006] G. Franceschini, D. Bigoni, P. Regitnig and G. A. Holzapfel. *Brain tissue deforms similarly to filled elastomers and follows consolidation theory.* Journal of the Mechanics and Physics of Solids, vol. 54, pages 2592–2620, 2006.
- [FreeSurfer] FreeSurfer software package. Martinos Center for Biomedical Imaging, Harvard University, USA, <http://surfer.nmr.mgh.harvard.edu/>, viewed in March 2012.

- [Galdames 2005] Francisco J. Galdames, Claudio A. Perez, Pablo A. Estévez and Claudio M. Held. *Segmentation of Renal SPECT Images Based on Deformable Models*. In First International Conference SURGETICA 2005: Computer-Aided Medical Interventions: tools and applications, pages 89–96, Chambéry, France, 19-20-21 January 2005.
- [Galdames 2007] Francisco J. Galdames, Pablo A. Estévez Claudio A. Perez, Claudio M. Held, Fabrice Jaillet, Gabriel Lobo, Gilda Donoso and Claudia Coll. *Registration of Renal SPECT and 2.5D US Images*. In Third International Conference SURGETICA 2007: Gestes médico-chirurgicaux assistés par ordinateur: outils et applications, pages 169–175, Chambéry, France, 19-20-21 September 2007.
- [Galdames 2011] Francisco J. Galdames, Claudio A. Perez, Pablo A. Estévez, Claudio M Held, Fabrice Jaillet, Gabriel Lobo, Gilda Donoso and Claudia Coll. *Registration of renal SPECT and 2.5D US images*. Computerized Medical Imaging and Graphics, vol. 35, no. 4, pages 302–314, June 2011.
- [Galdames 2012] Francisco J. Galdames and Fabrice Jaillet. *From Triangulation to Simplex Mesh, and Vice-Versa, a Simple and Efficient Conversion*. In International Conference on Computer Graphics Theory and Applications - VISIGRAPP-GRAPP 2012, pages 151–156, Rome, Italy, 24-25-26 February 2012.
- [Garg 2010] Ishita Garg, Siyi Ding, Aaron M. Coffey, Prashanth Dumpuri, Reid C. Thompson, Benoit M. Dawant and Michael I. Miga. *Enhancement of subsurface brain shift model accuracy: a preliminary study*. In SPIE Medical Imaging 2010: Visualization, Image-Guided Procedures, and Modeling, pages 76250J–76250J–11, 2010.
- [Garland 1997] Michael Garland and Paul S. Heckbert. *Surface simplification using quadric error metrics*. In Proceedings of the 24th annual conference on Computer graphics and interactive techniques, SIGGRAPH '97, pages 209–216, Los Angeles, CA, USA, 03-08 August 1997. ACM Press/Addison-Wesley Publishing Co.
- [Gee 1993] Jim C. Gee, Martin Reivich and Ruzena Bajcsy. *Elastically Deforming a Three-Dimensional Atlas to Match Anatomical Brain Images*. Journal of Computer Assisted Tomography, vol. 17, pages 225–236, 1993.

- [Gefen 2004] Amit Gefen and Susan S. Margulies. *Are in vivo and in situ brain tissues mechanically similar?* Journal of Biomechanics, vol. 37, pages 1339–1352, 2004.
- [Gérard 2002] Olivier Gérard, Antoine Collet Billon, Jean-Michel Rouet, Marie Jacob, Maxim Fradkin and Cyril Allouche. *Efficient model-based quantification of left ventricular function in 3-D echocardiography.* IEEE Transactions on Medical Imaging, vol. 21, no. 9, pages 1059–1068, 2002.
- [Gering 2001] David T. Gering, Arya Nabavi, Ron Kikinis, Noby Hata, Lauren J. O’Donnell, W. Eric L. Grimson, Ferenc A. Jolesz, Peter M. Black and William M. Wells. *An Integrated Visualization System for Surgical Planning and Guidance Using Image Fusion and an Open MR.* Journal of Magnetic Resonance Imaging, vol. 13, pages 967–975, 2001.
- [Ghadimi 2008] S. Ghadimi, H. Abrishami-Moghaddam, K. Kazemi, R. Grebe, C. Goundry-Jouet and F. Wallois. *Segmentation of scalp and skull in neonatal MR images using probabilistic atlas and level set method.* In 30th Annual International Conference of the IEEE Engineering in Medicine and Biology Society, pages 3060–3063, Vancouver, Canada, 21-24 August 2008.
- [Gili 2007] Jaume Gili and Julio Alonso. *Introducción biofísica a la resonancia magnética en neuroimagen.* Technical report, Universidad de Barcelona, Barcelona, España, 2007.
- [Gilles 2010] Benjamin Gilles and Nadia Magnenat-Thalmann. *Musculoskeletal MRI segmentation using multi-resolution simplex meshes with medial representations.* Medical Image Analysis, vol. 14, no. 3, pages 291–302, 2010.
- [Gouttard 2007] Sylvain Gouttard, Martin Styner, Sarang Joshi, Rachel G. Smith, Heather Cody and Guido Gerig. *Subcortical structure segmentation using probabilistic atlas priors.* In Progress in Biomedical Optics and Imaging - Proceedings of SPIE 2007, volume 6512, 2007.
- [Grau 2004] V. Grau, A. U. J. Mewes, M. Alcañiz, R. Kikinis and S. K. Warfield. *Improved Watershed Transform for Medical Image Segmentation Using Prior Information.* IEEE Transactions on Medical Imaging, vol. 23, no. 4, pages 447–458, Apr 2004.

- [Gray 1918] Henry Gray. *Anatomy of the human body*. Lea & Febiger, Philadelphia, USA, 1918.
- [Hagemann 1999] A. Hagemann, K. Rohr, H. S. Stiehl, U. Spetzger and J. M. Gilsbach. *Biomechanical Modeling of the Human Head for Physically Based, Nonrigid Image Registration*. *IEEE Transactions on Medical Imaging*, vol. 18, no. 10, pages 875–884, October 1999.
- [Hagemann 2002] A. Hagemann, K. Rohr and H. S. Stiehl. *Coupling of fluid and elastic models for biomechanical simulations of brain deformations using FEM*. *Medical Image Analysis*, vol. 6, pages 375–388, 2002.
- [Hahn 2000] Horst K. Hahn and Heinz-Otto Peitgen. *The Skull Stripping Problem in MRI Solved by a Single 3D Watershed Transform*. In 3th International Conference on Medical Image Computing and Computer-Assisted Intervention (MICCAI), volume 1935 of *Lecture Notes in Computer Science*, pages 134–143, Pittsburgh, Pennsylvania, USA, 11-14 October 2000. Springer.
- [Han 2007] Xiao Han and Bruce Fischl. *Atlas renormalization for improved brain MR image segmentation across scanner platforms*. *IEEE Transactions on Medical Imaging*, vol. 26, no. 4, pages 479–486, 2007.
- [Haque. 1998] Hasnine A Haque., Toshimitsu Musha and Masayuki Nakajima. *Numerical estimation of skull and cortex boundaries from scalp geometry*. In 20th Annual International Conference of the IEEE Engineering in Medicine and Biology Society, volume 4, pages 2171–2174, Hong Kong, China, 28 October - 1 November 1998.
- [Hartkens 2003] Thomas Hartkens, Derek L. G. Hill, Andy D. Castellano-Smith, David J. Hawkes, Calvin R. Maurer Jr., Alastair J. Martin, Walter A. Hall, Haiying Liu and Charles L. Truwit. *Measurement and analysis of brain deformation during neurosurgery*. *IEEE Transactions on Medical Imaging*, vol. 22, no. 1, pages 82–92, January 2003.
- [Hartley 2006] S. W. Hartley, A. I. Scher, E. S. C. Korf, L. R. White and L. J. Launer. *Analysis and validation of automated skull stripping tools: a validation study based on 296 MR images from the Honolulu Asia aging study*. *NeuroImage*, vol. 30, no. 4, pages 1179–1186, May 2006.

- [Hastreiter 2004] Peter Hastreiter, Christof Rezk-Salama, Grzegorz Soza, Michael Bauer, Günther Greiner, Rudolf Fahlbusch, Oliver Ganslandt and Christopher Nimsky. *Strategies for brain shift evaluation*. Medical Image Analysis, vol. 8, pages 447–464, 2004.
- [Heckbert 1999] Paul S. Heckbert and Michael Garland. *Optimal triangulation and quadric-based surface simplification*. Computational Geometry: Theory and Applications, vol. 14, no. 1-3, pages 49–65, November 1999.
- [Heckemann 2006] Rolf A. Heckemann, Joseph V. Hajnal, Paul Aljabar, Daniel Rueckert and Alexander Hammers. *Automatic anatomical brain MRI segmentation combining label propagation and decision fusion*. NeuroImage, vol. 33, no. 1, pages 115–126, 2006.
- [Heiervang 2006] E. Heiervang, T. E. J. Behrens, C. E. Mackay, M. D. Robson and H. Johansen-Berg. *Between session reproducibility and between subject variability of diffusion MR and tractography measures*. NeuroImage, vol. 33, no. 5, pages 867–877, November 2006.
- [Heinonen 1997] T. Heinonen, H. Eskola, P. Dastidar, P. Laarne and J. Malmivuo. *Segmentation of T1 MR scans for reconstruction of resistive head models*. Computer Methods and Programs in Biomedicine, vol. 54, no. 3, pages 173–181, 1997.
- [Held 1997] Karsten Held, Elena Rota Kops, Bernd J. Krause, William M. Wells III, Ron Kikinis and Hans-Wilhelm Müller-Gärtner. *Markov Random Field Segmentation of Brain MR Images*. IEEE Transactions on Medical Imaging, vol. 16, no. 6, pages 878–886, 1997.
- [Hendee 2002] William R. Hendee and E. Russell Ritenour. Medical imaging physics, fourth edition. Wiley-Liss, New York, 4 édition, June 2002.
- [Holden 2001] Mark Holden, Julia A. Schnabel and Derek L. G. Hill. *Quantifying small changes in brain ventricular volume using non-rigid registration*. In 4th International Conference on Medical Image Computing and Computer-Assisted Intervention (MICCAI), volume 2208 of *Lecture Notes in Computer Science*, pages 49–56, Utrecht, The Netherlands, 14-17 October 2001.

- [Horgan 2003] T. J. Horgan and M. D. Gilchrist. *The creation of three-dimensional finite element models for simulating head impact biomechanics*. International Journal of Crashworthiness, vol. 8, no. 4, pages 353–366, 2003.
- [Hrapko 2006] M. Hrapko, J. A. W. van Dommelen, G. W. M. Peters and J. S. H. M. Wismans. *The mechanical behaviour of brain tissue: Large strain response and constitutive modelling*. Biorheology, vol. 43, no. 5, pages 623–636, 2006.
- [Huang 2006] Albert Huang, Rafeef Abugharbieh, Roger Tam and Anthony Troubousee. *MRI Brain Extraction with Combined Expectation Maximization and Geodesic Active Contours*. In Sixth IEEE International Symposium on Signal Processing and Information Technology, pages 394–397, Vancouver, Canada, 27-30 August 2006.
- [Hwang 2011] Jinyoung Hwang, Yeji Han and HyunWook Park. *Skull-Stripping Method for Brain MRI Using a 3D Level Set with a Speedup Operator*. Journal of Magnetic Resonance Imaging, vol. 34, no. 2, pages 445–456, 2011.
- [Iglesias 2011] Juan Eugenio Iglesias, Cheng-Yi Liu, Paul Thompson and Zhuowen Tu. *Robust Brain Extraction Across Datasets and Comparison with Publicly Available Methods*. IEEE Transactions on Medical Imaging, vol. 30, no. 9, pages 1617–1634, 2011.
- [Iosifescu 1997] Dan V. Iosifescu, Martha E. Shenton, Simon K. Warfield, Ron Kikinis, Joachim Dengler, Ferenc A. Jolesz and Robert W. McCarley. *An automated registration algorithm for measuring MRI subcortical brain structures*. Neuroimage, vol. 6, no. 1, pages 13–25, 1997.
- [ITK] The Insight Segmentation and Registration Toolkit (ITK). www.itk.org, viewed in March 2012.
- [Jaccard 1912] Paul Jaccard. *The distribution of the flora in the alpine zone*. New Phytologist, vol. 11, no. 2, pages 37–50, Feb 1912.
- [Jenkinson 2005] Mark Jenkinson, Mickael Pechaud and Stephen Smith. *BET2: MR-based estimation of brain, skull and scalp surfaces*. In Eleventh Annual Meeting of the Organization for Human Brain Mapping, Toronto, Ontario, Canada, 12-16 June 2005.

- [Jia 2011] Hongjun Jia, Pew-Thian Yap and Dinggang Shen. *Iterative multi-atlas-based multi-image segmentation with tree-based registration*. NeuroImage, vol. 59, no. 1, pages 422–430, 2 January 2011.
- [Joldes 2009] Grand Roman Joldes, Adam Wittek, Mathieu Couton, Simon K. Warfield and Karol Miller. *Real-Time Prediction of Brain Shift Using Nonlinear Finite Element Algorithms*. In 12th International Conference on Medical Image Computing and Computer Assisted Intervention MICCAI, volume 5761 of *Lecture Notes in Computer Science*, pages 300–307, London, UK, 20-24 September 2009.
- [Kapur 1996] Tina Kapur, W. Eric L. Grimson, William M. Wells III and Ron Kikinis. *Segmentation of brain tissue from magnetic resonance images*. Medical Image Analysis, vol. 1, no. 2, pages 109–127, 1996.
- [Kaus 2001] Michael R. Kaus, Simon K. Warfield, Arya Nabavi, Peter M. Black, Ferenc A. Jolesz and Ron Kikinis. *Automated segmentation of MR images of brain tumors*. Radiology, vol. 218, no. 2, pages 586–91, 2001.
- [Kemper 2003] Corey Ann Kemper. Incorporation of diffusion tensor MRI in non-rigid registration for image-guided neurosurgery. Master’s thesis, Department of Electrical Engineering and Computer Science, Massachusetts Institute of Technology, Cambridge, Massachusetts, USA, 2003.
- [Kempton 2011] Matthew J. Kempton, Tracy S. A. Underwood, Simon Brunton, Floris Stylios, Anne Schmechtig, Ulrich Ettinger, Marcus S. Smith, Simon Lovestone, William R. Crum, Sophia Frangou, Steven C. R. Williams and Andrew Simmons. *A comprehensive testing protocol for MRI neuroanatomical segmentation techniques: Evaluation of a novel lateral ventricle segmentation method*. NeuroImage, vol. 58, no. 4, pages 1051–1059, 2011.
- [Khan 2008] Ali R. Khan, Lei Wang and Mirza Faisal Beg. *Freesurfer-initiated fully-automated subcortical brain segmentation in MRI using large deformation diffeomorphic metric mapping*. Neuroimage, vol. 41, no. 3, pages 735–746, 2008.
- [Klein 2010] Arno Klein, Satrajit S. Ghosh, Brian Avants, B. T. T. Yeo, Bruce Fischl, Babak Ardekani, James C. Gee, J. J. Mann and Ramin V. Parsey.

- Evaluation of volume-based and surface-based brain image registration methods.* NeuroImage, vol. 51, no. 1, pages 214–220, May 2010.
- [Kohandel 2006] M. Kohandel, S. Sivaloganathan, G. Tenti and J. M. Drake. *The constitutive properties of the brain parenchyma, Part 1. Strain energy approach.* Medical Engineering & Physics, vol. 28, no. 5, pages 449–454, 2006.
- [Kovacevic 2002] N. Kovacevic, N. J. Lobaugh, M. J. Bronskill, B. Levine, A. Feinstein and S. E. Black. *A Robust Method for Extraction and Automatic Segmentation of Brain Images.* NeuroImage, vol. 17, no. 3, pages 1087–1100, 2002.
- [Kwan 1999] Remi K.-S. Kwan, Alan C. Evans and G. Bruce Pike. *MRI simulation-based evaluation of image-processing and classification methods.* IEEE Transactions on Medical Imaging, vol. 18, no. 11, pages 1085–1097, November 1999.
- [Lee 2003] Jong-Min Lee, Uicheul Yoon, Sang Hee Nam, Jung-Hyun Kim, In-Young Kim and Sun I. Kim. *Evaluation of automated and semi-automated skull-stripping algorithms using similarity index and segmentation error.* Computers in Biology and Medicine, vol. 33, no. 6, pages 495–507, November 2003.
- [Lee 2010] Su-Lin Lee, Mirna Lerotic, Valentina Vitiello, Stamatia Giannarou, Ka-Wai Kwok, Marco Visentini-Scarzanella and Guang-Zhong Yang. *From medical images to minimally invasive intervention: Computer assistance for robotic surgery.* Computerized Medical Imaging and Graphics, vol. 34, no. 1, pages 33–45, January 2010.
- [Lemieux 1999] Louis Lemieux, Georg Hagemann, Karsten Krakow and Friedrich G. Woermann. *Fast, accurate, and reproducible automatic segmentation of the brain in T1-weighted volume MRI data.* Magnetic Resonance in Medicine, vol. 42, no. 1, pages 127–135, July 1999.
- [Lemieux 2003] Louis Lemieux, Alexander Hammers, Toby Mackinnon and Rebecca S.N. Liu. *Automatic segmentation of the brain and intracranial cerebrospinal fluid in T1-weighted volume MRI scans of the head, and its application to serial cerebral and intracranial volumetry.* Magnetic Resonance in Medicine, vol. 49, no. 5, pages 872–884, May 2003.

- [Letteboer 2005] Marloes M. J. Letteboer, Peter W. A. Willems, Max A. Viergever and Wiro J. Niessen. *Brain Shift Estimation in Image-Guided Neurosurgery Using 3-D Ultrasound*. IEEE Transactions on Biomedical Engineering, vol. 52, no. 2, pages 268–276, February 2005.
- [Leung 2011] Kelvin K. Leung, Josephine Barnes, Marc Modat, Gerard R. Ridgway, Jonathan W. Bartlett, Nick C. Fox and Sébastien Ourselin. *Brain MAPS: An automated, accurate and robust brain extraction technique using a template library*. NeuroImage, vol. 55, no. 3, pages 1091–1108, April 2011.
- [Liao 2008] Hongen Liao, Hirotaka Ishihara, Huy Hoang Tran, Ken Masamune, Ichiro Sakuma and Takeyoshi Dohi. *Fusion of Laser Guidance and 3-D Autostereoscopic Image Overlay for Precision-Guided Surgery*. In Takeyoshi Dohi, Ichiro Sakuma and Hongen Liao, editors, Medical Imaging and Augmented Reality, volume 5128 of *Lecture Notes in Computer Science*, pages 367–376. Springer Berlin / Heidelberg, 2008.
- [Liu 2009] Jia-Xiu Liu, Yong-Sheng Chen and Li-Fen Chen. *Accurate and robust extraction of brain regions using a deformable model based on radial basis functions*. Journal of Neuroscience Methods, vol. 182, no. 2, pages 255–266, 2009.
- [Lo 2005] Shaw Hwa Lo and Wencheng X. Wang. *Finite element mesh generation over intersecting curved surfaces by tracing of neighbours*. Finite Elements in Analysis and Design, vol. 41, no. 4, pages 351–370, 2005.
- [Lorensen 1987] William E. Lorensen and Harvey E. Cline. *Marching cubes: A high-resolution 3D surface construction algorithm*. SIGGRAPH Computer Graphics, vol. 21, no. 4, pages 163–169, July 1987.
- [Lunn 2006] Karen E. Lunn, Keith D. Paulsen, Fenghong Liu, Francis E. Kennedy, Alex Hartov and David W. Roberts. *Data-Guided Brain Deformation Modeling: Evaluation of a 3-D Adjoint Inversion Method in Porcine Studies*. IEEE Transactions on Biomedical Engineering, vol. 53, no. 10, pages 1893–1900, 2006.
- [Lunsford 1982] L. Dade Lunsford. *A dedicated CT system for the stereotactic operating room*. Applied Neurophysiology, vol. 45, no. 4-5, pages 374–378, 1982.

- [Lüthi 2008] Marcel Lüthi, Anita Lerch, Thomas Albrecht, Zdzislaw Krol and Thomas Vetter. *A hierarchical, multi-resolution approach for model-based skull-segmentation in MRI volumes*. In Conference Proceedings of the Workshop on 3D Physiological Human, Zermatt, Switzerland, 1-4 December 2008.
- [MacDonald 2000] David MacDonald, Noor Kabani, David Avis and Alan C. Evans. *Automated 3-D Extraction of Inner and Outer Surfaces of Cerebral Cortex from MRI*. NeuroImage, vol. 12, no. 3, pages 340–356, 2000.
- [Maciunas 1994] Robert J. Maciunas, Robert L. Galloway Jr. and Jim W. Latimer. *The application accuracy of stereotactic frames*. Neurosurgery, vol. 35, no. 4, pages 682–694, Oct 1994.
- [Maintz 1998] J. B. Antoine Maintz and Max A. Viergever. *A survey of medical image registration*. Medical Image Analysis, vol. 2, no. 1, pages 1–36, 1998.
- [Mansfield 1978] P. Mansfield, I. L. Pykett, P. G. Morris and R. E. Coupland. *Human whole body line-scan imaging by NMR*. British Journal of Radiology, vol. 51, pages 921–922, 1978.
- [Marieb 2006] Elaine N. Marieb and Katja Hoehn. Human anatomy & physiology, 7th edition. Benjamin Cummings, San Francisco, USA, 2006.
- [Marr 1980] D. Marr, and E. Hildreth. *Theory of edge detection*. Proceedings of the Royal Society of London. Series B, Biological Sciences, vol. 207, no. 1167, pages 187–217, 1980.
- [Matula 2002] Pavel Matula. *Effectivity of spherical object reconstruction using star-shaped simplex meshes*. In First International Symposium on 3D Data Processing Visualization and Transmission, pages 794–799, Padova, Italy, 19-21 June 2002.
- [Maurer 1998] Calvin R. Maurer, Derek L. G. Hill, Alastair J. Martin, Haiying Liu, Michael McCue, Daniel Rueckert, David Lloret, Walter A. Hall, Robert E. Maxwell, David J. Hawkes and Charles L. Truwit. *Investigation of intraoperative brain deformation using a 1.5-T interventional MR system: preliminary results*. IEEE Transactions on Medical Imaging, vol. 17, no. 5, pages 817–825, 1998.

- [McInerney 1996] T. McInerney and D. Terzopoulos. *Deformable models in medical image analysis: A survey*. Medical Image Analysis, vol. 1, no. 2, pages 91–108, 1996.
- [Merisaari 2009] Harri Merisaari, Riitta Parkkola, Esa Alhoniemia, Mika Teräs, Liisa Lehtonend, Leena Haataja, Helena Lapinleimu and Olli S. Nevalainen. *Gaussian mixture model-based segmentation of MR images taken from premature infant brains*. Journal of Neuroscience Methods, vol. 182, no. 1, pages 110–122, 2009.
- [Meshlab] Meshlab software. <http://meshlab.sourceforge.net/>, viewed in March 2012.
- [Metz 1970] Howard Metz, James McElhaney and Ayub K. Ommaya. *A comparison of the elasticity of live, dead and fixed brain tissue*. Journal of Biomechanics, vol. 3, no. 4, pages 453–458, Jul 1970.
- [Miga 1998] Michael I. Miga, Keith D. Paulsen, Francis E. Kennedy, P. Jack Hoopes, Alex Hartov and David W. Roberts. *Quantification of a 3D Brain Deformation Model Experiencing a Temporal Mass Expansion*. In IEEE 24th Annual Northeast Bioengineering Conference, pages 68–71, Hershey, Pennsylvania, USA, 9-10 April 1998.
- [Miga 1999a] Michael I. Miga, Keith D. Paulsen, Francis E. Kennedy, Alex Hartov and David W. Roberts. *Model-Updated Image-Guided Neurosurgery Using the Finite Element Method: Incorporation of the Falx Cerebri*. In Proceedings of the Second International Conference on Medical Image Computing and Computer-Assisted Intervention (MICCAI), volume 1679 of *Lecture Notes in Computer Science*, pages 900–909, Cambridge, UK, 19-22 September 1999.
- [Miga 1999b] Michael I. Miga, Keith D. Paulsen, John M. Lemery, Symma D. Eisner, Alex Hartov, Francis E. Kennedy and David W. Roberts. *Model-Updated Image Guidance: Initial Clinical Experiences with Gravity-Induced Brain Deformation*. IEEE Transactions on Medical Imaging, vol. 18, no. 10, pages 866–874, October 1999.
- [Miga 2000] Michael I. Miga, Keith D. Paulsen, P. Jack Hoopes, Jr. Francis E. Kennedy, Alex Hartov and David W. Roberts. *In Vivo Quantification of a Homogeneous Brain Deformation Model for Updating Preoperative*

- Images During Surgery*. IEEE Transactions on Biomedical Engineering, vol. 47, no. 2, pages 266–273, February 2000.
- [Miga 2001] Michael I. Miga, David W. Roberts, Francis E. Kennedy, Leah A. Platenik, Alex Hartov, Karen E. Lunn and Keith D. Paulsen. *Modeling of retraction and resection for intraoperative updating of images*. Neurosurgery, vol. 49, no. 1, pages 75–84, 2001.
- [Mikheev 2008] Artem Mikheev, Gregory Nevsky, Siddharth Govindan, Robert Grossman and Henry Rusinek. *Fully Automatic Segmentation of the Brain From T1-Weighted MRI Using Bridge Burner Algorithm*. Journal of Magnetic Resonance Imaging, vol. 27, no. 6, pages 1235–1241, 2008.
- [Miller 1997] Karol Miller and Kiyoyuki Chinzei. *Modelling of brain tissue mechanical properties: bi-phasic versus single-phase approach*. In 3rd International Symposium Computer Methods in Biomechanical and Biomedical Engineering, Barcelona, Spain, May 1997.
- [Miller 1999] Karol Miller. *Constitutive model of brain tissue suitable for finite element analysis of surgical procedures*. Journal of Biomechanics, vol. 32, no. 5, pages 531–537, 1999.
- [Miller 2000] Karol Miller, Kiyoyuki Chinzei, Girma Orssengo and Piotr Bednarz. *Mechanical properties of brain tissue in-vivo: experiment and computer simulation*. Journal of Biomechanics, vol. 33, pages 1369–1376, 2000.
- [Miller 2002] Karol Miller and Kiyoyuki Chinzei. *Mechanical properties of brain tissue in tension*. Journal of biomechanics, vol. 35, pages 483–490, 2002.
- [Miller 2005a] Karol Miller. *Method of testing very soft biological tissues in compression*. Journal of Biomechanics, vol. 38, no. 1, pages 153–158, 2005.
- [Miller 2005b] Karol Miller, Zeike Taylor and Wieslaw I. Nowinski. *Towards computing brain deformations for diagnosis, prognosis and neurosurgical simulation*. Journal of Mechanics in Medicine and Biology, vol. 5, no. 1, pages 105–121, 2005.
- [Montagnat 1998] Johan Montagnat and Hervé Delingette. *Globally Constrained Deformable Models for 3D Object Reconstruction*. Signal Processing, vol. 71, no. 2, pages 173–186, 1998.

- [Montagnat 2005] Johan Montagnat and Hervé Delingette. *4D deformable models with temporal constraints: application to 4D cardiac image segmentation*. Medical Image Analysis, vol. 2, no. 1, pages 87–100, 2005.
- [Mooney 1940] M. Mooney. *A theory of large elastic deformation*. Journal of Applied Physics, vol. 11, no. 9, pages 582–592, 1940.
- [Moré 1978] Jorge J. Moré. *The Levenberg-Marquardt Algorithm: Implementation and Theory*. In G. A. Watson, editor, Numerical Analysis, Lecture Notes in Mathematics, pages 105–116. Springer, Berlin, 1978.
- [Nabavi 2001] Arya Nabavi, Peter McL. Black, David T. Gering, Carl-Fredrik Westin, Vivek Mehta, Richard S. Pergolizzi, Mathieu Ferrant, Simon K. Warfield, Nobuhiko Hata, Richard B. Schwartz, William M. Wells III, Ron Kikinis and Ferenc A. Jolesz. *Serial intraoperative MR imaging of brain shift*. Neurosurgery, vol. 48, pages 787–798, 2001.
- [Nagashima 1990a] T. Nagashima, T. Shirakuni and S. Rapoport. *A two-dimensional, finite element analysis of vasogenic brain edema*. Neurologia Medico-Chirurgica, vol. 30, no. 1, pages 1–9, 1990.
- [Nagashima 1990b] T. Nagashima, Y. Tada, S. Hamano, M. Skakakura, K. Masaoka, N. Tamaki and S. Matsumoto. *The finite element analysis of brain edema associated with intracranial meningiomas*. Acta Neurochirurgica. Supplementum, vol. 51, pages 155–157, 1990.
- [Netter 2010] Frank H. Netter. Atlas of human anatomy: with student consult access, 5th edition. Saunders, Philadelphia, USA, 2010.
- [Nimsky 2000] C. Nimsky, O. Ganslandt, S. Cerny, P. Hastreiter, G. Greiner and R. Fahlbusch. *Quantification of, visualization of, and compensation for brain shift using intraoperative magnetic resonance imaging*. Neurosurgery, vol. 47, no. 5, pages 1070–1080, 2000.
- [Nimsky 2001] Christopher Nimsky, Oliver Ganslandt, Peter Hastreiter and Rudolf Fahlbusch. *Intraoperative Compensation for Brain Shift*. Surgical Neurology, vol. 56, no. 6, pages 357–364, December 2001.
- [Ogawa 1993] S. Ogawa, R. S. Menon, D. W. Tank, S. G. Kim, H. Merkle, J. M. Ellermann and K. Ugurbil. *Functional brain mapping by blood oxygenation level-dependent contrast magnetic resonance imaging. A comparison*

- of signal characteristics with a biophysical model.* Biophysical Journal, vol. 64, no. 3, pages 803–812, March 1993.
- [Otsu 1979] Nobuyuki Otsu. *A threshold selection method from gray-level histograms.* IEEE Transactions on Systems, Man, and Cybernetics, vol. 9, no. 1, pages 62–66, January 1979.
- [Pamidi 1978] M. R. Pamidi and S. H. Advani. *Nonlinear constitutive relations for human brain tissue.* Journal of Biomechanical Engineering, vol. 100, no. 1, pages 44–48, 1978.
- [Park 2009] Jong Geun Park and Chulhee Lee. *Skull stripping based on region growing for magnetic resonance brain images.* NeuroImage, vol. 47, no. 4, pages 1394–1407, 2009.
- [Pechaud 2006] M. Pechaud, M. Jenkinson and S. Smith. *BET2 - MRI-Based Estimation of Brain, Skull and Scalp Surfaces, FMRIB Technical Report TR06MP1.* Technical report, Oxford University, Oxford, England, UK, 2006.
- [Pennecc 2001] Xavier Pennec, Nicholas Ayache, Alexis Roche and Pascal Cachier. *Non-Rigid MR/US Registration for Tracking Brain Deformations.* In International Workshop on Medical Imaging and Augmented Reality, pages 79–86, Shatin, Hong Kong, 10-12 June 2001.
- [Penney 2002] G. P. Penney, J. A. Little, J. Weese, D. L. G. Hill and D. J. Hawkes. *Deforming a preoperative volume to represent the intraoperative scene.* Computer Aided Surgery, vol. 7, no. 2, pages 63–73, 2002.
- [Perez 2005] Claudio A. Perez, Guillermo D. Gonzalez, Leonel E. Medina and Francisco J. Galdames. *Linear versus nonlinear neural modeling for 2-D pattern recognition.* IEEE Transactions on Systems, Man, and Cybernetics. Part A-Systems and Humans, vol. 35, no. 6, pages 955–964, 2005.
- [Perona 1990] Pietro Perona and Jitendra Malik. *Scale-space and edge detection using anisotropic diffusion.* IEEE Transactions on Pattern Analysis and Machine Intelligence, vol. 12, pages 629–639, 1990.
- [Peters 2006] Terry M. Peters. *Image-guidance for surgical procedures.* Physics in Medicine and Biology, vol. 51, pages 505–540, 2006.

- [Pham 2000] Dzung L. Pham, Chenyang Xu and Jerry L. Prince. *A Survey of Current Methods in Medical Image Segmentation*. Annual Review of Biomedical Engineering, vol. 2, pages 315–337, August 2000.
- [Pitiot 2004] Alain Pitiot, Hervé Delingette, Nicholas Ayache and Paul M. Thompson. *Expert knowledge-guided segmentation system for brain MRI*. NeuroImage, vol. 23, no. 1, pages S85–S96, 2004.
- [Powell 2008] Stephanie Powell, Vincent A. Magnotta, Hans Johnson, Vamsi K. Jammalamadaka, Nancy C. Andreasen and Ronald Pierson. *Registration and machine learning-based automated segmentation of subcortical and cerebellar brain structures*. Neuroimage, vol. 39, no. 1, pages 238–247, 2008.
- [Prange 2002] Michael T. Prange and Susan S. Margulies. *Regional, Directional, and Age-Dependent Properties of the Brain Undergoing Large Deformation*. Journal of Biomechanical Engineering, vol. 124, no. 2, pages 244–252, 2002.
- [Raab 1979] F. Raab, E. Blood, O. Steiner and H. Jones. *Magnetic position and orientation tracking systems*. IEEE Transactions on Aerospace and Electronic Systems, vol. 15, pages 709–717, 1979.
- [Rehm 2004] Kelly Rehm, Kirt Schaper, Jon Anderson, Roger Woods, Sarah Stoltzner and David Rottenberg. *Putting our heads together: a consensus approach to brain/non-brain segmentation in T1-weighted MR volumes*. NeuroImage, vol. 22, no. 3, pages 1262–1270, 2004.
- [Rex 2003] David E. Rex, Jeffrey Q. Ma and Arthur W. Toga. *The LONI Pipeline Processing Environment*. NeuroImage, vol. 19, no. 3, pages 1033–1048, July 2003.
- [Rex 2004] David E. Rex, David W. Shattuck, Roger P. Woods, Katherine L. Narr, Eileen Luders, Kelly Rehm, Sarah E. Stolzner, David A. Rottenberg and Arthur W. Toga. *A meta-algorithm for brain extraction in MRI*. NeuroImage, vol. 23, no. 2, pages 625–637, Oct 2004.
- [Richard 2000] A. Richard. Biomedical imaging, visualization, and analysis. John Wiley & Sons, Inc., New York, NY, USA, 2000.

- [Rifai 2000] Hilmi Rifai, Isabelle Bloch, Seth Hutchinson, Joe Wiart and Line Garnero. *Segmentation of the skull in MRI volumes using deformable model and taking the partial volume effect into account*. Medical Image Analysis, vol. 4, no. 3, pages 219–233, 2000.
- [Rivlin 1948] R. S. Rivlin. *Large elastic deformations of isotropic materials. IV. Further developments of the general theory*. Philosophical Transactions of the Royal Society of London. Series A, Mathematical and Physical Sciences, vol. 241, no. 835, pages 379–397, 1948.
- [Roberts 1998] David W. Roberts, Alexander Hartov, Francis E. Kennedy, Michael I. Miga and Keith D. Paulsen. *Intraoperative brain shift and deformation: a quantitative analysis of cortical displacement in 28 cases*. Neurosurgery, vol. 43, pages 749–758, 1998.
- [Ronfard 1996] Rémi Ronfard and Jarek Rossignac. *Full-range Approximation of Triangulated Polyhedra*. In Proceeding of Eurographics, Computer Graphics Forum, volume 15, pages 67–76, August 1996.
- [Rosenblatt 1956] Murray Rosenblatt. *Remarks on some nonparametric estimates of a density function*. Annals of Mathematical Statistics, vol. 27, no. 3, pages 832–837, 1956.
- [Rouviere 1999] H. Rouviere and A. Delmas. *Anatomía humana descriptiva, topográfica y funcional*. Masson, France, 1999.
- [Russ 2011] John C. Russ. *The image processing handbook*, 6th edition. CRC Press, 2011.
- [Sadananthan 2010] Suresh A Sadananthan, Weili Zheng, Michael W L Chee and Vitali Zagorodnov. *Skull stripping using graph cuts*. Neuroimage, vol. 49, no. 1, pages 225–239, Jan 2010.
- [Sandeman 1994] D. R. Sandeman, N. Patel, C. Chandler, R. J. Nelson, H. B. Coakham and H. B. Griffith. *Advances in image directed neurosurgery preliminary experience with the ISG viewing wand compared with the Leksell-G frame*. British Journal of Neurosurgery, vol. 8, no. 5, pages 529–544, 1994.

- [Sandor 1997] S. Sandor and R. Leahy. *Surface-based labeling of cortical anatomy using a deformable atlas*. IEEE Transactions on Medical Imaging, vol. 16, no. 1, pages 41–54, Feb 1997.
- [Scharf 2009] S. Scharf. *SPECT/CT imaging in general orthopedic practice*. Seminars in Nuclear Medicine, vol. 39, no. 5, pages 293–307, Sep 2009.
- [Schiaivone 2009] Patrick Schiaivone, Fabrice Chassat, Thomas Boudou, Emmanuel Promayon, F. Valdivia and Yohan Payan. *In vivo measurement of human brain elasticity using a light aspiration device*. Medical Image Analysis, vol. 13, no. 4, pages 673–678, 2009.
- [Schiessel 1995] H. Schiessel, R. Metzler, A. Blumen and T. F. Nonnenmacher. *Generalized viscoelastic models: their fractional equations with solutions*. Journal of Physics A: Mathematical and General, vol. 28, pages 6567–6584, 1995.
- [Schnack 2001] H. G. Schnack, H. E. Hulshoff Pol, W. F. C. Baaré, M. A. Viergever and R. S. Kahn. *Automatic segmentation of the ventricular system from MR images of the human brain*. NeuroImage, vol. 14, no. 1, pages 95–104, 2001.
- [Ségonne 2004] F. Ségonne, A. M. Dale, E. Busa, M. Glessner, D. Salat, H. K. Hahn and B. Fischl. *A hybrid approach to the skull stripping problem in MRI*. NeuroImage, vol. 22, pages 1060–1075, 2004.
- [Serby 2001] D. Serby, M. Harders and G. Szekely. *A new approach to cutting into finite element models*. In Proceedings of the 4th International Conference on Medical Image Computing and Computer-Assisted Intervention (MICCAI), volume 2208 of *Lecture Notes in Computer Science*, pages 425–433, Utrecht, The Netherlands, 14-17 October 2001.
- [Shahidi 2002] Ramin Shahidi, Michael R. Bax, Calvin R. Maurer Jr., Jeremy A. Johnson, Eric P. Wilkinson, Bai Wang, Jay B. West, Martin J. Citardi, Kim H. Manwaring and Rasool Khadem. *Implementation, calibration and accuracy testing of an image-enhanced endoscopy system*. IEEE Transactions on Medical Imaging, vol. 21, no. 12, pages 1524–1535, 2002.
- [Shan 2002] Zu Y. Shan, Guang H. Yue and Jing Z. Liu. *Automated histogram-based brain segmentation in T1-weighted three-dimensional magnetic res-*

- onance head images*. Neuroimage, vol. 17, no. 3, pages 1587–1598, November 2002.
- [Shan 2007] Zuyao Y. Shan, Chia-Ho Hua, Qing Ji, Carlos Parra, Xiaofei Ying, Matthew J. Krasin, Thomas E. Merchant, Larry E. Kun and Wilburn E. Reddick. *A knowledge-guided active model method of skull segmentation on T1-weighted MR images*. In Society of Photo-Optical Instrumentation Engineers (SPIE) Conference Series, volume 6512, page 65122R, March 2007.
- [Shattuck 2001] David W. Shattuck, Stephanie R. Sandor-Leahy, Kirt A. Schaper, David A. Rottenberg and Richard M. Leahy. *Magnetic resonance image tissue classification using a partial volume model*. NeuroImage, vol. 13, no. 5, pages 856–876, 2001.
- [Shattuck 2009] David W. Shattuck, Gautam Prasad, Mubeena Mirza, Katherine L. Narr and Arthur W. Toga. *Online resource for validation of brain segmentation methods*. NeuroImage, vol. 45, no. 2, pages 431–439, 2009.
- [Shuhaiber 2004] Jeffrey H. Shuhaiber. *Augmented Reality in Surgery*. Archives of Surgery, vol. 139, no. 2, pages 170–174, 2004.
- [Sinha 2005] Tuhin K. Sinha, Benoit M. Dawant, Valerie Duay, David M. Cash, Robert J. Weil, Reid C. Thompson, Kyle D. Weaver and Michael I. Miga. *A Method to Track Cortical Surface Deformations Using a Laser Range Scanner*. IEEE Transactions on Medical Imaging, vol. 24, no. 6, pages 767–781, June 2005.
- [Skrinjar 1999] Oskar M. Skrinjar and James S. Duncan. *Real time 3D brain shift compensation*. In Lecture Notes in Computer Science, 16th International Conference on Information Processing in Medical Imaging, volume 1613, pages 42–55, Visegrád, Hungary, 28 June - 2 July 1999.
- [Skrinjar 2001] Oskar M. Skrinjar, Colin Studholme, Arya Nabavi and James S. Duncan. *Steps toward a stereo-camera-guided biomechanical model for brain shift compensation*. In Information Processing in Medical Imaging, 17th International Conference (IPMI), Lecture Notes in Computer Science, pages 183–189, Davis, CA, USA, 18-22 June 2001. Springer Berlin / Heidelberg.

- [Skrinjar 2002] Oskar M. Skrinjar, Arya Nabavi and James S. Duncan. *Model-driven brain shift compensation*. Medical image analysis, vol. 6, pages 361–373, 2002.
- [Smith 2002] S. M. Smith. *Fast robust automated brain extraction*. Human Brain Mapping, vol. 17, no. 3, pages 143–155, November 2002.
- [Soltanian-Zadeh 1997] Hamid Soltanian-Zadeh and Joe P. Windham. *A multiresolution approach for contour extraction from brain images*. Medical Physics, vol. 24, no. 12, pages 1844–1853, 1997.
- [Somasundaram 2011] K. Somasundaram and T. Kalaiselvi. *Automatic brain extraction methods for T1 magnetic resonance images using region labeling and morphological operations*. Computers in Biology and Medicine, vol. 41, no. 8, pages 716–725, 2011.
- [Sonka 1996] Milan Sonka, Satish K. Tadikonda and Steve M. Collins. *Knowledge-based interpretation of MR brain images*. IEEE Transactions on Medical Imaging, vol. 15, no. 4, pages 443–452, 1996.
- [StanfordRep] Stanford 3D scanning repository. <http://graphics.stanford.edu/data/3Dscanrep/>, viewed in March 2012.
- [Sun 2005] Hai Sun, Karen E. Lunn, Hany Farid, Ziji Wu, David W. Roberts, Alex Hartov and Keith D. Paulsen. *Stereopsis-Guided Brain Shift Compensation*. IEEE Transactions on Medical Imaging, vol. 24, no. 8, pages 1039–1052, August 2005.
- [Sutherland 1999] G. R. Sutherland, T. Kaibara, D. Louw, D. I. Hoult, B. Tomanek and J. Saunders. *A mobile high-field magnetic resonance system for neurosurgery*. Journal of Neurosurgery, vol. 91, pages 804–813, 1999.
- [Suzuki 2005] Naoki Suzuki, Asaki Hattori, Shigeyuki Suzuki, Yoshito Otake, Mitsuhiro Hayashibe, Susumu Kobayashi, Takehiko Nezu, Haruo Sakai and Yuji Umezawa. *Construction of a high-tech operating room for image-guided surgery using VR*. Studies in Health Technology and Informatics, vol. 111, pages 538–542, 2005.

- [Tada 1994] Y. Tada and T. Nagashima. *Modeling and simulation of brain lesions by the finite-element method*. IEEE Engineering in Medicine and Biology Magazine, vol. 13, no. 4, pages 497–503, 1994.
- [Taylor 2004] Zeike Taylor and Karol Miller. *Reassessment of brain elasticity for analysis of biomechanisms of hydrocephalus*. Journal of Biomechanics, vol. 37, pages 1263–1269, 2004.
- [Tejos 2009] Cristian Tejos and Pablo Irarrazaval. *Simplex Mesh Diffusion Snakes: Integrating 2D and 3D Deformable Models and Statistical Shape Knowledge in a Variational Framework*. International Journal of Computer Vision, vol. 85, no. 1, pages 19–34, 2009.
- [Thirion 1998] J. P. Thirion. *Image matching as a diffusion process: an analogy with Maxwell’s demons*. Medical image analysis, vol. 2, no. 3, pages 243–260, 1998.
- [Thompson 2001] Paul M. Thompson, Michael S. Mega, Roger P. Woods, Chris I. Zoumalan, Chris J. Lindshield, Rebecca E. Blanton, Jacob Moussai, Colin J. Holmes, Jeffrey L. Cummings and Arthur W. Toga. *Cortical change in Alzheimer’s disease detected with a disease-specific population-based brain atlas*. Cerebral Cortex, vol. 11, no. 1, pages 1–16, 2001.
- [Tosun 2006] Duygu Tosun, Maryam E. Rettmann, Daniel Q. Naiman, Susan M. Resnick, Michael A. Kraut and Jerry L. Prince. *Cortical reconstruction using implicit surface evolution: Accuracy and precision analysis*. NeuroImage, vol. 29, no. 3, pages 838–852, 2006.
- [Tu 2008] Zhuowen Tu, Katherine L. Narr, Piotr Dollár, Ivo Dinov, Paul M. Thompson and Arthur W. Toga. *Brain anatomical structure segmentation by hybrid discriminative/generative models*. IEEE Transactions on Medical Imaging, vol. 27, no. 4, pages 495–508, 2008.
- [Vigneron 2004] Lara M. Vigneron, Jacques G. Verly and Simon K. Warfield. *On extended finite element method (XFEM) for modelling of organ deformations associated with surgical cuts*. In Medical Simulation, Lecture notes in computer science, volume 3078, pages 134–143, 2004.
- [Vigneron 2009] L. Vigneron. *FEM/XFEM-Based Modeling of Brain Shift, Resection, and Retraction for Image-Guided Surgery*. PhD thesis, Université de Liège, Liège, Wallonia, Belgium, 2009.

- [Voo 1996] L. Voo, S. Kumaresan, F. A. Pintar, N. Yoganandan and A. Sances. *Finite element models of the human head*. Medical and Biological Engineering and Computing, vol. 34, no. 5, pages 375–381, 1996.
- [Wang 1998] Yongmei M. Wang and Lawrence H. Staib. *Boundary finding with correspondence using statistical shape models*. In IEEE Computer Society Conference on Computer Vision and Pattern Recognition, pages 338–345, Santa Barbara, CA, USA, 23-25 June 1998.
- [Wang 2005] Qian Wang, Dieter Seghers, Emiliano D’Agostino, Frederik Maes, Dirk Vandermeulen, Paul Suetens and Alexander Hammers. *Construction and validation of mean shape atlas templates for atlas-based brain image segmentation*. In 19th International Conference on Information Processing in Medical Imaging, volume 3565, pages 689–700, Glenwood Springs, CO, USA, 10-15 July 2005.
- [Wang 2009] Defeng Wang, Lin Shi, Winnie C. W. Chu, Jack C. Y. Cheng and Pheng Ann Heng. *Segmentation of Human Skull in MRI Using Statistical Shape Information From CT Data*. Journal of Magnetic Resonance Imaging, vol. 30, no. 3, pages 490–498, 2009.
- [Ward 1999] B. Douglas Ward. 3dIntracranial: Automatic segmentation of intracranial region. Milwaukee: Biophysics Research Institute, Medical College of Wisconsin, afni.nimh.nih.gov/afni/doc/manual/3dIntracranial/, viewed in March 2012. 1999.
- [Warfield 2000] Simon K. Warfield, Matthieu Ferrant, Xavier Gallez, Arya Nabavi, Ferenc A. Jolesz and Ron Kikinis. *Real-Time Biomechanical Simulation of Volumetric Brain Deformation for Image Guided Neurosurgery*. In Proceedings of the 2000 ACM/IEEE Conference on Supercomputing (CDROM), pages 1–16, Dallas, Texas, USA, 04-10 November 2000. Computer Society.
- [Warfield 2002] Simon K. Warfield, Florin Talos, Alida Tei, Aditya Bharatha, Arya Nabavi, Matthieu Ferrant, Peter McL. Black, Ferenc A. Jolesz and Ron Kikinis. *Real-Time Registration of Volumetric Brain MRI by Biomechanical Simulation of Deformation during Image Guided Neurosurgery*. Computing and Visualization in Science, vol. 5, no. 1, pages 3–11, 2002.

- [Weese 2001] Jürgen Weese, Michael Kaus, Christian Lorenz, Steven Lobregt, Roel Truyen and Vladimir Pekar 1. *Shape constrained deformable models for 3-D medical image segmentation*. In Information Processing in Medical Imaging, LNCS, volume 2082, pages 380–387, 2001.
- [Wels 2011] Michael Wels, Yefeng Zheng, Martin Huber, Joachim Hornegger and Dorin Comaniciu. *A discriminative model-constrained EM approach to 3D MRI brain tissue classification and intensity non-uniformity correction*. Physics in Medicine and Biology, vol. 56, no. 11, pages 3269–3300, Jun 2011.
- [West 2002] John D. West, Keith D. Paulsen, Souheil Inati, Francis Kennedy, Alex Hartov and David W. Roberts. *Incorporation of diffusion tensor anisotropy in brain deformation models for updating preoperative images to improve image-guidance*. In IEEE International Symposium on Biomedical Imaging, pages 509–512, Washington, DC, USA, 7-10 July 2002.
- [West 2004] Jay B. West and Calvin R. Maurer. *Designing Optically Tracked Instruments for Image-Guided Surgery*. IEEE Transactions on Medical Imaging, vol. 23, no. 5, pages 533–545, May 2004.
- [Withey 2007] D. J. Withey and Z. J. Koles. *Medical Image Segmentation: Methods and Software*. In Joint Meeting of the 6th International Symposium on Noninvasive Functional Source Imaging of the Brain and Heart and the International Conference on Functional Biomedical Imaging (NFSI-ICFBI), pages 140–143, Hangzhou, Zhejiang, China, 12-14 October 2007.
- [Wittek 2004] Adam Wittek, Jerome Laporte, Karol Miller, Ron Kikinis and Simon K. Warfield. *Computing reaction forces on surgical tools for robotic neurosurgery and surgical simulation*. In Australasian Conference on Robotics and Automation ACRA, Canberra, Australia, 6-8 December 2004.
- [Wittek 2005] Adam Wittek, Ron Kikinis, Simon K. Warfield and Karol Miller. *Brain Shift Computation Using a Fully Nonlinear Biomechanical Model*. In 8th International Conference on Medical Image Computing and Computer-Assisted Intervention MICCAI, volume 3750 of *Lecture Notes in Computer Science*, pages 583–590, Palm Springs, CA, USA, 26-29 October 2005.

- [Wittek 2007] Adam Wittek, Karol Miller, Ron Kikinis and Simon K. Warfield. *Patient-specific model of brain deformation: Application to medical image registration*. Journal of Biomechanics, vol. 40, pages 919–929, 2007.
- [Wolters 2002] Carsten Hermann Wolters, M. Kuhn, A. Anwander and S. Reitzinger. *A parallel algebraic multigrid solver for finite element method based source localization in the human brain*. Computing and Visualization in Science, vol. 5, no. 3, pages 165–177, 2002.
- [Wolters 2003] Carsten Hermann Wolters. *Influence of tissue conductivity inhomogeneity and anisotropy on EEG/MEG based source localization in the human brain*. PhD thesis, Max Planck Institute of Cognitive Neuroscience, Leipzig, Saxony, Germany, 2003.
- [Worth 1998] Andrew J. Worth, Nikos Makris, Mark R. Patti, Julie M. Goodman, Elizabeth A. Hoge, Verne S. Caviness Jr. and David N. Kennedy. *Precise segmentation of the lateral ventricles and caudate nucleus in MR brain images using anatomically driven histograms*. IEEE Transactions on Medical Imaging, vol. 17, no. 2, pages 303–310, 1998.
- [Wu 2006] Minjie Wu, Owen Carmichael, Pilar Lopez-Garcia, Cameron S. Carter and Howard J. Aizenstein. *Quantitative comparison of AIR, SPM, and the fully deformable model for atlas-based segmentation of functional and structural MR images*. Human Brain Mapping, vol. 27, no. 9, pages 747–754, 2006.
- [Xia 2004] Yan Xia, Qingmao Hu, Aamer Aziz and Wieslaw L Nowinski. *A knowledge-driven algorithm for a rapid and automatic extraction of the human cerebral ventricular system from MR neuroimages*. NeuroImage, vol. 21, no. 1, pages 269–282, 2004.
- [Xu 2001] Meihe Xu and Wieslaw L. Nowinski. *Talairach-Tournoux brain atlas registration using a metalforming principle-based finite element method*. Medical Image Analysis, vol. 5, no. 4, pages 271–279, 2001.
- [Xue 2001] Jing-Hao Xue, Su Ruan, Bruno Moretti, Marinette Revenu and Daniel Bloyet. *Knowledge-based segmentation and labeling of brain structures from MRI images*. Pattern Recognition Letters, vol. 22, no. 3-4, pages 395–405, 2001.

- [Yang 2005] Xunnian Yang. *Surface interpolation of meshes by geometric subdivision*. Computer-Aided Design, vol. 37, no. 5, pages 497–508, 2005.
- [Yang 2010] Xiaofeng Yang and Baowei Fei. *A skull segmentation method for brain MR images based on multiscale bilateral filtering scheme*. Medical Imaging 2010: Image Processing, Proceedings of the SPIE, vol. 7623, pages 76233K–76233K–11, 2010.
- [Yoon 2001] Ui-Cheul Yoon, June-Sic Kim, Jae-Seok Kim, In-Young Kim and Sun I. Kim. *Adaptable fuzzy C-Means for improved classification as a preprocessing procedure of brain parcellation*. Journal of Digital Imaging, vol. 14, no. 2, pages 238–240, 2001.
- [Yushkevich 2006] Paul A. Yushkevich, Joseph Piven, Heather Cody Hazlett, Rachel Gimpel Smith, Sean Ho, James C. Gee and Guido Gerig. *User-guided 3D active contour segmentation of anatomical structures: significantly improved efficiency and reliability*. Neuroimage, vol. 31, no. 3, pages 1116–1128, 2006.
- [Zener 1948] Clarence M. Zener. *Elasticity and anelasticity of metals*. Chicago University Press, 1948.
- [Zhao 2010] Lu Zhao, Ulla Ruotsalainen, Jussi Hirvonen, Jarmo Hietala and Jussi Tohka. *Automatic cerebral and cerebellar hemisphere segmentation in 3D MRI: Adaptive disconnection algorithm*. Medical Image Analysis, vol. 14, no. 3, pages 360–372, 2010.
- [Zhou 2005] Juan Zhou and Jagath C. Rajapakse. *Segmentation of subcortical brain structures using fuzzy templates*. NeuroImage, vol. 28, no. 4, pages 915–924, 2005.
- [Zhuang 2006] Audrey H. Zhuang, Daniel J. Valentino and Arthur W. Toga. *Skull-stripping magnetic resonance brain images using a model-based level set*. NeuroImage, vol. 31, no. 1, pages 79–92, August 2006.
- [Zorin 1996] Denis Zorin, Peter Schröder and Wim Sweldens. *Interpolating Subdivisions for Meshes with Arbitrary Topology*. In Proceedings of the 23rd annual conference on Computer graphics and interactive techniques, SIGGRAPH '96, pages 189–192, New York, NY, USA, 1996. ACM.

Anatomical Terms of Location

Some directional terms and anatomical planes are mentioned in the present work. These anatomical location terms are employed to have a reference framework to explain relative positions in the human body. The definitions of these terms can be found in [Rouviere 1999] and are as follows.

A.1 Directional Terms

A number of specific terms [Rouviere 1999] have been defined and accepted by convention to help in the effective study of anatomical structures. Considering the anatomical position (Figure A.1(a)), these terms are:

Superior or cephalic or cranial: Towards the head or towards the upper part of a structure or above. For example: the pectorals are superior to the abdominals.

Inferior or caudal: The direction towards the feet or towards the lower part of a structure or below. For example: the abdominals are inferior to the pectorals.

Anterior or ventral: It refers to a structure that is in front of another, or closer to the frontal part of the body. For example: the liver is anterior to the kidneys.

Posterior or dorsal: It refers to a structure that is behind another, or closer to the back of the subject. For example: The knuckles are located dorsally on the hand.

Mid line: Plane that divides the body into left and right halves.

Medial: Towards the mid line of the body. Also, It refers to something located near the mid line of the body or structure. For example: the trunk is medial to the arms.

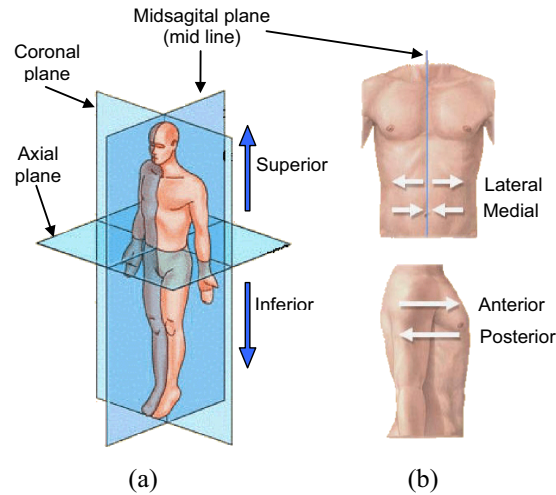


Figure A.1: Anatomical terms of location. (a) Human body in anatomical position with anatomical planes superimposed. (b) Some anatomical directional terms. (Source: Dr. Gary Farr. *Anatomy / Anatomical Terminology*. www.becomehealthynow.com/article/anatom/704/)

Lateral: Away from the mid line of the body or structure. For example: the arms are lateral to the torso.

Proximal: It refers to a position closer to the trunk, or closer to point where a limb joins the body. For example: between the knee and the ankle, the knee is more proximal to the pelvis.

Distal: It refers to a position farther to the trunk, or farther to the place where a limb joins the body. For example: between the elbow and the wrist, the wrist is more distal to the shoulder.

Superficial: Close to the outer surface of the body, or more external in relation to something. For example: the muscle is superficial to the bone.

Deep: Not close to the outer surface of the body, or less superficial in relation to something. For example: the bone is deep compared to the muscle.

Parietal: Related to or forming the walls of the organs or body cavities. For example: the parietal bones form the roof of the cranium.

Visceral: Related to the the body cavities, or the internal organs such as those within the chest or abdomen. For example: the intestine is a viscus within the abdominal cavity.

A.2 Anatomical Orientation Planes

There are three primary or cardinal planes that pass through the body [Rouviere 1999], and correspond to the three spatial dimensions (Figure A.1(a)). These planes can be traced from the anatomical position (Figure A.1(a)):

Sagittal plane: It divides the body into sinister and dexter (left and right) portions. When the plane is in mid line, it is called midsagittal or median plane.

Coronal or frontal plane: It divides the body into dorsal and ventral (back and front, or posterior and anterior) portions.

Axial or transverse plane: It divides the body into cranial and caudal (head and tail) portions.

APPENDIX B

Brain Anatomy

Since the problem addressed in this work is related to the brain, some knowledge of brain anatomy will be introduced in the present section. The information presented in this section can be found in [Gray 1918, Marieb 2006, Netter 2010].

B.1 General Brain Anatomy

The *brain* together with the *spinal cord* form the *central nervous system* (CNS). The basic pattern of the CNS consists of a central cavity surrounded by a gray matter core, external to which is white matter (myelinated fiber tracts). The brain exhibits this basic design but has additional regions of gray matter not present in the spinal cord (Figure B.1). Both the cerebral hemispheres and the cerebellum have an outer layer or “bark” of gray matter consisting of neuron cell bodies called a cortex. This pattern changes with descent through the brain stem. The cortex disappears, but scattered gray matter nuclei are seen within the white matter. At the caudal end of the brain stem, the basic pattern is evident.

The average adult man’s brain has a mass of about 1600 g (3.5 lb); that of a woman averages 1450 g (3.2 lb). In terms of brain mass per body mass, however, males and females have equivalent brain sizes. The brain can be divided in:

Cerebral hemispheres: They form the *telencephalon*, the largest part of the brain (sec. B.2).

Diencephalon: It includes the *thalamus*, *metathalamus*, *hypothalamus*, *epithalamus*, *prethalamus* or *subthalamus* and *pretectum*. The diencephalon is located near the midline of the brain, above the mesencephalon (midbrain).

Brain stem: Posterior part of the brain, adjoining and structurally continuous with the spinal cord. It is usually described as including the medulla oblongata (myelencephalon), pons (part of metencephalon), and midbrain (mesencephalon)

Cerebellum: It is main organ involved in the coordination of voluntary motor movements, balance and equilibrium, and muscle tone. It is located just above the brain stem and towards the back of the telencephalon. (see sec. B.3)

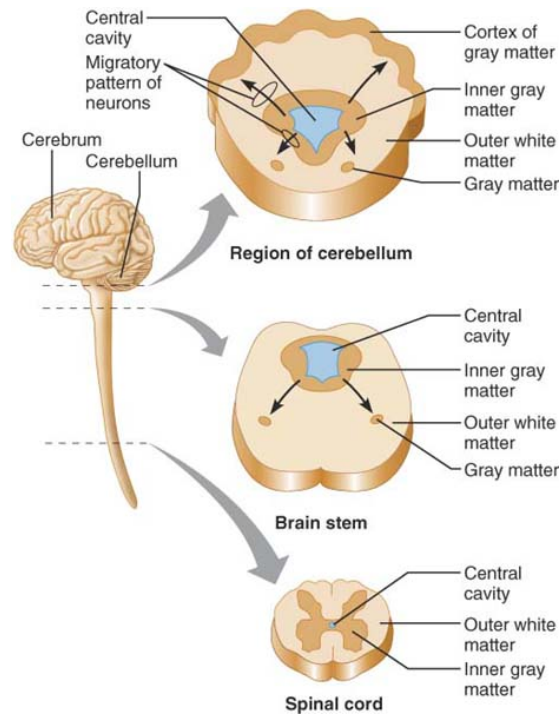


Figure B.1: Arrangement of gray and white matter in the CNS (highly simplified). Cross sections at three CNS levels. In each section, the dorsal position is at the top. In general, white matter lies external to gray matter; however, collections of gray matter migrate externally into the white matter in the developing brain (see black arrows). The cerebrum resembles the cerebellum in its external cortex of gray matter (Figure B.4). (Source: [Marieb 2006]).

The most important brain's parts for the present work are the *cerebral hemispheres* and the *cerebellum*. These parts constitute the brain parenchyma, and they will be explained in the following sections. Other anatomical structures related with the CNS, which are as well of interest for the work, such as the *meninges* (sec. B.4) and *cerebrospinal fluid* (sec. B.5), will be also explained.

B.2 Cerebral Hemispheres

Almost the entire surface of the cerebral hemispheres is marked by elevated ridges of tissue called *gyri*, separated by shallow grooves called *sulci*. The singular forms of these terms are gyrus and sulcus. Deeper grooves, called *fissures*, separate large regions of the brain. The more prominent gyri and sulci are similar in all people and are important anatomical landmarks. The hemispheres are separated medially by a deep cleft, named the *longitudinal cerebral fissure*, and each possesses a central cavity, the lateral ventricle (Figure B.8). Another large fissure, the *transverse cerebral fissure*, separates the cerebral hemispheres from the cerebellum.

Several sulci divide each hemisphere into five lobes

- Frontal
- Parietal
- Temporal
- Occipital
- Insula

All these lobes but the last are named for the cranial bones that overlie them (Figure B.2(a)). The *central sulcus*, which lies in the frontal plane, separates the frontal lobe from the parietal lobe. Bordering the central sulcus are the *precentral gyrus anteriorly* and the *postcentral gyrus posteriorly* (Figure B.3). More posteriorly, the occipital lobe is separated from the parietal lobe by the *parieto-occipital sulcus*, located on the medial surface of the hemisphere.

The deep *lateral sulcus* or *Sylvian fissure* outlines the temporal lobe and separates it from the parietal and frontal lobes. A fifth lobe of the cerebral hemisphere, the insula, is buried deep within the lateral sulcus and forms part of its floor (B.2(b)). The insula is covered by portions of the temporal, parietal, and frontal lobes.

The cerebral hemispheres fit snugly in the skull. In the ventral direction, the frontal lobes lie in the anterior cranial fossa. The anterior parts of the temporal lobes fill the middle cranial fossa. The posterior cranial fossa, however, houses the brain stem and cerebellum; the occipital lobes are located well superior to that cranial fossa.

Each cerebral hemisphere has three basic regions: a superficial cortex of gray matter; an internal white matter; and the basal nuclei, islands of gray matter situated deep within the white matter.

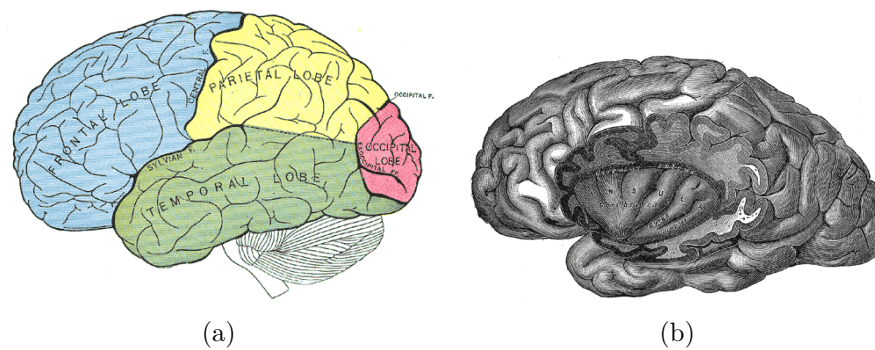


Figure B.2: Principal fissures and lobes of the brain. Figure (a) shows the frontal, parietal, temporal and occipital lobes. The insula, covered by portions of the temporal, parietal, and frontal lobes, is shown in (b). (Source: [Gray 1918]).

B.2.1 Cerebral Cortex

The cerebral cortex is the executive suite of the nervous system, where our conscious mind is found. It enables us to be aware of ourselves and our sensations, to communicate, remember, and understand, and to initiate voluntary movements. The cerebral cortex is composed of *gray matter*: neuron cell bodies, dendrites, associated glia and blood vessels, but no fiber tracts. It contains billions of neurons arranged in six layers. Although it is only 2-4 mm (about 1/8 inch) thick, it accounts for roughly 40% of total brain mass. Its many convolutions effectively triple its surface area.

Specific motor and sensory functions are localized in discrete cortical areas called domains. However, many higher mental functions, such as memory and language, appear to have overlapping domains and are spread over large areas of the cortex. The cerebral cortex contains three kinds of functional areas: motor areas, sensory areas, and association areas.

Motor Areas: As shown in Figure B.3 (red), the following motor areas of the cortex, which control voluntary movement, lie in the posterior part of the frontal lobes: primary motor cortex, premotor cortex, Broca's area, and the frontal eye field.

Sensory Areas: Areas concerned with conscious awareness of sensation, the sensory areas of the cortex, occur in the parietal, insular, temporal, and occipital lobes (see Figure B.3). These areas can be divided in: primary somatosensory cortex, somatosensory association cortex, visual areas, au-

ditory areas, olfactory (smell) cortex, gustatory (taste) cortex, visceral sensory area, and vestibular (equilibrium) cortex.

Multimodal Association Areas: The association areas (light red or blue in Figure B.3) are all tightly tied to one kind of primary sensory or motor cortex. Most of the cortex, though, is more complexly connected, receiving inputs from multiple senses and sending outputs to multiple areas. All these areas are called multimodal association areas (white in Figure B.3).

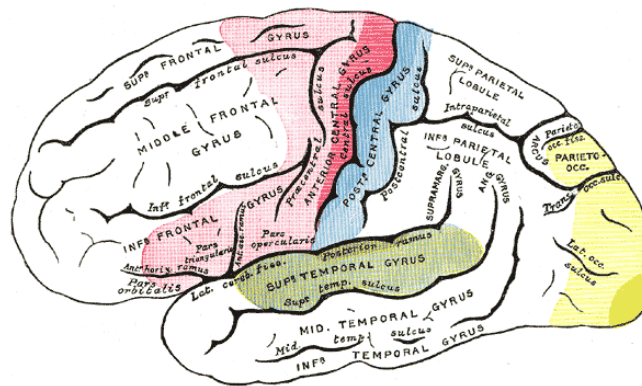


Figure B.3: Functional areas of the brain. Motor areas in red; sensory areas in blue; auditory areas in green; visual areas in yellow. Association areas are in light colors. (Source: [Gray 1918]).

In general, information flows from sensory receptors to the appropriate primary sensory cortex, then to a sensory association cortex and then on to the multimodal association cortex. Multimodal association cortex allows us to give meaning to the information that we receive, store it in memory if needed, tie it to previous experience and knowledge, and decide what action to take. Once the course of action has been decided, those decisions are relayed to the premotor cortex, which in turn communicates with the motor cortex. The multimodal association cortex seems to be where sensations, thoughts, and emotions become conscious.

B.2.2 White Matter

The second of the three basic regions of each cerebral hemisphere is the internal cerebral white matter. The white matter (Figure B.4) deep to the cortical gray matter is responsible for communication between cerebral areas and between the cerebral cortex and lower CNS centers. White matter consists largely of

myelinated fibers bundled into large tracts. These fibers and tracts are classified according to the direction in which they run as *commissural*, *association*, or *projection*:

Commissures: Tracts composed of commissural fibers, connect corresponding gray areas of the two hemispheres, enabling them to function as a coordinated whole. The largest commissure is the *corpus callosum*, which lies superior to the lateral ventricles, deep within the longitudinal fissure (see B.4). Less prominent examples are the *anterior and posterior commissures*.

Association fibers: They connect different parts of the same hemisphere. Short association fibers connect adjacent gyri. Long association fibers are bundled into tracts and connect different cortical lobes.

Projection fibers: These fibers enter the cerebral hemispheres from lower brain or cord centers, and also leave the cortex to connect to lower areas. They tie the cortex to the rest of the nervous system and to the body's receptors and effectors. In contrast to commissural and association fibers, which run horizontally, projection fibers run vertically as Figure B.4 (right) shows. At the top of the brain stem, the projection fibers on each side form a compact band, the internal capsule, that passes between the *thalamus* and some of the *basal nuclei*. Beyond that point, the fibers radiate in fan shape through the cerebral white matter to the cortex. This distinctive arrangement of projection tract fibers is known as the *corona radiata*.

B.3 Cerebellum

The cerebellum, exceeded in size only by the cerebrum, accounts for about 11% of total brain mass. The cerebellum is located dorsal to the pons and medulla (and to the intervening fourth ventricle). It protrudes under the occipital lobes of the cerebral hemispheres, from which it is separated by the transverse *cerebral fissure*.

By processing inputs received from the cerebral motor cortex, various brain stem nuclei, and sensory receptors, the cerebellum provides the precise timing and appropriate patterns of skeletal muscle contraction for smooth, coordinated movements and agility needed for our daily living. Cerebellar activity occurs subconsciously; that is, we have no awareness of its functioning.

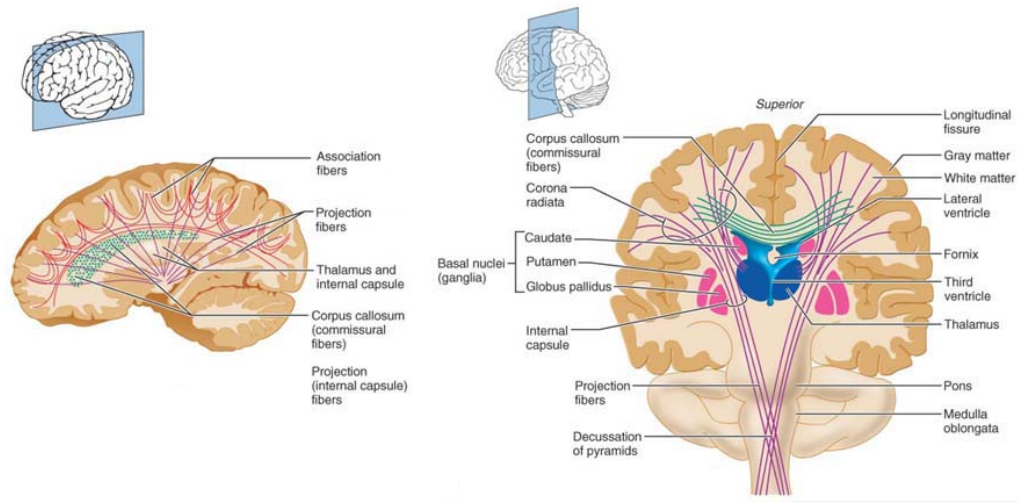


Figure B.4: Fibers tracts in white matter. (Source: [Marieb 2006]).

The cerebellum is bilaterally symmetrical; its two cerebellar hemispheres are connected medially by the *vermis*. Its surface is heavily convoluted, with fine, transversely oriented pleatlike gyri known as *folia*. Deep fissures subdivide each hemisphere into anterior, posterior, and flocculonodular lobes (Figure B.5). The small propeller-shaped flocculonodular lobes, situated deep to the vermis and posterior lobe, cannot be seen in a surface view.

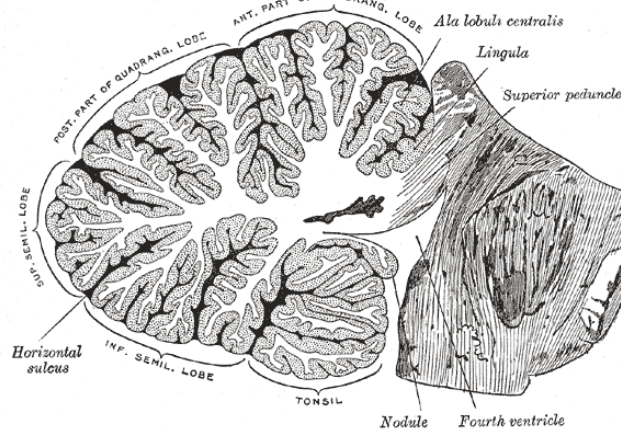


Figure B.5: Sagittal section of the cerebellum. Some lobes and interior structures are shown. The showed cut is near the mid line of the body. (Source: [Gray 1918]).

B.4 Meninges

Nervous tissue is soft and delicate, and neurons are injured even by slight pressure. However, the brain is protected by bone (the skull), membranes (the meninges), and a watery cushion (cerebrospinal fluid)(sec. B.5). Furthermore, the brain is protected from harmful substances in the blood by the blood-brain barrier.

The meninges are three connective tissue membranes that lie just external to the CNS organs. They cover and protect the CNS, protect blood vessels and enclose venous sinuses, contain cerebrospinal fluid, and form partitions in the skull. From external to internal, the meninges (singular: meninx) are the *dura mater*, *arachnoid mater*, and *pia mater* (Figure B.6(a)).

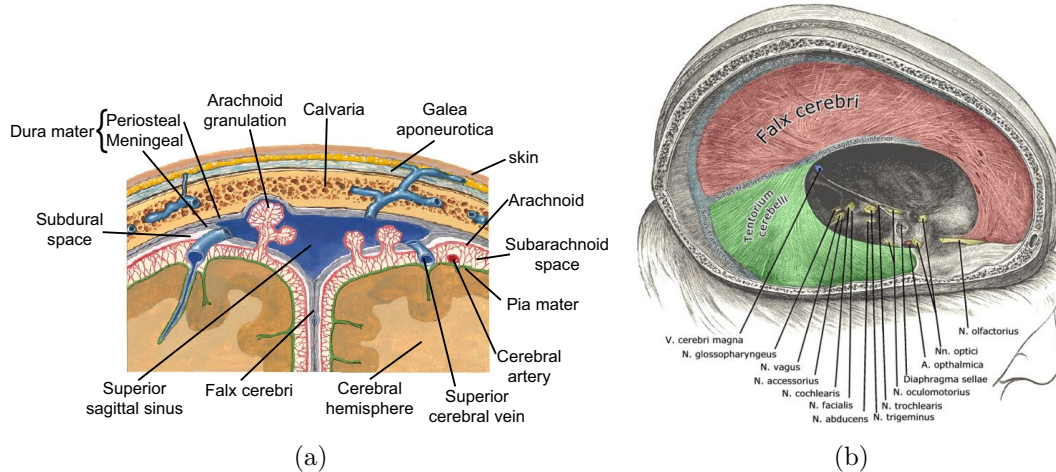


Figure B.6: (a) Coronal cut at the top of the head showing the relationship of the dura mater, arachnoid, and pia mater. The meningeal dura forms the falx cerebri. The superior sagittal venous sinus is enclosed by the dural membranes. (Source: [Netter 2010]). (b) Partitioning folds of dura mater: falx cerebri and tentorium cerebelli. (Source: [Gray 1918]).

B.4.1 Dura Mater

The leathery *dura mater*, meaning “tough mother”, is the strongest meninx. Where it surrounds the brain, it is a two-layered sheet of fibrous connective tissue. The more superficial *periosteal layer* is attached to the inner surface of the skull (the *periosteum*) (Fig B.6(a)). There is no dural periosteal layer surrounding the spinal cord. The deeper *meningeal layer* forms the true external covering of the brain and continues caudally in the vertebral canal as the dural sheath of

the spinal cord. The brain's two dural layers are fused together except in certain areas, where they separate to enclose dural sinuses that collect venous blood from the brain and direct it into the internal jugular veins of the neck.

In several places, the meningeal dura mater extends inward to form flat partitions that subdivide the cranial cavity. These dural septa, which limit excessive movement of the brain within the cranium, include the following (Fig. B.6(b)):

Falx cerebri: A large sickle-shaped (falks = sickle) fold that dips into the longitudinal fissure between the cerebral hemispheres. Anteriorly, it attaches to the *crista galli* of the *ethmoid bone*.

Falx cerebelli: Continuing inferiorly from the posterior falx cerebri, this small midline partition runs along the *vermis* of the cerebellum.

Tentorium cerebelli: Resembling a tent over the cerebellum, this nearly horizontal dural fold extends into the *transverse fissure* between the cerebral hemispheres (which it helps to support) and the cerebellum.

B.4.2 Arachnoid Mater

The middle meninx, the *arachnoid mater*, or simply the *arachnoid*, forms a loose brain covering, never dipping into the sulci at the cerebral surface (Fig. B.6(a)). It is separated from the dura mater by a narrow serous cavity, the *subdural space*, which contains a film of fluid. Beneath the arachnoid membrane is the wide *subarachnoid space*. Weblike extensions span this space and secure the arachnoid mater to the underlying pia mater. (Arachnida means “spider” and this membrane was named for its weblike extensions.) The subarachnoid space is filled with cerebrospinal fluid and also contains the largest blood vessels serving the brain. Because the arachnoid is fine and elastic, these blood vessels are poorly protected.

Projections of the arachnoid mater called *arachnoid granulations* protrude superiorly through the dura mater and into the *superior sagittal sinus*. Cerebrospinal fluid is absorbed into the venous blood of the sinus by these granulations (sec. B.5).

B.4.3 Pia Mater

The *pia mater*, meaning “gentle mother”, is composed of delicate connective tissue and is richly provided with tiny blood vessels (Fig. B.6(a)). It is the only

meninx that clings tightly to the brain, following its every convolution. Small arteries entering the brain tissue carry ragged sheaths of pia mater inward with them for short distances.

B.5 Cerebrospinal Fluid

Cerebrospinal fluid (CSF), found in and around the brain and spinal cord, forms a liquid cushion that gives buoyancy to the CNS structures (Fig B.7). By floating the brain, the CSF effectively reduces brain weight by 97% and prevents the brain from crushing under its own weight. CSF also protects the brain and spinal cord from blows and other trauma. Additionally, although the brain has a rich blood supply, CSF helps nourish the brain, and there is some evidence that it carries chemical signals (such as hormones and sleep- and appetite-inducing molecules) from one part of the brain to another.

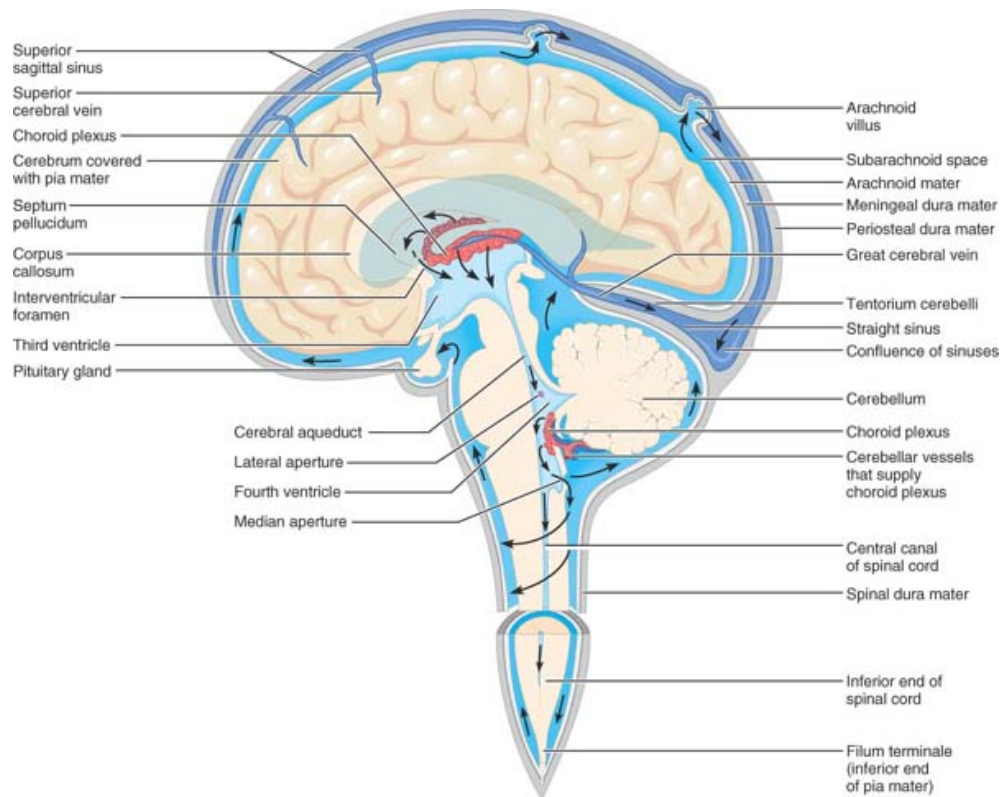


Figure B.7: Circulation of the CSF, produced in the choroid plexus and absorbed in the arachnoid granulations or villus (Fig. B.6(a)). (Source: [Marieb 2006]).

CSF is similar in composition to blood plasma, from which it is formed. However, it contains less protein than plasma and its ion concentrations are different. For example, CSF contains more Na^+ , Cl^- , and H^+ than does blood plasma, and less Ca^{2+} and K^+ . CSF composition, particularly its pH, is important in the control of cerebral blood flow and breathing.

The *choroid plexuses* that hang from the roof of each ventricle form the CSF (Figure B.7). These plexuses are clusters of broad, thin-walled capillaries (plex = interwoven) enclosed first by pia mater and then by a layer of ependymal cells lining the ventricles. These capillaries are fairly permeable, and tissue fluid filters continuously from the bloodstream. However, the choroid plexus ependymal cells are joined by tight junctions and have ion pumps that allow them to modify this filtrate by actively transporting only certain ions across their membranes into the CSF pool. This sets up ionic gradients that cause water to diffuse into the ventricles as well. In adults, the total CSF volume of about 150 ml (about half a cup) is replaced every 8 hours or so; hence about 500 ml of CSF is formed daily. The choroid plexuses also help cleanse the CSF by removing waste products and unnecessary solutes. Figure B.7 shows the circulation of the CSF in the central nervous system.

B.5.1 Ventricles

The ventricles are continuous with one another and with the central canal of the spinal cord (Figure B.8). The hollow ventricular chambers are filled with *cerebrospinal fluid* (sec. B.5) and lined by ependymal cells, a type of neuroglia.

The paired lateral ventricles, one deep within each cerebral hemisphere, are large C-shaped chambers. Anteriorly, the lateral ventricles lie close together, separated only by a thin median membrane called the *septum pellucidum*. Each lateral ventricle communicates with the narrow third ventricle in the *diencephalon* via a channel called *interventricular foramen* (*foramen of Monro*) (Fig. B.8). The third ventricle is continuous with the fourth ventricle via the canal-like *cerebral aqueduct* that runs through the midbrain. The fourth ventricle lies dorsal to the pons and superior to the medulla. It is continuous with the central canal of the spinal cord inferiorly. Three openings mark the walls of the fourth ventricle: the *paired lateral apertures* in its side walls and the *median aperture* in its roof. These apertures connect the ventricles to the *subarachnoid space*, a fluid-filled space surrounding the brain (sec. B.5).

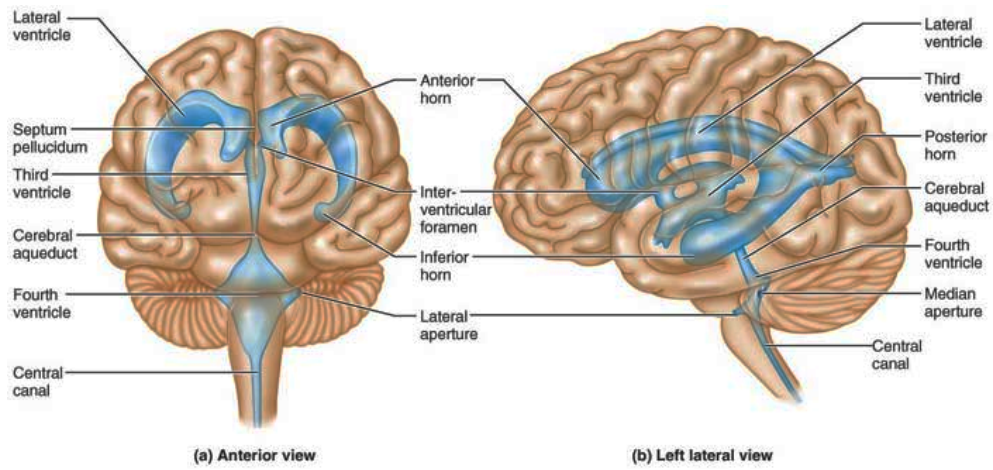


Figure B.8: Ventricles of the brain. (Source: [Marieb 2006]).

Magnetic Resonance Imaging

Magnetic Resonance Imaging (MRI) is a popular medical image modality, which allows to visualize detailed internal structures of the brain. Therefore, it has been naturally adopted as support in the present work. A brief introduction of this technique will be given in this section, aiming to help to better understand how the images are built, and how their characteristics may be exploited during a segmentation step, or any other application. The information presented in this section can be found in [Gili 2007].

C.1 Magnetic Resonance

Since its early stages in 1977, when the first MRI human body scan was acquired using a prototype device called “Indomitable” and developed by Raymond Vahan Damadian [Mansfield 1978] (Figure C.1(a)), the field of neuroimaging has benefited the most with the availability of such images. Using MRI, it is possible to obtain high-resolution images of soft tissues, at a level of detail that can be hardly reached using other 3D images modalities. Figure C.1(b) shows a MRI scanner.

Magnetic Resonance (MR) is a physical phenomenon occurring in some particles, such as electrons, protons; and in atomic nuclei with an odd number of protons (Z) and/or and odd number of neutrons (N). These particles can selectively absorb and re-emit electromagnetic energy if they are located in a magnetic field. The process of energy absorption is called *resonance*, and *relaxation* is the process in which the excess of energy is released as radio frequency waves. These waves can be detected by an antenna, and the received signal can be used to construct an image (MRI), to perform a spectrometric analysis (MRS), or a combination of both. From a general point of view, the process is shown in Figure C.2. Magnetic Resonance Imaging for clinical diagnosis utilizes the MR of the hydrogen nucleus (protons). Other nuclei, such as Na^{23} , have been studied to be used in neuroimaging, but they are not yet commonly utilized.

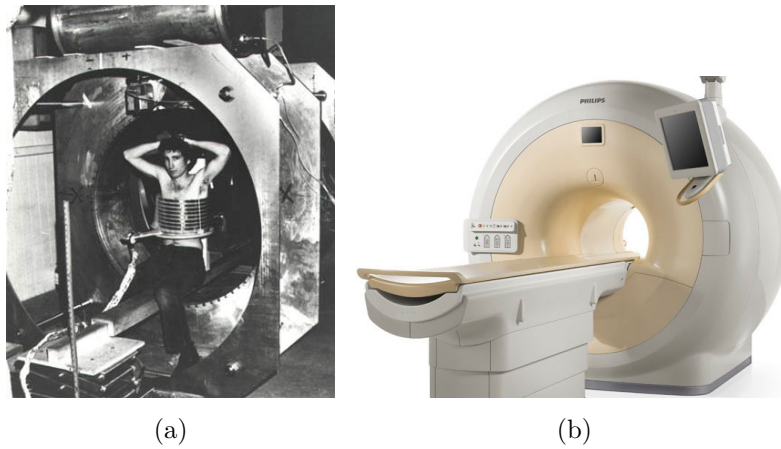


Figure C.1: (a) First Magnetic Resonance machine for acquiring images of the human body, developed by Raymond Vahan Damadian. The machine was called “Indomitable” and was used to acquire the first human body image in 1977. (Source: Fonar Corporation website 2012, <http://www.fonar.com/nobel.htm>). (b) MRI system Philips Achieva 1.5T A-series. (Source: Philip website 2012, http://www.healthcare.philips.com/us_en/).

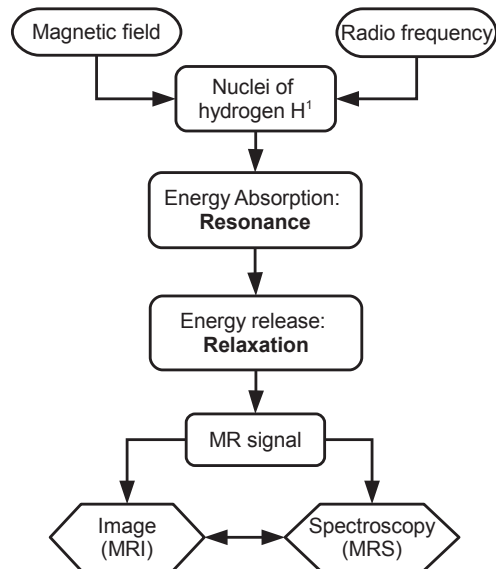


Figure C.2: MRI and MRS are two different ways to present the information obtained using the nuclear magnetic resonance phenomenon.

C.2 Image acquisition

To acquire information about body tissues through MR, first the magnetization \vec{M} of the tissue in the body is aligned using a powerful magnetic field \vec{B} (Figure C.3(a)). This magnetization \vec{M} is the sum of the magnetic moment of all the nuclei contained in the volume of the body. The magnetic moment of the nuclei $\vec{\mu}$ in this magnetic field can be in two states: UP (low energy) or DOWN (high energy). The magnetic moments precess around the direction of \vec{B} (Figure C.3(b)) with a frequency of precession or resonance f_p . Without intervention, the spin UP and DOWN follows a Boltzmann distribution in thermodynamic equilibrium. However, while the nuclei are in this field, they can absorb electromagnetic energy of the particular frequency f_p , phenomenon called *resonance*. If an electromagnetic signal with the appropriate frequency is emitted, the nucleus in state UP absorbs energy and moves to state DOWN. As the nuclei change their states, the tissue magnetization \vec{M} changes, and its electromagnetic momentum moves as shown in Figure C.4. This movement depends on the energy absorbed, i.e., on the number of nuclei that change their state. The displacement angle α of the electromagnetic momentum depends on the energy emitted by the electromagnetic pulse of frequency f_p . When the direction of the tissue magnetization is orthogonal to the external magnetic field, the number of nuclei in UP and DOWN states are equal. After the emission of a electromagnetic pulse, all the magnetic moments of the nuclei $\vec{\mu}$ are in phase; therefore the magnetization \vec{M} has a precession movement as shown in Figure C.4 (if nuclear moments have random orientation, \vec{M} has no preferential orientation in plane x,y and there is no precession).

If the radio frequency signal stops, the tissue magnetization returns to its initial state. This process is called *relaxation*. The relaxation continues until the ratio between UP and DOWN nuclei reach a Boltzmann equilibrium. The return of the magnetization to its initial state produces changes in the magnetic field that can be detected with antennas, inducing a signal known as the Free Induction Decay (FID) (Fig. C.5(a)). The relaxation process depends on many factors, such as the molecule in which the nuclei are, the material (tissue) in which the molecule is immersed, or the external magnetic field. Five different variables measures in the relaxation are used to built images: spin density, T_1 and T_2 relaxation times; and flow and spectral shifts. By changing the parameters in the scanner it is possible to weight the effect of one of these variables over others. This effect is used to create contrast among different types of body tissues. In addition

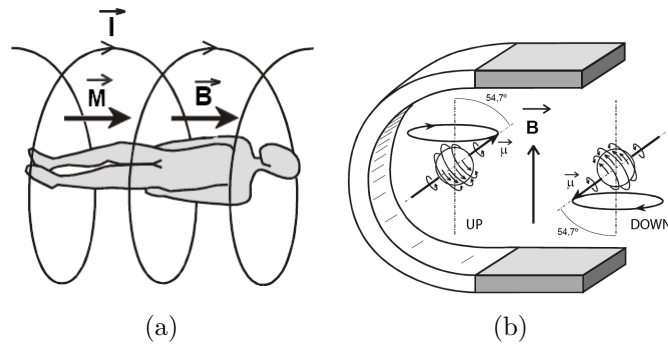


Figure C.3: (a) Magnetic field \vec{B} created by an helix-shaped conductor (solenoid) through which direct current flows \vec{I} . (b) Scheme of the interpretation on classical mechanics of the nuclei precession. This physical phenomenon is actually explained by quantum mechanics but the interpretation in classical mechanics is easier to understand. The scheme shows the precession of the magnetic moments of the nuclei $\vec{\mu}$ around the direction of the magnetic field \vec{B} . The two states “UP” (low energy) and “DOWN” (high energy) of the magnetic moments are shown. (Source: [Gili 2007]).

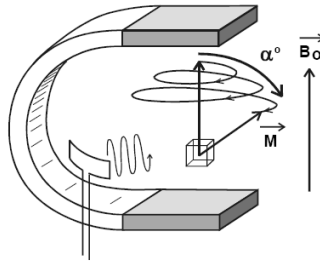


Figure C.4: Movement of the magnetization vector \vec{M} when the nuclei of a volume absorb energy in the resonance induced by the radio frequency signal of frequency f_p . (Source: [Gili 2007]).

to the traditional anatomical images, images with physiological or biochemical information, and dynamic images can also be acquired. The most used types of MR images are explained below:

Spin density weighted MRI: These images are also called proton density (PD) weighted. The value of the magnetization is proportional to the density of hydrogen nuclei. Therefore, when the relaxation starts, the signal detected by the antenna is proportional to the density. Thus, images of H density can be obtained.

T₁-weighted MRI: The projection of the magnetization vector of the tissue, \vec{M} , on the longitudinal axis is M_z (Fig. C.5(b)); and, as explained before,

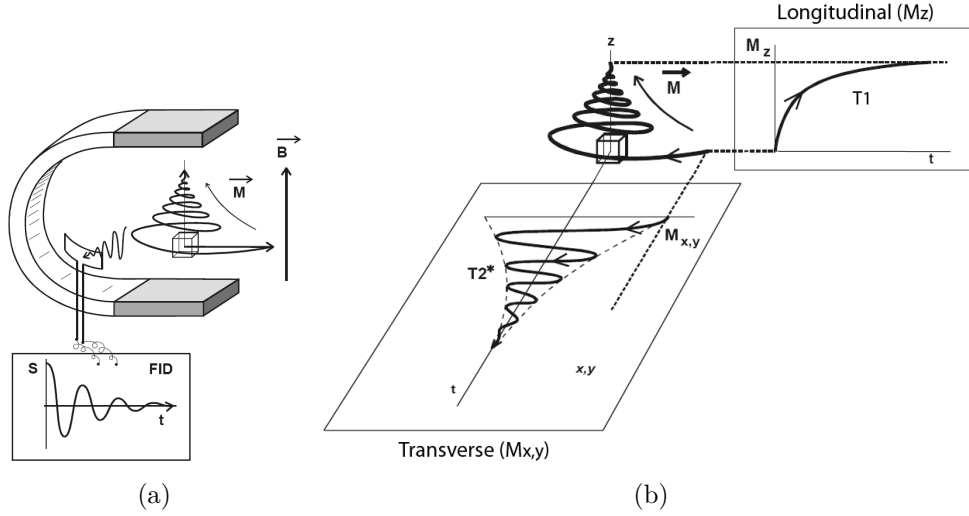


Figure C.5: (a) Detection of the changes in the electromagnetic field when the magnetization vector \vec{M} returns to its initial position in the relaxation process. The signal induced in the receiving antenna is known as the Free Induction Decay (FID). (b) The magnetization vector \vec{M} can be measured in the longitudinal z or transverse (x, y) plane. To obtain T_1 -weighted or T_2 -weighted images, the magnetization vector is measured in the longitudinal M_z or in the transverse plane $M_{x,y}$ respectively. (Source: [Gili 2007]).

\vec{M} recovers its initial value, aligned with the magnetic field \vec{B} , once the relaxation is complete. Therefore, when the relaxation is over (longitudinal relaxation), M_z will be equal to $M_{z,eq}$, the initial value of $\|\vec{M}\|$ when the moments of the nuclei are in thermodynamic equilibrium. Accordingly, the study of longitudinal relaxation shows how quickly the initial state is recovered. The longitudinal relaxation has an exponential form regulated by a time constant T_1 measured in milliseconds:

$$M_z(t) = M_{z,eq} (M_{z,eq} - M_z(0)) e^{(-t/T_1)} \quad (\text{C.1})$$

If \vec{M} is orthogonal to \vec{B} at the beginning of the relaxation (Fig. C.5(a)), then $M_z(0) = 0$ and the parameter T_1 can be seen as the time it takes to the magnetization \vec{M} to recover 63% of its initial value ($M_z(T_1) = M_{z,eq} (1 - e^{-1})$). The lower the value of T_1 is, the faster the initial state is recovered. Therefore, a short T_1 means a faster release of energy.

From a biophysical point of view, the energy release is an energetic exchange between the nucleus of H and the environment. The energy release occurs

because of the molecular structures which use this energy in their Brownian motions of rotation, vibration or translation. Hence, the T_1 value is strongly dependent on the type and mobility of molecules in interaction with H .

T_2 -weighted MRI: The projection of the magnetization vector of the tissue, \vec{M} , on the transverse plane is $M_{x,y}$ (Fig. C.5(b)). It is possible to obtain information related to the biochemical structure of the tissue by studying $M_{x,y}$ during relaxation (transverse relaxation).

After a electromagnetic pulse of frequency f_p , the nuclear moments are in phase (precession), but as time passes, they gradually go out of phase because of differences in the magnetic field sensed by each nucleus. When the nuclear spins have reached their random orientation, $M_{x,y} = 0$ and the magnetization vector, \vec{M} , is aligned with the magnetic field \vec{B} (Fig. C.5(b)). The value of the magnetic field sensed by each nucleus depends on the external magnetic field \vec{B} , but also on the biochemical environment because all the moving electric charges of its environment modify the value of the magnetic field locally, for example, the presence of ions. The evolution in time of the transverse magnetization corresponds to a sinusoid at the relaxation frequency, f_p , damped by an exponential decay (Fig. C.5(b)). If only the influence of an homogeneous external magnetic field, \vec{B} , is considered, the exponential decay of the transverse magnetization is governed by a time parameter called T_2 :

$$M_{x,y}(t) = M_{x,y}(0)e^{(-t/T_2)} \quad (\text{C.2})$$

The T_2 parameter can be seen as the time it takes to the transverse magnetization to lose 63% of its value ($M_{x,y}(T_2) = M_{x,y}(0)e^{-1}$). If the influence of the external magnetic field inhomogeneities, and the local magnetic variations that permanently act on the nuclei are also taken into account, the time parameter is called T_2^* . Usually T_2 is higher than T_2^* , because when all causes that can produce asynchronism are considered, the relaxation is more incoherent.

Figure C.6 shows a scheme for comparing the gray level of different tissues in the types of MR images explained above. These particularities will be exploited during the segmentation (sec. 2.3.1.3).

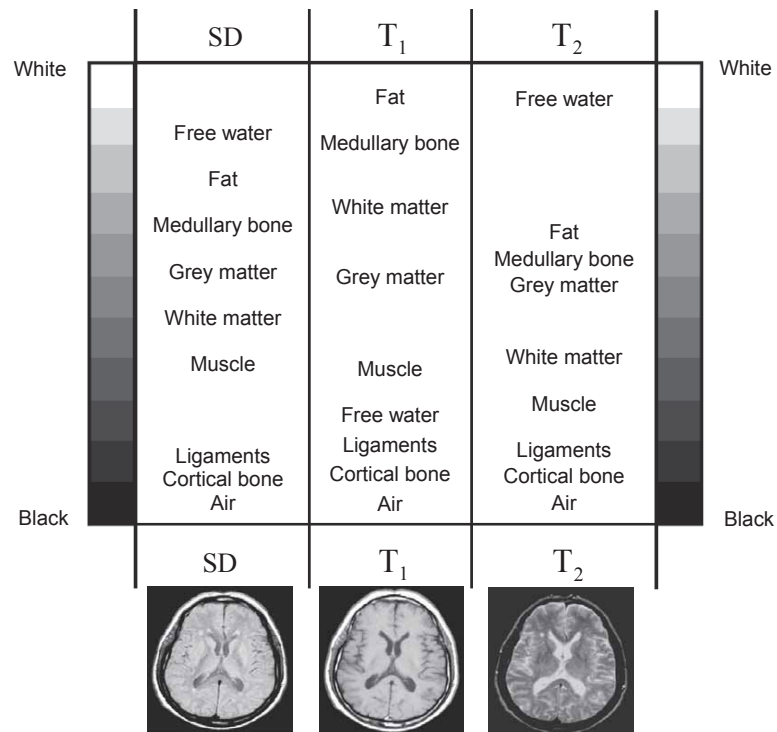


Figure C.6: Comparison between the gray level of different tissues in Spin Density (SD) weighted, T₁-weighted and T₂-weighted MR images. (Source: [Gili 2007]).

